Label-free Investigation of Cells with Phase Imaging, Diffraction Tomography, and Raman Spectroscopy

Zhengyuan Tang

Supervised by Prof Bryan Hennelly

A thesis presented for the degree of Doctor of Philosophy

ELECTRONIC ENGINEERING DEPARTMENT
MAYNOOTH UNIVERSITY

2022/10/10

Dedication

I would like to dedicate this thesis to everyone who I have met and cared about over these years.

Declaration

I hereby certify that the material contained within this thesis is entirely my own work, does not to the best of my knowledge breach any law of copyright, and has not been taken from the work of others save to the extent that such work has been cited and acknowledged within the text of my work.

Signed: zhengyuan Tang

ID Number: 15101304

Date: 10/25/2022

Acknowledgements

This PhD project is an achievement over five-years, including a difficult pandemic period. Without the support of others, it would be impossible to complete this thesis.

Most importantly, I would like to thank my supervisor, Prof. Bryan Hennelly, for giving me this opportunity to become a member of this great academic community and to work on this research project. Bryan Hennelly is an inspirational supervisor. Thanks for his patient guidance and support in my studies and life.

I would also like to thank Sinead Barton for patiently teaching me the theory of Raman spectroscopy when I was an academic novice. Also, thanks to Kevin O'dwyer for helping me in the lab and teaching me tips on building, aligning, and operating optical systems. Additionally, I would like to thank Winnik Julianna for her remote guidance on Optical Diffraction Tomography.

Once again, I would like to thank all the students and faculty in the Department of Electrical Engineering at MU for helping me pick myself up when I was down. I would also like to thank my friends at the gym for helping me reduce stress and maintain sufficient energy to face every challenge.

I will never forget the helps and encouragements from my friends and roommates. Thanks to Philip Cumiskey, David Boyle, Jing Tian, Zhengwei Wang, Anki Hu, Evian Hong and so on.

No one was more important to me in pursuing this research project than my family, whose love and guidance embraced me no matter how far away I was. I am deeply grateful to my family who have always supported me.

Studying and living in Ireland over the years has been a long journey, but everything I have experienced, learned, and absorbed during this journey will become the wealth of my life. Thank you to everyone I met on this journey.

Contents

List of Figures

List of Tables

Abstract

Typically microscopic imaging of cells requires labelling or staining of some kind in order to enhance the contrast of the cells. For example, hematoxylin and eosin are applied in clinical histopathology in order to perform diagnosis for a range of disease; a common example is the Pap Smear. Subsequent analysis is purely qualitative and relies on the experience and expertise of the observer. Another example is the use of fluorescent labels that can adhere to proteins and provide revealing images of sub-cellular features. In this thesis, we seek to avoid the use of labels entirely and to provide meaningful quantitative information about the morphology of cells as well as their chemical composition. The primary goal is to develop an optoelectronic platform that can classify cells into different disease groups using only non-invasive label free technology, which could provide a valuable tool to clinicians and basic researchers. To this end, this thesis develops a number of optical systems in the field of quantitative phase imaging, optical diffraction tomography, and Raman spectroscopy. Quantitative phase imaging provides morphological information by accurately measuring the phase delay on an illuminating laser that is imparted by the cell. Optical diffraction tomography extends this approach by recording phase images from different oblique illuminations and constructing a 3D tomographic image of the refractive index, and Raman spectroscopy provides chemical information by measuring the inelastic scattering from the molecular bonds within the sample. Several novel contributions are made in terms of new optical implementations or models, each being described by a separate chapter.

Chapter 1

Introduction

1.1 Label-Free Optical Microscopy for biology

Microbiology relates to living organisms which have too small size to obverse by eye. As a subclass of microbiology, cell biology plays an important role in the field of clinical pathology and disease diagnosis. For example, altered DNA activity can contribute to a change in the size of cell nucleus, which is a common feature in cancer cells and one which is often used as a diagnostic marker of disease. A change in cellular morphology can be qualitatively observed by microscopy, and provides a basis for cancer diagnosis by trained pathologists. In 1595, Zacharias Jansen invented the first compound light microscope and in 1676, the Dutch scientist, Antonie van Leeuwenhoek, who is considered as a father of microbiology, designed a single-lens microscope to observe microbes. In 1752, John Dollond invented the achromatic doublet lens, which could mitigate the problem of chromatic aberration, which was a significant milestone in the development of microscopy. Another milestone was the development of the oil immersion objective, invented by Sir David in 1812. Ernst Abbe is regarded as one of the most significant contributors to the development of microscopy. His work on imaging and diffraction theory forms the basis of modern optical design today. He also invented the first apochromatic microscope in 1868. Perhaps the most significant development since the work of Abbe is the advancement of cell fixation and staining methods that enabled microstructures such as organelles within cells to be observed.

In many cases, biological cells are effectively transparent or semi-transparent due to their inherently weak scattering property, and this results in the problem of low image contrast when using brightfield optical microscopy. A common solution to this problem is to enhance the image contrast by making use of cell labeling technology. This involves the addition of a stain or dye to the sample before the observation. Various staining materials have been developed; some stains, such as hematoxylin and eosin stains (H&E), add color contrast to the cell nucleus. Another staining process that is perhaps the single most important development in microbiology in the past century relates to fluorescence. The first working fluorescent microscope was developed by Oskar Heimstaedt in 1911 and since then the area has undergone significant development, particularly in the area of targeted fluorescent proteins that are capable

of attaching to specific subcellular features. The invention of the confocal microscope further enhances this approach providing three dimensional images of fluorescently labeled samples. These dyeing and staining methods for imaging biological samples have provided a rich accessibility to observe the micro-structure within cells. However, these cell labeling approaches can suffer from the photobleaching and phototoxicity, and thereby, impedes the cell activity and functionality. [7] It can be argued that cell labelling for image contrast enhancement is an invasive method with a necessary processing step to convert the naturally transparent cells into color cells. To avoid the disadvantages of staining and fluorescent labelling, various label-free and non-invasive microscopic imaging methods have also been developed over the past century. Two well established label-free contrast-enhancement microscopy methods for biological cells are phase contrast microscopy [8] and differential interference contrast (DIC) microscopy. [9] In the early 1930s, Zernike invented phase contrast microscopy, in which the phase difference between the unscattered beam and scattered beam could be modulated in order to construct an interference image that improves the contrast of subcellular features; however, the phase contrast microscopy suffers from the problem of the halo artifact that usually appears as phase contrast reversal on the edge of cells and prevents the technique from providing quantitative information relating to the phase delay (thickness×refractive index) imparted by the sample. DIC microscopy was inverted by Georges Nomarski in the mid-1950s and employs two orthogonally polarised illuminations to pass through the sample; the two resultant images are combined (with a slight relative displacement) to produce an image with a significant contrast enhancement. DIC allows observation of thicker biological cells and avoids the halo artifact. Phase contrast microscopy and DIC microscopy enable the visualization of the cellular features, but the quantitatively morphological information, such like depth and height of cells, cannot be obtained from either of these methods.

1.2 Quantitative phase imaging

Quantitative measurement of morphological features in a biological sample can be achieved using a broad class of methods known as quantitative phase imaging (QPI). Over recent decades several different QPI methods have been developed that enable measurement of the phase delay imparted by the specimen when light passes through it. [10, 11] QPI methods have been proven to be effective in studies of cellular dynamics relating to nanometric changes in cell morphology, [12, 13] imaging semiconductors, [14] and the study of material composition. [15] Depending on the type of light source, these QPI methods can be classified into sub-classes: one is coherent QPI methods such as digital holographic microscopy (DHM), [12, 13, 16, 17] and optical quadrature microscopy (OQM). [18–20] The second sub-class is partially coherent white-light QPI, such as spatial light interference microscopy (SLIM), [21, 22] differential phase contrast (DPC), [23,24] transport-of-intensity equation (TIE), [25,26] lensless microscopy. [27, 28] All of these QPI methods can quantify the phase delay introduced by the sample, but these methods differ in ease of implementation, imaging resolu-

tion, depth of field, and coherent noise. More details about QPI can be found in the review published by Gabriel Popescu's group. [10] Among all QPI methods, DHM is the earliest, and arguably still, and one of most popular QPI methods, and it plays an important role in this thesis. It is discussed in more detail below as well as in Chapter 2, 4, and 5. Although of lesser interest in the context of the thesis as a whole, the white-light QPI method known as SLIM is also implemented in this thesis and is reviewed in Chapters 2 and 3. SLIM uses white light source and requires the recording of four intensity images, each of which is the result of modulating the phase shift between the unscattered and scattered wavefields. The phase image of the sample is reconstructed via substituting the 4 recorded intensity images into a 4-step phase shift algorithm.

DHM utilizes a spatio-temporal coherent source to generate the object wavefield (the phase of which is to be measured) and a known reference wavefield. By combining these two wavefields interferometrically, DHM enables the encoding of both the amplitude and phase information of the object wavefield. The combination of the object wavefield and the reference wavefield generates an interference pattern called a 'hologram' on a digital camera plane. Following recording of the digital hologram, the object wavefield amplitude and phase information can be decoded via straight-forward numerical processing on the recorded hologram.

The origin of DHM begins with the concept of holography originally proposed by Dennis Gabor in 1948. [29] In the initial holography implementation, the hologram was recorded on a photographic film. Then, by using the reference beam to illuminate the recorded hologram, the complex twin images (including a virtual image and a real image that are conjugates of one another) of the object wavefield, together with a zero order (DC) term pattern could be reconstructed from the recorded hologram. Due to the invention of holography (and indeed its later success owing to the work of Leith and Upatnieks on off-axis holography), Dennis Gabor was awarded the Nobel prize in 1971. However, it must be noted that the Gabor's in-line holography has a significant drawback called the 'twin image problem' whereby the twin images are overlapping in space cannot be separated; this results from the inline design that is shown in Fig. 1.1(a). As shown in this figure, when the reference beam and the object beam follow the same optical path in the recording of the hologram, then in the reconstruction process, the zero order (DC) pattern and two twin images will spatially overlap on the same optical path; thereby, the desired reconstructed object wavefield from one of twin images is always marred by the presence of the defocused twin image and zero-order pattern.

Following the invention of Gabor holography, and as a consequence of the advancement of laser with its property of high temporal and spatial coherence, interference formation became easier and there was rapid progress and development in the area of holography. The most significant breakthrough appears in 1962, when, in order to overcome the 'twin image problem' occurring in Gabor's holography, Americans Emmett Norman Leith and Juris Upatnieks who were inspired by the theory of frequency modulation in the field of radio communication, designed the off-axis holography technique. [30] The illustration of the off-axis holography approach is shown in Fig. 1.1(b): In the figure, the reference beam and the object beam are seen to combine at an off-axis angle to record the hologram; Then, using the same reference beam illu-

minating on the hologram, the reconstructed twin images and zero order pattern are spatially offset such that the observation of object wavefield in one of twin image is isolated from the other terms.

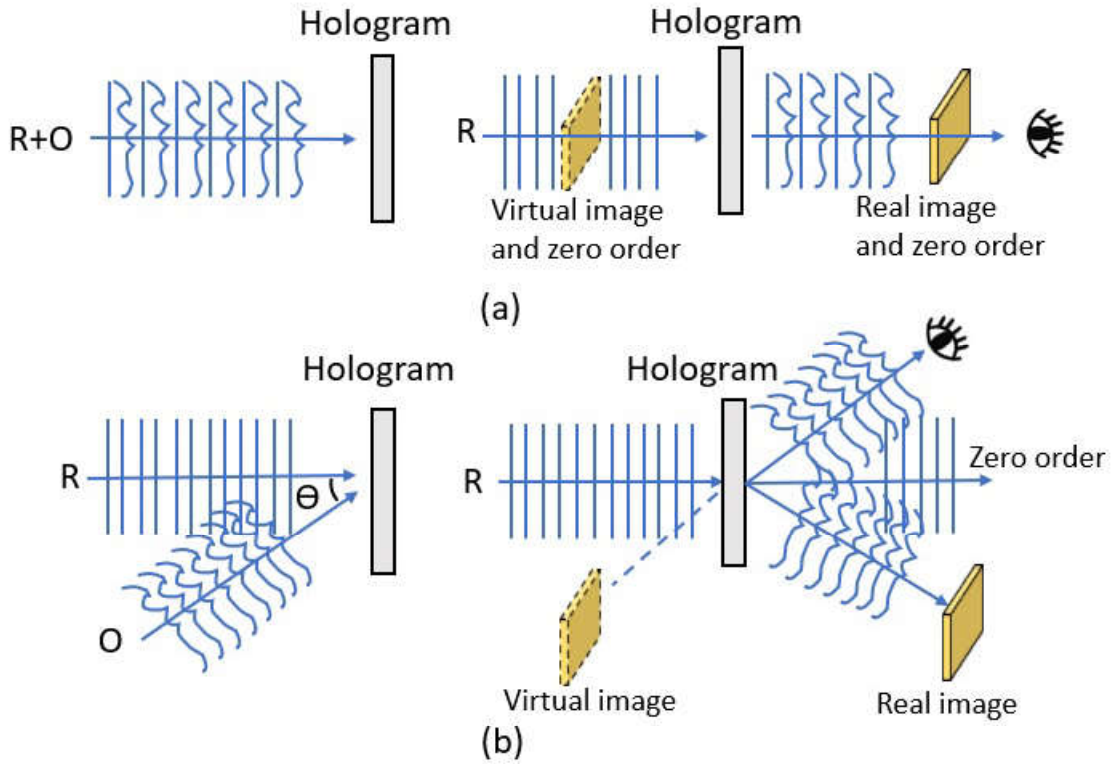

Figure 1.1: (a). Illustration of Gabor's inline holography. The hologram recording procedure is on left side: the reference beam and the object beam illuminate along the same path to construct the hologram; object wavefield reconstruction is on right side: the twin images and zero order term are seen to be overlapping along the observed optical path. (b). Illustration of off-axis holography. The hologram recording procedure is on left side: the reference beam and the object beam combine at an angle to create the hologram; object wavefield reconstruction is on right side: here the twin images and zero order term are spatially separated for an easy observation.

Owing to the development of computer science and photoelectric detection technology, digital holography was realised whereby a camera can be utilized to replace the photographic film in the recording process. The desired object wavefield can be numerically reconstructed from this digital hologram by numerical processing of Fourier transform and spatial filtering which are described in Section 2.2.2 and Section 2.2.6. Compared with conventional digital imaging systems, the image reconstructed from digital holography includes both the amplitude field and the phase field. Thus, the reconstructed image contains not only the intensity information (equal to the square of amplitude field) which is obtained by conventional digital imaging systems, but also the phase information. The concept of digital holography was originally proposed and implemented by Goodman *et. al.* in 1967. [31] However, the truly mature digital holography in the modern sense occurred after the rapid development of the charge-coupled

device (CCD) cameras and complementary metal oxide semiconductor (CMOS) cameras after 1990s. In 1994, Ulf Schnars and Werner Jüptner performed digital holography using a CCD camera with high resolution in their digital holography setup to begin the field of modern digital holographic recording and reconstruction. [32]

Digital Holographic Microscopy (DHM) is a method that combines the techniques of digital holography and optical microscopy. The use of optical microscopy enlarges the details of minute biological samples. DHM has several advantages over other coherent QPI methods. The first key advantage of DHM is the ability for computational aberration compensation in order to improve image quality. [33, 34] Another important advantage is the capability of refocusing the image using numerical propagation algorithms, [35, 36] which can be coupled with autofocus metrics for automatically focusing over a wide depth of field. [37, 38] The third advantage is that DHM has a large depth of field. [17] However, a disadvantage of DHM that must be mentioned is the presence of coherent noise in the image. Due to the use of a coherent laser source in DHM, the scatterers and reflections at various positions in the optical system will all contribute to an unwanted interference noise pattern. This speckle noise is unavoidably collected by camera but the problem can be mitigated by using a laser with a low coherence length [39–41] or by using a synthetic aperture method that will be applied in this thesis and be explained in Chapter 4.

DHM is particularly useful in imaging and analyzing biological cells or tissues. In the past few decades, DHM has received widespread interest in biology. Christian Depeursinge *et. al.* implemented both the reflective and the transmission DHM setup to analyse epithelial cells, pollen, live amoebas and neuronal cells of a rat, and achieved nanometric measurements of the thickness of cells and cellular morphology. [13,33,42] Björn Kemper *et al.* [12,37,43–45] made several early contributions in cell analysis used by DHM and Myung K. Kim *et. al.* was another pioneer of note in this area. [46]. Cuche E *et. al.* further developed the commercial reflective and transmission DHM setups, resulting in a company named *LyneeTec*. Several more applications of DHM in biology are reviewed by Iliyan Peruhov and Emilia Mihaylova. [47]

A recent development that builds on DHM (and the Born or Rytov approximation) is the emerging area of Optical Diffraction Tomography (ODT), which requires the recording of multiple phase images resulting from multiple angular illuminations. ODT can reconstruct a 3D refractive index map of object to reveal internal features within the cell body. The ODT technique is also investigated in this thesis, and a more detailed description of ODT research is provided in Chapter 2 and Chapter 5.

1.3 Chemical imaging using spectroscopy

The history of spectroscopy begins when Isaac Newton first used prisms to separate visible light into different colors. Spectroscopic methods can be divided into several main types. The first type is absorption spectroscopy, which results from the absorption of radiation of particular energy (or wavelength) by a sample of interest due to some manner of quantum mechanical change induced in the molecule or atom within

the sample. Common absorption spectroscopy methods include Near-infrared (NIR) spectroscopy [48] and Fourier transform infrared (FT-IR) spectroscopy [49]. The second type of spectroscopy is emission spectroscopy, which induces the atoms or molecules within the object to transition from an excited state to a lower energy state via interaction with electromagnetic radiation, and the photons that are emitted as a result of this transition have discrete energy (or wavelengths) which is related to the chemical structure of molecules and atoms within the sample. Examples of emission spectroscopy include fluorescence spectroscopy, [50] particle-induced X-ray emission (PIXE) spectroscopy, [51] and energy-dispersive X-ray spectroscopy (EDXS). [52]. The third type is inelastic scattering spectroscopy. Raman spectroscopy, which plays an important role in this thesis, belongs to this class and is further introduced in the following paragraphs and reviewed in more detail in Chapter 2. The other forms of spectroscopy mentioned above are not applied in this thesis and will not be expanded to present.

Raman spectroscopy (RS) is a non-invasive optical technique that can be applied to living cells without damaging them. RS results from the inelastic scattering of light from a sample with wavelengths that are different from the wavelength of the incident monochromatic light. Raman spectroscopy can provide detailed information about the chemical structure of a sample. Raman scattering results from the molecular rotation and vibration that are produced when the incident photons interact with specific molecular bonds; thus, different samples with different molecular composition will generate different Raman spectra that have different peaks at different wavelength positions. By measuring the peaks wavelength positions (relative to the excitation laser wavelength) and their relative amplitudes, various material types can be identified, and their relative concentration can be quantified. This indicates that Raman spectroscopy is a qualitative and quantitative optical technique.

The origin of Raman spectroscopy was the discovery of Raman scattering in 1921. In the voyage of returning to India from London, Chandrasekhara Venkata Raman considered if Rayleigh's light scattering explanation could explain the bluish glow in the Mediterranean Sea and surrounding glaciers and after arriving in India, he undertook experiments to observe the light scattering from water and ice blocks. In 1928, he proposed the phenomenon of light inelastic scattering from particles, which is now known as 'Raman scattering', [53] and due to this discovery, he was awarded Nobel prize in 1930. In the early stage of research in Raman spectroscopy, the sample of interest was usually contained in a long tube and irradiated along the length of the tube by using a filtered monochromatic beam emitted from a gas discharge lamp. Early implementations of Raman spectroscopy suffered from technical difficulties including the non-ideal excitation of the coherent monochromatic light source, the imprecise wavelength separation for the emitted Raman photons, and difficulties in the accurate detection and convenient collection of these photons. In the 1960s, the invention of laser and array detectors solved the aforementioned difficulties. Thus, Raman spectroscopy underwent an explosive development and was now been widely applied in the research of many fields such as mineralogy, environmental monitoring, food and beverage monitoring, pharmaceuticals, art and archaeology, forensic medicine, medicine and clinical

chemistry, pathological diagnosis, biology, etc. [54]

In this thesis, biological samples, especially cells, are the samples of interest. Raman spectroscopy has been proven to have an ability to identify chemical structure within cells, such as lipids, DNA and proteins. Raman spectroscopy has the advantage of not requiring staining or labeling of cells prior to the imaging (unlike fluorescence spectroscopy); thus, Raman spectroscopy is a label-free method. The second advantage of Raman spectroscopy is that cells can be easily analysed in aqueous environment by using Raman spectroscopy, because of the naturally weak Raman signal generated from water. Thereby, Raman spectroscopy is applicable to living cell analysis. It is important to note that the second advantage is not easy to achieve for other spectroscopic methods, such as infrared spectroscopy whose resultant spectra of biological samples in aqueous environments can be affected by the strong water background signal. Furthermore, Raman spectroscopy has an ability to effectively detect the disease-induced chemical structure alterations within biological samples, whether the disease is in a latent period or an illness period. Compared with QPI methods, Raman spectroscopy can provide complementary information relating to the chemical information of a cell that could not be obtained from the usage of QPI methods, which can only provide morphological information.

Raman Spectrocopy can be combined with optical microscopy to great advantage. In particular the confocal microscopy design, which was invented and patented by Marvin Minsky in 1957, has been proven to well with Raman spectroscopy. [55] In a confocal Raman micro-spectroscopy setup, a confocal aperture is placed in the collection path and is positioned in a conjugate plane to the sample plane with its alignment matched to the position of the laser spot on the sample; the effect is to reduce the scattering light generated from other points deeper in the sample and thereby produce a three-dimensional selectivity in the position of the samples that produces the recorded Raman spectrum. Although confocal Raman micro-spectroscopy loses a large number of Raman scattered photons, it provides excellent 3D spatial resolution, resulting in a greater chemical differentiation. Confocal Raman micro-spectroscopy has already had many successful applications in biology including for the diagnosis of bladder, cervical, breast, gastrointestinal tract and prostate cancer; [56–63]; the identification and differentiation of bacterial strains based on the investigation for Escherichia coli; [64–66]; as well as the chemical characterization of murine or human skin melanoma and brain tissues. [67–69]

The discussion thus far relates to spontaneous Raman spectroscopy, which is the basic format of Raman spectroscopy. Although they are not applied in this thesis, it would be remiss not to mention other forms of Raman spectroscopy that have evolved in recent decades, such as Coherent anti-Stokes Raman spectroscopy (CARs) and Surface-enhanced Raman spectroscopy (SERs). CARs is also interested in the same molecular signatures as spontaneous Raman spectroscopy. However, CARs employs three beams: a pump beam, a stoke beam and a probe beam with different frequencies to interact with interested object, and eventually enhance the corresponding Raman signal. The CARs signal has orders of magnitude larger than the spontaneous Raman spectroscopy signal. [70] However, CARs can't directly provide the quantitative information

without complicated methods. [71] SERs was firstly proposed by M Fleischmann *et. al.* in 1974 [72], and relies on using a metal surface with nano-scale roughness as a substrate; object molecules adsorbed on this surface can emit increased numbers of Raman photons. SERs is distinguished by its high specificity that enables to detect the specific molecular signatures with greater clarity than spontaneous Raman spectroscopy, coupled with an extraordinary enhancement in sensitivity. Raman signals produced from SERs have been shown to have an enhancement factor of $10^{10}-10^{11}$ relative to the collected signal from spontaneous Raman spectroscopy. [73, 74] When the experimental conditions are carefully controlled, SERs can be highly quantitative, [75] and the measurement standard is as same as Spontaneous Raman spectroscopy. However, the two Raman spectra output from SERs and spontaneous Raman spectroscopy for a same sample are generally different; indeed SERs is highly dependent on the SERs substrate and suffers from reproducibility issues.

In the next chapter, the background theory relating to Raman spectroscopy, quantitative phase imaging (with a focus on digital holographic microscopy) and optical diffraction tomography, is reviewed, which underpins the various contributions in the thesis. Each individual contribution is detailed in a new chapter. Below, these various contributions are briefly previewed, with reference to the chapter in which they are highlighted as well as the associated publications.

1.4 Contributions in this thesis

- **In Chapter 3**, the white light phase imaging approach known as SLIM is investigated. We implement the basic method using an inverted life-science microscope and a spatial light modulator (SLM) to investigate simple cell samples including a cheek cell and a diatom cell. The key contribution here is the investigation of an improved calibration protocol for the SLM. This protocol provides a superior estimate of the optimal phase patterns to be displayed in the SLM for retrieval of the SLIM phase image. This work was published in a conference paper: *Z. Tang, K. O'Dwyer, and B.M. Hennelly, "Calibration methods for Spatial Light Interference Microscopy", In Digital Holography and Three-Dimensional Imaging, pp. W1B-7. Optica Publishing Group, 2019.* Although progress was made in developing the SLIM technique in Chapter 3, a persistent issue with SLIM is the halo artifact. This artifact distorts the low frequency content of the sample. Although a numerical halo-removal algorithm was applied, its effectiveness in producing an accurate reconstructed phase map remains unconvincing. Consequently, the decision was made to discontinue using the SLIM technique for cellular classification. Instead, the research shifted focus to digital holographic microscopy, a method free from the halo artifact issue, for recording phase images in the remainder of the thesis.

- **In Chapter 4**, we propose an innovative optical system for Synthetic Aperture-Digital Holography Microscopy (SA-DHM) that combines three key features and offers clear advantages over previous SA-DHM implementations. The first note-

worthy feature is that it allows a single capture, thus significantly reducing acquisition time. It also has the feature of modular implementation due to the self-reference design, whereby an illumination module and a capture module can be added to an existing life science microscope with relatively low cost when compared with previous implementations. The third key feature of this SA-DHM system is its ability to meet the 'up-shift/down-shift' condition. This ensures that each aperture is optically re-positioned correctly in the spatial frequency domain, avoiding the need for numerical correction. A rigorous theoretical description of image formation is provided, the final outcome of which is a simple deconvoluton method that can be applied to the phase image to further enhance quality and image contrast. Using various cell samples we demonstrate the high quality, low noise and high resolution of the method. This work was been prepared as a journal paper to be submitted to Optica: *Z. Tang, and B.M. Hennelly, "Real-Time Synthetic-Aperture Digital Holographic Microscopy"*. However, it has not yet been submitted as we explore the possibility of securing intellectual property. We consider the work in Chapter 4 (and Chapter 5) to be the most important contribution in the thesis.

- **In Chapter 5**, the illumination and capture modules developed in Chapter 4 are further adapted such that a new imaging modality can be implemented, namely Optical diffraction tomography (ODT). ODT is an exciting new technology, which was been developed over the past decade and is only recently commercialised. ODT generates three-dimensional tomographic images of the spatial distribution of refractive index, permitting visualisation of subcellular features with optical resolution well below the Abbe diffraction limit. Our modular implementation is demonstrated to produce high quality ODT tomographic images of cells even using a relatively low numerical aperture of 0.8. The advantage of our modular approach over previous implementations of ODT (including current commercial implementations) is (i) low cost, (ii) easy modular addition to existing life science microscopes, (iii) high speed of acquisitions, (iv) since the method inherits/extends the design of the SA-DHM approach it is also able to implement SA-DHM. A bi-modal implementation of ODT/SA-DHM will be practically useful in the field of life-science. The work in Chapter 5 has been prepared as a journal paper to be submitted to Optics Letters: *Z. Tang, and B.M. Hennelly, "Optical Diffraction Tomography using an Inexpensive Module"*. However, as for the previous chapter, it has not yet been submitted as we explore the possibility of securing intellectual property.

- **In Chapter 6**, we simultaneously perform DHM and confocal Raman spectroscopy for the purpose of automated cell classification, by adding a confocal Raman module and a DHM module to an existing life science microscope, which builds on a recent automated Raman cytology system that was developed by the host group. However, it is important to acknowledge that the work presented in this chapter is not yet complete. Challenges such as the absence of an immersion medium for DHM and alignment errors of confocal pinhole in confo-

cal Raman spectroscopy have impacted the quality of the phase images and Raman spectra, hindering the attainment of accurate cell classification. Despite these limitations, this chapter successfully demonstrates a proof-of-concept and lays the groundwork for future advancements in cell classification using Raman spectroscopy and DHM. The work in this chapter has been partially published in *Z. Tang, K. O'Dwyer, A. Dignam, M. Butler, and B.M. Hennelly, "Application of Modular Digital Holographic Microscopy to Clinical Pathology Samples Before Histopathological Staining", in Proceedings Volume 11898, Holography, Diffractive Optics, and Applications XI. SPIE/COS Photonics Asia, 2021.*.

- **In Chapter 7**, we investigate the capacity of the confocal Raman system to quantify the concentration of chemical components in a mixture. In the context of the previous work, one could imagine that confocal Raman spectroscopy could be used to assess the quality of the growth medium in which a live cell culture is under investigation and to detect if changes to that medium need to be addressed. A model for the collection efficiency is developed, which explores the effect of the microscope objective (in terms of magnification and numerical aperture) as well as the confocal aperture size on the capacity of the system to quantify low concentrations of chemical in a mixture. A thorough review of more traditional Raman multi-component systems is provided and a comparison is given with our approach. This work is published in *Z. Tang, S.J. Barton, T.E. Ward, J.P. Lowry, M.M. Doran, H.J. Byrne, and B.M. Hennelly, "Multicomponent analysis using a confocal Raman microscope." Applied optics 57, no. 22 (2018): E118-E130.*

Chapter 2

Background

2.1 Introduction

The purpose of this chapter is to introduce the background theory of the optical techniques used in this thesis.

In Section 2.2, the background theory for Quantitative phase imaging (QPI) is provided. Firstly, the wave nature of light and propagation is introduced in Section 2.2.1. Secondly, the Fourier transform in optics and the concept of spatial frequency in an image are demonstrated in Section 2.2.2. Thirdly, based on Fourier optics, the angular spectrum and Fresnel diffraction are described in Section 2.2.3 and Section 2.2.4 respectively, which are the mathematical foundation for quantitative phase imaging. Section 2.2.5 explains the generation of phase delay, which is measured using QPI. Then, an overview of digital holography microscopy, which is most significant QPI method in the context of this thesis, is emphasized in Section 2.2.6. This includes discussion on the structure of DHM setup, the hologram recording, the numerical reconstruction, and other numerical processing (such as phase unwrapping). Finally, a very brief review for white light QPI is offered in Section 2.2.7.

The background for the optical diffraction tomography (ODT) technique is reviewed in Section 2.3. At first, the development of the ODT technique and categories of ODT setups are introduced in Section 2.3.1. In Section 2.3.2, two types of ODT reconstruction algorithms: projection algorithm and diffraction algorithm are generally discussed, and the diffraction phenomenon is emphasized to be a vital factor in the ODT research for biological sample. In Section 2.3.3, based on Helmholtz equation, a ODT reconstruction model is constructed to link the 3D refractive index map and multiple 2D scattered fields of the sample. Considering the issue of the diffraction phenomenon, the Born approximation and Rytov approximation for calculating the 2D scattered fields from multiple camera captures are respectively introduced in Section 2.3.4 and Section 2.3.5. The calculated 2D scattered fields could be mapped onto a 3D space to calculate the 3D refractive index map by using the Fourier diffraction theorem that is demonstrated in Section 2.3.6. At last, the nonnegativity constraint optimiztion (NNC) procedure is introduced in Section 2.3.7 to solve the classical missing frequency problem in the ODT technique.

The background theory for Raman spectroscopy is reviewed in Section 2.4. The general description for the physics of Raman spectroscopy is provided in Section 2.4.1. And the causes of Raman scattering associated with the molecular rotation and molecular vibration is illustrated in Section 2.4.2. The Section 2.4.3 briefly explains the limitation of Raman spectroscopy about the unwanted background signal generated from the optical setup. The design of a Raman spectroscopy setup is demonstrated in Section 2.4.4, which also emphasizes the effects of several components in Raman spectroscopy setup, including laser source, sample substrate, spectrometer, CCD camera, and confocal aperture.

2.2 Background theory for Quantitative phase imaging

2.2.1 the wave nature of light

In 1801, Thomas Young reported the classical double-slit experiment. It could be observed from the experiment that bright and dark fringes appear after monochromatic light passes through the double slits. Such these bright and dark fringes revealed the interference phenomenon, and also suggests that the light can be described as a wave. Then, in 1861, James Clerk Maxwell stated that light is a electromagnetic wave, [76] and in 1873, he formally proposed the very well-known Maxwell's Equations to explain the behaviours and the relationship of electric field and magnetic field using mathematical expressions. [77] Based on the description of the Maxwell's Equation, if $\vec{E}$ is denoted as the electric field vector of light at the time t, the following wave equation must be satisfied:

$$\nabla^2 \vec{E} - \frac{1}{c^2} \frac{\partial^2 \vec{E}}{\partial t^2} = 0 \tag{2.1}$$

where the ∇^2 denotes the Laplacian operator and c is the light speed in the vacuum. Further, considering linear polarized light (which means that the orientations of electric field vector and magnetic field vector are unchanged and perpendicular to each other, and both these two vectors are perpendicular to the light propagation direction z; and the polarization direction of the linear polarized light is equal to the orientation of electric field vector), Equation 2.1 could be modified for the harmonic and linear polarized wave in the electric field:

$$\frac{\partial^2 \vec{E}}{\partial z^2} - \frac{1}{c^2} \frac{\partial^2 \vec{E}}{\partial t^2} = 0 \tag{2.2}$$

Assuming light travelling in a 3d coordinate system, the propagated electric field vector $\vec{E}$ at the time t, at the position with the spatial vector $\vec{r} = (x, y, z)$, can be written as a complex (exponential) format:

$$E(x, y, z; t) = A \exp[j(\vec{k}\vec{r} - wt)] \tag{2.3}$$

where A is the amplitude of wave, j is the unit imaginary number equal to $\sqrt{-1}$, $|\vec{k}|$ is the wavenumber equal to $\frac{2\pi}{\lambda}$ (λ is the light wavelength), and $\vec{k}\vec{r} - wt$ is the phase of wave.

2.2.2 Fourier transform in Optics

The Fourier transform can convert a signal in the time/space domain into the signal in frequency domain. The Fourier transform has many applications in signal processing, including light wavefield analysis and digital image processing, which are required in this thesis. In the study of Fourier optics, it is assumed that a light wavefield is composed by the superposition of a series of plane waves. This assumption is similar with the Huygens-Fresnel principle, but the difference is that the Huygens-Fresnel principle assumes that the light wavefront is made up of the superposition of a series of spherical waves. Defining a complex wavefield function of light $g(x, y)$ in the space domain that contains an amplitude field $A(x, y)$ and a phase field $\phi(x, y)$:

$$g(x, y) = A(x, y) \exp(j\phi(x, y)) \tag{2.4}$$

Then, the 2D Fourier transform of g(x,y) is written as follows:

$$G(k_x, k_y) = \iint_{-\infty}^{\infty} g(x, y) \exp[-j2\pi(xk_x + yk_y)]\, dx\, dy \tag{2.5}$$

where $G(k_x, k_y)$ is the spectrum in the spatial frequency domain calculated from its corresponding wavefield, $g(x, y)$, in the spatial domain, and (k_x, k_y) is the spatial frequency coordinate that is associated with the propagation direction of plane wave $\exp[-j2\pi(xk_x + yk_y)]$ in the space domain. The wavefield, $g(x, y)$, could also be inversely obtained from its spectrum, $G(k_x, k_y)$, in the spatial frequency domain by using the inverse Fourier transform:

$$g(x, y) = \iint_{-\infty}^{\infty} G(x, y) \exp[j2\pi(xk_x + yk_y)]\, dk_x\, dk_y \tag{2.6}$$

Here, the frequency spectrum $G(k_x, k_y)$ could be considered as the weights for the different plane waves $\exp[j2\pi(xk_x + yk_y)]$. Thereby, the light wavefield $g(x, y)$ is equivalent to the superposition of these multiple plane waves multiplying their complex weights respectively.

Practically, the light wavefield of interest is often recorded as an intensity image via digital sensors, such as the CCD camera and CMOS camera. The camera sensor chip is made up of a regular array of discrete pixels, each of which is capable of transferring the collected photons into a corresponding digital signal magnitude. The image exported from the camera is a combination of the digital signal magnitudes from all pixels. The recorded digital image could be thought as a start point for the subsequent numerically processing (including the Fourier transform). Assuming that an recorded image consists of $N_x \times N_y$ pixels in two dimensions, the each pixel location could be considered as a spatial coordinate, and the continuous Fourier transform provided in Equation 2.5 can be adapted into a discrete matrix operation known as the discrete

Fourier transform (DFT), which is given by:

$$G(m_x\Delta_x, m_y\Delta_y) = \sum_{-\frac{N_x}{2}}^{\frac{N_x}{2}-1} \sum_{-\frac{N_y}{2}}^{\frac{N_y}{2}-1} g(n_x\delta_x, n_y\delta_y) \exp\left[-j2\pi\left(\frac{n_x m_x}{N_x} + \frac{n_y m_y}{N_y}\right)\right] \tag{2.7}$$

The notation appearing for the continuous FT, i.e. x, y, k_x, k_y in Equation 2.5 is now replaced with discrete variables that are sampled from the integer multiples of some specific sampling interval. The substitution relationship is below:

$$\begin{aligned} x &\Rightarrow n_x\delta_x, \quad n_x \in (-N_x/2, N_x/2-1) \\ y &\Rightarrow n_y\delta_y, \quad n_y \in (-N_y/2, N_y/2-1) \\ k_x &\Rightarrow m_x\Delta_x, \quad m_x \in (-N_x/2, N_x/2-1) \\ k_y &\Rightarrow m_y\Delta_y, \quad m_y \in (-N_y/2, N_y/2-1) \end{aligned}$$

where δ_x, δ_x are the sampling interval used in the two dimensions of the spatial domain, and are equal to the pixel width. Δ_x, Δ_y are the sampling intervals used in the two dimensions of the spatial frequency domain. Assuming the region in the spatial domain is limited by the $(N_x\delta_x, N_y\delta_y)$, then the corresponding region in the spatial frequency domain is $(\frac{1}{\delta_x}, \frac{1}{\delta_y})$. The sampling intervals Δ_x, Δ_y in the spatial frequency domain are equal to $(\frac{1}{N_x\delta_x}, \frac{1}{N_y\delta_y})$

Similarly, based on the inverse Fourier transform (Equation 2.6), the inverse discrete Fourier transform (IDFT) for converting a discrete spectrum into a discrete image in spatial domain could also be deduced:

$$g(n_x\delta_x, n_y\delta_y) = \sum_{-\frac{N_x}{2}}^{\frac{N_x}{2}-1} \sum_{-\frac{N_y}{2}}^{\frac{N_y}{2}-1} G(m_x\Delta_x, m_y\Delta_y) \exp\left[j2\pi\left(\frac{n_x m_x}{N_x} + \frac{n_y m_y}{N_y}\right)\right] \tag{2.8}$$

The DFT and IDFT can be calculated using the fast Fourier transform (FFT) algorithm and the inverse fast Fourier transform (IFFT) algorithm to increase the calculation speed greatly.

2.2.3 The Angular Spectrum

The angular spectrum method relates to the scalar diffraction theory in the field of Fourier optics and is used to represent the light wavefield at an arbitrary plane along the light propagation in free space. Relying on this technique, a complex object wavefield that is known at any propagated depth could be 'refocused' by numerically processing. It should be noted that angular spectrum method requires knowledge of the complex wavefield. Thereby, only the specific imaging techniques, such as DHM and SLIM, are capable of reconstructing the complex wavefield of an object; while most other microscopic imaging techniques, such as traditional brightfield microscopic imaging, record only the intensity. The derivation of angular spectrum technique is demonstrated below.

The angular spectrum method relates the known wavefield distribution denoted as $U_0(x_0, y_0, 0)$ and the unknown wavefield distribution at some propagation distance, z, denotes as $U(x, y, z)$. Based on the Fourier transform algorithm in Equation 2.5, the frequency spectrum of the known wavefield, $U_0(x, y, 0)$, is:

$$A_0\left(k_x, k_y; 0\right) = \iint_{-\infty}^{\infty} U_0\left(x_0, y_0, 0\right) \exp\left[-j2\pi\left(x_0 k_x + y_0 k_y\right)\right] dx_0 dy_0 \tag{2.9}$$

where k_x, k_y, and k_z, are 3 spatial frequency components that represent the propagation direction of each plane wave contributing to the light wavefield. These 3 spatial frequency components k_x, k_y, k_z are not independent. They must satisfy the relationship: $\lambda^2 {k_x}^2 + \lambda^2 {k_y}^2 + \lambda^2 {k_z}^2 = 1$, where λ denotes the wavelength of light, and thereby the frequency component k_z can be calculated: $k_z = \frac{\left(\sqrt{1-\lambda^2 {k_x}^2 - \lambda^2 {k_y}^2}\right)}{\lambda}$.

The spatial frequencies coordinates k_x, k_y can be rewritten as a format of cosines: $\frac{\cos\alpha}{\lambda}$, $\frac{\cos\beta}{\lambda}$, which are related to the angular components of the propagation direction of each plane wave. Thus, the Equation 2.9 now is given by:

$$A_0\left(\frac{\cos\alpha}{\lambda}, \frac{\cos\beta}{\lambda}; 0\right) = \iint_{-\infty}^{\infty} U_0\left(x_0, y_0, 0\right) \exp\left[-j2\pi\left(\frac{\cos\alpha}{\lambda} x_0 + \frac{\cos\beta}{\lambda} y_0\right)\right] dx_0 dy_0 \tag{2.10}$$

$A_0\left(\frac{\cos\alpha}{\lambda}, \frac{\cos\beta}{\lambda}; 0\right)$ is called the angular spectrum of the wavefield, $U\left(x, y, 0\right)$. Similarly, at the observation plane, the unknown wavefield, $U\left(x, y, z\right)$, has its corresponding angular spectrum, which is given by

$$A\left(\frac{\cos\alpha}{\lambda}, \frac{\cos\beta}{\lambda}; z\right) = \iint_{-\infty}^{\infty} U\left(x, y, z\right) \exp\left[-j2\pi\left(\frac{\cos\alpha}{\lambda} x + \frac{\cos\beta}{\lambda} y\right)\right] dx dy \tag{2.11}$$

Using the Helmholtz equation, the angular spectrum, $A\left(\frac{\cos\alpha}{\lambda}, \frac{\cos\beta}{\lambda}; z\right)$, of the unknown wavefield can be deduced from the angular spectrum of the known wavefield, which is given by:

$$A\left(\frac{\cos\alpha}{\lambda}, \frac{\cos\beta}{\lambda}; z\right) = A_0\left(\frac{\cos\alpha}{\lambda}, \frac{\cos\beta}{\lambda}; 0\right) \exp\left(j\frac{2\pi}{\lambda} z \sqrt{1 - (\cos^2\alpha + \cos^2\beta)}\right) \tag{2.12}$$

The basis of the angular spectrum method for calculating a propagated wavefield, is that a wavefield results from a linear combination of plane waves with different directions. Thereby, in Equation 2.12, the term, $(\cos^2\alpha + \cos^2\beta)$, must be less than 1 to guarantee that the spectrum is composed of plane waves. If $(\cos^2\alpha + \cos^2\beta) \geq 1$, the corresponding wave components are called evanescent waves that attenuate rapidly during propagation. The evanescent waves do not belong to the scalar diffraction theory in the field of Fourier Optics, and will not be expanded upon in this thesis.

Equation 2.12 can be rewritten as follows:

$$A\left(k_x, k_y; z\right) = A_0\left(k_x, k_y; 0\right) \exp\left(j\frac{2\pi}{\lambda} z \sqrt{1 - \lambda^2 {k_x}^2 - \lambda^2 {k_y}^2}\right) \tag{2.13}$$

where the exponential term, $\exp\left(j\frac{2\pi}{\lambda} z \sqrt{1 - \lambda^2 {k_x}^2 - \lambda^2 {k_y}^2}\right)$, could be seen as a transfer

function, $H(k_x, k_y)$, in the spatial frequency domain:

$$H\left(k_x, k_y\right) = \exp\left(j\frac{2\pi}{\lambda}z\sqrt{1-\lambda^2{k_x}^2-\lambda^2{k_y}^2}\right) \tag{2.14}$$

The unknown wavefield, $U\left(x, y, z\right)$, can be calculated from its angular spectrum, $A\left(k_x, k_y; z\right)$, via inverse Fourier transform:

$$U\left(x, y, z\right) = \iint_{-\infty}^{\infty} A\left(k_x, k_y; z\right)\exp\left[j2\pi\left(xk_x + yk_y\right)\right]dk_x dk_y \tag{2.15}$$

Two steps are required for calculating the unknown wavefield, $U\left(x, y, z\right)$, from the known wavefield, $U\left(x, y, 0\right)$, can be concluded below:

$$\begin{aligned} A_0\left(k_x, k_y; 0\right) &= \iint_{-\infty}^{\infty} U_0\left(x_0, y_0, 0\right)\exp\left[-j2\pi\left(x_0k_x + y_0k_y\right)\right]dx_0dy_0 \\ U\left(x, y, z\right) &= \iint_{-\infty}^{\infty} A_0\left(k_x, k_y; 0\right)H\left(k_x, k_y\right)\exp\left[j2\pi\left(xk_x + yk_y\right)\right]dk_x dk_y \end{aligned} \tag{2.16}$$

2.2.4 Fresnel diffraction

A definition of the diffraction phenomenon was proposed by Arnold Sommerfeld as *"any deviation of a light ray from rectilinear propagation, which is not caused by reflection nor refraction."* [78] A simple example of diffraction is the case where light illuminate an aperture. The resulting diffraction pattern at some distance z as shown in Fig. 2.1.

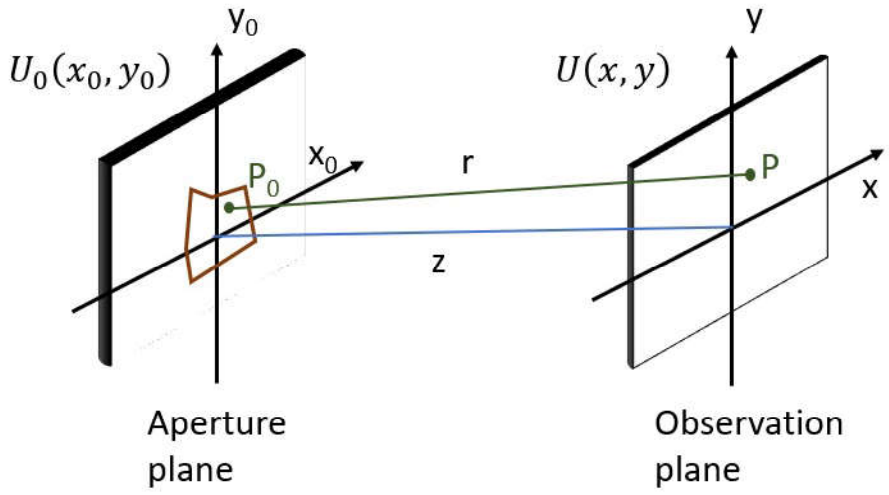

Figure 2.1: An aperture plane and an observation plane set for explaining Fresnel diffraction.

Here, r is assumed to be the distance between a point P_0 on the aperture plane and a point P on the observation plane. The optical wavefield on the observation plane, $U(x, y)$, can be calculated by convolving the wavefield $U_0(x_0, y_0)$ in the aperture plane

with a point spread function, $h(x-x_0, y-y_0)$. This can be given by:

$$U(x,y) = \iint_{-\infty}^{\infty} U_0(x_0,y_0)\, h(x-x_0, y-y_0)\, dx_0 dy_0 \tag{2.17}$$

where the point spread function, $h(x-x_0, y-y_0)$, can be given by,

$$h(x-x_0, y-y_0) = \frac{1}{j\lambda r}\exp(jkr) \tag{2.18}$$

where k is the wavenumber that is equal to $\frac{2\pi}{\lambda}$. The paraxial approximation is satisfied when the distance z is significantly larger than the aperture size. In this case,

$$r = \sqrt{z^2 + (x-x_0)^2 + (y-y_0)^2} \approx z\left[1 + \frac{1}{2}\left(\frac{x-x_0}{z}\right)^2 + \frac{1}{2}\left(\frac{y-y_0}{z}\right)^2\right] \tag{2.19}$$

The point spread function $h(x-x_0, y-y_0)$ is rewritten as:

$$h(x-x_0, y-y_0) = \frac{1}{j\lambda z}\exp(jkz)\exp\left\{j\frac{k}{2z}\left[(x-x_0)^2 + (y-y_0)^2\right]\right\} \tag{2.20}$$

The transfer function of Fresnel transform can be given by:

$$H(k_x, k_y) = \exp(jkz)\exp\left[-j\pi\lambda z\left(k_x^2 + k_y^2\right)\right] \tag{2.21}$$

Substituting the $h(x-x_0, y-y_0)$ in Equation 2.20 into the Equation 2.17, the Fresnel diffraction formula can be achieved:

$$U(x,y) = \frac{1}{j\lambda z}\exp(jkz)\iint_{-\infty}^{\infty} U_0(x_0,y_0)\exp\left\{j\frac{k}{2z}\left[(x-x_0)^2 + (y-y_0)^2\right]\right\} dx_0 dy_0 \tag{2.22}$$

The Fresnel diffraction formula can be described in terms of the Fourier transform:

$$\begin{aligned} U(x,y) = \frac{1}{j\lambda z}\exp(jkz)\exp\left[j\frac{k}{2z}(x^2+y^2)\right]\iint_{-\infty}^{\infty}\Big\{U_0(x_0,y_0) \\ \exp\left[j\frac{k}{2z}\left[(x_0)^2 + (y_0)^2\right]\right]\Big\}\exp\left[j\frac{k}{z}(xx_0 + yy_0)\right] dx_0 dy_0 \end{aligned} \tag{2.23}$$

It can be observed from Equation 2.23 that the Fresnel diffraction formula is a result of multiplying a quadratic phase exponential by a Fourier transform.

2.2.5 Phase delay from the biological sample

As mentioned in section 1.1, the majority of biological samples including cells and tissues are observed transparent, which produces a low contrast imaging problem. In the context of using a traditional bright-field optical microscopy and without using sample staining, light transmitting the biological samples will not modify the amplitude or intensity significantly, but can result in a spatially varying phase delay obviously due to the characteristics of the refractive index and the thickness of the sam-

ple. Thereby, this type of biological sample are so-called 'phase object'. In order to visualize a phase object, relying on the light natures of refraction, diffraction, interference, or polarization, several label-free microscopic imaging methods such as dark field microscopy [79], phase contrast microscopy [8, 80], differential interference contrast (DIC) microscopy [9, 81], and Rheinberg illumination [82–84] are invented for enhancing the image contrast, and have been applied in the modern life-science field broadly. However, these label-free contrast-enhanced imaging methods could only achieve the qualitative information of 'phase object'. The QPI methods are a series of methods that could quantitatively measure the spatially varying phase delay to further analyse the morphology and dynamics of biological samples. [10, 11] The Digital holography microscopy (DHM) and Spatial light interference microscopy (SLIM) are two of QPI methods that are investigated in this thesis, and will be discussed in details in next Sections.

2.2.6 Digital holography microscopy

DHM is a classical implementation of QPI, and because of its early origin and simple implementation it remains popular today; see brief introduction to DHM in Section 1.2. DHM is the most significant QPI method utilized in this thesis, and will be developed for imaging and analysing the biological samples in Chapter 4, 5, and 6. In this section, the background theory of DHM is reviewed in terms of the fundamental construction of the DHM setup, the experimental process of holographic recording, and the numerically processing for holographic reconstruction.

2.2.6.1 Digital holographic recording

Digital holography relies on recording an interference intensity pattern called a hologram on a digital camera. The interference results from a combination of two beams originating from the same coherent laser source: one is a spatially varying object beam modulated by the sample; another is spatially uniform reference beam. The wavefields from both beams are guided to arrive on the camera plane with the same optical path length to construct the hologram. The intensity distribution on this hologram can be calculated by the interference equation:

$$\begin{aligned} hol(x,y) &= \left|O(x,y)+R(x,y)\right|^2 \\ &= \left|O(x,y)\right|^2+\left|R(x,y)\right|^2+O(x,y)\overline{R(x,y)} \\ &+\overline{O(x,y)}R(x,y) \end{aligned} \tag{2.24}$$

where $hol(x,y)$ denotes the intensity distribution of the hologram; $R(x,y)$ and $O(x,y)$ denote the complex wavefields from reference beam and object beam that arrive on camera plane respectively; the bar on top of the wavefield denotes the conjugation of this complex wavefield; x and y are the 2D coordinates in the spatial domain. In the discussion that follows, the complex wavefields from the reference beam and object beam arriving on camera plane are abbreviated as reference wavefield and object wavefield for simplicity. In Equation 2.24, the first two terms represents the zero order

(DC component) pattern noise, and the third and fourth terms represent the twin images components that contain the information of the complex object wavefield. The complex object wavefield includes an amplitude field and a phase field of interest. The numerical analysis, which is based on the holography equation (Equation 2.24), will be discussed in sections later. Here, the hardware for hologram recording is highlighted. In Fig. 2.2, an example of the structure of a traditional DHM setup is shown to illus-

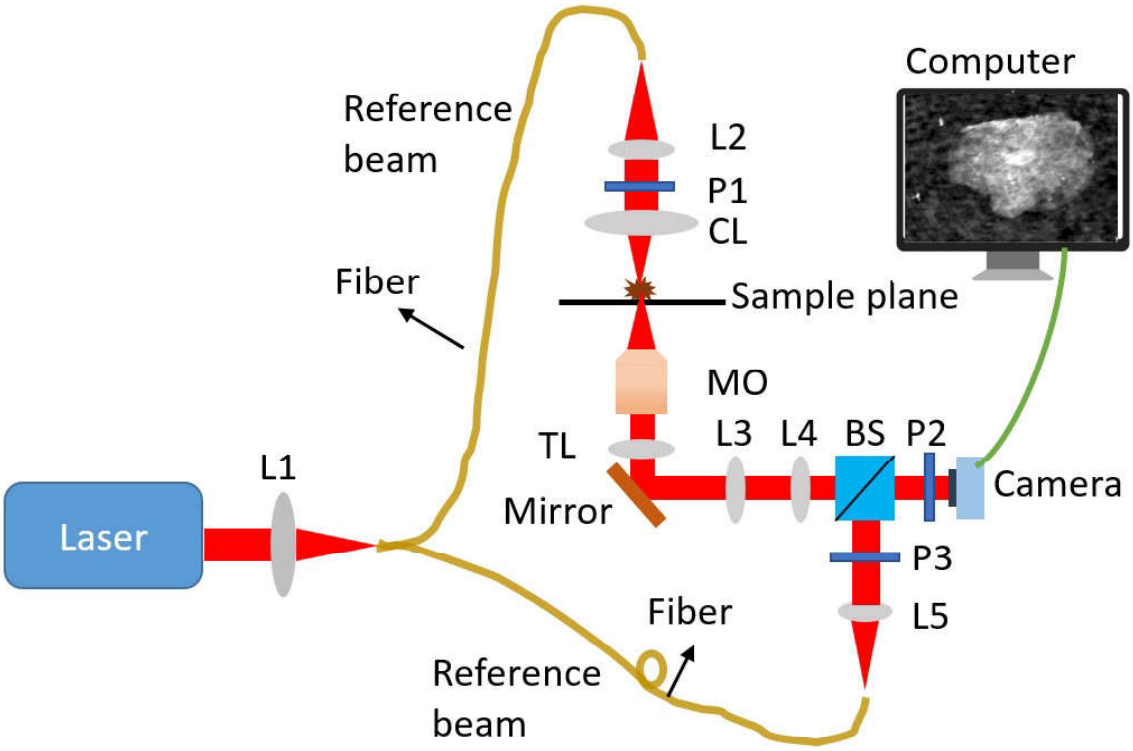

Figure 2.2: The structure of a traditional DHM setup: L, Lens; P, Polarizer; CL, condensor lens; MO, Microscope objective; TL, Tube lens; BS, Beamsplitter.

trate the concrete optical paths design for constructing a hologram. The laser beam is focused by a lens (**L1**) and coupled into a fiber splitter (1 input, 2 output) to create 2 beam paths. The beam from one output fiber is the object beam, this beam is converted into a collimated beam by a lens (**L2**), and then this beam is irradiated onto the sample of interest through a condenser lens (**CL**); the sample is imaged by a microscope objective (**MO**) and a tube lens, and a pair of lens (**L3** and **L4**) relays the image plane after the tube lens to generate a conjugated image plane for recording. The beam output from the other fiber is the reference beam. Unlike the object beam, the reference beam does not pass through the sample. The reference beam is first collimated beam by a lens (**L5**), and then is combined with the object beam via a beamsplitter (**BS**) to form an interference pattern on camera. The linear polarizers (**P1** and **P2**) used in the setup to tune the power ratio between the object beam and reference beam for optimal interference, and camera acquisition is set to avoid the problem of intensity saturation during the hologram recording. The camera captures the digital hologram which is then input to a numerical processing routine for holographic reconstruction.

The reference beam and object beam could be combined without an off-axis angle

using an inline design or with an off-axis angle to facilitate separation of the twin images in the Fourier domain. The difference between the inline and off-axis holography setups will be discussed in next section.

2.2.6.2 Inline DHM and off-axis DHM

The objective of DHM is to reconstruct the complex object wavefield $O(x, y)$ by recording a hologram $h(x, y)$. The recorded hologram $h(x, y)$ is a result of the interference between the reference wavefield $R(x, y)$ and the object wavefield $O(x, y)$. Here, we note that the reference wavefield $R(x, y)$ is from a plane wave that can be given by:

$$R(x, y) = \exp(j2\pi[xsin(\theta_x) + ysin(\theta_y)]/\lambda) \tag{2.25}$$

where θ_x and θ_y denote the included angles with respect to the object beam $O(x, y)$ in x and y directions.

For the case of inline DHM, there is negligible angle between object and reference i.e. $\theta_x = 0$, $\theta_y = 0$. A significant problem of inline DHM is that all four terms in the holography equation (Equation 2.24) are overlapped in the spectrum, and the desired twin image frequency bands cannot be extracted directly by using a simple spatial filtering method to retrieve the complex object wavefield $O(x, y)$. This problem can be approximately solved by using a Gercherg-Saxton(GS) algorithm [85, 86] and a ptychography algorithm [87, 88] based on recording multiple diffraction intensity images at different propagation planes (or different illuminations) to recover the phase field by time-consuming iterative calculation. Another phase retrieval method can also be used in inline DHM, which relies on recording four holograms with phase shifting of the object or reference. [89] This phase retrieval method is also employed in the SLIM method in this thesis, which is discussed in detail in Chapter 3. These various phase retrieval methods have the advantage of a higher spatial resolution, because they can use the bandwidth of the camera for the twin images. However, the requirement of multiple images recordings in these methods sacrifices the time-efficiency, which largely decrease the robustness of imaging and analysing the biological samples whose behaviour and movement change rapidly. Also the iterative methods are not in general accurate in recovery of the complex object wavefield O.

In off-axis DHM, an angle is introduced between the reference beam and object beam, which greatly simplifies the recovery of the complex object wavefield. After performing the discrete Fourier transform on the recorded hologram, the frequency bands related to different terms in Equation 2.24 can be separated in the spectrum. A diagram of the distribution of frequency bands calculated from Fourier transforming hologram is depicted in Fig. 2.3, where the blue frequency band describes the Fourier transform of zero order pattern from the first and second terms in Equation 2.24, and red frequency bands describe the Fourier transform of twin images from the third and fourth terms in Equation 2.24. Due to the successful isolation of the frequency bands in the DFT, each twin image frequency band that contains the phase field of object of interest is allowed to be extracted directly by using spatial filtering. Though such this spatial filtering approach for retrieving the phase field of object has a drawback of sacrificing

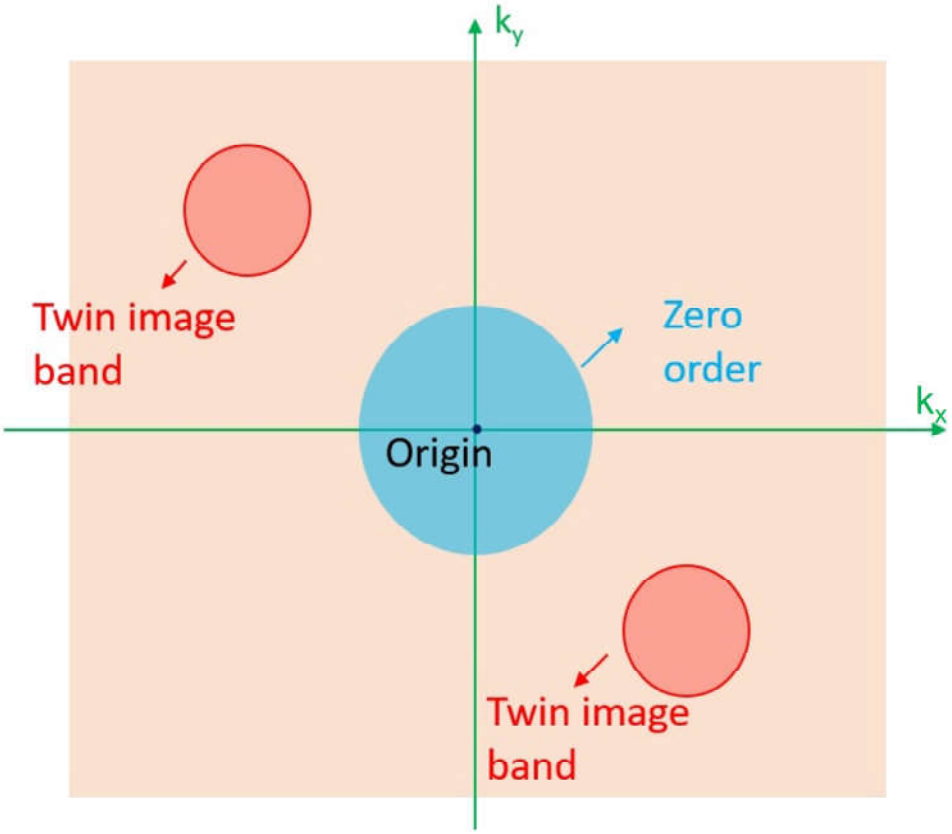

Figure 2.3: illustration of the Fourier transform of an off-axis hologram. The twin images are shifted and full separated from the other terms. The principle here is similar to that used for terrestrial radio where different channels are modulated to occupy different frequency bands. Application of a DFT to a digital hologram facilitates isolation of a twin image term and recovery of the complex object wavefield.

the bandwidth of the camera, the biggest advantage of this approach is that only one intensity image (hologram) is required to be recorded. Thereby, the off-axis DHM is suitable for real-time recording of a sample whose shape and motion change quickly. Additionally, the successful isolation of twin image frequency band enables the numerical refocusing for object imaging, which will be explained in Section 2.2.6.4. Numerical refocusing is an important advantage of off-axis DHM, while the conventional bright-field light microscopy can't realize. The off-axis DHM is the main QPI method investigated in this thesis. Thus, a concrete process of the numerical reconstruction for obtaining the desired phase field of object is introduced and will be also provided in Section 2.2.6.4.

2.2.6.3 Sampling

The hologram recorded by a digital camera is pixelated, and thus, discrete variables are used in the DHM numerical analysis. As mentioned previously, the recorded hologram is made up of pixels in the spatial domain, which are transformed into the Fourier domain to perform the spatial filtering for isolating the twin image frequency bands of interest. In the previous Section 2.2.2, the formula of the discrete Fourier transform

(DFT) has been provided in Equation 2.7, and the spatial coordinates x, y in Equation 2.24 can be rewritten in terms of these discrete variable:

$$\begin{aligned} x &= n_x \delta_x \qquad n_x \in (-N_x/2, N_x/2-1) \\ y &= n_y \delta_y \qquad n_y \in (-N_y/2, N_y/2-1) \end{aligned} \tag{2.26}$$

where δ_x and δ_y denote the length and height of a pixel, N_x and N_y represent the number of pixels in the horizontal and vertical dimensions in camera.

2.2.6.4 Numerical reconstruction

As described by Equation 2.24, the hologram, $h(x, y)$, recorded by the camera is composed of four terms. Focusing on the third term, which is a multiplication of the complex object wavefield, $O(x, y)$, and the conjugation of complex reference wavefield, $\overline{R(x, y)}$; here, the concept of the object transmittance function, $t(x, y)$, must now be introduced. For now, for simplicity, we simply say that the object wavefield, O, that is incident on the camera is in some way proportional to the object transmittance function, t. We will deal with this subject in much greater detail in Section 4.4 in Chapter 4. For now, we simply mention that the true relationship will be governed by the pupil function of the imaging system (controlled by the numerical aperture of the microscope objective) and the magnification. Assuming for now that $O = t$ and that O has a limited spatial frequency support, we proceed to discuss the optimal off-axis angle that must exist between the reference and object beams and then we discuss numerical reconstruction.

In the recording set up, care must be taken to choose a suitable angle between object beam and reference beam. As shown in Fig. 2.4, a small angle can result in the frequency band of $O(x, y)$ still partially overlapping with the unwanted frequency band of zero order band. A very big angle results in part of the desired frequency band of $O(x, y)$ exceeding the bandwidth support associated with the pixel array in the camera chip. Furthermore, we also pay an attention on the fourth term, $\overline{O(x.y)}R(x, y)$, in Equation 2.24. The term will shift in frequency in the opposite direction as a function of the off-axis angle. Thereby, The two twin image frequency bands associated with the object wavefield appear at opposite positions in spectrum. It is notable that the twins are simply conjugated of each other and therefore in numerical processing, either one can be spatially filtered in order to reconstruct the object transmittance function, $t(x, y)$.

After reconstructing the $\mathscr{F}\{O(x, y)\}$ using an inverse DFT, the next critical procedure is numerical refocusing. This is sometimes necessitated if the captured hologram does not produce an in-focus image, i.e. O is the result of propagating the wavefield t by some distance z. The great advantage of off-axis DHM is that the object can be out-of-focus in the camera plane, but the retrieved object field O can be 'numerically propagated' or 'numerically refocused' to reconstruct t. This advantage provides the freedom to arrange the positions of object and camera in off-axis DHM system. As mentioned in Section 2.2.3, the angular spectrum is a method for deducing an unknown wavefield from a known wavefield some distance away. Based on the Equation 2.16, the in-focus object wavefield denoted as $t(x, y)$ could be calculated by multiplying the

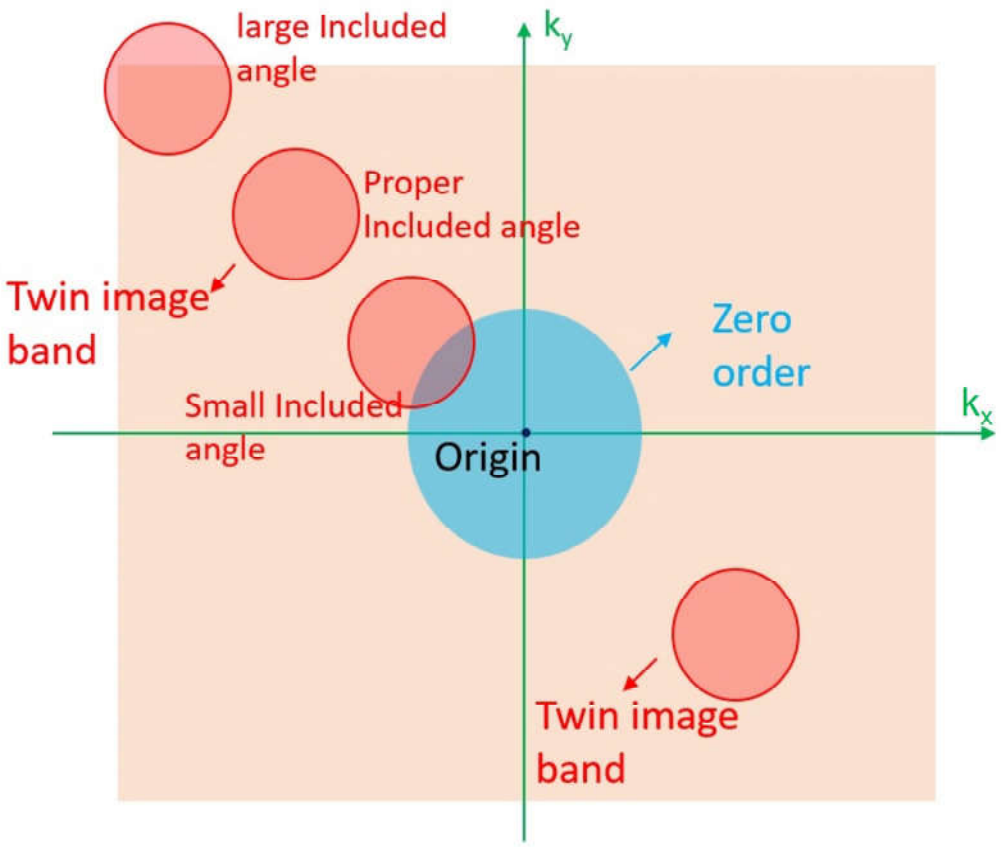

Figure 2.4: The discrete Fourier transform of a recorded hologram resulting from three different off-axis angles between the object beam and reference beam.

spectrum of out-of-focus object wavefield $\mathscr{F}\{O(x,y)\}$ on the camera plane by an exponential function mentioned in Equation 2.14, and then inverse Fourier transforming the resultant spectrum into the wavefield in the spatial domain:

$$t(x,y) = \mathscr{F}^{-1}\left[\mathscr{F}\{O(x,y)\}\exp\left(j\frac{2\pi}{\lambda}z\sqrt{1-\lambda^2{k_x}^2-\lambda^2{k_y}^2}\right)\right] \tag{2.27}$$

where $\mathscr{F}^{-1}$ denotes Inverse Fourier Transform function.

A second numerical refocusing method is based on Fresnel diffraction that has been discussed in Section 2.2.4. Similar to the angular spectrum method, the discrete Fresnel transform also relies on multiplying an exponential term to calculate the desired $t(x,y)$, which can be given by:

$$t(x,y) = \mathscr{F}^{-1}\left[\mathscr{F}\{O(x,y)\}\exp\left(-j\pi\lambda z(k_x^2+k_y^2)\right)\right] \tag{2.28}$$

Next, we recall that the images recorded by digital camera are pixelated, and the variables of discrete format must be used in the DHM numerical analysis. Therefore, the DFT and IDFT with the variables notations mentioned in Equation 2.7 and Equation 2.8 are used to more accurately describe numerical reconstruction. If we assume the exponential terms in Equation 2.27 and Equation 2.28 as a transfer function $H(k_x,k_y)$, the refocusing equation for reconstructing the in-focus object wavefield

$t(x,y)$ can be rewritten as follows:

$$t(n_x\delta_x, n_y\delta_y) = IDFT\left[DFT\left(O(n_x\delta_x, n_y\delta_y)\right)H(m_x\delta k_x, m_y\delta k_y)\right] \tag{2.29}$$

The more descriptions and comparison of the different numerical methods to reconstruct the in-focus object wavefield $o(x,y)$ from the recorded holograms are provided in Ref. 90, 91 for readers who are interested in.

2.2.6.5 Phase unwrapping

After numerical refocusing, an in-focus complex object wavefield, $t(x,y)$ is achieved. And the calculation of the required phase field $\phi(x,y)$ could be extracted from $t(x,y)$, which is given by:

$$\phi(x,y) = \tan^{-1}\frac{Imag[t(x,y))]}{Real[t(x,y)]} \tag{2.30}$$

where $Real[]$ denotes the real part in a complex number, and $Imag[]$ denotes the imaginary part in a complex number.

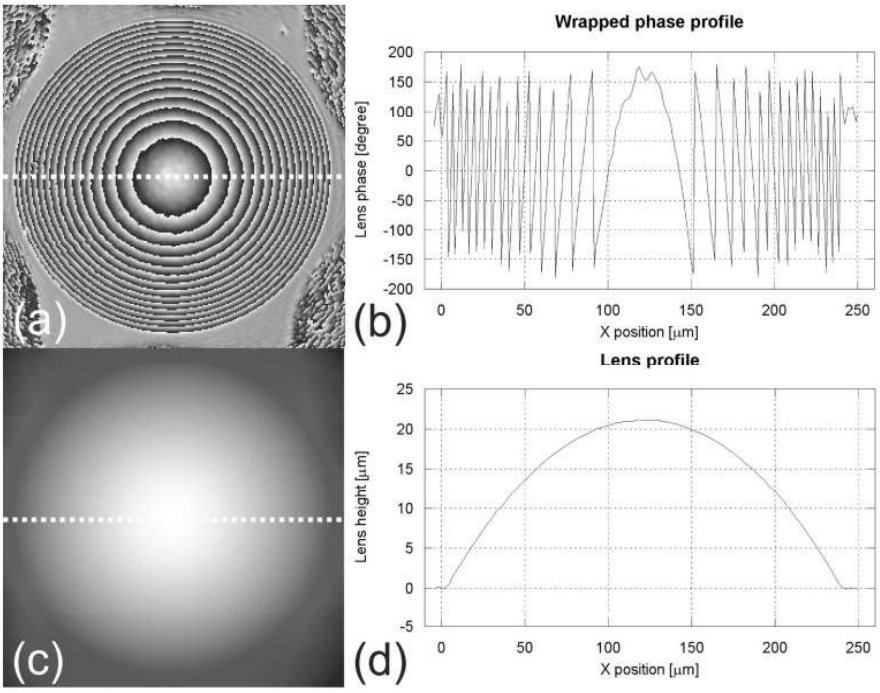

Figure 2.5: A description of phase wrapping and unwrapping for a microlens. (a) Phase wrapping of the microlens. (b) A profile of the phase wrapping microlens. (c) Phase unwrapping of the microlens. (d) A profile of the phase unwrapping microlens. (The figure is cited from Ref. 1)

Due to the periodicity of the trigonometric function, the calculated phase value is limited within a range of 2π, from $-\pi$ to π. However, considering that some biological samples are thick like the microlens example here; this results in the actual phase value reconstructed from such thick biological samples exceeding the limited phase range of 2π. However, the arctangent function forces the phase value that to be wrapped

within 2π; this presents a problem if we wish to reconstruct the sample shape from these wrapped phase values. An example of phase wrapping problem cited from Ref. 1 is shown in Fig. 2.5(a) to display a reconstructed phase field from a microlens. It can be seen that the phase is wrapped as a jagged pattern; And a profile is drawn along the centre of microlens, where the phase values oscillate between π and $-\pi$.

Thus, phase unwrapping is an indispensable procedure to recover the correct phase field associated with the accurate height and/or refractive index map of object. Choosing an immersion medium with an refractive index close to that of the object is one solution to alleviate the phase wrapping. However, not all objects are suitable to be surrounded by an immersion medium, and some objects are not easy to find immersion mediums that have a similar refractive index. Numerical phase unwrapping methods provide another solution in comparison of looking for a suitable immersion medium. An example of phase unwrapping is shown in Fig. 2.5(c) and (d), where the 2D phase field of the microlens is recovered and the curvature of the microlens is reconstructed. The numerical phase unwrapping method used for microlens can be found in Ref. 92.

Various numerical phase unwrapping methods have been proposed in the literature to not only serve the field of holography, but also serve for the fields of Magnetic Resonance Imaging (MRI), [93] Fringe Projection Profilometry (FPP), [94] and Interferometric Synthetic Aperture Radar (InSAR). [95] The numerical phase unwrapping methods are mainly split into two types: one is path-dependent [96–99] and another is path-independent [100–103]. The path-dependent methods are based on the research from Itoh [104] (which is a classical phase unwrapping method for 1D signal) to evaluate the features of wrapped phase image and determine a specific processing path to unwrap phase. In the unwrapping processing, the noise pattern component in wrapped phase image is processed by introducing the lower weights, which largely enhances the fidelity of unwrapped phase image. The path-dependent phase unwrapping methods can be usually efficient to deal with the discontinual phase with fast computation speed, but the determination of the processing path is difficult. The path-independent methods rely on minimizing a global function for the unwrapped phase image. The common manner of path-independent methods is to construct a global function and to employ the regularization and/or parametric operation for mapping the resultant unwrapped phase onto a hypothetical surface with minimum error, [101, 103] together with to use the L^p-norm to handle the phase differences between unwrapped and wrapped phase images. [102] The path-independent methods have a strong noise robustness, but they usually have a problem of big time-consuming, and may result in an overfitting (over-smooth) problem in unwrapped phase image. In this thesis, all works of phase unwrapping was achieved by the phase unwrapping method proposed in Ref. 105, which uses Modulo Wavelet Transform to adapt the path-independent method in Ref. 102. The Modulo Wavelet Transform enables to reduce the coefficients used in phase unwrapping calculation and accelerate the computation speed with a factor of up to 500.

2.2.7 White light QPI

DHM relies on using a coherent laser source to generate a hologram. However, the coherent light source can induce the coherent noise artifact, which results from the imperfect interference caused by the dust in the optical path and/or stains on the optical elements and also back reflections from the surface of elements. In Chapter 4, a synthetic aperture method is applied for DHM to remove the effect of coherent noise. But, in the researches of QPI, the most direct method of removing this noise is to use the incoherent or partial coherent light source, for example, white light.

QPI methods have been developed using white light sources. [10, 11, 21, 22, 25, 26, 106, 107] The Transport of intensity equation (TIE) is a classical white light QPI method that could retrieve the phase field of object by recording only three intensity images; one is an in-focus image and another two are slightly out-of-focus images distanced to the in-focus image at the opposite direction. The traditional TIE can be realized by the conventional brightfield microscopy. And the advanced TIE proposed by Zuo et. al. in Ref. 25 cooperates with the usage of a phase contrast annulus plate in the condenser to improve both imaging resolution and phase contrast. Spatial light interference microscopy (SLIM) is another white light QPI method. SLIM is based on the principle of phase contrast microscopy to generate an unscattered wavefield and a scattered wavefield. Relying on the usage of a spatial light modulator, four intensity images that are generated from four different phase differences between the unscattered wavefield and the scattered wavefield are recorded to calculate phase field of object. [21] Due to the characteristics of QPI, these two white light techniques have shown the potential to replace the more mature commercial qualitative label-free imaging methods of Phase contrast microscopy and DIC microscopy by enabling both the phase contrast image and DIC image to be simulated using the QPI image. [25] In chapter 3, SLIM is investigated and a novel calibration method for the spatial light modulator and the corresponding phase retrieving images are provided as well.

2.3 Background theory for Optical Diffraction Tomography

2.3.1 Introduction to Optical Diffraction Tomography

Before introducing the optical diffraction tomography (ODT) technique, we recall the phase delay map reconstructed from QPI methods. The phase delay map is highly related to the thickness and refractive index of biological samples, which enables measurement of the 3D morphological information of the sample of interest. However, the reconstruction of the phase delay map is dependent on the sample thickness and the average of refractive index within sample along the light propagation. Thus, the phase delay map reconstructed from QPI is 2D, and is not capable of reconstructing the 3D tomographic volume of sample.

Based on DHM, a microscopic imaging method called optical diffraction tomography (ODT) has been developed to quantify a 3D refractive index map of sample, and,

naturally, ODT inherits the label-free feature of QPI. ODT utilizes an intrinsic property of the sample: the refractive index as a non-embedded agent to provide the imaging contrast, and the reconstructed 3D refractive index map can be used to visualise subcellular features within a biological sample. The ODT theory was initially proposed by E.Wolf in 1969 by using holography to create a model connecting the multiple optical fields of the sample from different angular illuminations and the 3D Refractive index distribution of sample. [108] After the ODT theory was proposed, early experiments were conducted. [109–114] With the invention of laser sources, computing efficiency, and digital cameras, the ODT technique achieved a rapid development. In 2009, ODT was applied for the first time to image a biological sample by Sung et al. [115], in which human colon adenocarcinoma cells were investigated. Following this, more biological samples were investigated including red blood cells [116–124], white blood cells [117, 125–127], and eukaryotes [115, 117, 120, 125, 128–132]. Furthermore, ODT enabled some diseases such like babesiosis [124] and malaria [133] to be diagnosed.

Depending on the optical setup for ODT capture, the technique can be broadly classified into two types: sample rotation ODT [125, 134, 135] and illumination scanning ODT [115, 116, 135–142]. Sample rotation ODT uses a sample rotation holder to adjust the angle of the sample relative to a fixed illumination angle, thereby multiple optical fields projected from different areas of the sample are recorded for reconstruction of the 3D refractive index map. The advantage of the sample rotation ODT is that the full angle of 360° from the sample can be scanned, and thereby no sample information is missed in the reconstructed 3D refractive index map. However, sample rotation ODT has several disadvantages, including unnecessary perturbation on the sample from the mechanical rotation of the sample holder, slow acquisition speed due to the inherent slow rotation speed of the sample holder, and more importantly, the deformation of living cells may be produced in the process of sample rotation. [143] Illumination scanning ODT overcomes these limitations at the cost of some missing information in the tomographic image. In illumination ODT, the sample is static, and different angular illuminations irradiate the sample to construct the different angular optical fields for 3D tomographic reconstruction. In previous experiments, the angular illuminations could be produced by using galvo-scanning mirrors, [115, 135, 138, 139] SLM, [140–142] and digital micromirror device (DMD) [116, 117] with a fast scanning speed. The fixed sample position guarantees no unnecessary perturbation from mechanical movement. However, the illumination scanning ODT cannot scan all of the full-angle projection of the sample, but this problem can be mitigated using a Nonnegative Constraint Optimization (NNC) procedure, which will be demonstrated in Section 2.3.7.

2.3.2 Theory of Optical diffraction tomography

ODT is essentially an inverse scattering solution to reconstruct a desired 3D refractive map of sample from the measurement of intensity images or optical fields from multiple angular illuminations. In order to reconstruct the 3D refractive index map, two types of ODT reconstruction algorithms: projection and diffraction can be imple-

mented. The projection tomography algorithm is inspired from and analogous to the algorithm used for X-ray Computerized Tomography (CT). X-ray CT can reconstruct a 3D absorption-induced refractive index distribution of object by using the filtered back-projection algorithm to process a series of recorded X-ray images from different illumination angles. [144] The X-ray CT is broadly used in medical imaging to scan organic tissues inside human body. The ODT projection algorithm follows the work of filtered back-projection algorithm used in X-ray CT to reconstruct the 3D geometric characteristic of biological samples. [145] However, since the biological samples of interest are usually weakly scattering objects or called 'phase objects', ODT is not interested in the light absorption of the biological sample; instead it is concerned with how phase delay is induced by the refractive index variation. The projection algorithm used in X-ray CT and ODT assumes the light passing the sample along the straight line, and doesn't consider the diffraction factor. Because the wavelength of X-ray used in CT is much smaller than the size of the object of interest, overlooking the diffraction is sensible. However, in the ODT research, the wavelength is comparable to the size of biological samples, which makes diffraction impossible to ignore. The limitations of ODT projection algorithm have been experimentally proven in Ref. 143, and it can be found that the resolution loss, especially in the axial axis, manifests on the final reconstruction of the 3D refractive index map of phase objects. Thus, the ODT study in this thesis will not implement the projection algorithm. Considering the wave nature of light, the diffraction algorithm is generally used in ODT research (including the study in this thesis). In next sections, the ODT theory using diffraction algorithm is introduced.

2.3.3 Helmholtz equation

Firstly, in the context of scalar field approximation, based on the well-known Helmholtz equation, [146] the propagating light wavefield, $U_0(\mathbf{R})$, in 2D through a homogeneous medium (i.e. no sample is illuminated) can be given by:

$$(\nabla^2 + k_0^2 n(\mathbf{R})^2) U_0(\mathbf{R}) = 0 \tag{2.31}$$

where $k_0 = \frac{2\pi}{\lambda}$ denotes the wavenumber, and λ is the wavelength of used light source; n($\mathbf{R}$) denotes the refractive index of the homogeneous medium.

Considering the case of light propagating through an imhomogeneous medium (i.e. sample is illuminated), the corresponding 2D light wavefield, $U(\mathbf{R})$, can be given by:

$$(\nabla^2 + k_0^2 n_m^2) U(\mathbf{R}) = -F(\mathbf{R}) U(\mathbf{R}) \tag{2.32}$$

where

$$F(\mathbf{R}) = k_0^2 n_m^2 \left[\frac{n(\mathbf{R})^2}{n_m^2} - 1 \right] \tag{2.33}$$

Here $\mathbf{R}$ denotes the coordinate in the spatial domain, which can be 2D or 3D; $F(\mathbf{R})$ is defined as a 3D scattering potential function to describe the physical structure of sample, n_m denotes the refractive index of surrounding immersion medium, and $n(\mathbf{R})$

denotes the 3D refractive index map of sample of interest. The required refractive index map of the sample, $n(\mathbf{R})$, can be calculated, if the scattering potential function, $F(\mathbf{R})$, is known. Noted that the refractive index, $n(\mathbf{R})$, mentioned here is a complex number, where real part represents the refraction of light and imagine part represents the absorption attenuation. In term of investigating the weakly scattering biological samples, the absorption is inherently little, and thus the imagine part of complex refractive index is almost negligible. Also, noted that $\mathbf{R}$ in all wavefield functions is a 2D spatial coordinate resulting from camera recording, while $\mathbf{R}$ in scattering potential function, $F(\mathbf{R})$, and refractive index function, n($\mathbf{R}$) is the 3D spatial coordinate for tomographic reconstruction. The Helmholtz equation for imhomogeneous medium in Equation 2.32 provides the relationship between the recorded optical field and the scattering potential function.

2.3.4 Born approximation

Assuming that a sample is illuminated by plane wave, the optical field, $U(\mathbf{R})$, can be recorded. This recorded total field, $U(\mathbf{R})$, can be decomposed into a scattered field, $U_s(\mathbf{R})$, and an incident wavefield, $U_0(\mathbf{R})$. The incident wavefield, $U_0(\mathbf{R})$, follows the assumption of light propagating in homogeneous medium without transmitting through sample. The relationship between the incident field, $U_0(\mathbf{R})$, scattered field, $U_s(\mathbf{R})$, and the recorded field, $U(\mathbf{R})$, is given by

$$U(\mathbf{R}) = U_0(\mathbf{R}) + U_s(\mathbf{R}) \tag{2.34}$$

Based on the relationship in Equation 2.34, we subtract Equation 2.32 by Equation 2.31, and a relation between the 2D scattered field, $U_s(\mathbf{R})$, and the 3D scattering potential function, $F(\mathbf{R})$, is given by

$$(\nabla^2 + k_0^2 n_m^2) U_s(\mathbf{R}) = -F(\mathbf{R}) U(\mathbf{R}) \tag{2.35}$$

where $U_s(\mathbf{R})$ can be calculated via the Green's function. [108] The solution of Green's function for Helmholtz equation can be described as

$$(\nabla^2 + k_0^2 n_m^2) G(\mathbf{R} - \mathbf{R}') = -\delta(\mathbf{R} - \mathbf{R}') \tag{2.36}$$

$$G(\mathbf{R} - \mathbf{R}') = \frac{\exp(i k_0 |\mathbf{R} - \mathbf{R}'|)}{4\pi |\mathbf{R} - \mathbf{R}'|} \tag{2.37}$$

In Equation 2.36, $\delta(\mathbf{R} - \mathbf{R}')$ is the Dirac function that has a translation property:

$$\int \delta(\mathbf{R} - \mathbf{R}') F(\mathbf{R}') d^3\mathbf{R}' = F(\mathbf{R}) \tag{2.38}$$

Now, we multiply $-U(\mathbf{R})$ on the both side of Equation 2.38, and substitute the Dirac function by the left term of Equation 2.36 resulting in the following derivation:

$$\begin{aligned} -F(\mathbf{R})U(\mathbf{R}) &= -\int \delta(\mathbf{R}-\mathbf{R}')F(\mathbf{R}')U(\mathbf{R}')d^3\mathbf{R}' \\ &= \int (\nabla^2 + k_0^2 n_m^2)G(\mathbf{R}-\mathbf{R}')F(\mathbf{R}')U(\mathbf{R}')d^3\mathbf{R}' \\ &= (\nabla^2 + k_0^2 n_m^2)\int G(\mathbf{R}-\mathbf{R}')F(\mathbf{R}')U(\mathbf{R}')d^3\mathbf{R}' \end{aligned} \tag{2.39}$$

Comparing Equation 2.35 and Equation 2.39, the scattered field can be written as

$$U_s(\mathbf{R}) = \int G(\mathbf{R}-\mathbf{R}')F(\mathbf{R}')U(\mathbf{R}')d^3\mathbf{R}' \tag{2.40}$$

And the recorded total field, $U(\mathbf{R})$, can be given by

$$U(\mathbf{R}) = U_0(\mathbf{R}) + \int G(\mathbf{R}-\mathbf{R}')F(\mathbf{R}')U(\mathbf{R}')d^3\mathbf{R}' \tag{2.41}$$

In the Born approximation, the incident field, $U_0(\mathbf{R})$, is assumed to be much larger than the scattered field, $U_s(\mathbf{R})$, which can be described as $U_0(\mathbf{R}) >> U_s(\mathbf{R})$. Thus, the recorded total field is approximately equal to the incident field ($U(\mathbf{R}) \approx U_0(\mathbf{R})$). The scattered field, $U_B(\mathbf{R})$, output from the Born approximation can be given by:

$$u_B(\mathbf{R}) = \int G(\mathbf{R}-\mathbf{R}')F(\mathbf{R}')U_0(\mathbf{R}')d^3\mathbf{R}' \tag{2.42}$$

The limited condition of the Born approximation is considered now. Since $U_0(\mathbf{R})$ and $U_s(\mathbf{R})$ are two complex number, it's not easy to explain the relation of $U_0(\mathbf{R}) >> U_s(\mathbf{R})$ directly. But, as the biological samples of interest are phase objects that have an almost real refractive index, the absorption of $U_0(\mathbf{R})$ and $U_s(\mathbf{R})$ can be assumed to be neglected; and the refractive index contributes to the phase delay that modulates the wavefield. Thereby, the comparison of $U_0(\mathbf{R})$ and $U_s(\mathbf{R})$ can be transferred into how much phase delay could be produced from light passing a sample and reflect on the variation of phase fields between $U_0(\mathbf{R})$ and $U_s(\mathbf{R})$. A model of the sample-induced phase delay is given by: [147]

$$\Delta\Phi = \frac{2\pi}{\lambda}(n_a - n_m)s \tag{2.43}$$

where $\Delta\Phi$ denotes the induced phase change between two fields, s denotes the approximated thickness of biological sample of interest, n_a denotes the average refractive index of biological sample of interest, and n_m denotes the refractive index of medium. Based on Equation 2.34 to assume $U(\mathbf{R}) = U_0(\mathbf{R}) + U_s(\mathbf{R})$ and the condition of Born approximation requires $U(\mathbf{R}) \approx U_0(\mathbf{R})$; it can be derived that the resultant sample-induced phase delay $\Delta\Phi$ should be very small. Since the calculated complex phase delay has the limited phase range from 0 to 2π, in order to meet the relation of $U_0(\mathbf{R}) >> U_s(\mathbf{R})$, the resultant phase delay $\Delta\Phi$ must be much smaller than 2π:

$$\Delta\Phi << 2\pi \tag{2.44}$$

substituting the $\Delta\Phi$ by its expression written in Equation 2.43, the Relation 2.44 can be rewritten as

$$\frac{2\pi}{\lambda}(n_a - n_m)s << 2\pi \tag{2.45}$$

And a new relation can be given by

$$(n_a - n_m)s << \lambda \tag{2.46}$$

where $(n_a - n_m)s$ represents the average optical path length that light transmits through the sample of interest. Based on Equation 2.44 and Equation 2.46, it could be concluded that the usage of Born approximation is restricted by: (i) the phase delay induced by sample must be much smaller than 2π; and (ii) the average optical path length (thickness of sample) is much smaller than the wavelength of used light source. Obviously, this condition of Born approximation is not satisfied by most of biological samples which have a large thickness and produce $> \pi$ phase delay. [147]

2.3.5 Rytov approximation

The Rytov approximation is another solution to estimate the scattered field for reconstructing the refractive index map. The Rytov approximation assumes the recorded total field, $U(\mathbf{R})$, the incident field, $U_0(\mathbf{R})$, and the scattered field, $U_s(\mathbf{R})$, are in an exponential form, and their relation is given by:

$$U(\mathbf{R}) = \exp(\psi(\mathbf{R})) = U_0(\mathbf{R}) + U_s(\mathbf{R}) \tag{2.47}$$

$$U_0(\mathbf{R}) = \exp(\psi_0(\mathbf{R})) \tag{2.48}$$

$$\psi(\mathbf{R}) = \psi_0(\mathbf{R}) + \psi_s(\mathbf{R}) \tag{2.49}$$

where $\psi_s(\mathbf{R})$ is the phase term of the scattered field, $U_s(\mathbf{R})$. And $\psi(\mathbf{R})$ and $\psi_0(\mathbf{R})$ are respectively composed of an amplitude field and a phase field, which can be expressed by:

$$\psi(\mathbf{R}) = ln(\alpha(\mathbf{R})) + j\phi(\mathbf{R}) \tag{2.50}$$

$$\psi_0(\mathbf{R}) = ln(\alpha_0(\mathbf{R})) + j\phi_0(\mathbf{R}) \tag{2.51}$$

Now, the scattered field, $U_s(\mathbf{R})$, can be calculated:

$$\begin{aligned} U_s(\mathbf{R}) &= U(\mathbf{R}) - U_0(\mathbf{R}) \\ &= \exp[\psi_0(\mathbf{R}) + \psi_s(\mathbf{R})] - \exp(\psi_0(\mathbf{R})) \\ &= \exp(\psi_0(\mathbf{R}))[\exp(\psi_s(\mathbf{R})) - 1] \end{aligned} \tag{2.52}$$

Based on Equation 2.47, Equation 2.48 and Equation 2.52, the recorded total field, $U(\mathbf{R})$, can be derived and expressed as:

$$U(\mathbf{R}) = \exp(\psi(\mathbf{R})) = U_0(\mathbf{R})\exp(\psi_s(\mathbf{R})) \tag{2.53}$$

By recalling the Equation 2.32, here, the inhomogeneous Helmholtz equation used for Rytov approximation can be rewritten as follows:

$$(\nabla^2 + k_0^2 n_m^2)\exp(\psi(\mathbf{R})) = -F(R)\exp(\psi(\mathbf{R})) \tag{2.54}$$

Due to $\nabla^2\exp(\psi(\mathbf{R}))$ is equivalent to

$$\nabla^2\exp(\psi(\mathbf{R})) = \exp(\psi(\mathbf{R}))\left[\nabla^2\psi(\mathbf{R}) + (\nabla\psi(\mathbf{R}))^2\right] \tag{2.55}$$

Thus, Equation 2.54 can be rewritten as

$$\begin{aligned}\exp(\psi(\mathbf{R}))\left[\nabla^2\psi(\mathbf{R}) + (\nabla\psi(\mathbf{R}))^2 + k_0^2 n_m^2\right] &= -F(\mathbf{R})\exp(\psi(\mathbf{R})) \\ \left[\nabla^2\psi(\mathbf{R}) + (\nabla\psi(\mathbf{R}))^2 + k_0^2 n_m^2\right] &= -F(\mathbf{R})\end{aligned} \tag{2.56}$$

As shown in Equation 2.49, $\psi(\mathbf{R})$ can be transferred into $\psi_0(\mathbf{R}) + \psi_s(\mathbf{R})$. Then Equation 2.56 can be rewritten as follows:

$$\begin{aligned}\nabla^2\left[\psi_0(\mathbf{R}) + \phi_s(\mathbf{R})\right] + \left(\nabla\left[\psi_0(\mathbf{R}) + \psi_s(\mathbf{R})\right]\right)^2 + k_0^2 n_m^2 &= -F(\mathbf{R}) \\ \nabla^2\left[\psi_0(\mathbf{R}) + \phi_s(\mathbf{R})\right] + \left(\nabla\psi_0(\mathbf{R})\right)^2 + 2\nabla\psi_0(\mathbf{R})\cdot\nabla\psi_s(\mathbf{R}) + \left(\nabla\psi_s(\mathbf{R})\right)^2 + k_0^2 n_m^2 &= -F(\mathbf{R})\end{aligned} \tag{2.57}$$

Next, based on the homogeneous Helmholtz equation expressed in Equation 2.31 and a similar derivation from Equation 2.53 to Equation 2.56, an equation associated with $\psi_0(\mathbf{R})$ can be given by

$$\nabla^2\psi_0(\mathbf{R}) + (\nabla\psi_0(\mathbf{R}))^2 + k_0^2 n_m^2 = 0 \tag{2.58}$$

Removing those terms that sum to zero (shown in Equation 2.58) from Equation 2.57, the equation simplifies as follows:

$$\nabla^2\psi_s(\mathbf{R}) + 2\nabla\psi_0(\mathbf{R})\cdot\nabla\psi_s(\mathbf{R}) + \left(\nabla\psi_s(\mathbf{R})\right)^2 = -F(\mathbf{R}) \tag{2.59}$$

In the Rytov approximation, we need to consider the Laplacian of a product of two fields: $U_0(\mathbf{R})$ and $\psi_s(\mathbf{R})$

$$\nabla^2(U_0(\mathbf{R})\psi_s(\mathbf{R})) = \nabla^2 U_0(\mathbf{R})\cdot\psi_s(\mathbf{R}) + 2\nabla U_0(\mathbf{R})\cdot\nabla\psi_s(\mathbf{R}) + U_0(\mathbf{R})\nabla^2\psi_s(\mathbf{R}) \tag{2.60}$$

A simplified approximation for $\nabla^2 U_0(\mathbf{R})$ and $\nabla U_0(\mathbf{R})$ in Equation 2.60 is employed:

$$\nabla^2 U_0(R) = -k_0^2 n_m^2 U_0(\mathbf{R}) \tag{2.61}$$

$$\nabla U_0(\mathbf{R}) = U_0(\mathbf{R})\nabla\psi_0(\mathbf{R}) \tag{2.62}$$

Thus, Equation .2.60 can be rewritten as a new equation

$$(\nabla^2 + k_0^2 n_m^2)U_0(\mathbf{R})\psi_s(\mathbf{R}) = 2U_0(\mathbf{R})\nabla\psi_0(\mathbf{R})\cdot\nabla\psi_s(\mathbf{R}) + U_0(\mathbf{R})\nabla^2\psi_s(\mathbf{R}) \tag{2.63}$$

Currently, we look back the Equation 2.59, and multiply $U_0(\mathbf{R})$ on both sides of this equation

$$U_0(\mathbf{R})\nabla^2\psi_s(\mathbf{R}) + 2U_0(\mathbf{R})\nabla\psi_0(\mathbf{R})\cdot\nabla\psi_s(\mathbf{R}) + \left(\nabla\psi_s(\mathbf{R})\right)^2 U_0(\mathbf{R}) = -F(\mathbf{R})U_0(\mathbf{R}) \tag{2.64}$$

Moving the term: $\left(\nabla\psi_s(\mathbf{R})\right)^2 U_0(\mathbf{R})$ in Equation 2.64 to right side, we get

$$U_0(\mathbf{R})\nabla^2\psi_s(\mathbf{R}) + 2U_0(\mathbf{R})\nabla\psi_0(\mathbf{R})\cdot\nabla\psi_s(\mathbf{R}) = -F(\mathbf{R})U_0(\mathbf{R}) - \left(\nabla\psi_s(\mathbf{R})\right)^2 U_0(\mathbf{R}) \tag{2.65}$$

Then, by comparing Equation 2.63 and Equation 2.65, we finally obtain

$$\begin{aligned}(\nabla^2 + k_0^2 n_m^2)U_0(\mathbf{R})\psi_s(\mathbf{R}) &= -F(\mathbf{R})U_0(\mathbf{R}) - \left(\nabla\psi_s(\mathbf{R})\right)^2 U_0(\mathbf{R}) \\ &= -U_0(\mathbf{R})\left[(\nabla\psi_s(\mathbf{R}))^2 + F(\mathbf{R})\right]\end{aligned} \tag{2.66}$$

In the Rytov approximation, $\psi_s(\mathbf{R})$ is called the Rytov phase $\psi_R(\mathbf{R})$, and $(\nabla\psi_s(\mathbf{R}))^2$ is assumed much smaller than the scattering potential function: $F(\mathbf{R})$.

$$(\nabla\psi_s(\mathbf{R}))^2 << F(\mathbf{R}) \tag{2.67}$$

Thereby, $\left[(\nabla\psi_s(\mathbf{R}))^2 + F(\mathbf{R})\right]$ is approximated as $F(\mathbf{R})$, and Equation 2.66 is rewritten as

$$(\nabla^2 + k_0^2 n_m^2)U_0(\mathbf{R})\psi_s(\mathbf{R}) = -U_0(\mathbf{R})F(\mathbf{R}) \tag{2.68}$$

Here, we could perform the Green's function (as previously applied for the case of the Born approximation) from Equation 2.35 to Equation 2.42; the solution for $\psi_s(\mathbf{R})$ is given by:

$$\psi_s(\mathbf{R}) = \frac{\int G(\mathbf{R}-\mathbf{R}')F(\mathbf{R}')U_0(\mathbf{R}')d^3\mathbf{R}'}{U_0(\mathbf{R})} \tag{2.69}$$

By comparing the expression of the Rytov phase $\psi_s(\mathbf{R})$ obtained from the Equation 2.69 and the expression of the Born scattered field $U_B(\mathbf{R})$ obtained from Equation 2.42, the relationship between $\psi_s(\mathbf{R})$ and $U_B(\mathbf{R})$ is derived:

$$\psi_s(\mathbf{R}) = \frac{U_B(\mathbf{R})}{U_0(\mathbf{R})} \tag{2.70}$$

In the practical experiment, based on Equation 2.53, the Rytov phase $\psi_s(\mathbf{R})$ could be calculated by $ln\left(\frac{U(\mathbf{R})}{U_0(\mathbf{R})}\right)$

$$\begin{aligned}\psi_s(\mathbf{R}) &= ln\left(\frac{U(\mathbf{R})}{U_0(\mathbf{R})}\right) = ln\left(\frac{\exp(\psi(\mathbf{R}))}{\exp(\psi_0(\mathbf{R}))}\right) \\ &= ln\left(\exp(\psi(\mathbf{R}) - \psi_0(\mathbf{R})\right) \\ &= ln\left(\frac{\alpha(\mathbf{R})}{\alpha_0(\mathbf{R})}\right) + j(\phi(\mathbf{R}) - \phi_0(\mathbf{R}))\end{aligned} \tag{2.71}$$

It can be seen from Equation 2.71 that the Rytov phase $\psi_s(\mathbf{R})$ is straight-forward to calculate, assuming that DHM can be used to reconstruct the amplitude fields and the phase fields of $U(\mathbf{R})$, and also to measure the incident field, $U_0(\mathbf{R})$. We note that an un-

wrapping phase algorithm should be performed on the subtraction of the phase fields $\phi(\mathbf{R}) - \phi_0(\mathbf{R})$, in order to avoid the wrapped phase problem that have been described in Section 2.2.6.5.

2.3.5.1 Validity of Rytov approximation

As shown in Equation 2.67, the Rytov approximation assumes $(\nabla\psi_s(\mathbf{R}))^2$ is much smaller than scattering potential function F($\mathbf{R}$).

$$(\nabla\psi_s(\mathbf{R}))^2 << F(\mathbf{R}) \tag{2.72}$$

where $F(\mathbf{R}) = k_0^2 n_m^2 [\frac{n(\mathbf{R})^2}{n_m^2} - 1]$. Thus, it can continue to deduce:

$$\begin{aligned} (\nabla\psi_s(\mathbf{R}))^2 &<< k_0^2 n_m^2 [\frac{n(\mathbf{R})^2}{n_m^2} - 1] \\ n(\mathbf{R})^2 &>> n_m^2 \left[\frac{(\nabla\psi_s(\mathbf{R}))^2}{k_0^2 n_m^2}\right] + n_m^2 \\ n(\mathbf{R})^2 - n_m^2 &>> \frac{(\nabla\psi_s(\mathbf{R}))^2}{k_0^2} \end{aligned} \tag{2.73}$$

Compared with the validity condition of the Born approximation that is associated with the sample thickness (mentioned in Equation 2.46), the above Equation 2.73 implies that Rytov approximation is no longer constrained by the sample thickness. Actually, the validity of Rytov approximation is greatly related to the refractive index distribution of the sample, $n(\mathbf{R})$, which can be investigated further below.

We denote $\varepsilon(\mathbf{R})$ as the refractive index variation between the refractive index distribution of sample, $n(\mathbf{R})$, and the refractive index of medium, n_m:

$$\varepsilon(\mathbf{R}) = n(\mathbf{R}) - n_m \tag{2.74}$$

Then, Equation 2.73 can be rewritten as,

$$2n_m\varepsilon(\mathbf{R}) + \varepsilon(\mathbf{R})^2 >> \frac{(\nabla\psi_s(\mathbf{R}))^2}{k_0^2} \tag{2.75}$$

Based on the work in Ref. 138, $\varepsilon(\mathbf{R})$ is approximately equal to 0.03-0.04. Thereby, the term $\varepsilon(\mathbf{R})^2$ is almost equal to zero, and can be ignored. Thereby, Equation 2.75 could be rewritten as,

$$2n_m\varepsilon(\mathbf{R}) >> \frac{(\nabla\psi_s(\mathbf{R}))^2}{k_0^2} \tag{2.76}$$

Now, applying the square root to both sides of Equation 2.76, a new inequality can be given by:

$$\frac{|\nabla\psi_s(\mathbf{R}))|}{2\pi} << \frac{\sqrt{2n_m|\varepsilon(\mathbf{R})|}}{\lambda} \tag{2.77}$$

which is equivalent to:

$$\frac{|d\psi_s(\mathbf{R}))|}{2\pi|d\mathbf{R}|} << \frac{\sqrt{2n_m|\varepsilon(\mathbf{R})|}}{\lambda} \tag{2.78}$$

The Equation 2.77 and Equation 2.78 can be explained as follows: with respect to any point **R** within the sample, the gradient of the phase delay induced from sample is scaled by a period of 2π and this scaled phase gradient should be much smaller than the refractive index variation, $\varepsilon(\mathbf{R})$, over the wavelength λ.

Again, noting that in terms of the biological samples (phase objects) of interest in ODT research, only the real part of the complex refractive index, $n(\mathbf{R})$, is associated with the phase delay induced by sample. Based on the Rytov assumption for recorded total field: $U(\mathbf{R}) = U_0(\mathbf{R})\exp(\psi_s(\mathbf{R}))$ in Equation 2.53, and since the incident field $U_0(\mathbf{R})$ is a plane wavefield, the Rytov phase, $\psi_s(\mathbf{R})$, is equivalent to the sample-induce phase delay, $\Delta\Phi(\mathbf{R})$,

$$\psi_s(\mathbf{R}) = \Delta\Phi(\mathbf{R}) \tag{2.79}$$

Here, $\Delta\Phi(\mathbf{R})$ could be understood as the amount of induced phase delay before light arrives on the point **R** within the sample. We assume that light travels through the sample along an approximately straight line along the z-axis, and a model for estimating the phase delay $\Delta\Phi(\mathbf{R})$ can be given by: [147]

$$\Delta\Phi(\mathbf{R}) = \psi_s(\mathbf{R}) \approx \frac{2\pi}{\lambda}\int_{-\inf}^{\xi} \varepsilon(x,y,z')dz' \tag{2.80}$$

The above model is valid when light is assumed to propagate following a straight line. This validity is true for almost all biological samples that have the size bigger than the wavelength, λ. For simplicity, a length scale l_s larger than wavelength λ, ($l_s > \lambda$), is defined to represent a spatial distance that light propagates along a straight line within the sample. Synthesizing Equation 2.79 and Equation 2.80, the absolute value of the gradient of the Rytov phase, $|\nabla\psi_s(\mathbf{R})|$, can be deduced as:

$$|\nabla\psi_s(\mathbf{R})| \approx \frac{2\pi}{\lambda}\left|\int_0^{l_s} \nabla\varepsilon(\mathbf{R})dz\right| \quad , \quad l_s > \lambda \tag{2.81}$$

where, $|\int_0^{l_s}\nabla\varepsilon(\mathbf{R})dz|$ on the right side of Equation 2.81 can be approximately equal to $l_s|\nabla\varepsilon(\mathbf{R})|$ (derived from Equation A.27 to Equation A.29 in Ref. 147). Thus, the absolute value of the gradient of Rytov phase, $|\nabla\psi_s(\mathbf{R})|$, can be approximated as:

$$|\nabla\psi_s(\mathbf{R})| \approx \frac{2\pi}{\lambda} l_s|\nabla\varepsilon(\mathbf{R})| \quad , \quad l_s > \lambda \tag{2.82}$$

By comparing Equation 2.77 and Equation 2.82, the valid condition of the Rytov approximation can be obtained:

$$|\nabla\varepsilon(\mathbf{R})| = |\nabla(n(\mathbf{R}) - n_m)| << \frac{\sqrt{2n_m|\varepsilon(\mathbf{R})|}}{l_s} \quad , \quad l_s > \lambda \tag{2.83}$$

since n_m is a constant that doesn't influence the result of gradient calculation, the n_m

in $|\nabla(n(\mathbf{R}) - n_m)|$ can be neglected, and Equation 2.83 can be rewritten as

$$|\nabla(n(\mathbf{R})| << \frac{\sqrt{2n_m|\varepsilon(\mathbf{R})|}}{l_s} \quad , \quad l_s > \lambda \tag{2.84}$$

The scale length l_s in the denominator of right term in Equation 2.84 is a very small positive number; thus, the right side of inequality is a large positive number. Thereby, the above inequality (Equation 2.84) can be satisfied easily. Now, the valid condition of Rytov approximation is determined by the gradient of refractive index within sample. The samples thickness, which limits the use of Born approximation, will not place a constraint on the Rytov approximation. This makes Rytov approximation suitable to apply on biological samples.

2.3.6 Fourier diffraction theorem

As demonstrated previously, in the context of considering the wave nature of diffraction, the relationship between the propagated light field and reflective index dependent scattering potential function, $F(\mathbf{R})$, can be constructed by using Helmholtz Equation. Then, the Born or Rytov approximation could be employed to estimate the Born scattered field, $U_B(\mathbf{R})$, or Rytov phase, $\psi_s(\mathbf{R})$, respectively with the help of Green function. The mathematical expression of the Born scattered field, $U_B(\mathbf{R})$, and Rytov phase, $\psi_s(R)$, are respectively shown in Equation 2.40 and Equation 2.69. However, it can be observed that these two equations, with the inclusion of the Green function, are difficult to calculate for reconstruction of the desired scattering potential function, $F(\mathbf{R})$. A method called the Fourier diffraction theorem is introduced here, which can directly connect the scattering potential function, $F(\mathbf{R})$, to the Born scattered field, $U_B(\mathbf{R})$, and/or the Rytov phase, $\psi_s(R)$ [108], which is based on the following description. As

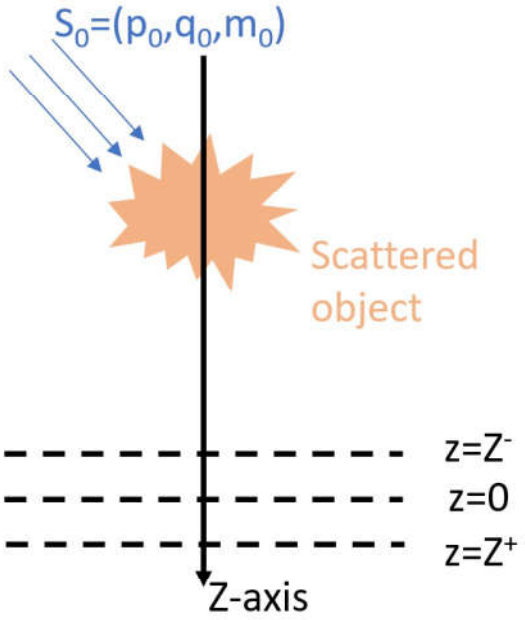

Figure 2.6: A sample is illuminated by incident light of plane wave.

shown in Fig. 2.6, we assume that a sample is in an xyz Cartesian coordinate system, where $x-y$ plane represents the lateral plane, and z represents the axial direction. Thus, each point $\mathbf{R}$ within sample expressed previously is equivalent to have a 3D coordinate (x,y,z). The sample is assumed to be illuminated by a monochromatic plane wave. We assume that the total field, $U(\mathbf{R})$, is recorded by a camera located on the plane of $z=0$, and the planes of the propagating optical field before and after the camera plane are respectively denoted as $z=z^-$ and $z=z^+$ respectively. By decomposing the recorded total field, $U(\mathbf{R})$, the propagation of incident plane wavefield, $U_0(\mathbf{R})$, can be described:

$$U_0(\mathbf{R}) = \exp(jk_0 s_0 \mathbf{R}) \tag{2.85}$$

where $s_0=(p_0,q_0,m_0)$ is the unit spatial frequency vector of incident light. (p_0,q_0,m_0) is the three components of vector that corresponds to the directions of the x,y,z axis in spatial domain, and the relation of these three components is given by

$$m_0 = \sqrt{1-p_0^2-q_0^2} \tag{2.86}$$

Substituting this expression of $U_0(\mathbf{R})$ from Equation 2.85 into Equation 2.40, the Born scattered field, $U_B(\mathbf{R})$, is given by:

$$u_B(\mathbf{R}) = \int G(\mathbf{R}-\mathbf{R}')F(\mathbf{R}')\exp(jk_0 s_0 \mathbf{R})d^3\mathbf{R}' \tag{2.87}$$

where infinity is set for the limits of integration, because the region outside the $F(\mathbf{R})$ is zero and doesn't affect the integration result. The Green function $G(\mathbf{R}-\mathbf{R}')$ here could be understood as a description of spherical scattered wave, [148]

$$G(\mathbf{R}-\mathbf{R}') = \frac{jk_0}{8\pi^2}\iint_{-\infty}^{+\infty}\frac{1}{m}\exp\{jk_0[p(x-x')+q(y-y')+m(z-z')]\}dpdq \tag{2.88}$$

where (q,p,m) is the unit spatial frequency vector of an arbitrary scattered wave, and the vector components q, g, m meet the relation:

$$m = \sqrt{1-(p^2+q^2)} \quad , \quad p^2+q^2 \le 1 \tag{2.89}$$

We only consider the case of $p^2+q^2 \le 1$, because, as mentioned in Section 2.2.3, when $p^2+q^2>1$, the scattered wave is an evanescent wave. The evanescent wave will attenuate rapidly during propagation, and will not be discussed in this thesis. Now substituting $G(\mathbf{R}-\mathbf{R}'))$ from Equation 2.88 into Equation 2.87, we can obtain the following expression:

$$\begin{aligned} u_B(\mathbf{R}) = \int \frac{jk_0}{8\pi^2}\iint_{-\infty}^{+\infty}\frac{1}{m}\exp\{jk_0[p(x-x')+q(y-y')+m(z-z')]\}dpdq \\ \times F(\mathbf{R}')\exp(jk_0 s_0 \mathbf{R'})d^3\mathbf{R}' \end{aligned} \tag{2.90}$$

Equation 2.90 can be rewritten as follows:

$$u_B(\mathbf{R}) = \iint_{-\infty}^{+\infty} A(p,q;p_0,q_0)\exp[jk_0(px+qy+mz)]\,dpdq \tag{2.91}$$

where

$$A(p,q;p_0,q_0) = \frac{jk_0}{8\pi^2}\int F(\mathbf{R}')\exp\{-jk_0[(p-p_0)x'+(q-q_0)y'+(m-m_0)z']\}d^3\mathbf{R}' \tag{2.92}$$

Now performing the 3D Fourier transform on the scattering potential function, $F(\mathbf{R}) = F(x,y,z)$, the spectra of scattering potential can be given by:

$$\begin{aligned}\tilde{F}(k_x,k_y,k_z) &= \mathscr{F}[F(x,y,z)] \\ &= \frac{1}{(2\pi)^3}\iiint_{-\infty}^{+\infty} F(x,y,z)\exp[-j(k_x x+k_y y+k_z z)]\,dxdydz\end{aligned} \tag{2.93}$$

where (k_x,k_y,k_z) is the spatial frequency coordinate:

$$\begin{aligned}k_x &= k_0 p \\ k_y &= k_0 q \\ k_z &= k_0 m\end{aligned} \tag{2.94}$$

Thus, Equation 2.92 can be rewritten as follows:

$$\begin{aligned}A(p,q;p_0,q_0) &= \frac{jk_0\pi}{m}\tilde{F}[k_0(p-p_0),k_0(q-q_0),k_0(m-m_0)] \\ &= \frac{jk_0\pi}{m}\tilde{F}(k_x-k_0p_0,k_y-k_0q_0,k_z-k_0m_0)\end{aligned} \tag{2.95}$$

Assuming that the 2D Fourier transform with respect to the variables of x and y is performed on the Born scattered field, $U_B(x,y,z)$, which can be given by:

$$\tilde{U}_B(k_x,k_y;z) = \frac{1}{(2\pi)^2}\iint_{-\infty}^{+\infty} U_B(x,y,z)\exp[-j(k_x x+k_y y)]\,dxdy \tag{2.96}$$

then, $A(p,q;p_0,q_0)$ can be described as:

$$A(p,q;p_0,q_0) = k_0^2\exp(-jk_0mz)\tilde{U}_B(k_x,k_y;z) \tag{2.97}$$

Comparing Equation 2.95 and Equation 2.97, we can derive a relationship between the 3D spectrum of scattering potential function and the 2D spectrum of Born scattered field:

$$\begin{aligned}\tilde{F}(k_x-k_0p_0,k_y-k_0q_0,k_z-k_0m_0) &= -\frac{jk_0m}{\pi}\exp(-jk_0mz)\tilde{U}_B(k_x,k_y;z) \\ &= -\frac{jk_z}{\pi}\exp(-jk_zz)\tilde{U}_B(k_x,k_y;z)\end{aligned} \tag{2.98}$$

Further, if the total field $U(\mathbf{R})$ is recorded at $z = 0$, Equation 2.98 can be simplified as follows:

$$\tilde{F}(k_x - k_0 p_0, k_y - k_0 q_0, k_z - k_0 m_0) = -\frac{j k_z}{\pi} \tilde{U}_B(k_x, k_y; z = 0) \tag{2.99}$$

The above description is the derivation of Fourier diffraction theorem for the Born approximation. The derivation of the Fourier diffraction theorem for the Rytov approximation is similar. Based on Equation 2.70, the Born scattered field, $U_B(\mathbf{R})$, is equivalent to the multiplication of the Rytov phase, $\psi_R(\mathbf{R})$, and the incident field, $U_0(\mathbf{R})$. Thus, for the Rytov approximation, Equation 2.99 can be rewritten as follows:

$$\tilde{F}(k_x - k_0 p_0, k_y - k_0 q_0, k_z - k_0 m_0) = -\frac{j k_z}{\pi} \tilde{U}_\dagger(k_x, k_y; z = 0) \tag{2.100}$$

where

$$\tilde{U}_\dagger(k_x, k_y; z = 0) = \mathscr{F}[U_\dagger(x, y; z = 0)] \tag{2.101}$$

where $\mathscr{F}$ denotes the 2D Fourier transform performed on x and y variables, and

$$U_\dagger(x, y; z = 0) = U_0(x, y; z = 0)\psi_R(x, y; z = 0) \tag{2.102}$$

In order to implement the Fourier Diffraction theorem, we spatially shift the spectrum, $\tilde{F}(k_x - k_0 p_0, k_y - k_0 q_0, k_z - k_0 m_0)$, and Equation 2.100 should be rewritten as follows:

$$\tilde{F}(k_x, k_y, k_z) = -\frac{j(k_z + k_0 m_0)}{\pi} \tilde{U}_\dagger(k_x + k_0 p_0, k_y + k_0 q_0; z = 0) \tag{2.103}$$

Here, the expression of incident field, $U_0(\mathbf{R})$, in Equation 2.85 is recalled. It is important to note that the wavefield in the 2D spatial domain divided by the 2D incident field $U_0(\mathbf{R})$ has the effect to move the resultant spectrum with a shift of $(-k_0 p_0, -k_0 q_0)$. Therefore, the term of $\tilde{U}_\dagger(k_x + k_0 p_0, k_y + k_0 q_0; z = 0)$ on the right side of Equation 2.103 can be obtained as follows:

$$\begin{aligned} \tilde{U}_\dagger(k_x + k_0 p_0, k_y + k_0 q_0; z = 0) &= \mathscr{F}\left[\frac{U_\dagger(x, y; z = 0)}{U_0(x, y; z = 0)}\right] \\ &= \mathscr{F}\left[\frac{U_0(x, y; z = 0)\psi_R(x, y; z = 0)}{U_0(x, y; z = 0)}\right] \\ &= \mathscr{F}[\psi_R(x, y; z = 0)] \\ &= \tilde{\psi}_R(k_x, k_y, z = 0) \end{aligned} \tag{2.104}$$

Thus, Equation 2.103 can be rewritten as

$$\tilde{F}(k_x, k_y, k_z) = -\frac{j(k_z + k_0 m_0)}{\pi} \tilde{\psi}_R(k_x, k_y, z = 0) \tag{2.105}$$

Now, focusing on Equation 2.103, if a number of different angular illuminations with different spatial frequency vectors are illuminated on the sample, the 3D spec-

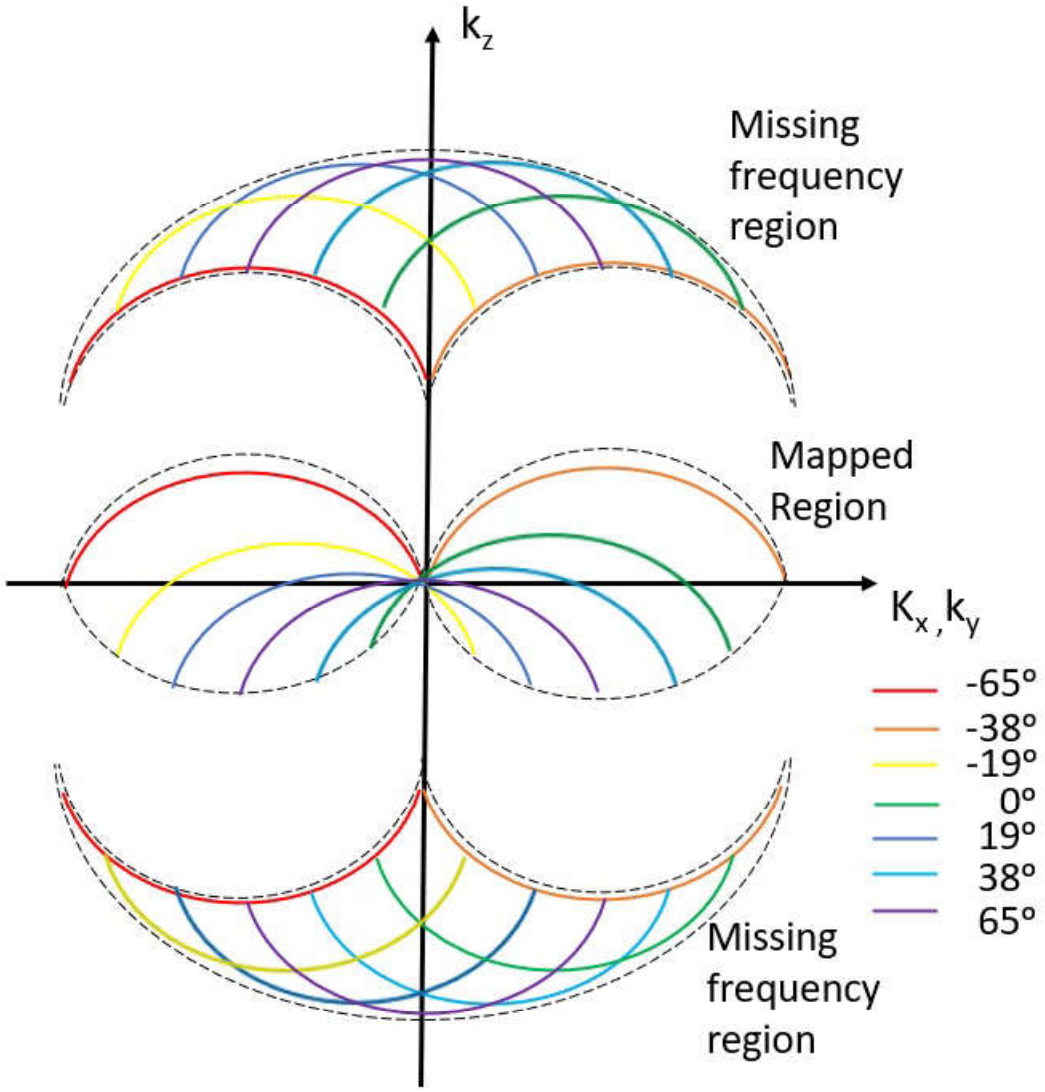

Figure 2.7: The result of 3D mapped Ewald sphere from seven incident illuminations at angles: $-65°$, $-38°$, $-19°$, $0°$, $19°$, $38°$, $65°$.

trum of the scattering potential function, $\widetilde{F}(k_x, k_y, k_z)$, is a result of mapping multiple 2D spectra from different angular illuminations, $\widetilde{U_\dagger}(k_x + k_0 p_0, k_y + k_0 q_0; z = 0)$, onto a spherical surface in a 3D space. This spherical surface is also called the well-known Ewald sphere. In order to demonstrate the Ewald sphere, in Fig. 2.7, we make a rough drawing of the Ewald sphere from seven incident illumination angles: $-65°$, $-38°$, $-19°$, $0°$, $19°$, $38°$, $65°$. It can be seen that, based on the different spatial frequency vectors of illuminations, the 2D spectra of $\widetilde{U_\dagger}(k_x + k_0 p_0, k_y + k_0 q_0; z = 0)$ from different incident illuminations can be mapped onto different positions on the 3D Ewald sphere. However, as mentioned previously, the illumination scanning ODT used in this research suffers from the limited numerical aperture of the condenser lens and the microscope objective, and only the middle region of Ewald sphere in Fig. 2.7 can be mapped, and a large region in the Fourier domain including the top and bottom regions in Fig. 2.7 is missing. This missing area of frequency component is the so-called 'missing-cone' problem. This 'missing-cone' problem can be mitigated by a numerical processing of nonnegativity constraint optimization (NNC) procedure, which will be demonstrated in Section 2.3.7.

Finally, we perform inverse Fourier transform on the spectrum of the scattering potential function, $\widetilde{F}(k_x, k_y, k_z)$, obtained in Equation 2.105, and the desired 3D refractive index distribution of the sample,$n(\mathbf{R})$, can be extracted based on Equation 2.33.

2.3.7 Nonnegativity Constraint Optimization

As mentioned previously, the illumination scanning ODT faces a 'missing-cone' problem that results from a missing region in the 3D spectrum of the scattering potential function (Ewald sphere) in the spatial frequency domain. Thereby, partial information of sample will be lost after tomographic reconstruction, and also, the result of reconstruction will be distorted along the axial optical axis. In this section, in order to replenish the missing frequency region on the 3D frequency domain, a nonnegative constraint optimization (NNC) procedure referred from [149] is described, and will later be applied in Chapter 5. This NNC procedure is divided into two piecewise iterative constraint algorithms.

The first algorithm is the 'total variation iterative constraint' (TVIC) algorithm. TVIC algorithm connects the recorded phase images (sinograms) and scattering potential function on the spatial domain. This algorithm is designed to minimize the total variation (TV) of the scattering potential function, F, and automatically generate the corresponding constraint. [150–152] The mathematical description for TVIC algorithm is given by:

$$\begin{aligned} &\text{minimize} \quad ||F||_{TV} \\ &\text{subject to} \quad MF = g, \quad F_i \geq 0 \end{aligned} \tag{2.106}$$

where F is the scattering potential function, which is transferred as the form of vector that has a length of N, where is the number of elements that the scattering potential function has; $F_i(\mathbf{i} = 1, 2, ..., N)$ denotes the **i**th element in the scattering potential func-

tion, M is the projection operator, g is the phase images (sinograms) which are combined and transferred into a vector with a length of P, which is the number of elements in all sinograms. In Equation 2.106, two constraints are set for minimizing $||F_{TV}||$: one is $MF = g$, which is designed to keep the consistence between the tomographic reconstruction and the sinograms; another constraint is $F_i \geq 0$, which is a nonnegative constraint to make sure that the calculated refractive index of the sample is greater than or equal to the refractive index of the surrounding medium. Theoretically, The problem of TV minimization could be solved by numerous optimization algorithms. In Chapter 5, the Chambolle-Pock algorithm [153, 154] is performed to define the projection operator M. The goal of using this TVIC algorithm is to determine the spatial limit (edge) of sample in the reconstructed scattering potential function. This spatial limit can be automatically generated as a constraint, which can be output as a 3D binary mask to realize cell segmentation in the spatial domain. The output 3D binary mask will be subsequently used in the second iterative constraint algorithm.

The second iterative constraint algorithm is the Gerchberg-Papoulis (GP) algorithm. This GP algorithm is designed to stuff the missing region in the frequency domain. In each iteration, the steps of GP algorithm for ODT research are as follow: [155, 156]

(1) $\tilde{F}'_i = (1 - \beta_i \Omega)\tilde{F}_{i-1} + \beta_i \Omega \tilde{F}_0$

(2) $F_i = \mathscr{F}^{-1}(\tilde{F}'_i)$

(3) $F'_i = g^{-1}(P_{\beta_i} P_+ \mathscr{R}\{g(F_i)\})$

(4) $\tilde{F}_i = \mathscr{F}(F'_i)$

The replenishment of the missing region in the frequency domain is described in Step (1). $\tilde{F}_0$ is the spectrum of the initial scattering potential function that results from mapping all the 2D Rytov phase spectra from different angular illuminations onto the Ewald sphere. However, this spectral mapping can result in a problem whereby multiple spectral values are overlapped and superimposed on a certain number of voxels on the Ewald sphere. In particular, the low frequency signal will be increased incorrectly. In order to solve this problem, a nearest neighbour method is performed by averaging the overlapped spectral values on the certain number of voxels, and the incorrectly superimposed spectral value are repaired. $\tilde{F}_i$ represents the recovered spectrum of the scattering potential function from **i**th iteration. Ω is a 3D binary mask to distinguish the known region resulting from the mapping of the Rytov phase spectra and another missing area in the frequency domain, β_i is a relaxation parameter that is gradually descending during iterations. Initially, the value of β_i in the first iteration is set as 1, and then β_i in each iteration is updated by multiplying the relaxation parameter used in last iteration (β_{i-1}) by a descending coefficient of 0.99, which is expressed as: $\beta_i = 0.99\beta_{i-1}$. Step (2) transfers $\tilde{F}_i$ in the frequency domain into the spatial domain by using an inverse DFT. $\mathscr{F}^{-1}$ denotes the operator of inverse DFT, and F_i denotes the calculated scattering potential function in the spatial domain. Based on the calculation from the previous TVIC algorithm, a 3D binary mask, which is used to determine the

sample region in the spatial domain, is applied on the scattering potential function in order to remove the unwanted information from non-sample region. In Step (3), g is a function to return a subtraction difference between the complex refractive index of sample and the refractive index of the surrounding immersion medium.

We recall from the previous sections that only the real part in the complex number represents the effect of refraction; thus, a function $\mathscr{R}$ is used for extracting the real part from the complex subtraction difference. P_+ is an operator to set a nonnegative constraint for subtracting the difference of refractive indexes. In other words, this P_+ operator corrects the calculated refractive indexes of the sample that are less than the refractive index of the background surrounding immersion medium, and changes their value back to the refractive index of the background surrounding immersion medium. P_{β_i} is an operator to multiply a coefficient of $1-\beta_i$ on the padded region to suppress the oversampling. The padded region is actually a signal domain extension resulting from mapping 2D spectra of the Rytov phase fields with a small size onto a 3D spectrum of the scattering potential function with a large size in the frequency domain. g^{-1} is an inverse function of g to revert the scattering potential function. Step (4) performs a DFT on the scattering potential function to obtain its corresponding spectrum for next iteration.

In overview, this GP algorithm is a 'Ping-Pong' iterative procedure based on the signal conversion between spatial domain and frequency domain. In the frequency domain, the missing frequency region is stuffed and continually corrected during iterations by gradually reducing the influence of the signal from the known region associated with the mapping from the Rytov phase spectra. In the spatial domain, a nonnegative constraint is set for correcting the reconstructed refractive to be greater/equal than that of the background immersion medium. Thereby, the fidelity of tomographic reconstruction could be improved. Simultaneously, the replenishment of the original missing frequency area in the frequency domain can mitigate the distortion problem along the axial axis for the tomographic reconstruction, and help the recovered refractive index map to obtain a better resolution. Generally, 100-200 iterations are sufficient to find the convergent result for tomographic reconstruction.

2.4 Background theory for Raman Spectroscopy

Raman spectroscopy is also a label-free method that probes the chemical structures within unstained or stained biological samples. Unlike QPI methods and the ODT technique, which can only measure morphological information from biological samples, Raman spectroscopy probes chemical information from biological samples.

2.4.1 Physics of Raman Spectroscopy

As the laser interacts with the sample, a small amount of light is emitted light in all directions around the sample with lower energy than the laser light. This phenomenon is called light scattering. If the incident beam is irradiated on the sample from a monochromatic light source, or from a light source with a very narrow wavelength band, most of

resultant emitted scattered photons have the same energy and wavelength as the incident beam photons; this phenomenon is called elastic Rayleigh scattering. There is also a small remaining number of scattered photons which are emitted with less or more energy and at different wavelengths relative to the incident beam; this phenomenon is called Raman scattering. Normally, Raman scattering light is much weaker than Rayleigh scattering light, and the occurrence ratio of Raman scattering to Rayleigh scattering is only $1/10^7$. [157] It's notable that other scattering also takes place, namely: Mie, Brillouin, Thompson, or Compton scattering. [158] However, the occurrence rate of these scattering phenomenons is smaller, and these scattering phenomenons nearly don't influence the result obtained from Raman spectroscopy. Thus, Mie, Brillouin, Thompson, or Compton scattering phenomenon will not be discussed in this thesis.

The quantum theory of radiation can be used for understanding the Raman scattering. [159] Based on the energy change occurring in the interaction between the chemical molecules and the incident beam, a diagram of the molecules energy levels for undergoing Rayleigh scattering and Raman scattering is demonstrated in Fig. 2.8. It can be assumed that in a static environment, the molecules within a sample stay at the initial energy levels E_0 or E_1 on the ground state. When the photons from the incident beam collide onto the molecules within sample, the molecules will be excited into a virtual energy state $E_0 + h\upsilon_0$ or $E_1 + h\upsilon_0$ with higher energy. If the collision is perfectly elastic, the molecules energy return the original ground state and emit the photons with the same wavelength as the incident beam; this is Rayleigh scattering. However, if the collision is inelastic, the energy from molecules excited onto the virtual energy state can't return their original ground state. As a result, the molecules will gain or lose energy due to the collision, which is consistent with the laws of quantum theory, to generate the emitted photons with the discrete wavelengths different from the monochromatic wavelength of incident beam. More concretely, in the case of the molecules excited from E_0 and back to E_1, the scattered photons have a higher wavelength than the wavelength of monochromatic incident beam. These scattered photons are referred as 'Stokes' Raman photons. Conversely, the scattered photons called 'Anti-Stokes' Raman photons have lower wavelengths than the wavelength of monochromatic incident beam, which is the result of the molecules being excited from E_1 and back to E_0. Generally, in room temperature, the number of molecules at E_0 is much more than molecules at E_1. Thereby, the occurrence rate of Stokes Raman scattering is much higher than that of Anti-Stokes Raman scattering, and generally the Stokes scattered photons are measured in Raman spectroscopy due to the higher Raman collection efficiency. The energy shift of Raman scattered photons can be described by an equation as below:

$$\Delta\tilde{\nu}(cm^{-1}) = \left[\frac{1}{\lambda_{incident}(nm)} - \frac{1}{\lambda_{scattered}(nm)}\right] \times \frac{10^9(nm)}{10^2(cm)} \tag{2.107}$$

where $\Delta\tilde{\nu}$ is the wavenumber (cm^{-1}) representing the energy shift from Raman scattering, $\lambda_{incident}$ and $\lambda_{scattered}$ denote the wavelength of incident beam and the wavelength of scattered photons respectively. It can be seen from Equation 2.107 that the wavenumber is a function of the wavelength of the scattered photons (the wavelength

of incident beam is known), and can be transferred from the wavelength of the scattered photons. In the practical Raman analysis, the wavenumber is generally used as the independent variable to correspond to the intensity of collected Raman photons (dependent variable).

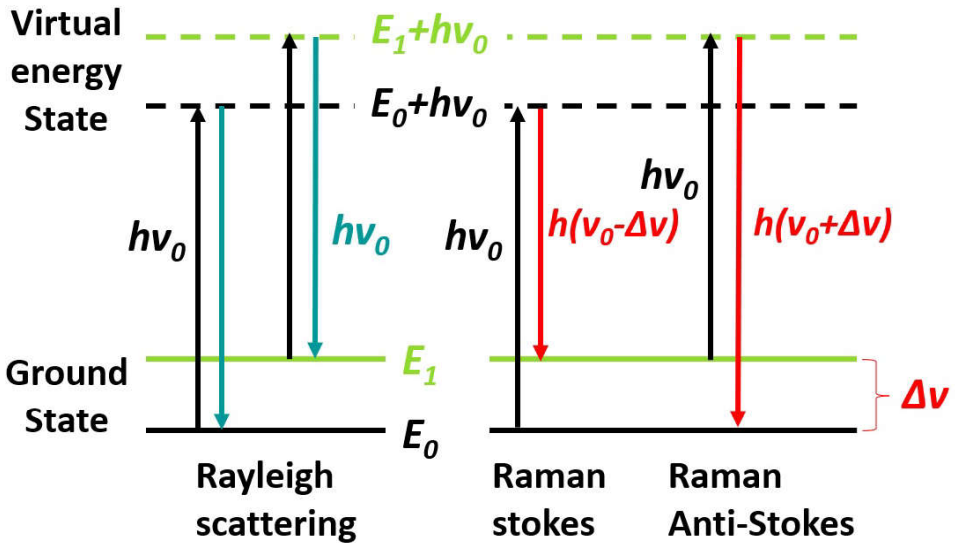

Figure 2.8: A diagram of energy shift resulting from Rayleigh scattering and Raman scattering

The Raman scattered photons can be collected and recorded as a Raman spectrum. By observing the Raman spectrum of a sample, it is possible to discover one or more (Raman) peaks at specific wavenumber positions. The specific wavenumber positions of peaks are a result of the molecular vibration and/or rotation within this specific sample. Thus, for the different samples that naturally have different molecular structures, the Raman peaks in the corresponding Raman spectra of these samples are located at the different wavenumber positions and have different magnitudes. Thereby, the Raman peaks at different wavenumber positions could be associated with the molecule structure of a specific sample as a 'fingerprint' to identify the different samples. The magnitude of Raman peaks can be related to the concentration of the chemical inducing the Raman effect, which is useful in sample quantification, such as measuring the concentrations of chemicals in mixture liquid, which is the subject of Chapter 7. Due to the characteristics of identification and quantification, the recorded Raman spectral dataset from a biological sample (cells and tissues) or body-fluid could be used to train a supervised or unsupervised statistical classification and/or regression model to realize applications in diagnostics. For example, by recording and analysing the multiple Raman spectra of diseased, normal and cancerous cells, these cells with different pathological status can be detected and classified from spectra for the aim of disease diagnosis, [160–162] which is the subject of Chapter 6. Additionally, in some cases, the concentrations of one or more specific chemicals related to disease occurrence from body-fluid can be measured by analysing the magnitudes of corresponding Raman peaks. For example, the concentration of glucose in blood, which is a standard to diagnose the pre-diabetes and diabetes, could be measured by Raman spectroscopy. [163]

2.4.2 The basic theory for Rotational/Vibrational Raman spectroscopy

As mentioned in the previous section, the Raman energy shift is generated from the molecular rotation and/or vibration. In this section, we provide a basic theory to explain how molecular rotation or vibration results in Raman scattering.

2.4.2.1 Rotational Raman spectroscopy

In terms of rotational Raman scattering, we first consider how the molecule is affected in a static electric field. In such a static electric field, within molecules, the positive nucleus will move toward the negative pole of the field, and the negative electrons will move toward the positive pole of the field. Thus, the charge separation generates an induced dipole moment within the molecule. As such, this molecule can be thought to be polarised. It is notable that not all molecules will undergo rotational Raman scattering, and only those molecules that do not have permanent diople moments, such as O_2 and N_2, will undergo the rotational Raman scattering. [164] In the following, an equation of the positively proportional relationship between the induced dipole moment and the amplitude of the electric field is given by:

$$\mu = \alpha E \tag{2.108}$$

where μ denotes the size of induced dipole moment, α denotes the polarizability of the molecule, and E denotes the amplitude of the electric field. The polarizability of the molecule α reveals to what extent the electrons in the molecule can be distorted in the static electric field.

Next, we consider the situation where the molecule is in an electromagnetic field from a monochromatic incident beam (laser beam). This means the electric field could be rewritten as a format of time dependent, $E(t)$:

$$E(t) = E_0 \sin(2\pi \upsilon t) \tag{2.109}$$

where E_0 is the amplitude of electric field from the monochromatic incident beam, and υ is the frequency of the monochromatic incident beam. In this case, the induced dipole moment, μ, that is mentioned in Equation 2.109, can be rewritten as below:

$$\mu = \alpha E(t) = \alpha E_0 \sin(2\pi \upsilon t) \tag{2.110}$$

The emitting scattered photons result from the dipole oscillation. Most of emitted photons have the same oscillation frequency υ as the monochromatic incident beam, which can be explained by Rayleigh scattering. However, another few emitted photons are also affected by molecular rotation. Molecular rotation can periodically change the polarizability of the molecule, and produce the extra rotational oscillation added on the dipole oscillation. Assuming that a rotational molecule is oscillated with a frequency, υ_R, the change in polarizability $\alpha(t)$ over time can be given by:

$$\alpha(t) = \alpha_0 + \Delta\alpha \sin(2\pi \upsilon_R t) \tag{2.111}$$

where a_0 is a constant to represent the average polarizability in one cycle of rotational oscillation, and $\Delta\alpha$ is the time-dependent polarizability variation along with the one cycle of molecular rotation. Therefore, substituting the time-dependent polarizability $\alpha(t)$ into the Equation 2.110, the induced dipole moment can be expressed:

$$\begin{aligned}\mu = \alpha E(t) &= [\alpha_0 + \Delta\alpha \sin(2\pi \upsilon_R t)]\, E_0 \sin(2\pi \upsilon t) \\ &= \alpha_0 E_0 \sin(2\pi \upsilon t) + E_0 \sin(2\pi \upsilon t)\Delta\alpha \sin(2\pi \upsilon_R t)\end{aligned} \tag{2.112}$$

Based on the trigonometric relation:

$$\sin(A)\sin(B) = \frac{1}{2}[\cos(A-B) - \cos(A+B)]$$

The Equation 2.112 is transformed as:

$$\mu = \alpha E(t) = \alpha_0 E_0 \sin(2\pi \upsilon t) + \frac{1}{2}\Delta\alpha E_0 [\cos 2\pi(\upsilon - \upsilon_R)t - \cos 2\pi(\upsilon + \upsilon_R)t] \tag{2.113}$$

It can be observed from Equation 2.113 that the dipole is not only oscillated at frequency υ to emit the Rayleigh scattered photons, but also at the frequency $\upsilon + \upsilon_R$ and $\upsilon - \upsilon_R$ relating to anti-Stokes Raman scattered photons and Stokes Raman scattered photons. Thereby, it can be concluded that the changed polarizability resulting from molecular rotation with a frequency $\pm\upsilon_R$ is a key to Raman scattering. In addition, the quantum effect on the molecule also should be considered as a model to explain Raman scattering. In the context of quantum effect, a molecule can be similar to a motor and an anharmonic oscillator with vibrational and rotational free of degrees. This results in lots of different energy levels existing at the ground state, even though the molecule is in a static electric field and is not illuminated by an electromagnetic radiation. Only two energy levels are shown on the ground state in Fig. 2.8 for simplicity, but, actually, there are many energy levels resulting from the molecular rotation and vibration at the ground state due to the quantum effect. We generally conclude the Raman energy shift from higher energy levels (E_1) to lower energy levels (E_0) as Raman anti-Stokes, while Raman energy shift from lower energy levels (E_1) to higher energy levels (E_0) as Raman Stokes. Based on the Boltzmann statistics, [165] in a context of setting a temperature T, the intensity ratio between the Raman anti-Stokes and Raman Stokes $\frac{\upsilon+\upsilon_R}{\upsilon-\upsilon_R}$ in the process of Raman excitation can be given by:

$$\frac{\upsilon + \upsilon_R}{\upsilon - \upsilon_R} = \exp\left(\frac{-h\upsilon_R}{k_B T}\right) \tag{2.114}$$

where υ_R is frequency of Raman shift, h is the Planck's constant, and k_B is the Boltzmann's constant. It can be deduced from Equation 2.114 that the occurrence of Stokes Raman scattering is dominant in comparison of the extremely weak anti-Stokes Raman scattering at room temperature. [166] This is the reason that (basic spontaneous) Raman spectroscopy typically collects the much stronger Stokes Raman signal rather than anti-Stokes Raman signal. A final point is that Boltzmann's statistics predicts that most molecules are on the ground state relative to the excited state before the electro-

magnetic radiation irradiates the molecules. This is why Raman scattering occurs and can be collected. [167–169]

2.4.2.2 vibrational Raman spectroscopy

Similar to the effect of molecular rotation, molecular vibration can also result in a change of polarizability and produce Raman scattering. At the outset, we point out that all diatomic molecules, within which the interaction between nucleus and electrons, can lead to the effect of Raman molecular vibration. [164] For polyatomic molecules, it is complex to directly judge whether the vibrations can produce Raman scattering active or not. Generally, two rules can be applied to polyatomic molecules for judging whether the Raman vibration occurs: (i) if the polyatomic molecule has asymmetry (such as HCN), usually all the resultant vibration modes can be used for producing Raman scattering, but such vibrations from asymmetric polyatomic molecules are very weak; (ii) if the polyatomic molecule is symmetric (such as H_2O), the corresponding vibrations could produce a strong Raman scattering. Excepting the above two general rules, group theory, which is a complex method for judging Raman active from the vibration modes, can be used to analyse specific polyatomic molecules. The details of group theory can be founded in [170] for the interested reader.

The expression of vibrational Raman scattering is similar to the rotational Raman scattering mentioned in the last section. The difference is that polarizability is changed resulting from the vibrations of molecular bonds. During the molecular vibration, the electron distribution is stretched and compressed periodically, and this results in the polarizability oscillating along the orientation of electric field. Assuming the frequency of the vibrational oscillation is υ_{vib}, the polarizability $\alpha(t)$ is given by:

$$\alpha(t) = \alpha_0 + \Delta\alpha \sin(2\pi \upsilon_{vib} t) \tag{2.115}$$

where α_0 is a constant to represent the average polarizability in one cycle of vibrational oscillation, and $\Delta\alpha$ is the time-dependent polarizability variation along with the one cycle of molecular vibration. Similar to the Equation 2.113, the induced dipole moment resulting from molecular vibration can be given by:

$$\mu = \alpha E(t) = \alpha_0 E_0 \sin(2\pi \upsilon t) + \frac{1}{2}\Delta\alpha E_0 [\cos 2\pi(\upsilon - \upsilon_{vib})t - \cos 2\pi(\upsilon + \upsilon_{vib})t] \tag{2.116}$$

where υ is the frequency of the monochromatic radiation, $\upsilon + \upsilon_{vib}$ is the frequency of emitted anti-Stokes Raman scattering, and $\upsilon - \upsilon_{vib}$ is frequency of emitted Stokes Raman scattering.

From the description above in the Section 2.4.2.1 and Section 2.4.2.2, the photons of Raman scattering could be generated by two different mechanisms: rotation and vibration. And these scattered photons generated from the molecular rotation and vibration can be collected and are expressed as the different Raman peaks at different wavenumber positions in a Raman spectrum. Note that the unit, wavenumber, used in a Raman spectrum can be transferred from the light wavelength used by Equation 2.107. We emphasise that in this thesis Raman spectroscopy is applied to com-

pare/identify samples based on the positions and amplitudes of the Raman peaks and also to quantify the relative concentrations of two or more samples. Thereby, which peaks resulting from the molecular rotation or molecular vibration in a single spectrum is not important in the context of this thesis. The topic about what are the exact frequencies (wavenumber) of Raman peaks produced from a particular molecular rotation or vibration relates to the field of physical chemistry and is not considered in any great detail in this thesis, save for some minor wavenumber assignments in Chapter 6 relating to the cell lines that are tested. Readers who are interested in such this topic can look into the Chapter-1 of the Raman spectroscopy review referred in Ref. 170.

2.4.3 The limitation of Raman spectroscopy

Raman spectroscopy is a non-invasive optical method that can be used to diagnose disease in real-time. Due to these features, Raman spectroscopy has an advantage over many other diagnostic techniques. However, Raman spectroscopy has limitations. During acquisition, the desired Raman signal is often recorded together with a strong unwanted background signal. The mix of the Raman signal and the background leads to a difficulty to differentiate the Raman signal of interest for subsequent numerical analysis. The background signal could come from the scattering, absorption and fluorescence from any substance (lenses, sample container, glass slide, immersion medium, and even the sample itself in the form of auto-fluorescence) in the optical path. Many methods have been proposed to reduce/remove the background signal. Firstly, the choice of sample substrate is significant; the sample substrate, which is used for holding the biological sample, is the substance nearest to the biological sample. For example, a strong unwanted background signal is generated from glass substrate under the illumination of near-infrared (NIR) laser, but if the substrate is quartz or calcium fluoride (CaF2) this background is weak. Although still present, the background for glass is much weaker when using blue of green excitation. Secondly, the background signal can be greatly reduced by using a confocal aperture, because the confocal aperture is able to spatially isolate the signal from a small 3D volume in/on the sample. The background signal can also be numerically removed via software after the Raman spectra recorded. A series of background signal removal algorithms, which are used for pre-processing the recorded Raman spectra in this thesis, will be demonstrated in Chapter 6.

2.4.4 The setup design of Raman spectroscopy

2.4.4.1 Fundamental Raman spectroscopy setup

In the experimental environment, a Raman spectroscopy setup must be designed to guide the light source onto the desired sample to generate Raman scattering, and the Raman scattered photons must be collected to produce the recorded Raman spectrum. An example of the fundamental Raman spectroscopy setup is shown in Fig. 2.9, which is made up of 4 parts: (1) a monochromatic radiation source or a light source with a very narrow wavelength band (i.e. laser); (2) an optical system to guide the light source

onto the sample; (3) a collection system to collect the Raman photons with high efficiency, and to remove the Rayleigh scattered photons, (4) a detection system to record the spectrum. An example of the fundamental Raman spectroscopy setup is shown in Fig. 2.9.

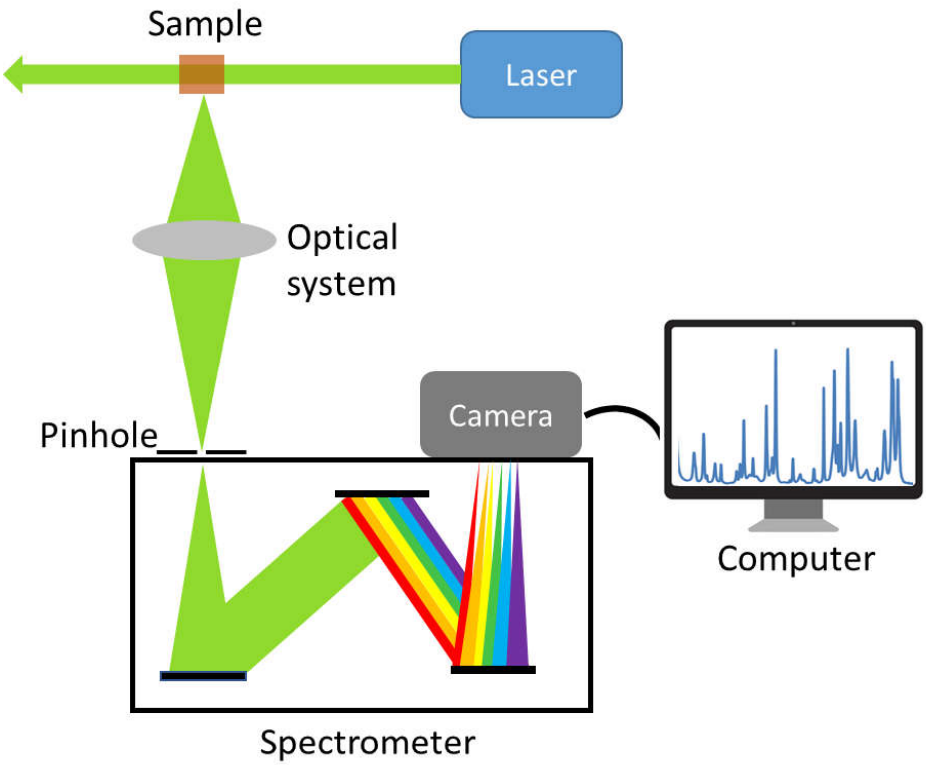

Figure 2.9: A fundamental setup for Raman spectroscopy

Not depicted in Fig. 2.9 are filters in the collection path to reduce the Rayleigh scattered signal and the other unwanted signals. A confocal pinhole can also be placed in an appropriate position in the collection path. Further details about the Raman spectroscopy setup will be demonstrated in Chapter 6 and 7. In the next few sections, we will highlight several important components used in the Raman spectroscopy setup, including the laser source, sample substrate, confocal aperture, spectrometer and camera; and explain how these components affect the performance of Raman spectroscopy.

2.4.4.2 Laser source

A laser source with the characteristic of high temporal coherence is essential for Raman spectroscopy. The choice of laser source requires several considerations: (i) choosing an appropriate laser power for not damaging biological samples, (ii) considering the laser penetration depth into sample (NIR wavelengths propagate deeper into tissue due to lower absorption), and (iii) reducing the unwanted background signal associated with the laser wavelength produced from the components in the optical path.

As mentioned in Section 2.4.3, during the Raman recording, a wavelength-dependent background signal can be generated, which pollutes the weak Raman spectrum. The

background signal includes the fluorescence signal resulting from the materials in the optical path. For example, glass, the material of most lenses, will provide a large background fluorescence signal if the incident laser wavelength is from the blue region up to the red/NIR region. Additionally, Mie scattering from biological samples can also generate an unwanted background baseline in recorded spectrum. [171] Mie scattering and auto-fluoresence can be reduced by using a laser in the NIR but the glass signal is strong for this laser. [172]

It is also important to note that the laser wavelength will determine the number of Raman scattered photons, even for the same power. Without considering the resonant condition, the intensity of the collected Raman photons I is positively proportional to the fourth power of the incident laser frequency υ which is shown below:

$$I \propto \upsilon^4 \tag{2.117}$$

It can be calculated from Equation 2.117 that the intensity ratio of the collected Raman photons generated by the 473 nm blue laser and 830 nm NIR laser can reach to 9.48.This proves that lower wavelength lasers can produce stronger Raman scattering than higher wavelength lasers, which implies that the shorter acquisition time is required in the Raman recording by using a shorter wavelength laser.

The light absorption is another significant element that needs to be considered. In terms of the biological samples, the laser wavelength range from 700 nm to 900 nm in the NIR region is proved to generate the minimal absorption. [173] This implies that the laser in NIR region wavelength (700 nm to 900 nm) can probe deeper into the sample and to cause less damage on biological samples, [172] when compared with visible wavelengths.

The heat generated by a laser in Raman spectroscopy can raise the temperature of the sample, potentially leading to heat-induced denaturation. This is particularly concerning for proteins, which can start losing their native structure at temperatures as low as 40-50°C. This process that is often irreversible and results in protein aggregation or coagulation. [174, 175] While higher laser power can enhance the throughput of a Raman system, it also increases the likelihood of such sample damage. Additionally, the system's throughput is influenced by exposure time; longer exposure improves the signal-to-noise ratio (SNR) by capturing more Raman signal, crucial for identifying minute details or components present in low concentrations. However, this extended exposure can harm sensitive biological materials due to thermal and photochemical effects. Therefore, it's vital to carefully control laser power and exposure time in Raman spectroscopy.

2.4.4.3 sample substrate

A good substrate should meet several requirements: (i) it should produce a low background signal; (ii) it should be transparent in the wavelength range of the laser, otherwise this substrate could be considered as a color filter; (iii) a good substrate should be bio-friendly without damaging the biological samples; (iv) the cost of the substrate should not be too expensive. Many substrates have been investigated including alu-

minium, [176–178] quartz, [179–181] glass [182, 183] calcium fluoride, [184–187] and 3D collagen gels [188] for Raman spectroscopy. However, the cost of substrates is often expensive, and different purities or thicknesses of the substrates can produce different background signals.

2.4.4.4 Spectrometer and CCD camera

In a Raman spectroscopy setup, a spectrometer and a CCD camera are combined as a module called a spectragh, which is used to disperse the collected Raman photons for recording. In our Raman experiments, a commercial spectrograph: Andor Shamrock 500 (Andor Technology Ltd., Belfast, UK) operating with an Andor iDus cooled CCD camera (DU420A-BR-DD, Andor Ltd., UK) is used. The design of this commercial spectrograph is based on the conventional Czerny-Turner structure, which is shown within the purple polygonal area in Fig. 2.10. Inside the spectragh, the Raman scattered light firstly is focused into the entrance slit by using a lens. The divergent light after the entrance slit is guided toward the diffraction grating via a collimated concave mirror. The collimated concave mirror has an effect to collimate the rays onto the diffraction grating surface with the same direction, which makes sure that the same wavelength rays have the same diffraction order positions. The diffraction grating is fabricated on a reflective material with a array of periodic grooves. A concave mirror is used to reflect the outgoing rays towards the different pixel positions on the CCD camera. Each pixel in the CCD camera is an individual photodiode, which can transfer the collected photons into electrons and export a digital signal to represent an collected intensity. Thermal energy in the pixels results in thermal noise, such as dark current. In order to repress such this noise, the CCD must be cooled.

The diffraction grating plays an important role in the spectrograph, to separate individual wavelength component and has several important characteristics. The spectral bandwidth represents how large the range of light wavelength (or wavenumber) can be recorded by a camera and the spectral resolution describes how fine the resolved spectral details can be recorded from Raman spectroscopy. The grating equation relates the period of the grooves on the grating to the angular dispersion, which in turn determines the bandwidth and resolution of the spectrometer. [189] The focal length of the spectrometer is also important in this context with a longer focal length producing lower bandwidth and higher resolution. The commercial spectrograph used by us has three rotated gratings with 300 grooves/mm (gr/mm), 600 gr/mm, and 900 gr/mm respectively. The sensitivity of the spectrograph will determine the acquisition time for spectral recording. The sensitivity depends on the diffraction efficiency of grating (which is in spectrometer) and the quantum efficiency of CCD camera, as well as the optical transmittance of optical elements, such as lenses, beamsplitter and filters, in Raman spectroscopy setup.

2.4.4.5 Confocal aperture

The utilization of Raman spectroscopy is usually combined with confocal microscopy by inserting a tiny confocal aperture after the MO. Confocal microscopy has the ability

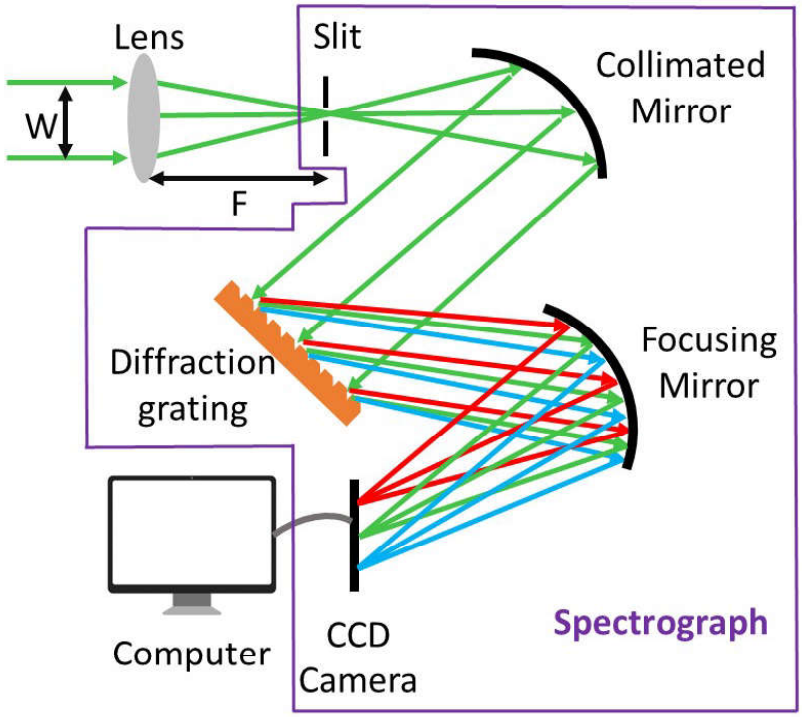

Figure 2.10: The spectrograph for the case of the conventional Czerny-Turner architecture.

of optical sectioning to isolate the sample signal from a small 3D volume. The principle of optical sectioning from confocal aperture is shown in Fig. 2.11. It can be seen that only the red signal from the sample of interest can pass the confocal aperture, while another purple lateral or orange axial signals are prevented by the confocal aperture. Thereby, the usage of confocal aperture in Raman spectroscopy has an excellent advantage to greatly reduce the unwanted background signals generated from optical elements at the defocused positions. The size of confocal aperture affects the spatial resolution and also affects the spectral resolution in the same way as the slit width.

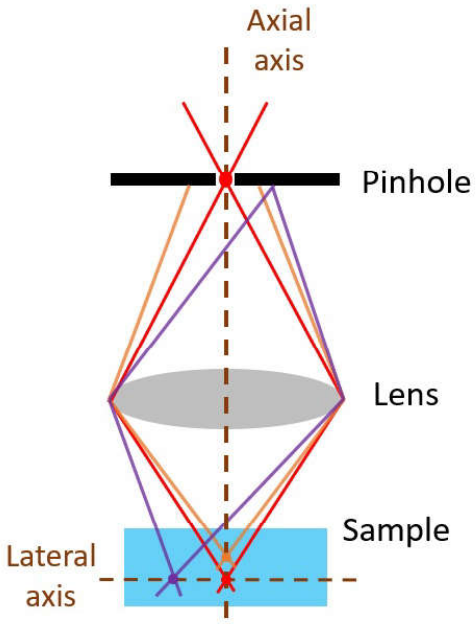

Figure 2.11: The effect of optical sectioning from confocal aperture

Chapter 3

Calibration for Spatial light interference microscopy

Part of the work in this chapter has been published in the following: Z. Tang, K. O'Dwyer, and B.M. Hennelly, "Calibration methods for Spatial Light Interference Microscopy", In Digital Holography and Three-Dimensional Imaging, pp. W1B-7. Optica Publishing Group, 2019. with the abstract reproduced below:

The Spatial Light Interference Microscopy technique uses four annular phase shifting patterns sequentially displayed on a spatial light modulator. The steps involved in accurately determining the optimal values of these four phase patterns are discussed.

3.1 Introduction

In Chapter 1 and Chapter 2, QPI has been mentioned as a set of methods that can quantify the spatial phase delay map imparted on the light that passes through a sample of interest. The accurate measurement of phase delay map provides information on the three-dimensional (3D) morphology of the sample, including information on the volume, dry mass, mean thickness, etc. [190–192] QPI methods have several advantages over the brightfield microscopy that use labels (chemical staining or fluorescence labeling) imaging methods, and other traditional label-free methods in the field of biological research such as Zernike's phase contrast method or Differential Interference Contrast. QPI provides improved imaging contrast for weakly scattering biological samples while avoiding the need for staining or fluorescent labeling, which can damage a living cell via photobleaching and/or toxicity. Importantly, QPI methods produce quantitative imaging that can be input to numerical analysis. The spatial light interference microscopy (SLIM) method, which is one such QPI method, has previously been proposed as an add-on module to a life science microscope. The SLIM method has the advantages of low speckle noise, and a relatively simple design when compared with interferometric methods like DHM. In This chapter, the fundamental

system design and numerical processing for SLIM are introduced and a method for optimising the system is proposed. In following, a diffraction grating calibration method is proposed for SLIM, and the factor of temporal coherence influencing on this calibration method is also emphasized to be investigated and discussed.

It is important to point out the contribution contained within this chapter at the outset. A key component in the SLIM technique is the use of Spatial Light Modulator (SLM), which displayed four phase only patterns in the generation of four intensity images to be used for phase retrieval. In the review of SLIM and SLM calibration described in the sections that follow we discovered a shortcoming in the traditional method of calibrating the SLM to determine the optimal phase values to be used on this SLM. This shortcoming relates to the effect of temporal coherence of the light source on the calibration protocol and the resultant phase values that are determined to be 'optimal' for SLIM. Using three light sources with varying degrees of temporal coherence, we develop an adaptation of the traditional calibration protocol for enhanced phase image retrieval using SLIM. Although SLIM imaging provides high quality phase images as demonstrated in this chapter, we discover that the issue of halo removal, inherent to the SLIM technique, presents an insurmountable problem for cell characterisation and for this reason this is the only chapter that uses the SLIM technique. The chapters that follow employ digital holographic microscopy.

3.2 Introduction to spatial light interference microscopy

3.2.1 Recording system

In 2011, Wang *et al.* [21] initially proposed the SLIM technique, which combines the concepts of inline holography and phase contrast microscopy. In Fig. 3.1(a), the structure of the basic SLIM setup is provided. The SLIM setup consists of a phase contrast microscope and an add-on module positioned at the output port of microscope. An image of the add-on module used in our own implementation of the SLIM experiment is displayed in Fig. 3.1(b).

A multi-functional commercial Olympus IX81 microscope is used for imaging. The phase contrast annular 'IX-PH2' filter is used in the filter plane of the condenser. This microscope uses a white light halogen-tungsten for illumination which is described as both temporally and spatially incoherent. Such illumination source provides images with no speckle noise. The white light is guided via the condenser lens to irradiate onto the sample. The light after the sample can be described as being made up of two components: a reference (unscattered) beam and an object (scattered) beam. In terms of Zernike phase contrast approach, an annular filter within the microscope objective (at the Fourier plane of the sample plane) will delay the unscattered light by $\pm\frac{\pi}{2}$. Thus, image formation will include interference between the object beam and the reference beam after phase modulation, enabling high image contrast for cellular features which are otherwise invisible using brightfield microscopy. In our experiments the IX-PH2 filter is inserted into the filter plane of the condenser lens and a matching phase contrast microscope objective (40x Mag/ 0.55NA; Olympus UPlanFlan40X Ph) is used. The

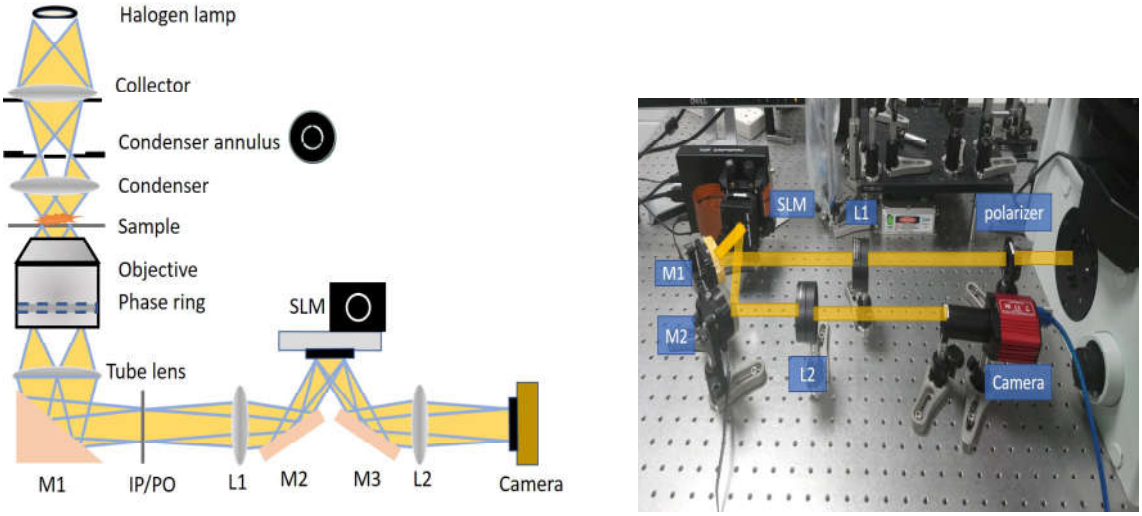

(a) (b)

Figure 3.1: Experimental setup for spatial light interference microscopy: (a). A schematic of the basic structure of the Spatial light interference microscopy; (b). The add-on module that was built in our lab to implement SLIM. (M, mirror; IP, Image plane; PO, polarizer; L1, Lens; SLM, Spatial light modulator)

position of the annular filter is adjusted to match the position of the phase ring within the MO.

However, for phase contrast microscopy only one fixed phase shift modulation of the unscattered light is applied. This is not sufficient for quantitatively recovering the complex phase field of the sample. The SLIM technique overcomes this problem by introducing four different phase shifts. An add-on module with a $4f$-design is positioned at the image plane of the microscope. As shown in Fig. 3.1(b), this module utilizes a lens (250mm focal length; Thorlab) that projects the Fourier transform of the image onto the SLM, on which the annular light is focused, so that the SLM can modulate the phase of unscattered light by displaying a ring pattern aligned with the focused light annulus. The SLM is a reflective liquid crystal spatial light modulator (SLM) purchased from Meadowlark optics, Inc, and has specifications of 1920 × 1152 pixels, 9.2 μm pixel size, >4π phase shifting at 714 Hz. The light annulus that is projected onto the SLM has been modulated by the MO, so the phase of unscattrered light has been shifted by $\pi/2$ of a wavelength. Furthermore, it has been scaled by the MO by approximately 0.25 in amplitude relative to the unscattered field. The advancement of using the SLM is that arbitrary phase shift can be applied to the unscattered reference field while leaving the object beam unmodulated.

The light reflected from the SLM then passes another lens to generate the final image, which is captured by a monochromatic CMOS camera (CS895MU; Thorlab). The SLIM technique requires to capture four intensity images, which are formed by using the SLM to introduce four effective phase differences: 0, $\frac{\pi}{2}$, π, $\frac{3\pi}{2}$ between the reference beam and the object beam. Based on these four intensity images, it is possible to estimate the quantitative phase image of the sample as demonstrated in next section.

3.2.2 Numerical processing

3.2.2.1 4-step phase shift formula

As mentioned in the previous section, SLIM requires to record four intensity images. Each intensity image can be considered to be an interferogram or a digital hologram resulting from the interference between the reference beam and the object beam. As discussed in Chapter 2, a hologram consists of four super-positioned images: the two DC terms and the two twin images. It is precisely because there are four unknown terms in the sum that we require four SLIM intensity patterns; this is equivalent to the problem of solving four simultaneous equations with four unknowns. Here, the SLM enables the coefficients of these four variables to be varied over the four recorded 'holograms'. Assume that the reference beam is a spatially uniform wavefield denoted as $U_0(x,y)$, and the object beam is a spatially varying wavefield denoted as $U_1(x,y) = |U_1(x,y)|e^{j\Delta\phi(x,y)}$, the formation of a single hologram is described by the well-known holography formula:

$$I(x,y,\phi_m) = |U_0(x,y)|^2 + |U_1(x,y)|^2 + 2|U_0(x,y)||U_1(x,y)|\cos(\phi_m + \Delta\phi(x,y)) \tag{3.1}$$

where x,y denote the 2d coordinates in the spatial domain, $I(x,y,\phi_m)$ denotes the recorded hologram after using the SLM to modulate the phase difference between the reference beam and the object beam, ϕ_m denotes the known phase modulated by the SLM to be introduced between the reference beam and the object beam. $\Delta\phi(x,y)$ denotes the phase delay map.

In order to calculate the unknown phase delay map $\Delta\phi(x,y)$, the four phase differences from 0 to $\frac{3\pi}{2}$ at an increment of $\frac{\pi}{2}$ are respectively introduced between the object beam and the reference beam to construct the four intensity images (holograms). Based on Equation 3.1, these four holograms can be expressed as follows:

$$I(x,y,0) = |U_0|^2 + |U_1|^2 + 2|U_0||U_1|cos(\Delta\phi(x,y)) \tag{3.2}$$

$$I\left(x,y,\frac{\pi}{2}\right) = |U_0|^2 + |U_1|^2 - 2|U_0||U_1|\sin(\Delta\phi(x,y)) \tag{3.3}$$

$$I(x,y,\pi) = |U_0|^2 + |U_1|^2 - 2|U_0||U_1|\cos(\Delta\phi(x,y)) \tag{3.4}$$

$$I\left(x,y,\frac{3\pi}{2}\right) = |U_0|^2 + |U_1|^2 + 2|U_0||U_1|\sin(\Delta\phi(x,y)) \tag{3.5}$$

The phase delay map $\Delta\phi(x,y)$ can be calculated by a classical 4-step shift retrieval equation below, [89]

$$\Delta\phi(x,y) = \tan^{-1}\left[\frac{I\left(x,y,\frac{3\pi}{2}\right) - I\left(x,y,\frac{\pi}{2}\right)}{I(x,y,0) - I(x,y,\pi)}\right] \tag{3.6}$$

SLIM images of a diatom cell and a cheek cell were recorded using our setup and are the basis of the investigation that follows. The four diatom cell holograms and the

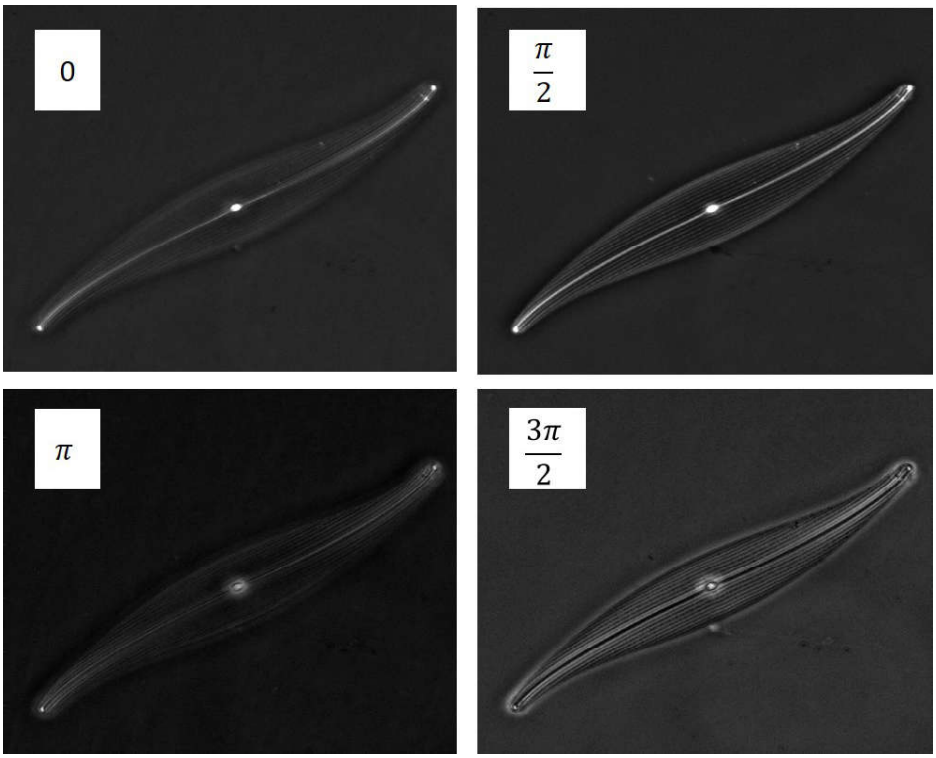

Figure 3.2: Four diatom cell holograms recorded using the SLIM setup: the phase differences ϕ_m with 0, $\frac{\pi}{2}$, π, $\frac{3\pi}{2}$ are introduced between the reference beam and the object beam using the SLM.

four cheek cell holograms are recorded via the SLIM setup and displayed in Fig. 3.2 and Fig. 3.3 respectively. Note that the $\pi/2$ and $3\pi/2$ are equivalent to the phase contrast images that would be recorded by a MO with a phase ring of $\pi/2$ or $-\pi/2$ phase shift; both types of MO have been produced by microscope companies. The phase delay map, $\Delta\phi(x,y)$, of the diatom cell and the cheek cell can be calculated by Equation 3.6, which are shown in Fig. 3.4(b) and (d), respectively.

3.2.2.2 The β formula for calculating the quantitative phase image

The calculation for the phase delay map $\Delta\phi(x,y)$ from Equation 3.6 has the advantage of simple calculation. However, the usage of the 4-step phase shift formula also has disadvantages. On one hand, as shown in Fig. 3.4(b) and (d), the phase delay map $\Delta\phi(x,y)$ is contaminated by unwanted noise; secondly, the phase delay map $\Delta\phi(x,y)$ only represents the phase field of the object beam $U_1(x,y)$, and omits the reference beam U_0 which also has an affect on the formation of the quantitative phase image. The desired phase field should be the phase of complex sum of the reference beam and the object beam: $U_0 + U_1(x,y)$. The desired phase field is denoted as $\phi(x,y)$ and can be calculated from $\Delta\phi(x,y)$ as follows [193]:

$$\phi(x,y) = \tan^{-1}\left\{\frac{\beta(x,y)\sin[\Delta\phi(x,y)]}{1+\beta(x,y)\cos[\Delta\phi(x,y)]}\right\}, \tag{3.7}$$

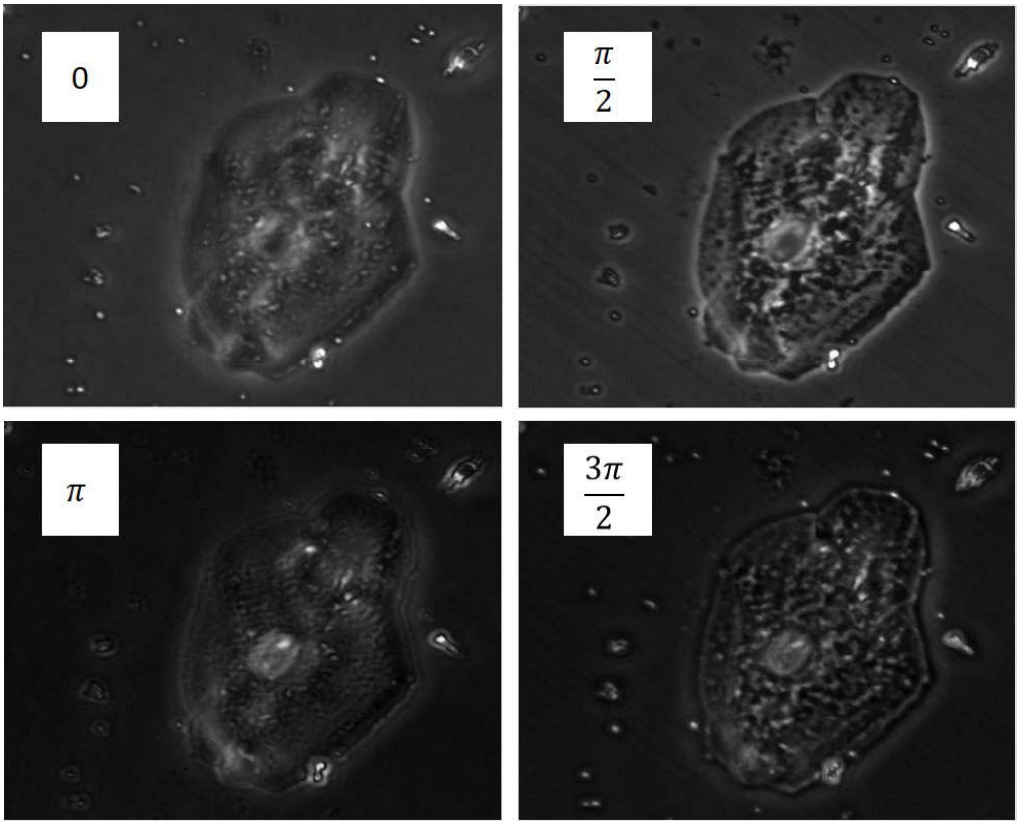

Figure 3.3: Four cheek cell holograms recorded using the SLIM setup: the phase differences ϕ_m with 0, $\frac{\pi}{2}$, π, $\frac{3\pi}{2}$ are introduced between the reference beam and the object beam using the SLM.

where $\beta(x,y)$ is equal to $|U_1(x,y)|/|U_0|$, which is the result of dividing the amplitude field of the spatially varying scattered wavefield $|U_1(x,y)|$ by the amplitude field of the spatially uniform unscattered wavefield $|U_0|$. The factor $\beta(x,y)$ can be obtained as follows:

$$\beta(x,y) = \frac{[I(x,y,0) - I(x,y,\pi) + I(x,y,\frac{3\pi}{2}) - I(x,y,\frac{\pi}{2})]}{4|U_0|^2[\sin(\Delta\phi(x,y)) + \cos(\Delta\phi(x,y))]} \tag{3.8}$$

where $|U_0|^2$ can be estimated by recording a background image resulting from the no sample image. Similarly, we can also deduce the amplitude field, $A(x,y)$, on the image plane:

$$A(x,y) = |1 + \beta(x,y)\cos[\Delta\phi(x,y)] + j\beta(x,y)\sin[\Delta\phi(x,y)]| \tag{3.9}$$

The amplitude fields of the diatom cell and the cheek cell are shown in Fig. 3.4(a) and (c), respectively. And quantitative phase images are shown in Fig. 3.5(a) and (b). Focusing on the phase image of diatom cell in Fig. 3.5(a), the cellular micro-structures, such as central nodule, polar nodule, raphe, cell wall, and especially the lines of small pores are observed clearly. However, these structures are hard to observe in the amplitude field in Fig. 3.4(a). The inset of Fig. 3.5(a) provides a phase profile of the diatom along the red dotted line, from which the different micro-structures can be seen, appearing almost like a ruled diffraction grating. However, the phase image obtained from the SLIM technique contains an unwanted distortion of the phase image called

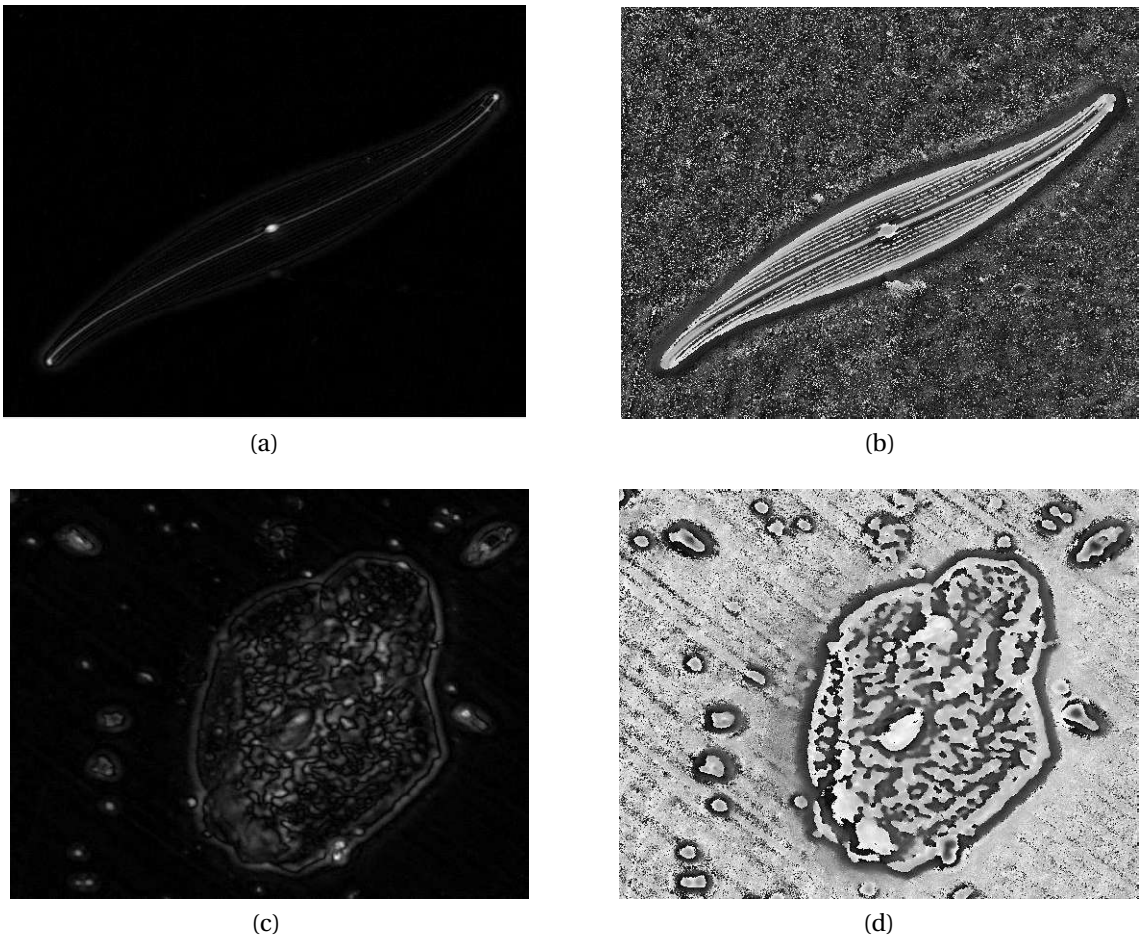

(a) (b)

(c) (d)

Figure 3.4: (a) The amplitude field of the diatom cell; (b) The phase delay map $\Delta\phi(x, y)$ from the diatom cell; (c) The amplitude field of the cheek cell; (d) The phase delay map $\Delta\phi(x, y)$ from the cheek cell.

halo artifacts, which distort the true phase value. The halo effect is clearly visible in the negative phase values surrounding the cell wall, and also results in a drop in the phase values within the cell region. This problem of halo artifact is explained more in Section 3.2.2.3. The texture of the cheek cell in Fig. 3.5(b) is more complicated than that of diatom cell. Similarly, the phase image of the cheek cell in Fig. 3.5(b) shows significantly better image contrast and cellular detail compared with its corresponding amplitude image in Fig. 3.4(c). In particular, the nucleus in the cheek cell can be clearly distinguished in the phase image. Once again, however, the halo problem still exists in the cheek cell phase image.

3.2.2.3 Halo removal

The halo artifact problem is a well-known drawback in phase contrast microscopy, and mainly reflects on the contrast reversal error surrounding the cell. The halo artifact results from the thickness of the phase ring, which obviously modulates more than only the zero DC frequency. Halo removal methods can be divided into two kinds. One kind is based on modifying the optical instrument. [25, 194–200] This kind of halo removal

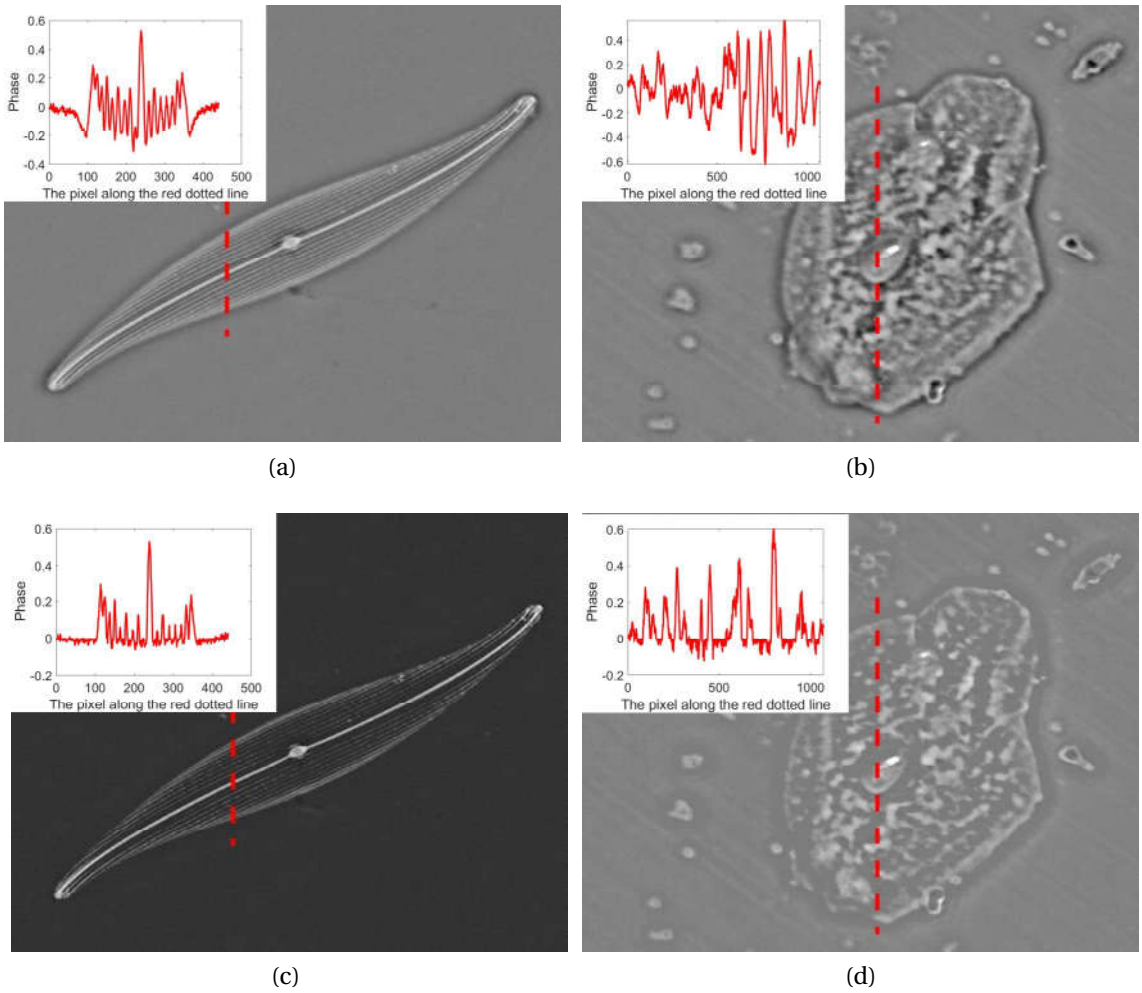

Figure 3.5: (a) The phase image of the diatom cell; (b) The phase image of the cheek cell; (c) The phase image of the diatom cell after halo removal; (d) The phase image of the cheek cell after halo removal. (The inset images represent the phase profile along the red dotted line)

methods requires additional modification of the hardware. The second kind is numerical processing. [201–205]. These numerical halo-removal methods don't need to modify the hardware, but they always suffer from numerical convergence delay that results in lengthy computation time, preventing real-time application of SLIM imaging.

In this project, a numerical halo removal method proposed by Mikhail *et al.* [206] is used. This numerical halo removal method has the advantages of not requiring additional hardware and relatively short computation time when compared with other halo-removal methods. This method performs the Hilbert transform along the different directional phase derivatives in order to correct the distorted low spatial frequency details associated with the halo artifact while leaving the high spatial frequency details unchanged for the phase images. The steps of this method are listed as below:

- The phase field image $\phi(x, y)$ is transformed into $\Phi(u_x, u_y)$ in the frequency domain by using the Fourier transform.
- The three directional stripe-shape filters along 0°, 45°, and 90°, respectively, are

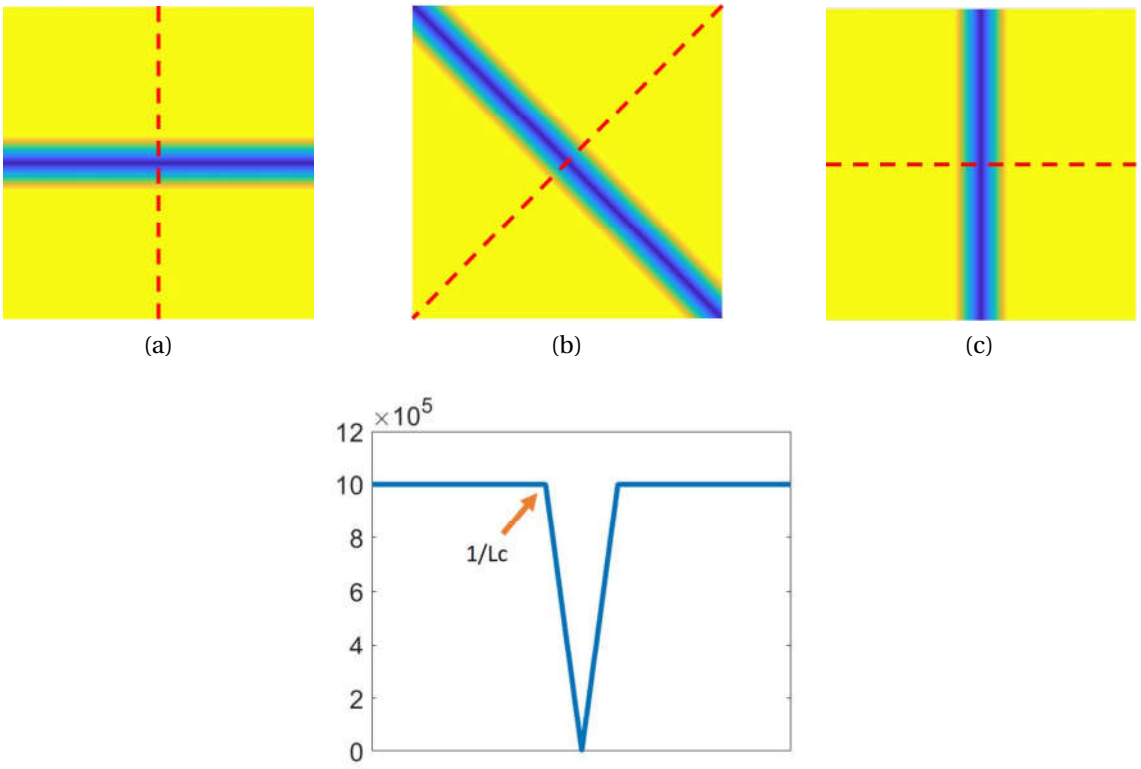

Figure 3.6: (a) The 0° filter; (b) The 45° filter; (c) The 90° filter; (d) The profile along the red dotted lines that perpendicularly transverse the stripes in three filters, where the value set in each one of three filters are the perpendicular distance from each pixel's frequency coordinate to the frequency coordinates on the middle line of the stripe, and the distance threshold ($\frac{1}{Lc}$) is set to limit the range of stripe.

designed (see Fig. 3.6(a), Fig. 3.6(b), Fig. 3.6(c)). A profile along the red dotted lines perpendicularly transverse to the stripes in the three filters is shown in Fig. 3.6(d), which reveals how these stripe filters are designed. From the very middle line of the stripe outwards, the amplitude of the filter increases and is equal to the perpendicular distance from that line. The amplitude increase is limited by a threshold $\frac{1}{L_c}$. Depending on the image size, the value of L_c is set as 0.6 μm. This value has been demonstrated to be optimal in Ref. 206.

- The Fourier transform $\Phi(u_x, u_y)$ is multiplied by the three directional filters to produce three functions in the frequency domain.
- An inverse Fourier transform is applied to each of these three functions to produce three phase images: $\phi'_0(x,y)$, $\phi'_{45}(x,y)$, and $\phi'_{90}(x,y)$.
- The maximum value is selected from these three images as well as the original image in a pixel-wise; the result is a halo-free image.

The phase fields of diatom cell and cheek cell after halo removal are shown in Fig. 3.5(c) and Fig. 3.5(d). Comparing phase images of the diatom cell before (Fig. 3.5(a))

and after (Fig. 3.5(c)) halo removal, it can be discovered that the problem of the negative phase error surrounding the edge of the cell has been solved. This improvement is further emphasized by the two phase profiles in the insets. Furthermore, the drop in phase values within the cell region has also been improved and it can expected that the phase image after halo-removal is a truer representation of the diatom cell. Solving the halo problem for the cheek cell phase image is more challenging. In Ref. 206, the halo artifacts are successfully removed for morphologically simpler cases such as microbeads, sperm, red blood cells and neurities; however, this halo-removal method is less accurate when applied to thicker or more complicated structures containing both low and high frequency content and the cheek cell is one such example. The comparison of phase images of cheek cell before and after halo removal in Fig. 3.5(b) and (d) shows that many features in the cheek cell are washed out after halo-removal processing. A considerable part of cell region contains low frequency information that is similar to the halo artifact surrounding the cell; therefore, halo removal filter is essentially a form of high-pass filter (see filter profile in Fig. 3.6(d)). Despite this shortcoming, halo-removal improves the accuracy of the overall phase image and can be achieved in efficient computational time without any requirement to modify the optical setup.

3.3 Calibration of the spatial light interference microscopy

As outlined in Section 3.2.2.1, four intensity images corresponding to four specific phase delays of the unscattered field, must be recorded to generate the SLIM image. It is essential that the 'correct' phase delays are applied to the SLM pixels. However, it is not able to directly know what these phase delays should be. The difficulty is twofold: firstly, the effective wavelength of the white-light illumination is not known and so the absolute delays of $\lambda/4$, $\lambda/2$, $3\lambda/4$, which correspond to the desired phase shifts cannot be known without some form of measurement. Secondly, the voltage-phase delay characteristic of the SLM is not known, and so we cannot immediately determine what gray levels to apply to the pixels to impart a desired phase delay.

The key component integrated inside the SLM to modulate phase is a liquid crystal layer. Liquid crystal has a property of birefringence, which means the refractive index of the liquid crystal can be varied depending on the polarization of incident light and the orientation of liquid crystal itself. A controllable electrical voltage is input into the SLM to change the orientation of the liquid crystal, thereby changing the refractive index of liquid crystal and producing a specific phase delay for light that is appropriately polarised. In practical terms, the liquid crystal layer in SLM is controlled by an input image with the size of 1920 × 1152 pixels, where the gray level value of each pixel controls the voltage that will be applied to the liquid crystal in that pixel. A gray value between 0 and 255 can be written for each pixel to determine the controllable voltage applied to all of the liquid crystal pixels. These gray values, therefore, effectively result in controllable orientations of the liquid crystals within each pixel, which translates to a spatially varying phase delay across the surface of the SLM.

The problem for SLM calibration relates to characterise the relationship between

the gray level value and the resultant phase delay. The general calibration methods for SLM include interferometry method, [207–209] polarization method, [210,211] and binary diffraction grating method. [212–214] Considering the simple setup design and operation simplicity, we select the binary diffraction grating method for further analysis. The calibration module utilizing the binary diffraction grating method is displayed in Fig. 3.7(a). This calibration module only requires a removal of the first lens in the SLIM module, and the phase contrast annulus is removed from the condenser to implement brightfield illumination; the condenser iris is closed to increase the spatial coherence of the illumination. Therefore, the calibration module is not required to be constructed separately, and can be implemented with only a small modification of the SLIM module.

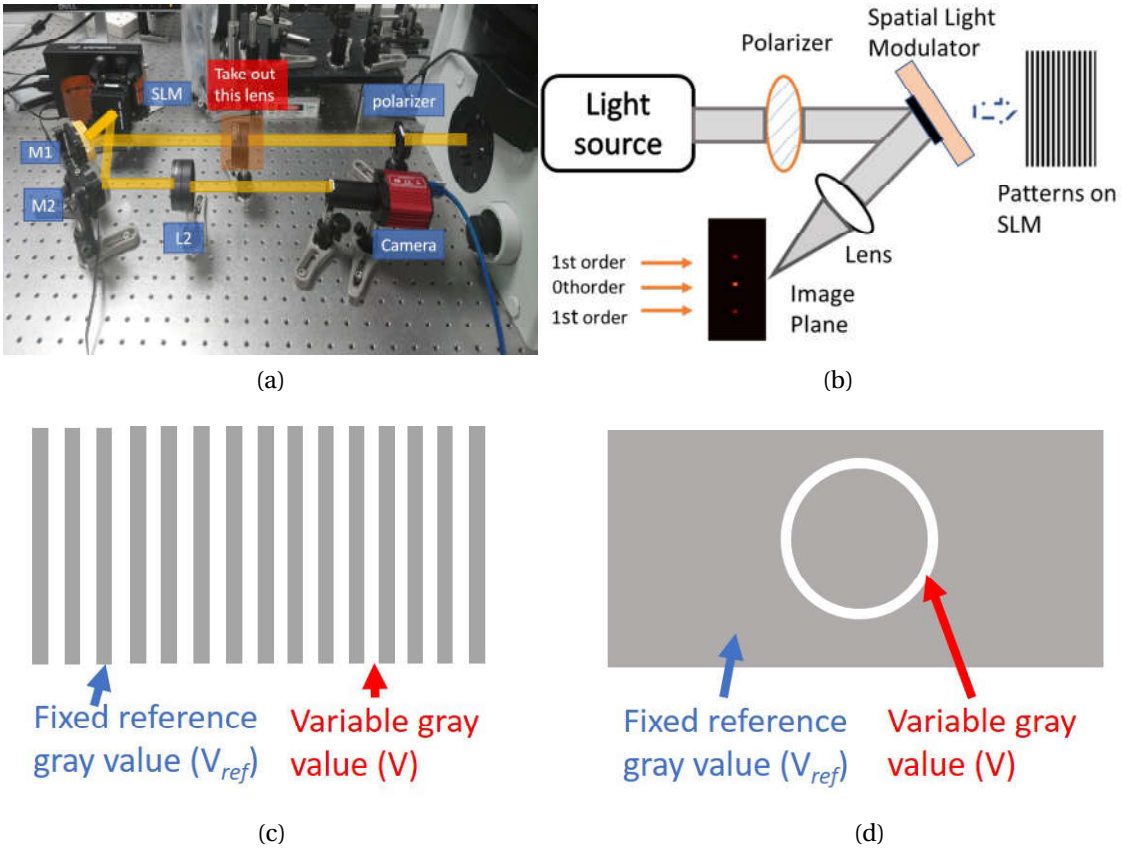

(a) (b)

(c) (d)

Figure 3.7: (a) Image of the SLM calibration module used in our lab; (b) The schematic diagram of the calibration set-up; (c) An illustration of the periodic stripes representing a diffraction grating that are displayed on the SLM for calibration: In total, 256 images comprising alternated stripes are written into the SLM sequentially. The blue arrow points to the stripes that contain a fixed reference gray value (V_{ref}) that remains constant in all 256 images, the red arrow points to the stripes that have a variable gray value (V) which increases from 0 to 255 over the sequence of images. Note that, for ease of display, the image shown here is only a cropped region of the actual image displayed on the SLM. In the experiment, the width of each stripe is 8 pixels; (d) The annular pattern image written into the SLM, where the annular area is set by four specific gray values (V) and background area is given by a fixed reference gray value (V_{ref}).

The schematic diagram of diffraction grating method for calibration is shown in Fig. 3.7(b). Firstly, the beam output from the microscope passes a polarizer to generate a linearly polarized light. This polarized orientation of the light is set to align with the extraordinary (long) axis of the liquid crystals. Now the SLM is in the phase modulation mode and this phase modulation can be realized by changing the orientation of the liquid crystal via externally inputting voltage associated with the writable gray value. A total of 256 periodic stripe images are written into the SLM. These periodic stripes could be thought as a binary diffraction grating that is illustrated in Fig. 3.7(c). Each stripe image among the 256 images contains alternating stripes of a fixed reference gray value (V_{ref}) and a variable gray value (V) that increases sequentially from 0 to 255. The light reflected from the SLM generates different diffraction orders. By using a lens, these diffraction orders can be focused into spots on the camera plane. As the binary pattern changes sequentially on the SLM, by tracking and recording the variation of the normalized intensity from 0th and/or 1st diffraction orders, the phase difference produced from the gray value difference between V_{ref} and 256 possible V can be deduced by simple formulas as follows: [215, 216]

$$\phi_m = \cos^{-1}(2I_{n_0} - 1) \tag{3.10}$$

$$\phi_m = \cos^{-1}(1 - 2I_{n_1}) \tag{3.11}$$

where ϕ_m denotes the phase difference produced from the gray value difference between V_{ref} and V. I_{n_0} and I_{n_1} are the normalized intensity from the 0th diffraction order and the 1st diffraction order respectively. The calibration process for SLIM can be described as finding one V_{ref} and four V values denoted as V_0, $V_{\frac{\pi}{2}}$, V_π, $V_{\frac{3\pi}{2}}$ to produce the 0, $\frac{\pi}{2}$, π, $\frac{3\pi}{2}$ phase delays of the unscattered light relative to the scattered light. Here, an example is provided for finding this set of V values. Assuming that V_{ref} is set as 140, the distribution of normalized intensity from 0th diffraction order along with the increment of V from 0 to 255 is shown in Fig. 3.8(a). Based on Equation 3.10, the resultant phase difference produced from the gray value difference between V_{ref} and V is calculated and shown in Fig. 3.8(b), where an available set of V_0, $V_{\frac{\pi}{2}}$, V_π, $V_{\frac{3\pi}{2}}$ is labelled by four red dots.

In following, the SLIM module is reassembled and the phase contrast annulus is inserted into the condenser again. An annular pattern shown in Fig. 3.7(d) is written into the SLM. This annular pattern matches the light annulus on the SLM plane. By inputting four annular pattern images into the SLM, four intensity images $I(x,y,0)$, $I(x,y,\frac{\pi}{2})$, $I(x,y,\pi)$, $I(x,y,\frac{3\pi}{2})$ are recorded. For each annular pattern image, the region of annular pattern sequentially takes four predetermined values V_0, $V_{\frac{\pi}{2}}$, V_π, $V_{\frac{3\pi}{2}}$ while the background remains fixed at V_{ref}.

3.4 The effect of temporal coherence on SLIM

Previous literature on SLM calibration has primarily used temporally coherent light (e.g., light from a laser diode) to perform phase delay. [207–215, 217] However, white

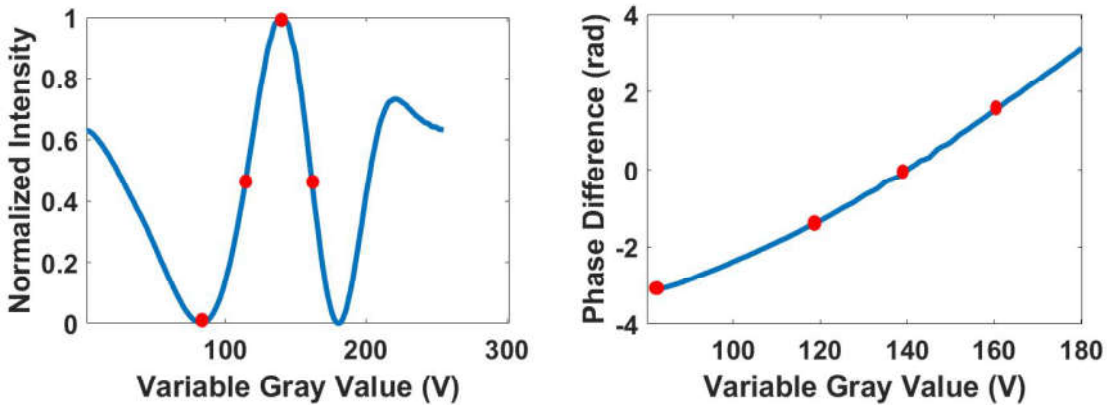

(a) (b)

Figure 3.8: (a) The normalized intensity distribution from 0th diffraction order versus V from 0 to 255, when V_{ref} is 140;(b) Phase difference calculated from the gray value difference between V_{ref}=140 and V ranging from 0 to 255. The red dots in both subfigures represent one set of four variable gray values that will produce the desired phase difference of 0, $\frac{\pi}{2}$, π, $\frac{3\pi}{2}$ used in the SLIM technique.

light suitable for SLIM has relatively low temporal coherence. Therefore, it is interesting to evaluate the effect of temporal coherence of the light source on the SLIM technique; in particular the effect using white light for SLM calibration has not been reported in the literature. Here, we investigate this effect in some detail.

The same diffraction grating calibration experiment described earlier in Fig. 3.7(a) and (b) is applied. In this case, however, three different light sources with different temporal coherence properties are considered: (i) a white light source from a halogen lamp within the Olympus inverted microscope (Ix81); (ii) the same white light source but filtered by a bandpass filter at 532 nm with a passband of 10 nm (Thorlabs; FL532-10); (iii) a collimated and spatially filtered red laser diode (thorlab; HLS635) with 1.5 mW power, 635 nm wavelength and linewidth of <1 nm. The temporal coherence for these three light sources varies from low to high: (i)<(ii)<(iii). In this experiment, the values of V_{ref} is respectively set as 0 and 210 to generate two sets of 256 periodic stripes (diffraction grating) images. For each light source, these two sets of images are sequentially imported to the SLM to yield the intensity-varying diffraction orders that are required for calibration. In Fig. 3.9 we show the normalized intensity distribution from the 0th and 1st diffraction orders varying for the 3 light sources; the phase difference associated with the gray value difference between V_{ref} and V can be calculated using Equation 3.10 and Equation 3.11. The local maxima and minima indicate the points of $\pm n\pi/2$ where n is an integer.

In Fig. 3.9(i) and (ii), the normalized intensity distribution from the 0th and 1st diffraction orders for the three light sources are obtained, when the V_{ref} is set as 0. Typically, V_{ref} is set as 0 for the various calibration methods that have been reported in the literature. [218, 219] It can be observed in Fig. 3.9(i) and (ii) respectively that the normalized intensity distributions from the filtered green light source and the red laser source have the similar shape, and the maxima and the minima in intensity dis-

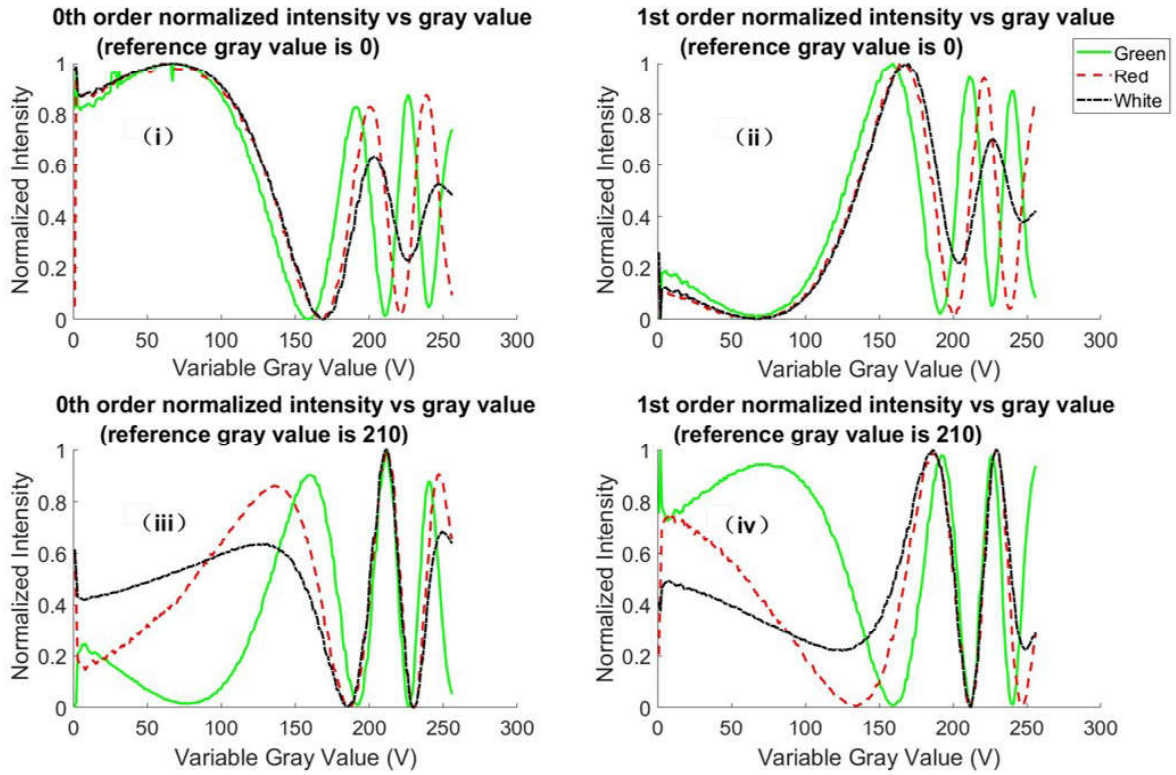

Figure 3.9: The normalized intensity from 0th and 1st diffraction orders from the three light sources versus the variable gray value (V); (i) and (ii) show the normalized intensity distributions from 0th and 1st diffraction orders for V_{ref}=0; (iii) and (iv) show the 0th and 1st diffraction orders for V_{ref}=210.

tributions from two light sources have the similar amplitude. Simultaneously, because two light sources have different wavelengths, these maxima and minima occur at different gray values as expected. The normalized intensity distribution from the white light source is quite different to that from the red laser source and the filter green light source. This difference reflects on the amplitude reduction of the maxima and minima as V increases. This problem results from the low temporal coherence of the light source. The greater the difference between $V_{ref} = 0$ and V, the more pronounced this reduction in amplitude. This presents a clear problem for the SLIM technique since now we can expect not only a phase delay as V increases (for the annulus) but also an undesired amplitude reduction in the interference pattern. We have discovered that it is possible to mitigate this problem by setting the background V_{ref} value to be large; here we set $V_{ref} = 210$. For this case, the normalized intensity distribution from the 0th and 1st diffraction orders from three light sources are shown in Fig. 3.9(iii) and (iv). In this case, choosing the maxima and minina at and near the gray value 210 in the normalized intensity distributions could effectively avoid the problem of amplitude reduction and produce the phase difference of 0, $\frac{\pi}{2}$, π, $\frac{3\pi}{2}$ required by SLIM technique.

3.5 Conclusion

This chapter describes the SLIM phase imaging technique from construction of the set-up to the numerical processing steps, which include the phase-retrieval and halo removal algorithms. We also review the traditional methods used for calibrating the phase values on the SLM, which is the key component in SLIM; calibration involves the display of a diffraction grating like pattern on SLM and sequential variation of the phase values used in this pattern with synchronised measurement of the zero and first diffraction order power ratio. This calibration method has the advantage of minimal modification on the SLIM module and following application of the calibration routine, four sets of binary phase values are determined for use in the annular patterns to be displayed as part of SLIM imaging.

In our review of SLIM and SLM calibration we discovered that there was no attention in the literature given to effect of temporal coherence on the calibration protocol. In this chapter, we emphasize the effect of temporal coherence of the light source on the calibration protocol for the case of using the diffraction grating method. We discover that temporal incoherence can have a significant effect on image formation in SLIM and that care must be taken when selecting the four optimal phase values to be used for SLIM. This discovery results from applying the traditional calibration protocol for three different light sources with varying degrees of temporal coherence. We show that the calibration protocol must be adapted when using temporally incoherent light in order to obtain the optimal set of phase values to be used for the annular patterns in SLIM. This is the key contribution in this chapter.

As part of this chapter's work, the phase fields of a diatom cell and a cheek cell are imaged using SLIM technique. The reconstructed phase image of the diatom cell is clearly improved following application of the halo removal algorithm; however, the cheek cell cannot be improved as easily using the halo removal algorithm. One cannot deny that the SLIM technique has the advantages of a simple setup construction, good setup stability, and the fast phase retrieving speed. Despite these advantages, halo removal remains an unsolved problem in SLIM research and the presence of the halo presented a difficulty that could not be tolerated for our research - the goal of which is ultimately to be able to characterise cells in a label free manner. For this reason, we turned our attention to digital holographic microscopy. The traditional DHM technique is more challenging experimentally, but it provides an accurate estimate of the phase image that contains no halo artifact. Two significant limitations of traditional DHM when compared with SLIM are (i) high levels of coherent noise that corrupt the phase image and (ii) a lower resolution. In next chapter, we propose an advanced synthetic aperture approach for DHM to address these two limitations associated with traditional DHM. This advanced method employs an annular illumination with partial coherence to expand the transfer function aperture of optical system, thereby increasing imaging resolution and reducing coherent noise.

Chapter 4

A single capture self-reference Digital holography microscopy using synthetic aperture

The work in this chapter has been prepared for submission to a journal: Z. Tang, and B.M. Hennelly, "Real-Time Synthetic-Aperture Digital Holographic Microscopy", To be submitted to Optica with the abstract reproduced below:

Synthetic aperture digital holographic microscopy extends the resolution and noise limitations of coherent digital holographic microscopy. Typically this involves the capture of sequence of holograms with different illumination angles, followed by a careful reconstruction process that re-positions and combines the images in spatial frequency. Here, we propose a single capture implementation with real-time numerical reconstruction. Furthermore, we employ a modular approach, such that an illumination module and an self-reference capture module can be attached to an existing life-science microscope with low cost and straightforward alignment. A mathematical model of image formation enables the inclusion of a non-blind deconvolution step in the real-time reconstruction process to enhance small features. The results on a range of biological samples clearly demonstrate the high quality and practical utility of the method for imaging biological samples and the improvement of the method over classical coherent holographic microscopy in terms of resolution and noise.

4.1 Introduction

Quantitative phase imaging (QPI) [10, 11] techniques enable real-time measurement of the phase-delay imparted by a specimen, and provide a powerful means to study the three-dimensional shape of biological samples, [220–223] as well as cellular dynamics with high accuracy. [12, 13] QPI methods include partially coherent white-light methods such as spatial light interference microscopy (SLIM), [21, 22] which was investigated in the previous chapter, differential phase contrast (DPC), [224, 225] and transport-of-intensity equation (TIE). [25, 26] The earliest and, arguably still, the most

popular QPI method is Digital Holographic Microscopy (DHM), [12, 13, 16, 17] which makes use of a coherent source that produces an object and reference wavefield; the interference pattern between these two wavefields is recorded on a digital sensor.

In the previous chapter, the SLIM technique was investigated for cell imaging and an improved calibration protocol was proposed. SLIM has several advantages over coherent DHM including a simpler optical set-up, insensitivity to vibration, low coherent noise, and a higher resolution. DHM on the other hand has a number of advantages over incoherent QPI methods like SLIM, including large depth of field, [17] computational aberration compensation [33, 34] and numerical refocusing, [35, 36, 226] which can be coupled with autofocus metrics. [37,38] Another advantage is the ability of DHM to capture the phase image in a single capture of the camera, while SLIM requires four. Perhaps the most important advantage of DHM over SLIM is the absence of the halo artifact. However, DHM suffers from coherent noise, which is sometimes mitigated using a laser with a low temporal coherence. [39–41] DHM also suffers from a lower resolution than SLIM and the other aforementioned white-light QPI methods. One solution to these shortcomings is synthetic aperture DHM (SA-DHM), [227] which involves the recording of several subsequent DHM phase images, each of which captures a different portion (aperture) of the spatial frequency content of the transmittance function; typically this requires different oblique illuminations. Careful realignment and stitching of these different apertures together in the spatial frequency domain generates the SA-DHM phase image. The resolution enhancement of SA-DHM is well known: whereas a single DHM phase image will have spatial frequency support with radius given by NA/λ (where NA corresponds to the numerical aperture of the microscope objective and λ is the laser wavelength), the SA-DHM image will have a larger support with radius $NA/\lambda + \alpha$ where α is proportional to the angular range in oblique illumination. Furthermore, the combination of different apertures results in a significant reduction in coherent noise.

In the early 1970s, Ueda el. al. proposed the earliest techniques to achieve a synthetic aperture (SA) using off-axis holography [228, 229] in which different oblique illuminations were applied to the object and the holograms were recorded on a photosensitive material. Several decades later, this work was extended using digital cameras and various methods of implementing different oblique illumination including the use of: (i) a spatially separated array of different light sources, [230–233] (ii) a single fixed oblique illumination with rotating sample stage, [234, 235] (iii) one or more diffraction gratings in the illumination path that are either fixed or rotating, [236, 237] (iv) a motorized rotating mirror [238] or wedge, [239, 240] (v) a galvo-scanning mirror, [118, 241–243] and (vi) a phase-only LCOS Spatial Light Modulator [244–247] or a digital micromirror device. [116] The latter two methods provide both high-speed and a continuous range of oblique angles and have also found application in the related area of optical diffraction tomography. [136, 138, 143, 248] A more complete review of the various methods for SA phase imaging can be found in Ref. 227.

In the context of this study, we have identified three classes of SA-DHM techniques with features that are particularly pertinent to the present contribution. These classes are as follows: (i) 'up-shift/down-shift' methods for which the reference wave changes

angle synchronously with the illumination angle, such that each recorded aperture is optically re-positioned to its correct location in the spatial frequency domain. [230–232, 249–258] This approach simplifies the algorithm used to reconstruct the synthetic aperture; (ii) Self-reference methods, whereby the reference wave is generated from a copy of the object wavefield. This approach lends itself to the development of a module that can readily be attached to the output port of a commercial brightfield microscope; [119, 120, 131, 137, 232, 233, 236, 259, 260] and (iii) Single-capture or 'one-shot' methods that have the key advantage of recording several spatial-frequency apertures within a single camera acquisition. [230, 247, 254–256, 261–263] These three classes of methods are reviewed in more detail in Section 4.2.

The system proposed in this chapter contains all three features listed above enabling real-time recording of an SA-DHM hologram in a single capture, with single step real-time numerical reconstruction. Moreover, we employ a modular approach, such that an illumination module and an image capture module can be attached to an existing life-science microscope with low cost and straight forward alignment as described in Section 4.3. A detailed mathematical model is provided in Section 4.4, which facilitates the development of a non-blind deconvolution step in the real-time reconstruction process in Section 4.5. The results presented in Section 4.7 clearly demonstrate the high quality and practical utility of the method for imaging biological samples. We note that in the next chapter, the module presented here will be adapted such that it can record a 3D tomographic reconstruction of cells using the principle of optical diffraction tomography. Much of the mathematics presented in this chapter relating to image formation is transferable to the next chapter as well.

Before proceeding, we refer the reader to Section 2.2.6 in Chapter 2, which covers much of the background material and mathematics that underpin the work presented here on digital holographic microscopy.

4.2 Brief background review for SA-DHM

In this Section, we briefly review three classes of SA-DHM techniques with features that are associated with the contributions of this study by employing our proposed SA-DHM setup. These are discussed in the three subsections that follow.

4.2.1 Class 1: Up-shift/Down-shift methods.

A key feature of the method proposed in this chapter is that the off-axis reference wave changes angle synchronously with respect to the oblique illumination angle, such that each recorded aperture is optically re-positioned to its correct location in the spatial-frequency domain. We describe this approach as 'up-shift/down-shift' because the oblique illumination serves to shift the Fourier Transform of the object transmission function by some two-dimensional (2D) vector, while the corresponding reference wave angle is chosen to shift the Fourier Transform of the real image (in the recorded hologram) by an equal and opposite 2D vector. The main advantage of this method is that multiple apertures can be recorded simultaneously and superimposed in time so long

as the illumination and reference angles are carefully matched, and each aperture is generated by a mutually incoherent source. In such case, there is an additional advantage that the multiple apertures do not need to be numerically combined using a synthetic aperture reconstruction algorithm that requires careful calibration and phase-matching. [118] In this subsection, we review several papers that have previously employed the 'up-shift/down-shift' concept, although we believe we are the first to utilise it to its full potential.

Schwarz et. al. [249] first proposed the idea in 2003, which was further developed by the same group in several more contributions [250–253]. Notably, in all of this work a real-valued interference image is generated, not a quantitative phase image; i.e. the synthetic aperture is Hermetian symmetric. Also, the apertures are selected not to overlap, but rather to concatenate, such that the extent of the synthetic aperture is maximised. In their initial contribution [249], three illumination angles were employed, two of which were outside the numerical aperture (NA) of the microscope objective (MO), one in each axis orthogonal to the optical axis. This scheme provides only three distinct apertures in Fourier space. In addition to the three interference images, several further exposures are required to subtract the darkfield and background images, in order to generate a single interference image with an extended numerical aperture of 0.9 using a MO with a NA of 0.4. The same three-angle illumination system was subsequently extended [250, 252] to achieve an interference image approaching a theoretically maximal synthetic aperture by recorded further interference images for which the sample itself was tilted with respect to the optical axis, thereby producing a further 'up-shift' in the Fourier Transform of the object transmission function. Consequently, the reference beam angle must also be adjusted in order to 'down-shift' in equal measure. Areas of the synthetic aperture that contained an overlapping of two aperture bands were normalised using filtering.

Interestingly, this method of synthetic aperture imaging is not necessarily dependent on the 'up-shift/down-shift' approach, since the different interference images would have been recorded with a fixed off-axis reference beam, and the apertures numerically re-positioned to their correct locations in the spatial-frequency domain in order to generate the synthetic aperture image. This point is highlighted in Ref.251 in which a fixed reference beam angle is applied for the same three-angle illumination system, which is achieved using a common-path design where the reference is generated by a second illumination at the limiting angle of acceptance of the MO. We note that the same authors further develop this approach using solid immersion media in order to maximise the possible synthetic aperture, achieving a resolution of down to a few tens of nanometers. [253]

A second research group investigated a similar set of 'up-shift/down-shift' imaging modalities in parallel. [230–232, 236, 254] A key difference with the work of this group compared with the former is that the synthetic aperture image is a quantitative phase image and not an interference image. In their initial contribution, [230] Mico. et al. employed a linear VCSEL array to illuminate the object and achieve a synthetic aperture along one dimension; the VCSELs are positioned in the Fourier plane of the condenser lens in order to generate a series of plane wave illuminations with different

oblique angles. A beamsplitter before the object is used to generate a reference wave and a Mach-Zender architecture is used to achieve an off-axis digital holographic image. The mutual incoherence of the various VCSEL sources enables the interference patterns generated by each independent source to be superimposed on the camera without cross-interference and, therefore, all of the VCSELs can be used simultaneously. The 'up-shift/down-shift' condition is automatically met since the reference and illuminating wavefields originate from the same VCSEL source and, therefore, have matching oblique angles with respect to the camera normal. The number and position of the VCSEL sources places a constraint on the number and separation of the apertures that are superimposed in the spatial-frequency domain.

This approach was extended to 2D aperture synthesis using a 2D array of VCSELs, whereby a similar Mach-Zender set-up was used, this time with a microscope objective, and using spherical illumination from the VCSELs (i.e. no condenser lens was used). [231] The holograms generated by each of the five VCSEL sources were recorded sequentially for simplicity of implementation, which was necessitated by a mismatch in the 'up-shift' imparted by the oblique illumination angle and the 'down-shift' imparted by the reference angle. In the DFT of each hologram the apertures were filtered and re-positioned in order to achieve the 'down-shift'. Notably, in this paper, the authors make no attempt to achieve a matching 'up-shift/down-shift' condition; however, the authors note that a single-capture approach is achievable if this condition is met. A similar setup is used in Ref. 232, in which the beamsplitter is positioned after the sample to create the self-reference design, and a pinhole mask in located in the Fourier plane to generate the reference beams. The authors mention that the optics in the system could be selected in order to satisfy the 'up-shift/down-shift' condition necessary for single-capture SA-DHM. More recently, the authors have proposed a lensless holography synthetic aperture approach based on the original Gabor in-line holography concept. [256] Here, a number of different point sources provide spherical illumination to a weakly scattering sample. Since the reference and illuminating wavefields are one and the same, the reference angle and the illumination angle are automatically matched thereby providing the correct 'up-shift/down-shift' condition. Mico et al. [236] propose a self-reference DHM architecture, whereby the reference beam is generated from the wavefield exiting the MO. Unlike previous self-reference architectures, this method employs an illumination scheme made up of two mutually coherent plane-waves at different angles, produced using a sequence of diffraction gratings. The first propagates along the optical axis; the second propagates at an angle that is greater than (double) the collection angle/numerical aperture of the MO. This second plane wave can be rotated in an annular pattern by rotating the diffraction gratings. The first plane wave is linearly polarised before illuminating the sample, while the second is unpolarised. A polarising beam splitter is used immediately after the MO to separate the object and reference paths. The object paths is made up of photons scattered only from the second (off-axis) plane-wave illumination, while the reference has contribution from both plane waves. A pinhole filter in the reference path serves to generate a clean plane-wave reference for interferometry. A sequence of holograms are recorded from different annular positions of the gratings providing different complex amplitudes cor-

responding to different bands of the objects Fourier transform. The sample used in this research is a 1951 USAF high resolution test. Nine holograms (including one on-axis holograms and 8 off-axis holograms) are recorded and stitched together to produce a synthetic aperture holograms that has three times the bandwidth of a single recorded hologram; using a 0.14 NA, 5x MO, the resolution was shown to improve threefold to 0.58 μm.

A matching 'up-shift/down-shift' condition has also been implemented by a number of other groups. A pulse laser was employed by Yuan et al. [255] with two beamsplitters to illuminate an object from three different angles. A second optical system is used to generate three reference beams with matching angles such that the 'upshift/down-shift' condition is satisfied by each of the three interference patterns. For each of the three illumination/reference cases, the path length differs such that cross interference is not possible. Owing to the high pulse rate, all three interference patterns will be superimposed within a single camera acquisition. A matching 'upshift/downshift' condition has also been used in some recent contributions [257, 258] based on the principle of total internal relection (TIR). In Ref. 258 the authors adapt a typical TIR fluoresence set-up to produce a synthetic aperture phase image. The premise is that the coverslip on the sample will partially reflect the epi-luminescent plane wave, the angle of which is varied in an annular pattern. The reflected component produces a reference wave, which has an angle that matches the illumination angle such that the 'upshift-downshift' condition is satisfied. A single camera acquisition can capture the superposition of the interference patterns from a continuous range of illumination angles, and results are shown for six angles. This is effectively an 'in-line' synthetic-aperture holography approach and suffers from the presence of DC artifacts. A similar approach is presented in Ref. 257, which also utilises a rotating diffuser to reduce the coherence of the illumination and improve image quality.

4.2.2 Class 2: Self-reference methods

Self-reference refers to the generation of the reference wave from a copy of the object wavefield, which is subject to filtering in order to produce a plane wave or similar. This approach is particularly useful because it decouples the reference wavefield from the source laser and therefore, facilitates the development of stand-alone modules that can be integrated to the exit (image) port of an existing microscope. In the context of SA-DHM, there have been several proposed self-reference architectures, primarily by two research groups. The three contributions of Mico et al. [232, 233, 236] that were described in the previous section in the context of 'upshift-downshift' SA-DHM methods, can also be classified as self-reference methods. For the case of both Refs. 232, 236 a cube beamsplitter in inserted immediately after the microscope objective; this approach enables to readily lend itself to the development of module that can be added to the image port of the microscope, as proposed in this chapter. In Ref. 233, a diffraction grating is inserted in a suitable position before the camera such that the first diffraction order generates an off-axis reference wave. Since no filtering is applied to this reference wavefield, there exists a limiting condition on this system that the object it-

self must contain no scattering particles in a sufficiently wide area, such that this area will constitute the clean reference wavefield generated by the first diffraction order. A second research group has also proposed two common-path architectures in the area of SA-DHM [119,120,131,137,259] or more specifically, in area of optical diffraction tomography, which requires a similar recording scheme. One system [119, 120, 131, 259] utilises a second set of galvo-scanning mirrors located approximately in the image plane, which synchronously 'de-scan', or counteract the angular tilt imparted by the galvo-scanning mirrors in the illumination. The effect of this correction ensures the object field will propagate parallel to the optical axis, regardless of illumination angle. A diffraction grating located in a conjugate image plane is imaged to the camera via a 4-f system. The first diffraction order is used to generate the reference wavefield, which is filtered using a pinhole in the Fourier plane. In the context of SA-DHM, this system has a number of disadvantages with respect to the system proposed in our chapter: Firstly this system cannot be used for single capture SA-DHM. The two galvo-scanning mirrors used for correcting the angle of the object wavefield are located in two separate planes close to the image plane. Therefore, a consequence of correcting the angle of the wavefield is a small shift of the image on the camera sensor. This shift can be easily corrected for each individual capture in order to enable SA-DHM or optical diffraction tomography, but it limits the application of the system to single capture SA-DHM. Secondly, the system utilises three 4-f system to process the image wavefield exiting the microscope; the system proposed in this chapter uses only a single 4-f system. The same research group also propose a simpler self-reference architecture for diffraction tomography, [137] which uses Rochon polarizer before the camera, which splits the beam and generates an off-axis reference wavefield. Similar to the method proposed by Mico et al. [233] there exists a limiting condition that the object itself must contain no scattering particles in a sufficiently wide area, such that this area will constitute the clean reference wavefield. A similar self-reference architecture for diffraction tomography is proposed by Hsu et al. [260] which places a diffraction grating in the image plane of the microscope. This is imaged via a 4-f imaging system to the camera. Once again, this system requires the sample to contain no scattering particles in a sufficiently wide area.

4.2.3 Class 3: Single Capture methods.

Single-capture or 'one-shot' methods have the advantage of recording several spatial-frequency apertures within a single camera acquisition. [230,247,254–256,261–263] In the earliest single-capture SA-DHM contribution, [230] the authors propose a system for which the 'up-shift/down-shift' condition is satisfied optically as described in Section 4.2.1. The use of mutually incoherent VCSEL sources allows for the simultaneous capture of different apertures in a single off-axis hologram, without cross-interference. There are several differences with respect to the system proposed here: firstly, it is not a self-reference architecture; secondly, the number of independent point sources (and, therefore, apertures are small); and thirdly, the VCSELS are arranged in a line, which limits the SA to one dimension. In Ref. 247, a system is proposed that captures five

apertures in a single hologram. A matching 'up-shift/down-shift' condition is not satisfied optically, which necessitates subsequent numerical down-shifting. The five apertures are generated by SLM illumination and are separated in the Fourier domain of the hologram in order to avoid cross-interference.

In Ref. 261 three lasers with different wavelengths (red, blue, green) are incident on a sample with three different angles of illumination. A diffraction grating is placed after the microscope objective and a monochromatic camera captures the first diffraction order of each of the three wavelengths. These three wavefields interfere with three reference wavefields from the lasers, all of which are combined to propagate at the same off-axis angle; three is no cross-interference between wavefields of different wavelength. The effect of the grating is to impart a different diffraction angle to each of the three wavelengths, and in this way the three different object wavefields are spatially separated in the discrete Fourier domain of the camera. The system is limited to three apertures in a single capture, and also requires numerical down-shifting. The same group propose a similar system in Ref. 254, this time without the use of the diffraction grating. In this case, the three different interference patterns are recorded using the three channels on a color camera. A simpler red, green, blue laser illumination system is proposed by the same group, [256] which has previously been discussed in Section 4.2.1. In this case, three adjacent point sources produce three different in-line Gabor holograms. The three different angles of the spherical illumination will produce three different apertures, all of which are captured simultaneously by a colour camera. Although the matching 'up-shift/down-shift' condition is satisfied, the three holograms are spatially shifted and must be carefully realigned. Further, only three apertures are captured, and each of these is corrupted by the presence of the twin-image and DC components, which have not been separated in the Fourier domain; this prevents the application of this approach for quantitative phase imaging.

The pulse-laser system described in the previous section [255] can also be classified as a single-capture SA method. Like the methods proposed in this chapter, a matching 'up-shift/down-shift' condition is utilised which negates the need for any subsequent numerical processing. However, in this case only three apertures are recorded in a single capture, and the system is complicated by the use of a pulse-laser and a system of six beamsplitter and ten mirrors.

In Ref. 262, a system is proposed that capture two apertures simultaneously using the sample laser split to produce two different angles of illumination. Two reference wavefields at different angles ensure separation of the apertures in the Fourier domain and cross-interference is prevented by using orthogonal states of polarisation. The 'up-shift/down-shift' condition is not matched and post-processing is required to reposition the apertures. A similar system is proposed in Ref. 263 where two SLMs are used to control the angle and polarisation state of the illumination. Both of these systems are capable of capturing only two apertures in a single camera acquisition.

4.3 Optical System

The schematic diagram of the real-time SA-DHM setup is shown in Fig. 4.1. A modular approach is taken such that two modules, an illumination module and a capture module, can be attached to an existing commercial microscope. The illumination module is attached to the condenser of the microscope, and the capture module is positioned at the output image port. This capture module, which we name the 'X-Module' owing its unusual crisscrossing of light paths. The two modules are completely detached in the sense that no reference beam is directed from the illumination module into the X-module. Instead the X-module uses the principle of 'self-reference' whereby a reference wavefield is generated from the object wavefield; this feature is often found in self-reference DHM as described in Section 4.2.

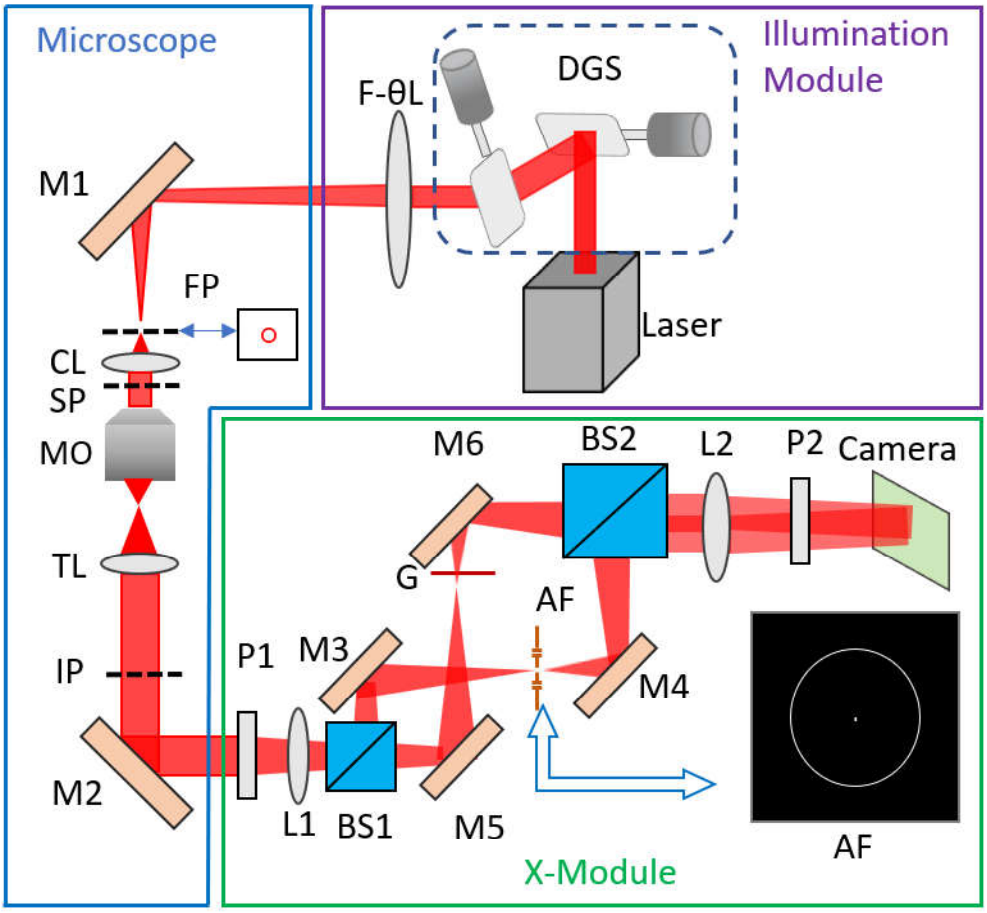

Figure 4.1: Schematic of real-time SA-DHM, which comprises an illumination module and an X-module attached to an existing microscope: DGS, dual-axis galvo system; F-θL, F-theta lens; M, mirror; FP, filter-plane, i.e. back focal plane of the condenser lens, also known as the 'filter plane'; CL, condenser lens; SP, sample plane; MO, microscope objective; TL, tube lens; IP, intermediate image plane; L1 and L2, matching achromatic lens; BS1, polarising beamsplitter; BS2, broadband beamspltter; AF, Annular spatial filter; G, transparent glass with matching thickness to AF; P, polarizer.

4.3.1 The illumination Module

The illumination module includes a portable low-cost 635 nm handheld red diode laser (Thorlabs; HLS635), which is fiber coupled and collimated into a dual-axis galvo mirror system (Thorlabs; GVS012) assembled with an F-Theta lens (Thorlabs; FTH254-1064). This galvonometer is driven by a signal function generator (R&S^{TM} AM300 Dual generator) with a sinusoidal AC signal such the focused laser produces an annular pattern at the focal plane of the F-theta lens; this plane is also the back focal plane of the condenser lens (CL), which is often referred to as the 'filter plane' (FP) in microscopy. This pattern is analogous to the annular filter used in phase contrast microscopy, in SLIM [21] and recent implementations of TIE imaging. [25] Each point in the annular pattern corresponds to the laser focus at one instant of time, which produces an angled incident plane wave illumination on the sample via the condenser lens.

The use of scanning annulus in the filter plane has an advantage over traditional solid condenser annular filters that are used in phase contrast microscopy, SLIM, and TIE. The diameter of the annulus generated from the Galvo-scanner can be arbitrarily customized to suit the properties of the imaging system making it more practicable for a wider range of microscope objectives. Furthermore, the illumination is not limited to annular patterns; individual point sources or other light shape can also be generated. Moving point source illumination is the basis for diffraction tomography (ODT), [115] and various shaped illuminations are used in DPC microscopy. [224, 264]

4.3.2 The microscope

The approach taken in this study is to use an illumination module and a capture module that can readily be added to any existing life-science microscope. Here, we build a bespoke microscope using a microscope objective (Olympus; MPlan 40x, 0.85NA) coupled with a tube lens (Olympus; SWTLU-C, f=180mm), which together produce an image of the sample at the image plane (IP). The condenser lens (Nikon; Plan Apo 20x, 0.75) is mounted on a manual translation stage (Thorlabs; MT1-M), which is adjusted to ensure Kohler illumination. The sample is mounted on an electronic translation stage (ASI; MS-2000, LX-4000) and the MO is also mounted on an electronic translation stage (ASI; MS-50, LX-4000) to facilitate automated focusing. Both stages are controlled using the open-source Micro-Manager platform. [265]

4.3.3 The X-Module

The image capture module is positioned close to the image plane as illustrated in Fig. 4.1. This module is built on a small breadboard such that it can easily moved and added to the output port of a commercial microscope. The module uses a 4-f imaging system to relay the image to a digital camera using two identical lenses, L1 and L2, (Thorlabs UK; LB4282) of focal length 200mm, which are positioned at a distance of one focal length from the image plane and one focal length from the detector plane, respectively. A polarising beamsplitter (Thorlabs UK; PBS201) splits the wavefield into two paths, which cross each other via mirror pairs (M3,M4) and (M5,M6) before being

recombined using a second beamsplitter (Thorlabs UK; BS031), which in this case is a 50/50 broadband cube beamsplitter of larger size than BS1 in order to fully capture the shifted object and reference wavefields. Initially, these mirror pairs are aligned to produce a matching overlapping image on the detector from both paths, each with an angle of incidence on the detector that is equal in magnitude and opposite in sign for both paths. This angle is adjusted to produce the optimal off-axis condition for holography, which is described in more detail in Section 4.4.2. The back focal plane of lens L1 is also the conjugate plane of the FP discussed in Section 4.3.1, and therefore, the annular pattern is reproduced there. A customised annular filter (JD-Photo, UK) is positioned in this plane mounted on three-dimensional translation stage (Thorlabs UK; DT12XYZ/M), which transmits only the annular scanning focused laser. The filter is composed of a 25×25×3 mm glass plate with a chrome photo-mask of optical density > 3 produced using photo-lithography. The annular filter is 2.5 mm in radius and the annulus is 15 μm thick. The filter also has a single pinhole in the centre of the annulus of diameter 15 μm, which facilitates centering of the filter, and also permits recording of a coherent hologram similar to other self-referencing DHM systems that have been reported in the literature. [266, 267] An identical piece of glass but with no photomask is inserted into the object path in order to maintain phase-matching between both paths. Two linear polarisers, P1 and P2 (Edmund Optics UK; LPVISE200-A), on rotation mounts are positioned at the input and output of the module; together with BS2 the polarisers enable control of the object and reference power that is incident on the monochrome digital camera (Thorlabs; CS895MU). This camera has 4096×2160 pixels of size 3.45×3.45 μm.

The crisscross configuration of the object and reference paths in the X-module is preferred to the Mach-Zender architecture because it enables close positioning of the mirrors relative to the two beamsplitters and more easily facilitates the off-axis condition, which frees up the space between the mirrors to use for filtering. This configuration also has a smaller form factor overall when compared with Mach-Zender. The X-module has the advantage of being able to record both a coherent hologram (using the single pinhole filter) as well as SA hologram (using the annular filter). This provides a convenient means to directly observe the resolution enhancement and noise reduction afforded by the SA approach.

In this chapter, all SA-DHM images were obtained by configuring the Galvo scanning rate to 50 Hz for annular illumination. Additionally, the exposure time of camera is set to 20 ms to synchronize with the scanning rate, enabling real-time imaging. It's important to note that the exposure time can be reduced if the scanning rate is increased.

4.3.4 Alignment Protocol

The steps to achieve the optimal off-axis angle are as follows: (0) A DC voltage is applied to the galvo-scanner and the mirror M1 is adjusted such that the focused laser is approximately in the centre of the AF; (1) In the initial assembly the filter plate and glass plate are omitted from the reference and object paths, respectively. The mirror

pairs (M3,M4) and (M5,M6) illustrated in Fig. 4.1 are adjusted to produce approximate co-alignment of both paths with zero off-axis angle; (2) A sample is placed on the stage and the mirror pairs are finely adjusted to ensure that the images from both paths are overlapping, and the interference pattern is from an in-line hologram; (3). Selecting one of the paths, one mirror is adjusted to move the image horizontally by a set number of pixels, and the second mirror is adjusted to return the image to its original position; (4) This is repeated for the other path but in this case the image is moved in the opposite direction; (5) Steps 3 and 4 are repeated for the vertical direction; (6) An FFT algorithm is applied to observed the DFT. Steps 3-5 are repeated until the optimal off-axis angle is achieved based on the supports of the twin images and DC terms; (7) The filter and glass plate are added to the reference and object paths. In practice, determining the correct position and tilt of the annular filter in the Fourier plane is difficult to realize. Without changing the voltage to the galvo, the centre pinhole in the filter is aligned in three-dimensions with the focused laser. The resulting interference pattern is an off-axis hologram similar to that reported in Ref. 266. For simplicity, we refer to this as the coherent hologram or 'DC hologram' in the text; (8) The DC signal is changed to a sinusoidal AC signal, which is adjusted to match the radius of the annular filter. The hologram resulting from the annular scanning illumination is referred to as the SA hologram; (9) Step 6 is repeated due to the larger spatial frequency support of the twin image terms in the SA hologram.

4.4 Theory of Image Formation

In this section, the theory that describes image formation in the proposed real-time SA-DHM imaging system is developed. The first subsection begins with an analysis of traditional multi-capture SA-DHM, whereby a sequence of plane wave illuminations are applied from various angles while a constant reference wavefield is maintained for each hologram. Each illumination produces a single digital hologram corresponding to a different aperture in Fourier space. These captures can be processed and combined to produce a single synthetic aperture phase image. In the second subsection, the same theoretical basis is used to demonstrate that the X-module can utilise only a single capture to produce a similar synthetic aperture phase image.

4.4.1 Traditional Multi-Capture SA-DHM

The illustration of a 4-f imaging system with illumination from a condenser lens in Fig. 4.2(a) is used to aid the description of image formation in this section. It is assumed that all planes shown in this diagram are a focal length away from each lens. The sample plane and the image plane are conjugate planes, and the filter plane and the pupil plane are also conjugate planes. The filter plane and sample plane are related by a Fourier transform; so too are the pupil plane and the image plane. We define (u_x, u_y) to be a coordinate in the illumination/pupil plane, and (x, y) is a coordinate in the sample/image plane. For simplicity, the effect of magnification due to the different focal lengths of the various lenses is omitted in following analysis. The Fourier

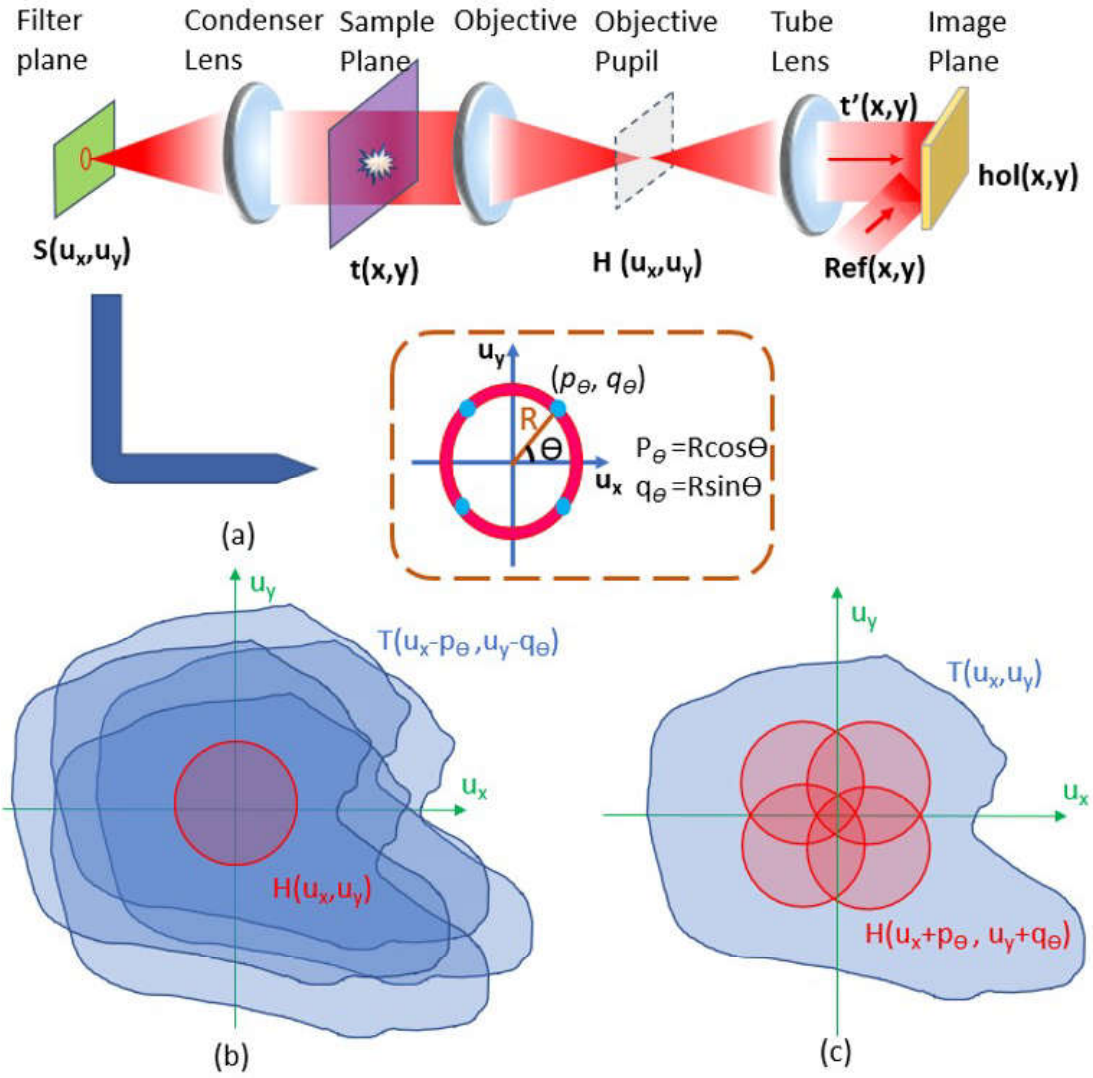

Figure 4.2: **(a)** Simplified illustration of traditional SA-DHM imaging that uses different point sources in an annular pattern; **(b)** The distribution of the wrong upshift frequency bands of sample transmittance $T(u_x - p_\theta, u_y - q_\theta)$ and the unchanged transfer function $H(u_x, u_y)$; **(c)** The correct and fixed sample transmittance $T(u_x, u_y)$ and the downshift frequency bands of the transfer function $H(u_x + p_\theta, u_y + q_\theta)$. Note that only 4 frequency bands from 4 point sources are shown in the figure for a concise display.

transform and inverse Fourier transform are defined as follows:

$$\begin{aligned} F(u_x,u_y) &= \mathscr{F}\{f(x,y)\}(u_x,u_y) \\ &= \iint_{-\infty}^{\infty} f(x,y)\exp\big[-2\pi(u_x x+u_y y)\big]dxdy \end{aligned} \tag{4.1}$$

$$\begin{aligned} f(x,y) &= \mathscr{F}^{-1}\{F(u_x,u_y)\}(x,y) \\ &= \iint_{-\infty}^{\infty} F(u_x,u_y)\exp\big[2\pi(u_x x+u_y y)\big]du_x du_y \end{aligned} \tag{4.2}$$

where f and F are a Fourier transform pair, and $\mathscr{F}$ and $\mathscr{F}^{-1}$ are the operators for the Fourier and inverse Fourier transforms. A constant scaling factor is omitted in the definitions above. The forward and inverse Fourier transforms can be related as follows:

$$\mathscr{F}\{f(x,y)\}(u_x,u_y) = \mathscr{F}^{-1}\{f(x,y)\}(-u_x,-u_y) \tag{4.3}$$

The distribution in the filter plane in Fig. 4.2(a) is represented by $S(u_x,u_y)$. For the case of traditional DHM, which utilises only a single temporally and spatially coherent plane wave illumination, the distribution in the filter plane reduces to only one delta-correlated point light source at the origin, i.e. $S(u_x,u_y)=\delta(u_x,u_y)$, and the illumination wavefield in the sample plane, $s(x,y)$ reduces to unity; $S(u_x,u_y)$ and $s(x,y)$ are related by an inverse Fourier transform, i.e. $s(x,y)=\mathscr{F}^{-1}\{S(u_x,u_y)\}(x,y)$.

The complex image wavefield in the detector plane, $t'(x,y)$, is a result of the convolution of the complex sample transmittance $t(x,y)$ with the point spread function $h(x,y)$ of the coherent imaging system as follows:

$$t'(x,y) = \iint s(x',y')\,t(x',y')\,h(x-x',y-y')dx'dy' \tag{4.4}$$

Since the illumination term, $s(x',y')$, is unity, it can be ignored in this equation.

The Fourier transforms of $t(x,y)$, $h(x,y)$ and $t'(x,y)$ are given by $T(u_x,u_y)$, $H(u_x,u_y)$ and $T'(u_x,u_y)$, respectively. The following relationship is provided by the convolution theorem of the Fourier transform [268]:

$$T'(u_x,u_y) = T(u_x,u_y)\,H(u_x,u_y) \tag{4.5}$$

Typically, image formation in a microscope is based on the assumption that the transfer function of the imaging system, $H(u_x,u_y)$, is a simple pupil function. More specifically, $H(u_x,u_y)=circ(u_x\lambda/NA,u_y\lambda/NA)$, where the $circ(u_x,u_y)$ function is defined to unity within a circle of radius 1, i.e. for values of (u_x,u_y) for which $u_x^2+u_y^2<1$ and zero outside; NA is the numerical aperture of the microscope objective and λ is the wavelength of the illumination. The complex image $t'(x,y)$ cannot be directly recorded; rather, the intensity, $I(x,y)$, recorded in the detector plane is given by:

$$I(x,y) = |t'(x,y)|^2 \tag{4.6}$$

Acquiring the complex image $t'(x,y)$ requires the use of a reference wavefield using the

well-known equation for holography:

$$\begin{aligned} hol(x,y) &= \left|O(x,y)+Ref(x,y)\right|^2 \\ &= \left|O(x,y)\right|^2+\left|Ref(x,y)\right|^2+O(x,y)\overline{Ref(x,y)} \\ &+\overline{O(x,y)}Ref(x,y) \end{aligned} \tag{4.7}$$

where Ref represents the reference wavefield and the bar represents the complex conjugate, and O represents the object wavefield. Assuming the off-axis angle of the reference wavefield is sufficiently large, the complex valued function $t'(x,y)$ can be calculated by filtering the discrete Fourier transform of the recorded digital hologram. [221]

4.4.1.1 Annulus scanning point source

Angular illumination can be provided by moving the position of delta-correlated point light source in the filter plane away from the origin to a point (p_θ, q_θ). The illumination function is denoted now as $S_{p_\theta,q_\theta} = \delta(u_x - p_\theta, u_y - q_\theta)$, which produces an off-axis plane wave illumination in the sample plane:

$$\begin{aligned} s_{p_\theta,q_\theta}(x,y) &= \mathscr{F}^{-1}\{\delta(u_x-p_\theta,u_y-q_\theta)\} \\ &= \exp\left[j2\pi(xp_\theta+yq_\theta)\right] \end{aligned} \tag{4.8}$$

In Fig. 4.2(a), four such point sources are illustrated in the Illumination plane, all of which are located on a circle (or annulus) of radius R centered at the origin. Polar coordinates can be used to define any point on this circle:

$$\begin{aligned} p_\theta &= R\cos\theta \\ q_\theta &= R\sin\theta \end{aligned} \tag{4.9}$$

For a given point source on this circle, which is uniquely defined by the angle θ, the complex transmittance, t, defined in Equation 4.4 can be written as t'_θ as follows:

$$t'_\theta(x,y) = \iint \exp[j2\pi(xp_\theta+yq_\theta)]\,t(x',y')h(x-x',y-y')dx'dy' \tag{4.10}$$

The complex image defined in Equation 4.10 has a Fourier transform given by:

$$T'_\theta(u_x,u_y) = T(u_x-p_\theta,u_y-q_\theta)H(u_x,u_y) \tag{4.11}$$

The result of angular illumination, therefore, is to shift (or 'upshift' in the context of the earlier discussion) the sample spatial frequency spectrum, before multiplication of the pupil function which remains at the origin. In this way different bands of frequencies can be captured by the imaging system, depending on position of the point source in the filter plane. The effect is illustrated in Fig. 4.2(b) in which the sample spectrum is shown in four different shifted positions, resulting from the four different point source locations. The transfer function, H, remains static at the origin.

4.4.1.2 Piecemeal Numerical Reconstruction

In traditional SA-DHM, a sequence of images are recorded corresponding to an integer number, M, of point source positions uniformly distributed on the annulus at the angles $\theta_n = 2\pi n/M$, where n takes the values $0 \rightarrow (M-1)$. The coordinate of the nth point source is denoted as $(p_{\theta_n}, q_{\theta_n})$, and the resulting complex image has a spatial frequency spectrum given by:

$$T'_{\theta_n}(u_x, u_y) = T(u_x - p_{\theta_n}, u_y - q_{\theta_n})H(u_x, u_y) \tag{4.12}$$

For the example shown in Fig. 4.2(a) and (b), only four point sources are illustrated producing four captured images; however, typically SA-DHM can employ hundreds of point sources with small angular shifts between captures, often facilitated by a galvo-scanning mirror and an f-theta lens, which scans a focused laser in an annulus located in the filter plane of the condenser lens.

A core component in traditional SA-DHM is the reconstruction of the SA-image by numerically recombining the captured images, each containing a portion of unique frequencies. It is essential that each of the captured complex images is first 'downshifted' in spatial frequency by an amount that equals the 'upshift' attributed to the angle of illumination. Any disparity in the amount of 'downshift' will have deleterious effect on the quality of the resultant SA-image, and error correction algorithms are often employed to ensure high quality. [269] Once each of the captured images has been appropriately 'downshifted' in the spatial-frequency domain, these can simply be superimposed and added together to produce the SA-image. The Fourier transform of this image, T', is given by:

$$\begin{aligned} T'(u_x, u_y) &= \sum_{n=1}^{M} T'_{\theta_n}(u_x + p_{\theta_n}, u_y + q_{\theta_n}) \\ &= \sum_{n=1}^{M} T(u_x, u_y)H(u_x + p_{\theta_n}, u_y + q_{\theta_n}) \\ &= T(u_x, u_y)\sum_{n=1}^{M} H(u_x + p_{\theta_n}, u_y + q_{\theta_n}) \end{aligned} \tag{4.13}$$

where the synthetic aperture is, therefore, defined as follows:

$$SA(u_x, u_y) = \sum_{n=1}^{M} H(u_x + p_{\theta_n}, u_y + q_{\theta_n}) \tag{4.14}$$

This is the effective transfer function of this multi-capture imaging system and results from the overlapping of all ('downshifted') transfer function associated with the various point sources on the scanning annulus. An example of image reconstruction is shown in Fig. 4.2(c), where $T(u_x, u_y)$ now remains centred at the origin and four transfer function frequency bands corresponding to the four different point sources have been shifted relative to the point source position on the annulus. Numerical deconvolution is typically applied in order to account for the non-uniform shape of $SA(u_x, u_y)$

and re-balance the power ratio between low and high frequencies components in the image.

4.4.2 Real-Time Synthetic Aperture DHM

4.4.2.1 Single Capture over a Full 2-π Scan

The X-module records the complex wavefield, $t'_\theta(x,y)$, by scanning over a continuous 2π range of the illumination angle θ, whereby the hologram is the integral in time of the interference patterns resulting from each angle of illumination. Such an approach would not be possible using conventional SA-DHM, which employs a fixed reference wavefield, and which therefore necessitates numerical 'downshift' of each individual recording before integration. For the X-module, the reference wavefield, $Ref(x,y)$ in Equation 4.7 is generated by $t'_\theta(x,y)$ in the module, such that it can optically 'downshift' the object wavefield at each instance of time.

The output wavefield from the microscope image port (which is given by $t'_\theta(x,y)$) is incident on a polarising beam splitter, which splits it into two paths; both paths image the image plane, IP, to the digital sensor via two achromatic lenses (a $4-f$ imaging system). In the object path, the image wavefield $t'_\theta(x,y)$ is reproduced at the camera plane at an off-axis angle. In the reference path, a narrow annulus serves to filter the incoming wavefield and passes only the lowest spatial frequencies. As an approximation, we model the effect of the annulus in a given instance of time as a pinhole, which matches the point source position of the illuminating point source in the filter plane. The aim of the filter is to remove all frequency component from the reference wavefield except the zero frequency plane wave that will produce a suitable reference beam. The sample transmittance, t_θ, can be approximately described by the weak object approximation [25, 224] whereby the object field is separated into a scattered field, a_θ, and an unscattered field, represented by unity:

$$t_\theta(x,y) \cong 1 + a_\theta(x,y) = 1 + \mu_\theta(x,y) + j\psi_\theta(x,y) \tag{4.15}$$

where μ denotes the absorption (amplitude) distribution of the object and ψ denotes the phase distribution of object. With this substitution, Equation 4.10 can be rewritten as follows:

$$\begin{aligned} t'_\theta(x,y) = \iint & \exp\left[j2\pi(x'p_\theta + y'q_\theta)\right]\left[1 + a_\theta(x',y')\right] \\ & h(x-x', y-y')\,dx'\,dy' \end{aligned} \tag{4.16}$$

Similarly, Equation 4.12 can also be rewritten:

$$\begin{aligned} T'_\theta(u_x,u_y) = {} & \delta(u_x - p_\theta, u_y - q_\theta)H(u_x,u_y) \\ & + A_\theta(u_x - p_\theta, u_y - q_\theta)H(u_x,u_y) \end{aligned} \tag{4.17}$$

where $A_\theta = \mathscr{F}\{a_\theta\}$ and $\delta(x,y)$ represents the Dirac-delta functional. [268] Assuming the δ function lies inside the support of the transfer function $H(u_x,u_y)$, and the transfer

function describes a simple pupil function of unit amplitude, the above equation can be rewritten:

$$\begin{aligned} T'_\theta(u_x,u_y) &= \delta(u_x-p_\theta,u_y-q_\theta) \\ &\quad + A_\theta(u_x-p_\theta,u_y-q_\theta)H(u_x,u_y) \end{aligned} \tag{4.18}$$

The aim of filtering with the annulus is to pass only light at positions (p_θ, q_θ) in the Fourier domain, thereby passing only the delta-function in the above equation for a given θ. The resulting reference wavefield, Ref_θ is therefore given by:

$$Ref_\theta(x,y) = \exp\left[j2\pi(xp_\theta + yq_\theta) + j\phi_\theta\right] \tag{4.19}$$

where ϕ_θ represents a constant phase shift resulting from slightly different path lengths in the object and reference arms for illumination angle θ.

By appropriate angling of mirror pairs (M3,M4) and (M5,M6) in the X-Module (see Fig. 4.1) both the object and reference wavefields can be tilted at small (opposing) off-axis angles in x and y represented by Δ_x and Δ_y. The recorded hologram at a single instance of time, $hol_\theta(x,y)$ corresponding to illumination angle θ, is given by the interference of object wavefield $O_\theta(x,y)$ and reference wavefield $Ref_\theta(x,y)$ as follows:

$$\begin{aligned} hol_\theta(x,y) &= \left|O_\theta(x,y) + Ref_\theta(x,y)\right|^2 \\ &= \left|O_\theta(x,y)\right|^2 + \left|Ref_\theta(x,y)\right|^2 \\ &\quad + O_\theta(x,y)\overline{Ref_\theta(x,y)} + \overline{O_\theta(x,y)}Ref_\theta(x,y) \end{aligned} \tag{4.20}$$

where the object and reference wavefields are augmented with linear phase terms as follows:

$$O_\theta(x,y) = t'_\theta(x,y)\exp\left[\frac{j2\pi(x\Delta_x - y\Delta_y)}{\lambda f}\right] \tag{4.21}$$

$$\begin{aligned} Ref_\theta(x,y) = &\exp\left[j2\pi(xp_\theta + yq_\theta) + j\phi_\theta\right] \\ &\exp\left[\frac{-j2\pi(x\Delta_x - y\Delta_y)}{\lambda f}\right] \end{aligned} \tag{4.22}$$

where λ is the laser wavelength; f is the focal lens of the achromatic lens used in the module, and O_θ and Ref_θ take the place of O and Ref in Equation 4.7. The interference pattern, hol_θ, at an instance of time corresponding to illumination angle θ is given by:

$$\begin{aligned} hol_\theta(x,y) = &\left|t'_\theta(x,y)\right|^2 + 1 \\ &+ t'_\theta(x,y)\exp\left[\frac{j4\pi(x\Delta_x - y\Delta_y)}{\lambda f}\right]\exp\left[-j2\pi(xp_\theta + yq_\theta) - j\phi_\theta\right] \\ &+ \overline{t'_\theta(x,y)}\exp\left[\frac{-j4\pi(x\Delta_x - y\Delta_y)}{\lambda f}\right]\exp\left[j2\pi(xp_\theta + yq_\theta) + j\phi_\theta\right] \end{aligned} \tag{4.23}$$

which has a Fourier transform, HOL_θ, given by:

$$\begin{aligned} HOL_\theta(u_x,u_y) &= \mathscr{F}\{|t'_n(x,y)|^2\}(u_x,u_y)+\delta(u_x,u_y) \\ &+\exp(-j\phi_\theta)T'_\theta\Big(u_x+\frac{2\Delta_x}{\lambda f}+p_\theta,u_y-\frac{2\Delta_y}{\lambda f}+q_\theta\Big) \\ &+\exp(j\phi_\theta)\overline{T'_\theta\Big(u_x-\frac{2\Delta_x}{\lambda f}-p_\theta,u_y+\frac{2\Delta_y}{\lambda f}-q_\theta\Big)} \end{aligned} \tag{4.24}$$

Real-time SA-DHM is achieved by extending the acquisition time of the camera to equal to the time for the point source to continuously move over a full circle: $\theta = 0 \rightarrow 2\pi$. In practice, this acquisition time will be limited by the speed of the Galvo-scanner in the illumination module. For our case this was 20 ms but faster time can be achieved with other systems with higher specification. The resultant intensity, $hol(x,y)$, in the camera plane is given by:

$$hol(x,y)=\int_0^{2\pi} hol_\theta(x,y)d\theta \tag{4.25}$$

and the Fourier Transform of $hol(x,y)$ is given by:

$$\begin{aligned} Hol(u_x,u_y) &= \int_0^{2\pi} Hol_\theta(u_x,u_y)d\theta \\ &= 2\pi\delta(u_x,u_y)+\int_0^{2\pi}\mathscr{F}\{|t'_\theta(x,y)|^2\}(u_x,u_y)d\theta \\ &+\int_0^{2\pi}\exp(-j\phi_\theta)T'_\theta\Big(u_x+\frac{2\Delta_x}{\lambda f}+p_\theta,u_y-\frac{2\Delta_y}{\lambda f}+q_\theta\Big)d\theta \\ &+\int_0^{2\pi}\exp\big(j\phi_\theta\big)\overline{T'_\theta\Big(u_x-\frac{2\Delta_x}{\lambda f}-p_\theta,u_y+\frac{2\Delta_y}{\lambda f}-q_\theta\Big)}d\theta \end{aligned} \tag{4.26}$$

Substituting the expression for T'_θ in Equation 4.13 into this equation results in the following simplification:

$$\begin{aligned} Hol(u_x,u_y) &= \int_0^{2\pi} Hol_\theta(u_x,u_y) \\ &= 2\pi\delta(u_x,u_y)+\int_0^{2\pi}\mathscr{F}\{|t'_\theta(x,y)|^2\}(u_x,u_y)d\theta \\ &+T\Big(u_x+\frac{2\Delta_x}{\lambda f},u_y-\frac{2\Delta_y}{\lambda f}\Big)\int_0^{2\pi}\exp\big(-j\phi_\theta\big) \\ &H\Big(u_x+\frac{2\Delta_x}{\lambda f}+p_\theta,u_y-\frac{2\Delta_y}{\lambda f}+q_\theta\Big)d\theta \\ &+\overline{T\Big(u_x-\frac{2\Delta_x}{\lambda f},u_y+\frac{2\Delta_y}{\lambda f}\Big)}\int_0^{2\pi}\exp\big(j\phi_\theta\big) \\ &\overline{H\Big(u_x-\frac{2\Delta_x}{\lambda f}-p_\theta,u_y+\frac{2\Delta_y}{\lambda f}-q_\theta\Big)}d\theta \end{aligned} \tag{4.27}$$

This can be rewritten in terms of the effective real-time synthetic aperture, SA, as fol-

lows:

$$\begin{aligned} Hol(u_x,u_y) &= \int_0^{2\pi} Hol_\theta(u_x,u_y) \\ &= 2\pi\delta(u_x,u_y) + \int_0^{2\pi} \mathscr{F}\{|t'_\theta(x,y)|^2\}(u_x,u_y)d\theta \\ &+ T\Big(u_x+\frac{2\Delta_x}{\lambda f}, u_y-\frac{2\Delta_y}{\lambda f}\Big)SA(u_x,u_y) \\ &+ T\Big(u_x-\frac{2\Delta_x}{\lambda f}, u_y+\frac{2\Delta_y}{\lambda f}\Big)SA(u_x,u_y) \end{aligned} \tag{4.28}$$

where,

$$SA(u_x,u_y) = \int_0^{2\pi} \exp(-j\phi_\theta)H\Big(u_x+\frac{2\Delta_x}{\lambda f}+R\cos\theta, u_y-\frac{2\Delta_y}{\lambda f}+R\sin\theta\Big)d\theta \tag{4.29}$$

4.4.2.2 Numerical Reconstruction

Unlike traditional SA-DHM, which requires multiple captures and subsequent numerical reconstruction applied to each capture, only one step is required to reconstruct the real-time SA-DHM hologram. This involves a discrete Fourier transform (DFT) to transform the digital hologram to the Fourier domain, followed by spatial filtering the real (or imaginary) image, followed by an inverse DFT. The DFT can be implemented efficiently using the fast Fourier transform algorithm [268]. In order to gain an appreciation of the numerical reconstruction process, an illustration of Hol, resulting from the DFT of the recorded hologram, is given in Fig. 4.3. The yellow bounded area represents the spatial frequency support of the detector and is defined by the inverse of the pixel size, P_w, and the magnification of the microscope, M. The two DC terms, given by the first two terms in Equation 4.28 are located in the centre. The centres of the twin image terms are separated from the origin by an amount $2\Delta_x/\lambda f$ and $2\Delta_y/\lambda f$ in dimensions u_x and u_y, respectively, which directly relates to the relative angle between the object and reference in the X-module. The Fourier transform of the sample, T, remains static in the twin image terms, while the centre of the transfer function, H, (illustrated with the red circle bands) moves in time in a circular pattern with radius R and angle θ (see Fig. 4.2). Four unique positions of H are shown corresponding to four instances of time, and in Fig. 4.3(b) the result of integrating H over all continuous angles θ is shown which corresponds to the amplitude of the synthetic aperture, SA, defined in Equation 4.29. The profile of the synthetic aperture is shown in Fig. 4.3(c).

Numerical reconstruction is straightforward so long as certain conditions are met: The off-axis angles Δ_x and Δ_y should be selected to separate the twin image terms sufficiently, such that they can be isolated from the other terms but not so far as to move into the next DFT period; this selection will depend on the support of the synthetic aperture, SA, the pixel size of the camera, the values of M and NA. The support of SA is equal to the diameter of H plus the diameter of the illumination scanning annulus, which is given by $2NA/\lambda + 2R$; this assumes that there is a magnification of unity between the filter plane and the Pupil Plane of the MO. If this is not the case, the $2R$ value

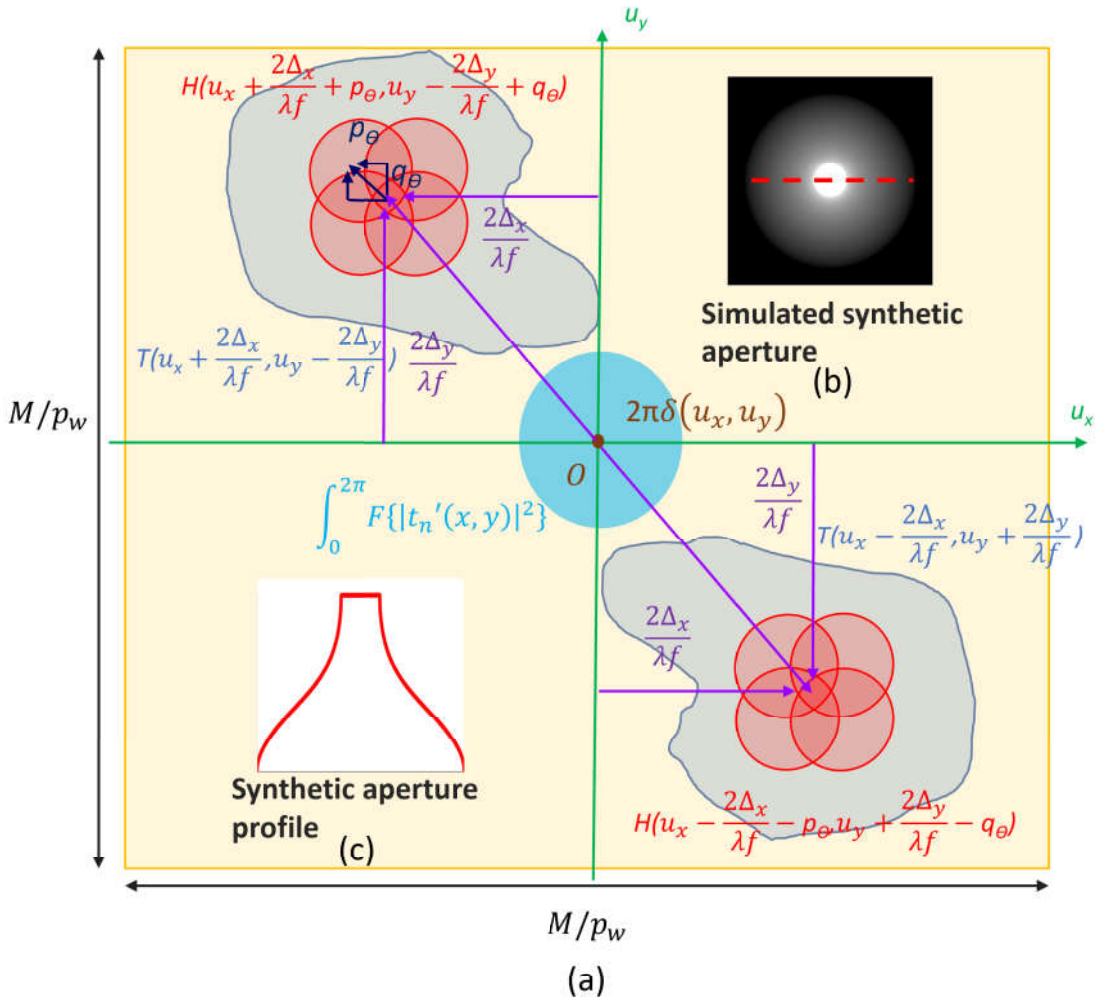

Figure 4.3: **(a)** Illustration of $HOL(u_x, u_y)$ in Equation 4.28 in the spatial-frequency domain. The yellow bounded area represents the spatial frequency support of the detector where M denotes the magnification of the microscope and p_w is the pixel pitch; the blue area in the centre (and the delta function within) represents the DC terms corresponding to the first two terms in Equation 4.28, and the twin images are separated due to the off-axis angle between the reference and object wavefields. The red circles represent the pupil function of the system, H_θ, at four instances of time corresponding to four angles θ similar to the case illustrated in Fig. 4.2. Actually, due to scanning of the annulus over a continuous 2π angle, the pupil function moves continuously and the superposition of these pupils within the acquisition time of the camera produces the SA function defined in Equation 4.29, which is illustrated in **(b)** and the profile of this is illustrated in **(c)**.

must be scaled accordingly. The maximum support that can be achieved is $4NA/\lambda$, for the case that the scanning circle is just inside of the pupil function. Knowledge of the shape of SA permits the reconstruction process to be augmented with deconvolution, as discussed in the next section. It should be noted that the off-axis condition outlined in this paragraph is more strict than for the traditional case of coherent DHM, for which the twin image terms have smaller support.

4.5 Deconvolution for real-time SA DHM

The description of deconvolution presented in this section is based on the example presented in Fig. 4.4. Two holograms of the same diatom specimen are shown in Fig. 4.4(a) and (b); Fig. 4.4(a) is the result of recording using a single coherent point source in the filter plane. The annular filter was designed with a small $15\mu m$ pinhole in the centre of the annulus, which facilitates the X-module to implement an in-line self-reference coherent imaging mode, similar to other designs. [266] The resulting hologram is equivalent to classical DHM using a coherent laser source. [12, 13] The corresponding real-time SA hologram is shown in Fig. 4.4(b). The coherent noise has clearly been reduced in this case due to the effective incoherence afforded by real-time SA-DHM, and this is further evidenced by examining the magnified region shown in the bottom left of each image; since the coherent point source is circularly scanned over the acquisition time of the camera, the effect is the same as if a temporally incoherent source fully illuminated the same circle simultaneously. A simpler interpretation is that the coherent noise resulting from each instantaneous position of the point source is independent and therefore averages away in the superposition. Notably, although the coherent noise is reduced, the contrast of the fringe pattern has not been reduced; this contrast will depend on the values of ϕ_θ in Equation 4.29. If ϕ_θ varies by a large amount over θ, the instantaneous fringe patterns (resulting from an instantaneous position of the point source) will move in phase and the contrast of the superposition of these fringe patterns will reduce. Variation in ϕ_θ can be reduced by small adjustment of mirrors M4 and/or M6.

In Fig. 4.4(c) and (d) the DFTs of both holograms are shown; for both cases the twin images are clearly separated from the DC terms and the real image can be isolated (blue squares), which are shown in Fig. 4.4(e) and (f). It is clear that the real image term for the case of real-time SA-DHM in Fig. 4.4(f) contains more high frequency content compared with the twin image in Fig. 4.4(e) owing to the larger support of SA compared with H. In the previous section, it was shown how SA could be estimated based on the value of R, NA, and λ. It is also possible to experimentally determine the shape of SA with high accuracy. Close inspection of the twin image for the coherent DHM case shown in Fig. 4.4(e) reveals a small ring of speckles as highlighted and expanded in the yellow box in the figure. This is weak scattering from the annular filter, and therefore the radius R can be experimentally determined. Similarly the radius of H, can also be determined by using a log scale for the twin image Fig. 4.4(e), which clearly reveals the pupil function. Taking the measured radius of H and R to be r_H and

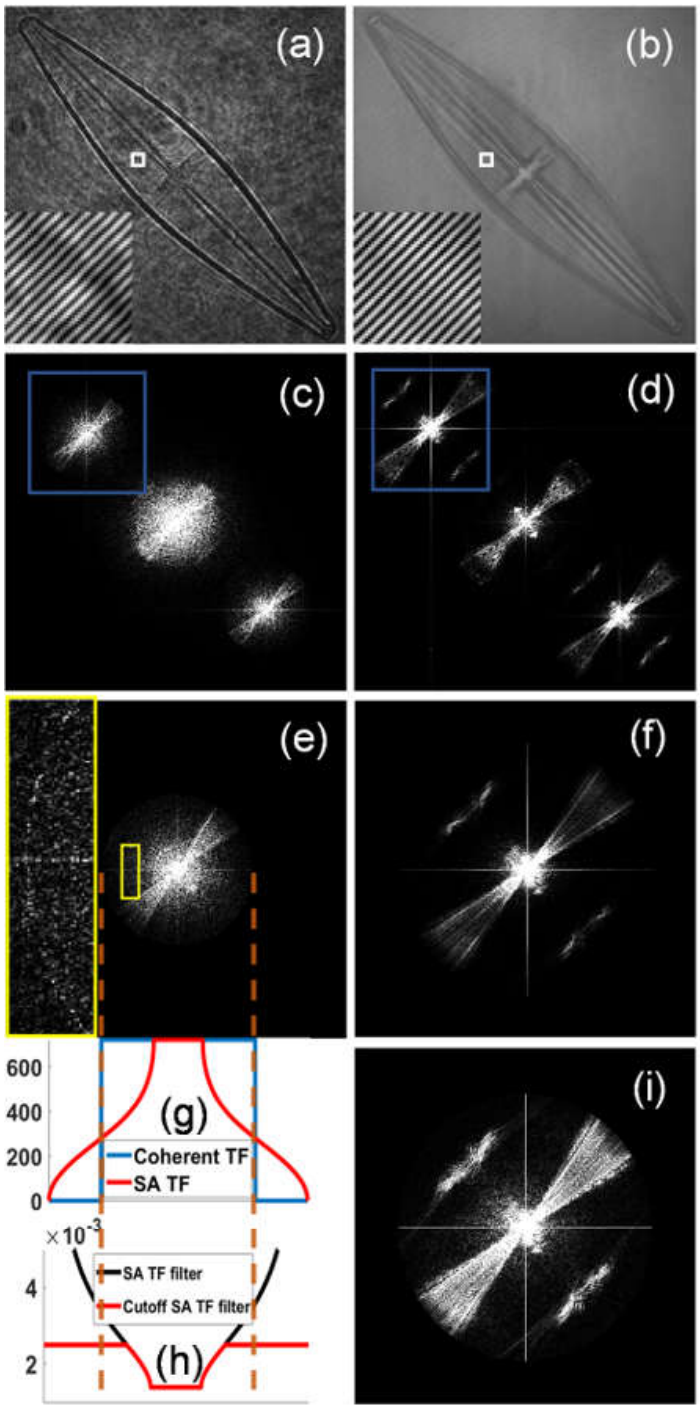

Figure 4.4: Results for a diatom cell that highlight the process of deconvolution. **(a)** Coherent hologram with inset showing enlarged area of interference pattern; **(b)** SA hologram with similar inset; **(c)** and **(d)** are the DFTs of the holograms in **(a)** and **(b)**, respectively; the twin image in the blue box in both images is enlarged in **(e)** and **(f)**. The yellow box in **(e)** highlights a partial weak image of the annulus, as a result of the weak light passing the hollow annular area in the filter when imaging for the coherent case; **(g)** the profiles of the transfer function for the case of coherent and SA-DHM. The SA profile has been calculated using the radius of the arc in **(e)**; **(h)** The profile of the deconvolution filter used in SA-DHM. The actual filter is shown in red: a threshold is applied to limit the value of $1/SA$ shown in black to avoid the amplification of noise; **(i)** The result of applying this filter to the twin image term in **(f)**.

r_R samples, it is straightforward to compute a numerical representation of SA with the same sampling interval; the profile of SA is shown in Fig. 4.4(g) overlaid with the profile of H. The larger support of the synthetic aperture (radius $r_{SA} = r_H + r_R$) is evident in this figure. In our setup, NA=0.85, r_H=214 samples, r_{SA} = 360 samples corresponding to a numerical aperture of 1.43.

Deconvolution is achieved by multiplying the twin image term in Fig. 4.4(f) by the inverse of the transfer function, $1/SA$. The profile of this function is illustrated by the black line in Fig. 4.4(h). In order to avoid the amplification of noise in higher frequency regions, the maximum value of $1/SA$ is capped and the resultant profile is shown in red in Fig. 4.4(h). The resultant twin image term is shown in Fig. 4.4(i), in which it can be seen that the higher frequency content has been amplified when compared with Fig. 4.4(f). This simple approach of estimating SA and thresholding its inverse provides excellent results and we have found it to be preferable to using a regularisation parameter based on signal to noise ratio as used in other methods such as Weiner deconvolution.

4.6 Sample Preparation

Amphipleura pellucida diatom cells were obtained pre-mounted (Brunel Microscopes Ltd, UK). These cells are mounted on a glass slide with a standard coverslip. The mounting medium is Naphrax with a refractive index of 1.73.

A buccal epithelial cell was collected from the cheek of a healthy adult volunteer onto a glass coverslip. This was mounted onto a standard glass slide with a water medium and using parafilm as a spacer.

HeLa cells were cultured in DMEM media (Sigma-Aldrich) supplemented with 5% fetal bovine serum. Flasks were maintained in a humidified environment at 37 °C and 5% CO_2. When the cells reached 90% confluency, the culture media was removed and the cells were washed with sterile PBS. Trypsin-EDTA solution (0.25%) was added and the cells were incubated at 37 °C for 5 min until the cells detached. DMEM media was added to the flask to neutralise the trypsin, and the entire contents were transferred to a sterile falcon tube. The cells were centrifuged for 5 min at 1500 rpm. The supernatant was removed, and the cell pellet was resuspended in fresh DMEM media. The cells were counted, using a haemocytometer. After counting the cells, the cells were seeded at 1×10^5 cells/mL onto a coverslip in a 12-well cell tissue plate. The next day, when the cells had reached 70% confluency the coverslip was removed, washed with PBS, and formalin fixed. The coverslip was mounted on a glass slide using an aqueous mounting medium.

4.7 Results

The reconstructions relating to the holograms of the diatom cell presented in Fig. 4.4 are shown in Fig. 4.5. Fig. 4.5(a), (b), and (c) are the phase images reconstructed from the coherent hologram, the real-time SA hologram, and the deconvolved SA hologram.

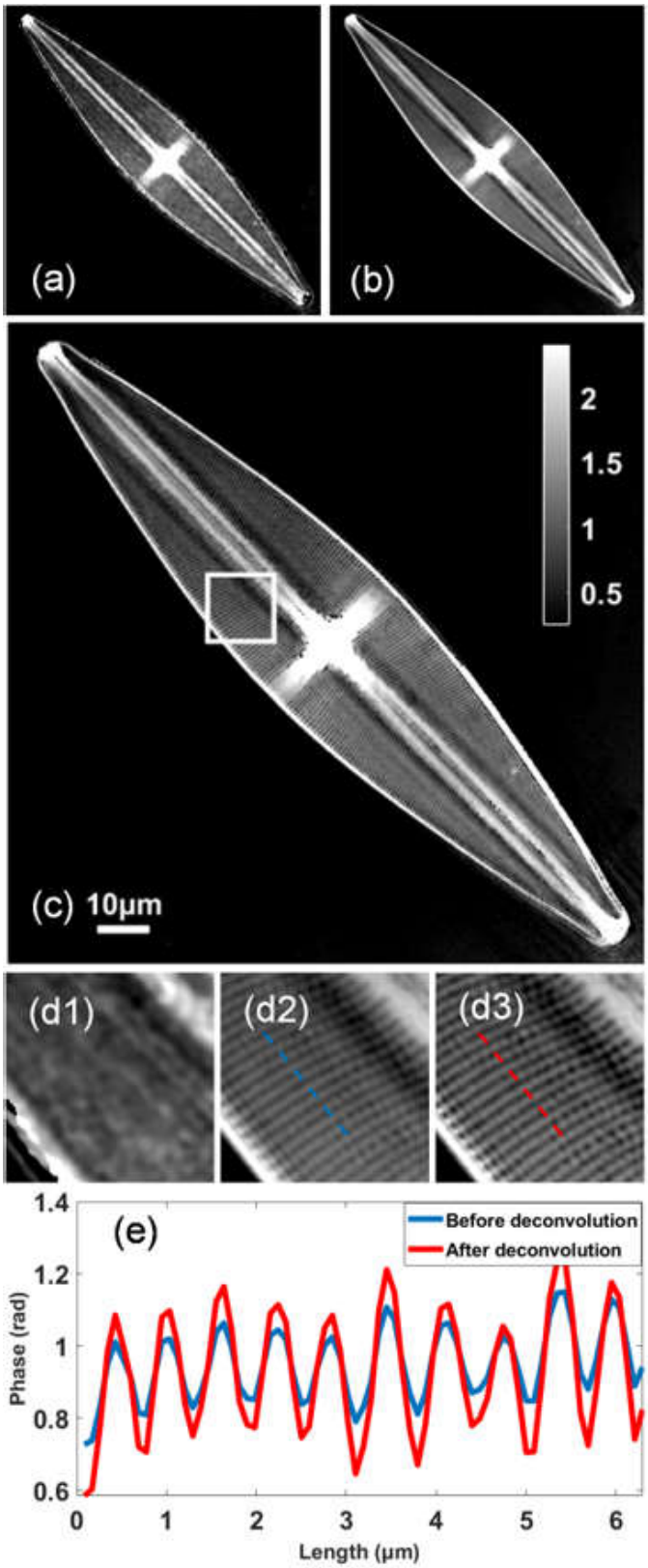

Figure 4.5: Phase image of diatom cell recorded by SA-DHM; **(a)** Phase image recorded using coherent DHM; **(b)** Phase image recorded using SA-DHM; **(c)** The SA-DHM phase image following deconvolution; The area highlighted in the white box is magnified in **(d1)-(d3)** corresponding to images **(a)(b)** and **(c)**, respectively; **(e)** The phase profiles of the line shown in **(d2)(d3)**, before and after deconvolution.

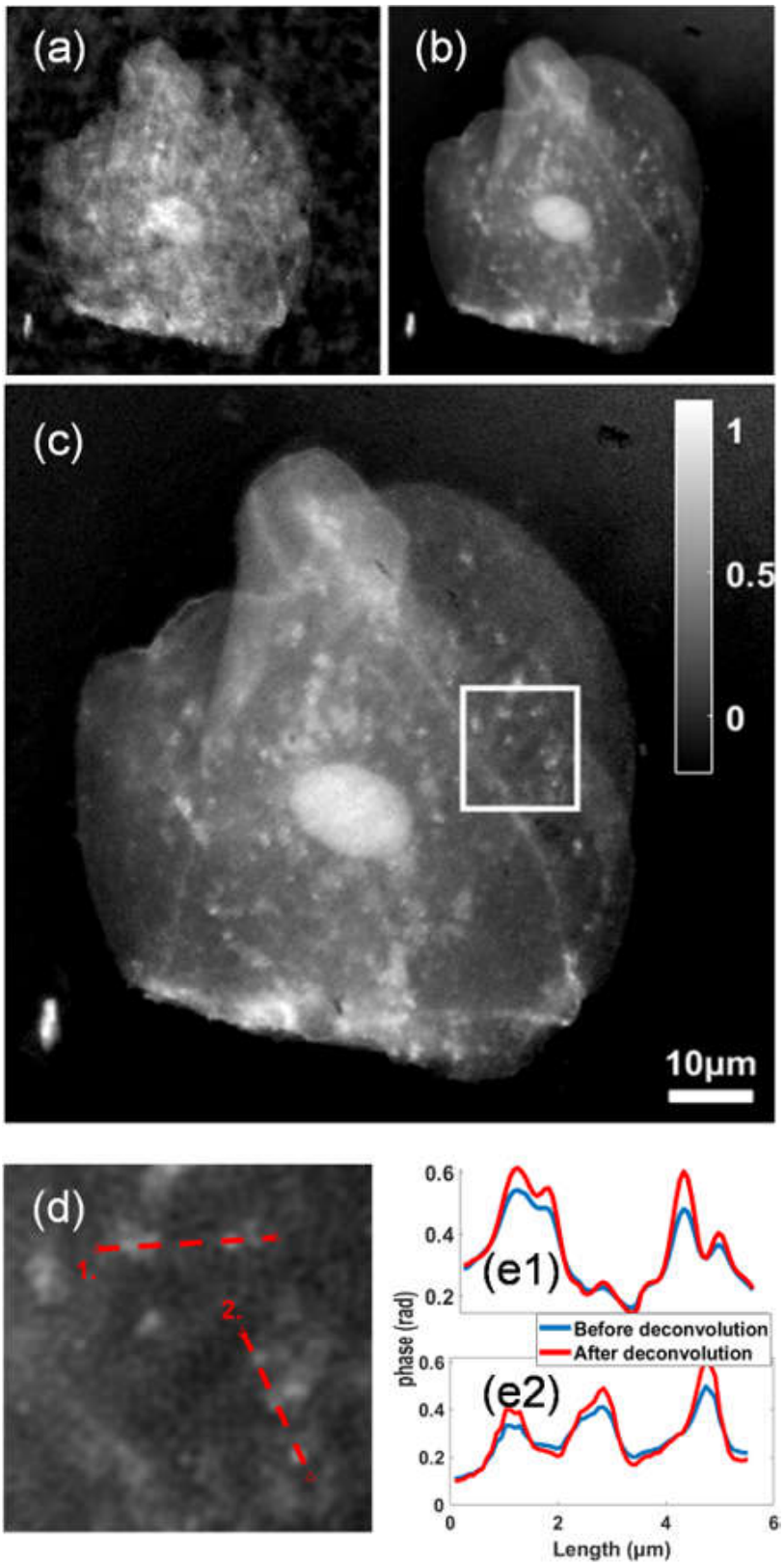

Figure 4.6: Phase image of buccal epithelial cell using the SA-DHM setup. **(a)** Phase image recorded using coherent DHM; **(b)** Phase image recorded using SA-DHM; **(c)** The same phase image following deconvolution; **(d)** The enlarged area from the white rectangular area in **(c)**; **(e1)** The phase profiles from line 1 shown in (d), before and after deconvolution. **(e2)** The phase profile from line 2 shown in (d), before and after deconvolution.

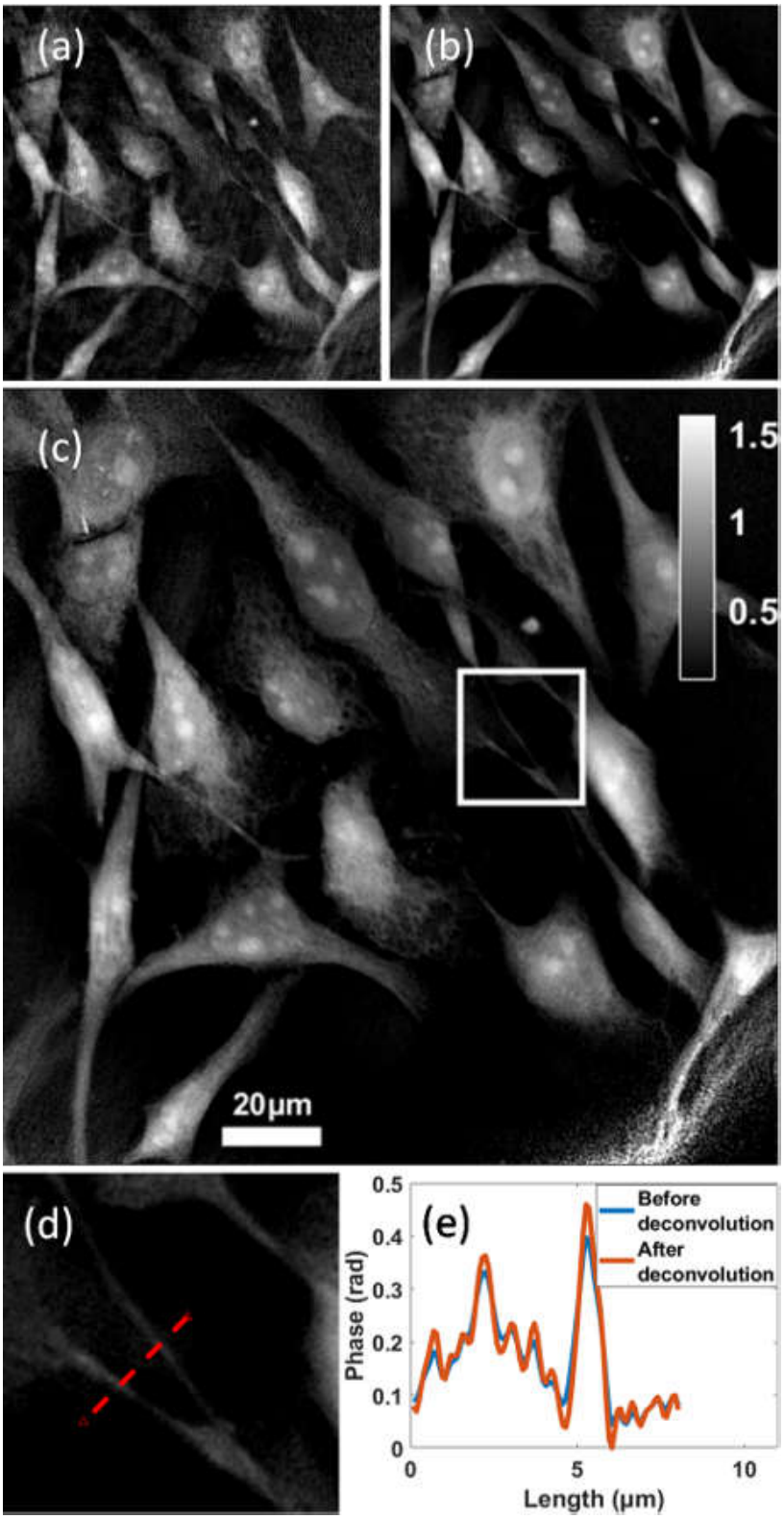

Figure 4.7: The set of phase images of HeLa cells recorded by our SA-DHM setup. **(a)** Coherent phase image; **(b)** SA phase image without using transfer function correction filter; **(c)** SA phase image after using cutoff value transfer function correction filter; **(d)** The enlarged area from the white rectangular area in **(c)**; **(e)** The phase profiles of the line shown in **(d)**, before and after deconvolution.

These images are obtained by applying an inverse DFT to the images shown in Fig. 4.4(e), (f), and (i), respectively. A small region is of the diatom is expanded for all three images as shown Fig. 4.5(d1), (d2), and (d3). The grating like structure of the diatom cell is completely lost for the case of coherent DHM, for which case the numerical aperture is not large enough to capture this spatial frequency. This feature is recovered in real-time SA DHM for which case the enlarged synthetic aperture is now large enough to capture it. The contrast of the structure is clearly enhanced after deconvolution. The profile of this feature before and after deconvolution is shown in Fig. 4.5(e) as further evidence of the improved contrast afforded by deconvolution for high frequency content in the image.

A buccal epithelial cell phase image is shown in Fig. 4.6. Fig. 4.6(a), (b), and (c) are, respectively, the phase images reconstructed from the coherent hologram, the real-time SA-hologram, and the deconvolved SA-hologram. A small region is highlighted in this figure and shown in Fig. 4.6(d). The phase profiles from two lines in this figure are shown in Fig. 4.6(e1) and (e2) before and after deconvolution. It is clear that the contrast of small features in the phase image have been enhanced following deconvolution.

Phase images of fixed HeLa cells are shown in Fig. 4.7. Fig. 4.7(a), (b), and (c) are, respectively, the phase images reconstructed from the coherent hologram, the real-time SA-hologram, and the deconvolved SA-hologram. A small region is highlighted in this figure and shown in Fig. 4.7(d). The phase profiles from the line in this figure is shown in Fig. 4.7(e) before and after deconvolution processing. Once again it is clear that the contrast of small features in the phase image have been enhanced following deconvolution.

In all three results shown in this section, it is clear that there is a marked improvement in the image quality when comparing the coherent hologram to the real-time SA-DHM case. Further, there is a clear enhancement in the contrast of small features in the phase image when comparing the result of real-time SA-DHM case before and after deconvolution.

Noted that limited by the length of each page, The reconstructed phase images from the coherent hologram, the real-time SA hologram, and the deconvolved SA hologram for all investigated cells (e.g. Fig. 4.5(a), (b), and (c)) cannot compare with the same size in this chapter. These reconstructed phase images from different holographic recording modes will be illustrated in the **Appendix A** to provide the same size for comparison.

4.8 Discussion and Conclusion

In this chapter, a real-time synthetic aperture DHM system has been presented. A modular approach is taken such that an illumination module and capture module can be easily attached to the condenser lens and output image port of an existing life science microscope; the illumination module comprises of a galvo-scanning laser, and the capture module is 4-f imaging system containing two beamsplitters and a cus-

tomised spatial filter for a self-referencing. The narrow annular filter matches the annular scan of the focused laser in the filter plane of the condenser. A mathematical model of the system is proposed, which predicts the improvement in coherent noise and the shape of the real-time synthetic aperture transfer function, which can be accurately measured by recording a single coherent hologram (see Fig. 4.4 and analysing the pattern in the DFT); the transfer function is used to design a simple single step non-blind deconvolution that can be included in the real-time numerical reconstruction of the image. Several images of biological cell samples clearly demonstrate the improved noise and frequency response of the system when compared with traditional coherent DHM. The resolution improvement provided by the synthetic aperture relates to the numerical aperture of annular scan in the filter plane. The maximal achievable improvement in resolution is given by a factor of two when compared with coherent DHM; however, this requires a condenser with numerical aperture equal to that of microscope objective. The overall illumination and capture system is relatively inexpensive with a total cost of approximately €10,000.

Although an extensive literature review has been provided in Section 4.2, there are two reports in the literature that are not classified as synthetic aperture methods, but which are particularly relevant to the present discussion. The first relates to a single capture implementation of Spatial Light Interference Microscopy, [270] which uses a grating at the output port of the microscope to generate a common-path white light interferometer employing an annular filter at the zeroth diffraction order that matches an annular filter. Like the real-time SA-DHM method proposed here, instantaneous-SLIM employs an annular pattern in the filter plane of the condenser and a matching annular filter to generate a reference wavefield. The second is the Coherence-controlled holographic microscope (CCHM), [271] which is also based on white-light interference; in this case two separate paths are generated for the object and reference wavefields beginning at the lamp. One path passes through the traditional microscope containing the sample, while the second passes through and identical microscope to generate the coherently matched reference wavefield. In terms of numerical aperture and resolution, instantaneous-SLIM, CCHM, and the real-time SA-DHM method proposed here are all equivalent. Both instantaneous-SLIM and CCHM have the advantage of using white light, providing lower temporal coherence, and therefore low background noise. They both also have the advantage of being instantaneous, unlike our method, which is limited by the necessity to complete an annular scan of the laser inside the acquisition time of the camera. However, instantaneous-SLIM uses annular filters that are significantly larger (in terms of annulus width) than the narrow filters employed in this work; our annulus thickness relates to the size of a focused laser spot, while SLIM uses filters that can pass enough white light from the illumination lamp for imaging. The result is that SLIM is disadvantaged by the Halo effect, [206] a deleterious effect that produced erroneous phase values, whereas real time SA-DHM suffers no such limitation. CCHM has the disadvantage of requiring very accurate and alignment and the need for a second microscope, with condenser, MO, and tube lens all matching the first microscope, which adds both expense and size to the implementation.

We believe the high phase accuracy, low noise, low cost of the real-time SA-DHM

method and its simple modular nature, facilitating the addition to any existing microscope will make it practically useful in life-science laboratories. In the next chapter, we demonstrate how the X-module can be adapted to implement optical diffraction tomography. This adaptation involves only a change in the filter used within the module and a different illumination and alignment protocol. The mathematical formulation developed in this chapter is the foundation for the next chapter. Indeed such are the close similarities between the ODT module in the next chapter and the X-module presented here, we demonstrate that the ODT module can also record the SA-DHM single capture hologram as well.

Chapter 5

Optical Diffraction Tomography using an Inexpensive Module

The work in this chapter has been prepared for submission to a journal: Z. Tang, and B.M. Hennelly, "Optical Diffraction Tomography using an Inexpensive Module", To be submitted to Optics Letters with the abstract reproduced below:

We develop an inexpensive modular approach to optical diffraction tomography comprising an illumination module based on Galvo-mirrors and a capture module that employs the principle of self-reference off-axis holography. Both modules can be attached to a life-science microscope using an automated alignment protocol. Our design has a number of benefits over existing approaches, including the additional capability for real-time synthetic aperture digital holographic microscopy. Experimental results are provided using a kidney cancer cell line.

5.1 Introduction

Optical diffraction tomography (ODT) is a label-free microscopic imaging method that enables visualisation of the three-dimensional (3D) refractive index (RI) variation within a sample. We refer the reader to Chapter 2 Section 2.3 for a review of the background theory of ODT. ODT shares some similarities with Synthetic-Aperture Digital Holographic Microscopy (SA-DHM), discussed in the previous chapter, in that they both require a series of holograms to be recorded over a range of oblique illuminations; while SA-DHM simply stitches the frequency bands together to form a synthetic aperture, ODT is based on a complex reconstruction process that calculates the 3D scattering potential function. The underlying theory of ODT was first proposed by E. Wolf in 1969 [108] and since then various optical implementations and numerical reconstruction processes have been proposed. [272–274] There are two fundamental types of ODT systems: sample rotation ODT [125,134,135] and illumination scanning ODT [136–138, 275]; the former uses a sample rotation stage to adjust the angle of the sample relative to a fixed illumination angle and multiple projections are used to reconstruct the 3D

RI map. However, this approach suffers from slow acquisition time and alignment issues. Illumination scanning ODT is far more common and has recently been enhanced by numerical reconstruction methods that can mitigate the problem of the missing 'apple-core' in the 3D potential function using nonnegativity constraint optimisation methods [149,155] as discussed in Chapter 2 Section 2.3.7. Scanning illumination ODT has been demonstrated to be a powerful method for the investigation of biological cells and cellular dynamics. [119,120]

Various method of implementing scanning ODT have been proposed in the literature on the basis of interferometry and at this time at least two such methods are commercially available. On the illumination side, the oblique scanning illumination angle can be provided by Galvo-mirrors, [119,120,131,259] a spatial light modulator or digital micro-mirror device, [116,117,150] or a rotating mirror system. [276] Most implementations make use of a single laser source that is split into object and reference paths before being recombined at the camera. Typically the reference wave is incident on the camera at a fixed off-axis angle, which separates the complex twin images in Fourier space; each captured aperture can be filtered from the Fourier domain via a discrete Fourier transform (DFT) operation and mapped onto 3D Fourier space for tomographic reconstruction. Recently, a number of self-reference methods have been proposed by the Park group, whereby the object wavefield can be used to generate a reference wavefield just before the camera. This type of approach is more easily attached as an add-on to an existing microscope. In Ref. 137, a Ronchon polarizer is positioned just before the camera, which generates two copies of the object wave with one at an off-axis angle. While simple, this method requires that the object field be sparse in the area of overlap. In Ref. 119,120,131,259, an implementation is proposed that overcomes this limitation; once again the object wavefield is used to generate the reference wavefield but in this case a diffraction grating produces a copy of the object wave which is then filtered by a pinhole in order to generate a plane wave reference. While powerful, this method suffers from a large form factor requiring a $12-f$ imaging system before the camera. Furthermore, a second 2D Galvo-mirrors is required at the capture side in order to redirect the zero frequency through a single static pinhole filter as the illumination angle changes.

In this chapter, we propose a self-reference module similar to that proposed in Chapter 4 that is significantly smaller in size and cost when compared with Ref. 120. Furthermore, the module can easily be adapted to record a real-time SA-DHM. No previous implementation of ODT has been able to merge these modalities.

5.2 Structure of ODT setup

The structure of the proposed self-reference ODT setup is shown in Fig. 5.1 and is divided into three parts: an illumination module, a microscope, and a capture module. This modular approach is made possible by the self-reference design, which facilities decoupling of the illumination and capture modules. The ability to attach these relatively low-cost modules to any existing life-science microscope is an important feature

of the design.

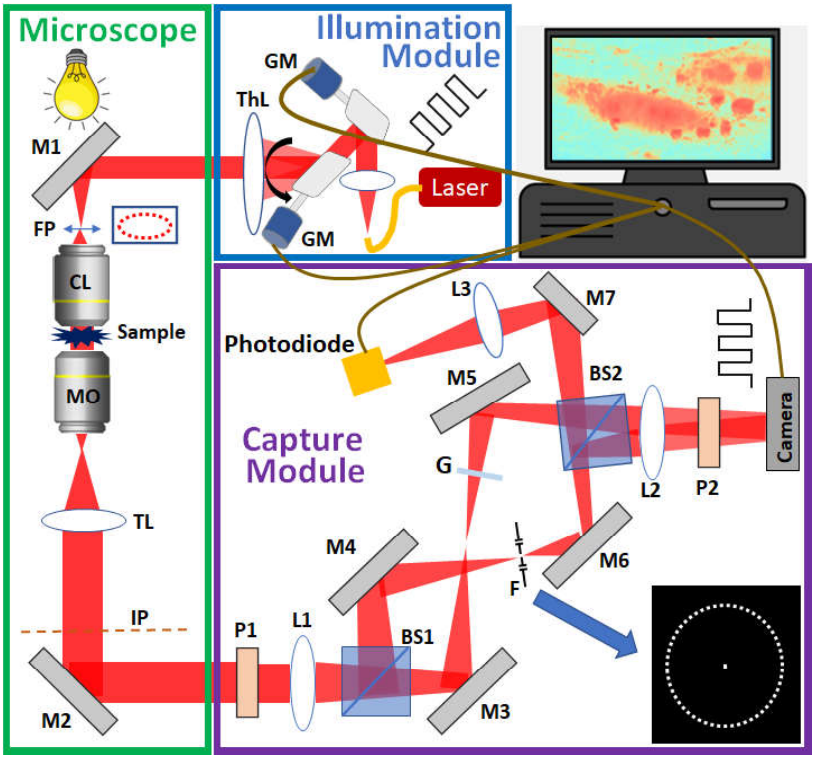

Figure 5.1: The structure of our self-reference ODT setup that includes an illumination module, a microscopy and a capture module: GM, Galvo-mirrors; ThL, theta lens; F, filter plane; CL, condenser lens; MO, microscope objective; TL, Tube lens; IP, image plane; M, mirror; L, lens; BS, beamsplitter; F, annular-pinholes filter; G, transparent glass that has the same thickness with the pinholes filter; P, polarizer.

The illumination module uses a low cost 635 nm, 2 mW laser diode source with single mode fiber output (Thorlabs; HLS635); the output of the fiber (Thorlabs; SM600) is collimated using a plano-convex lens (Thorlabs; LA1131-A) with focal length 5 cm. The resultant beam is input to a two-dimensional Galvonometer scanning system (Thorlabs GVS012) with repeatability 15 μrad, which comprises of two voltage controlled Galvo-mirrors and a servo driver board. This board is driven by the analog output of a digital acquisition (DAQ) card (National Instruments Corp; USB-6003); the card acts as a digital-to-analog converter that is controlled by Labview Software. This system steers the beam to an F-theta lens (Thorlabs FTH254-1064) with focal length 254 mm, which focuses the light to a spot at back focal plane of the microscope condenser lens, denoted in the figure as the filter plane (FP). The position of the spot is programmed to move to a sequence of 180 discrete positions in an annular pattern in the filter plane, which is discussed in further detail below.

A bespoke microscope is used with microscope objective (Olympus; MPlan 40x) with numerical aperture $NA_{MO} = 0.85$ and tube lens (Olympus; SWTLU-C, f=180mm). The condenser lens (Nikon; Plan Apo 20x, 0.75) is mounted on a manual translation stage (Thorlabs; MT1-M), which is adjusted to ensure Kohler illumination. The sample is mounted on an electronic translation stage (ASI; MS-2000, LX-4000) and the MO is also mounted on an electronic translation stage (ASI; MS-50, LX-4000) to facilitate

automated focusing. Both stages are controlled using the open-source Micro-Manager platform. [265]

The capture module is attached after the image plane of the microscope. This module is similar to the 'X-module' described in Chapter 4, with some small additions: the annular filter in the 'X-module' is replaced with a multi-pinhole filter and a photodiode is added to facilitate alignment of the Galvo-mirrors with respect to these pinholes. In summary, the capture module has a $4f$ imaging system mapping the image plane to the detector plane making use of two identical lenses (Thorlabs UK; LB4282, 200 mm focal length). A polarising beamsplitter immediately after the first lens splits the wavefield into an object and reference that cross each other via mirror pairs (M3,M4) and (M5,M6) before being recombined using a 50/50 broadband cube beamsplitter (Thorlabs UK; BS031). The mirror pairs are aligned to produce a matching overlapping image on the detector from both paths (in the absence of F), each with an angle of incidence on the detector that is equal and opposite; these angles combined provide the off-axis condition as described in more detail in Chapter 4 Section 4.3.4. Two rotatable linear polarisers, P1 and P2 (Edmund Optics UK; LPVISE200-A), at the input and output of the module enable independent control of the object and reference power on the monochrome digital camera (Thorlabs; CS895MU), which has 4096×2160 pixels of size 3.45×3.45 μm. The 180 focused laser spots in the FP are reproduced at the back focal plane of the first lens in the reference path where these are aligned with 180 pinholes on a customised filter, (JD-Photo, UK). This filter, F, is mounted on three-dimensional translation stage (Thorlabs UK; DT12XYZ/M) and is composed of a 25×25×3 mm glass plate with a chrome photo-mask of optical density > 3 produced using photo-lithography. The pinholes are located on a circle of 2.5 mm radius and have 15 μm diameter. The filter also includes a pinhole in the centre of the annulus to facilitate initial alignment. An identical piece of glass without photomask is inserted into the object path in order to maintain phase-matching between both paths. Following an alignment protocol, described below, the precise set of galvonometer voltages that align the laser focus with the 180 pinholes in the filter is obtained. The 180 holograms are recorded in sequence using a square-wave software trigger that steers the galvanometer to each pinhole, and synchronously controls the camera acquisition time to match the dwell time of the laser focus at each pinhole. The total time taken to record all holograms is 10s using an acquisition time of 40ms for each hologram. It's worthy to note that using a laser with higher power could greatly reduce this exposure time. The exposure time for recording each hologram is not linked to the number of pinholes. However, increasing the number of recorded holograms (more pinholes used) will lead to a longer total exposure time.

5.3 Image formation

The laser focus is moved in the filter plane to 180 discrete position in a circle around the origin, where each unique position denoted by index n is given by (p_n, q_n). The resulting oblique plane wave illumination in the sample plane is given by $\exp[jk(xp_n+yq_n)]$,

where $k = 2\pi/\lambda$, $p_n = NA_{ill}\cos[2\pi/(n-1)]$, $p_n = NA_{ill}\sin[2\pi/(n-1)]$, and NA_{ill} is the numerical aperture of the illumination that must satisfy $NA_{ill} \leq NA_{MO}$. The resulting complex image, $t'_n(x,y)$, in the image plane of the microscope has a Fourier transform, $T'_n(u_x,u_y)$, defined in Equation 5.1:

$$T'_n(u_x,u_y) = T(u_x - p_n, u_y - q_n)H(u_x,u_y) \tag{5.1}$$

where (x,y) and (u_x,u_y) denote the spatial and spatial frequency coordinates. $T(u_x,u_y)$ is the Fourier transform of the sample transmittance function, $t(x,y)$, and $H(u_x,u_y)$ is the transfer function of the microscope, which is defined as a pupil function of radius equal to NA_{MO}/λ, where λ is the laser wavelength. For each illumination n, the resulting object and reference wavefields in the detector plane are given by:

$$\begin{aligned} O_n(x,y) &= t'_n(x,y)\exp[jk(\alpha x + \beta y)] \\ R_n(x,y) &= \exp[jk(xp_n + yq_n) + j\phi_n]\exp[-jk(\alpha x + \beta y)] \end{aligned} \tag{5.2}$$

The reference wavefield is produced by filtering the unscattered field using a pinhole at position (p_n,q_n) on the filter plane. The off-axis angles of the object and reference are opposite and equal are related to α and β in the above expression. The phase term ϕ_n in the reference account for any small misalignment in the object and reference arms with respect to slight tilt of the filter or slight path length mismatch. The resulting hologram is given by:

$$\begin{aligned} hol_n(x,y) &= \left|t'_n(x,y)\right|^2 + 1 \\ &+ t'_n(x,y)\exp[j2k(\alpha x + \beta y)]\exp[-jk(xp_n + yq_n) - j\phi_n] \\ &+ \overline{t'_n(x,y)}\exp[-j2k(\alpha x + \beta y)]\exp[jk(xp_n + yq_n) + j\phi_n] \end{aligned} \tag{5.3}$$

which has a Fourier transform, HOL_n, given by:

$$\begin{aligned} HOL_n(u_x,u_y) = \mathscr{F}\{|t'_n(x,y)|^2\}(u_x,u_y) &+ \delta(u_x,u_y) \\ &+ \exp(-j\phi_n)T'_n(u_x + 2\alpha + p_n, u_y + 2\beta + q_n) \\ &+ \exp(j\phi_n)\overline{T'_n(u_x - 2\alpha - p_n, u_y - 2\beta - q_n)} \end{aligned} \tag{5.4}$$

where $\mathscr{F}$ is the Fourier transform operator. This equation can be rewritten in terms of the original transmittance as follows:

$$\begin{aligned} HOL_n(u_x,u_y) = \mathscr{F}\{|t'_n(x,y)|^2\}(u_x,u_y) &+ \delta(u_x,u_y) \\ &+ \exp(-j\phi_n)T(u_x + 2\alpha, u_y + 2\beta) \\ &\times H(u_x + 2\alpha + p_n, u_y + 2\beta + q_n) \\ &+ \exp(j\phi_n)\overline{T(u_x - 2\alpha, u_y - 2\beta)} \\ &\times \overline{H_n(u_x - 2\alpha - p_n, u_y - 2\beta - q_n)} \end{aligned} \tag{5.5}$$

Interestingly the position of T in this expression remains constant regardless of the illumination index n, which is the basis of real time SA-DHM in Chapter 4; see Equations

4.13 and 4.14. This is a unique feature of our ODT implementation when compared with other systems.

5.4 Alignment protocol

The initial alignment is based on steering the galvo-scanner to focus at the centre of the filter plane, FP. In the absence of any filter or glass plate in the capture module, the mirrors are adjusted to produce an aligned image of an arbitrary sample in the detector plane for both paths. Maintaining image alignment for both paths, the mirrors are further adjusted to produce an in-line interference pattern, i.e. both paths are co-linear. Using both pairs of mirrors (M3,M5) and (M4,M6) the object and reference paths are 'walked' (in the context of 'walking the beam') to produce equal and opposite off-axis angles, always maintaining image alignment, such that a suitable off-axis condition is satisfied. The filter, F, and glass plate, G, are added to the capture module, and the former undergoes 3-D translation/tilt to optimise light transfer through the centre pinhole.

The second step in alignment is to determine the 180 discrete voltage pairs to be applied to the two Galvo-mirrors in order to achieve optimal light transfer through the 180 annular pinholes. This is achieved by raster-scanning in the approximate region of each pinhole (the approximate region being determined by geometry) and recording the intensity of the throughput using a photodiode; the maximal intensity recorded by photodiode corresponds to the optimum steer angle. This entire process is automated by synchronously controlling the Galvo-mirrors and reading the output from the photodiode using the DAQ and takes approximately 5 minutes. This second step must be undertaken frequently depending on vibrations; for our system it was sufficient to perform this daily.

5.5 Methods of numerically tomographic reconstruction

This description in this section is based on an existing understanding on the Rytov approximation, the three-dimensional scattering potential, and the nonnegativity constraint to recover the missing core problem. We refer the reader to Sections 2.3.5-2.3.7 for an overview of these topics. The *first step* in reconstruction is to compute the complex images for each projection by filtering the twin image term in the DFT of each hologram as described in Chapter 4 Section 4.4.2.2. Four such filter twin image terms are shown in Fig. 5.2(a1-a4) for a sample described later in the text. The *second step* is to reconstruct the 3D spectrum of the scattering potential function, $F(u_x, u_y, u_z)$, by superimposing the 180 DFTs of the complex images each of which is mapped onto an Ewald sphere in 3D Fourier space. More specifically, we use the Rytov approximation to produce 180 Rytov phase terms: $\Psi_n(x,y) = \ln[t'_n(x,y)/t_{n_0}(x,y)]$ where t_{n_0} is the background complex image recorded using no sample. These are then mapped to the Ewald sphere as follows: $F_n(u_x, u_y, u_z) = -\frac{j(u_z+u_0 m_0)}{\pi}\mathcal{F}\{\Psi_n(x,y)\}$, which are superpositioned to produce F; the result of this process is shown in Fig. 5.2(b). Typically in

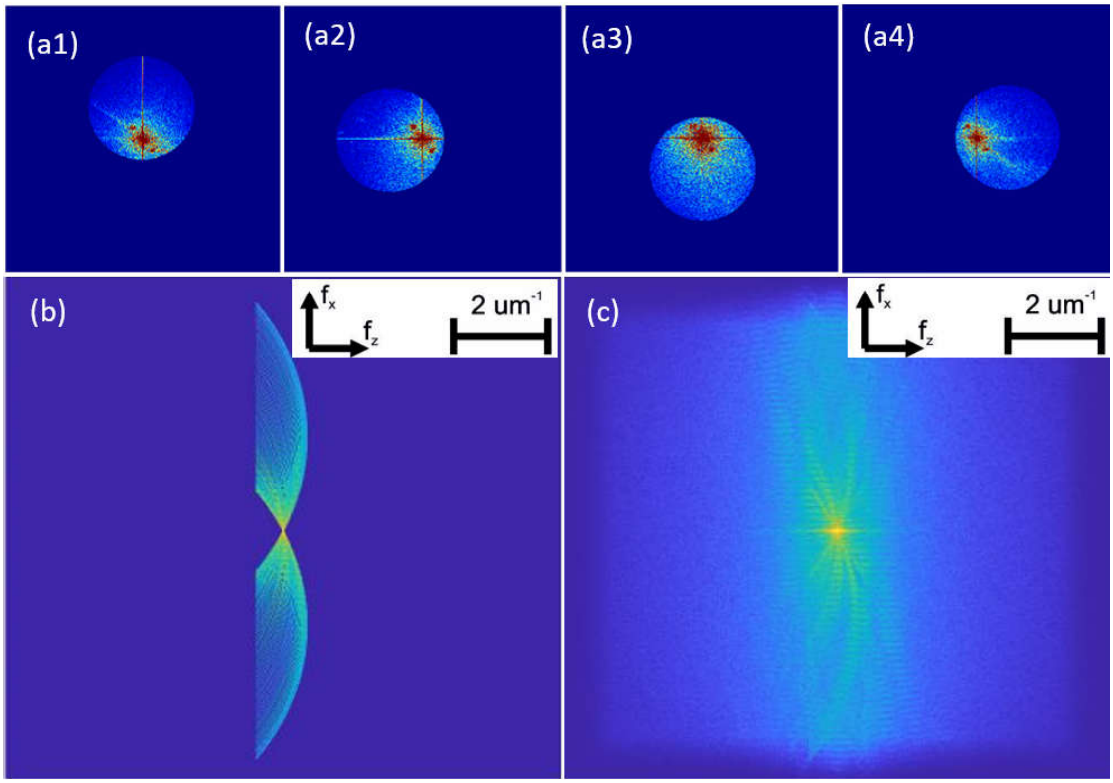

Figure 5.2: (a1-a4). Four apertures of T captured using the module. Note that the apertures, H_n, move in position in the DFT as a consequence of the self-reference design such that the zero-frequencies are co-located; (b) The four spectra and 176 others are projected on the Ewald sphere in 3D Fourier space to produce F; (c) The missing values are filled in by Nonnegative constraint optimization procedure that is introduced in Section 2.3.7.

ODT, the division of t_{n_0} will reposition the twin images in 2D Fourier space such that the zero frequencies are co-aligned for all cases. In our implementation this repositioning is achieved optically as a natural consequence of the self-reference design in which the reference angle changes synchronously with the illumination angle as shown for four cases in Fig. 5.2(a1-a4). Phase matching of each of the DFTs is also required, $\mathscr{F}\{\Psi_n\}$, [269] such that the zero frequency components have the same phase value; this is due to small path length differences, i.e ϕ_n is not constant.

Due to the limited illumination angle and numerical aperture there are large areas in F with missing information. The *third step* is to employ an iterative non-negativity constraint algorithm, known as the total variation iterative constraint Gerchberg- Papoulis (TVIP-GP) algorithm to fill in the missing information. The TVIC algorithm [149] is a minimisation algorithm that is first applied to F, to generate a binary mask, M, that defines the spatial support of the specimen, which is then passed to the GP algorithm. The GP algorithm is based on four iteratively repeated steps where: [155, 156]

(1) $\tilde{F_i'} = (1-\beta_i\Omega)\tilde{F}_{i-1} + \beta_i\Omega\tilde{F_0}$

(2) $f_i = \mathscr{F}^{-1}(\tilde{F_i'})$

(3) $f_i' = g^{-1}(P_{\beta_i}P_+\mathscr{R}\{g(f_i)\})$

(4) $\tilde{F_i} = \mathscr{F}(F_i')$

where $\tilde{F_0} = F$ and $\tilde{F_i}$ represents the recovered spectrum of the scattering potential function from the ith iteration. Ω is a 3D binary mask to distinguish the known region relating to the mapping of Rytov phase values; β_i is a relaxation parameter (with initial value of 1) that is gradually reduced during iterations according to ($\beta_i = 0.99\beta_{i-1}$); g is a function to recover the complex refractive index of the sample by subtracting the refractive index of the surrounding immersion medium and has inverse g^{-1}. $\mathscr{R}$ is an operator to extract the real part of the complex function; P_+ is an operator to apply the nonnegative constraint and P_{β_i} is an operator to multiply a coefficient of $1-\beta_i$ to the padded regions in order to suppress oversampling. We applied 200 iterations of the GP algorithm to generate the tomographic reconstruction presented in this paper and the final result, $\tilde{F_{200}}$ is shown in Fig. 5.2(c) for the sample described below.

5.6 Results

HEK cells from kidney cancer cell line are chosen as sample used in this tomographic experiment. These HEK cells were grown on coverslip and mounted on glass slide using FluorSave Reagent ($n_m = 1.36$). In total, 180 holograms were recorded using the module in approximately 10 seconds, and the reconstructed spectrum of the scattering potential function is shown in Fig. 5.2(c).

From this, two x-y slices of the refractive index volume are extracted and shown in Fig. 5.3(a1) and (b1) with one slice centered in the cell nuclei and the other 2.95 μm below. The same region in both images, highlighted by the white box, is magnified in

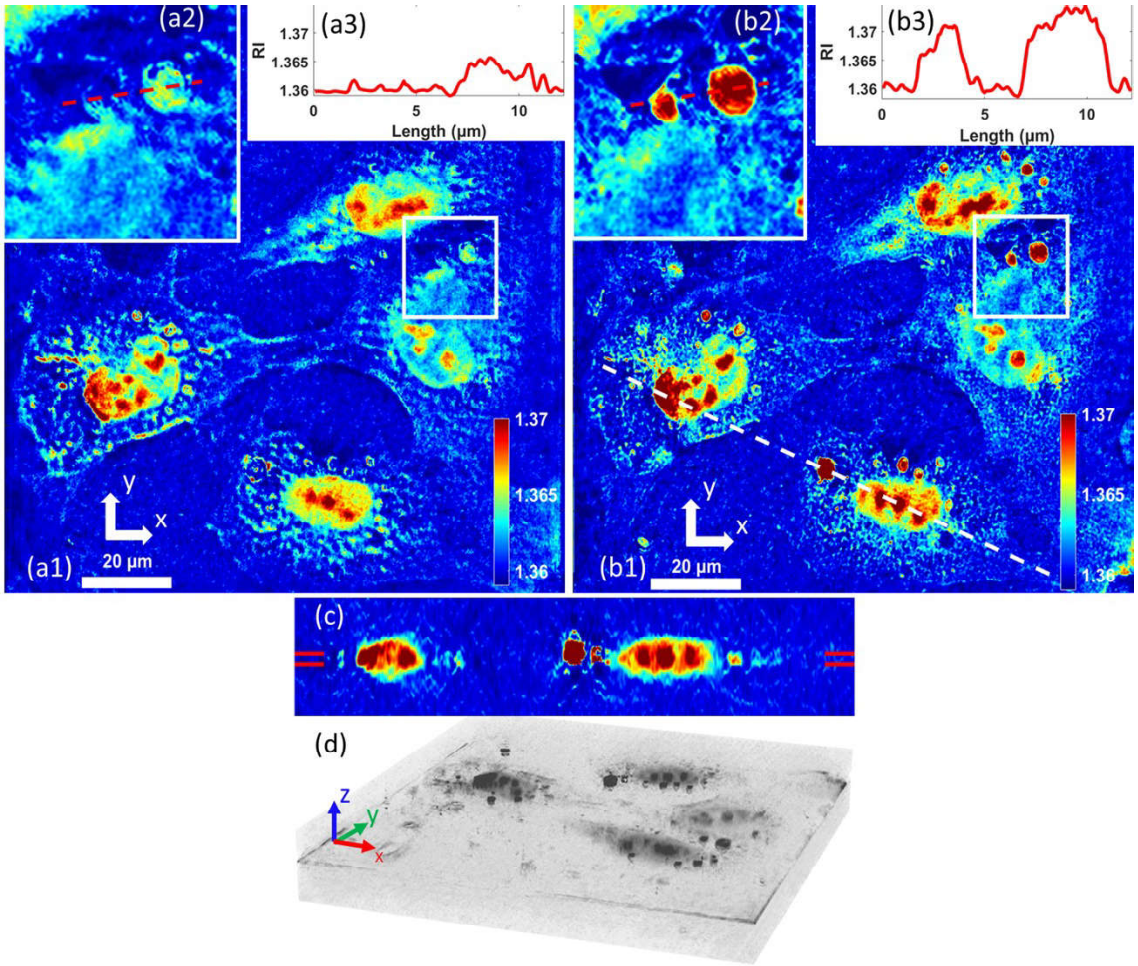

Figure 5.3: Tomographic reconstruction of cells; see text for details.

Fig. 5.3(a2) and (b2) for comparison, in which it can be seen that there exist a number of small features, possibly lipid droplet formations, that are spatially resolved in the z direction. This is further emphasised using the profile of the refractive index across these feature shown in Fig. 5.3(a3) and (b3). A vertical z slice through the white dashed line shown in Fig. 5.3(b1), which cuts through two cell nuclei, is shown in Fig. 5.3(c); sub-cellular features are clearly resolved in the z direction. A point-cloud tomographic reconstruction is provided in Fig. 5.3(d).

5.7 Real-time Synthetic Aperture Digital Holographic Microscopy

An important feature of the proposed module is that it can be used to implement a second modality, that of real-time SA-DHM, previously developed in Chapter 4, by extending the acquisition time of the camera to equal the time for each point source to move over all pinhole positions $n : 1 \rightarrow M$, where in our case $M = 180$ and recording a superposition hologram, which is the average of all of the individual holograms recorded from previous ODT collection. This is similar to the system described in Chapter 4 except in that case continuous scanning of the laser focus was filtered using a continuous narrow annular filter in lieu of the pinhole filters used in this paper. Here, the acquisition time for the SA-DHM modality will be practically limited by the speed of the Galvo-scanner to steer the laser focus to each pinhole position and remain there for some short time. In this case, the single-capture SA-DHM hologram is given by:

$$\begin{aligned} Hol(u_x,u_y) &= \sum_{n=1}^{M} Hol_n(u_x,u_y) \\ &= M\delta(u_x,u_y) + \sum_{n=1}^{M} \mathscr{F}\{|t'_n(x,y)|^2\}(u_x,u_y) \\ &+ T(u_x+2\alpha,u_y+2\beta)SA(u_x,u_y) \\ &+ \overline{T(u_x-2\alpha,u_y-2\beta)SA(u_x,u_y)} \end{aligned} \tag{5.6}$$

where,

$$SA(u_x,u_y) = \sum_{n=1}^{M} \exp(-j\phi_n) H(u_x+2\alpha+p_n, u_y+2\beta+q_n) \tag{5.7}$$

The support of SA is given by $(NA_{MO} + NA_{ill})/\lambda$. It is important that the laser is switched off during the transition of the laser focus from one fixed pinhole position to the next, in order to preserve the diffraction efficiency of the single capture SA-DHM hologram; if the laser remains active as the laser focus moves in between pinholes, no reference wave is incident on the camera while the object wavefield remains, and therefore, the DC term would be increased relative to the twin images. In order to avoid this, synchronisation of the galvo-scanner with a strobe laser using TTL-logic, or with a chopper, is required. This was beyond the capability of the laser diode used in our set-up, and for this reason, we simulate the real-time SA-DHM modality by adding together the 180 raw holograms that were captured for ODT and reconstructing the

image using only two FFT algorithms. The result is given in Fig. 5.4(a). Despite the use

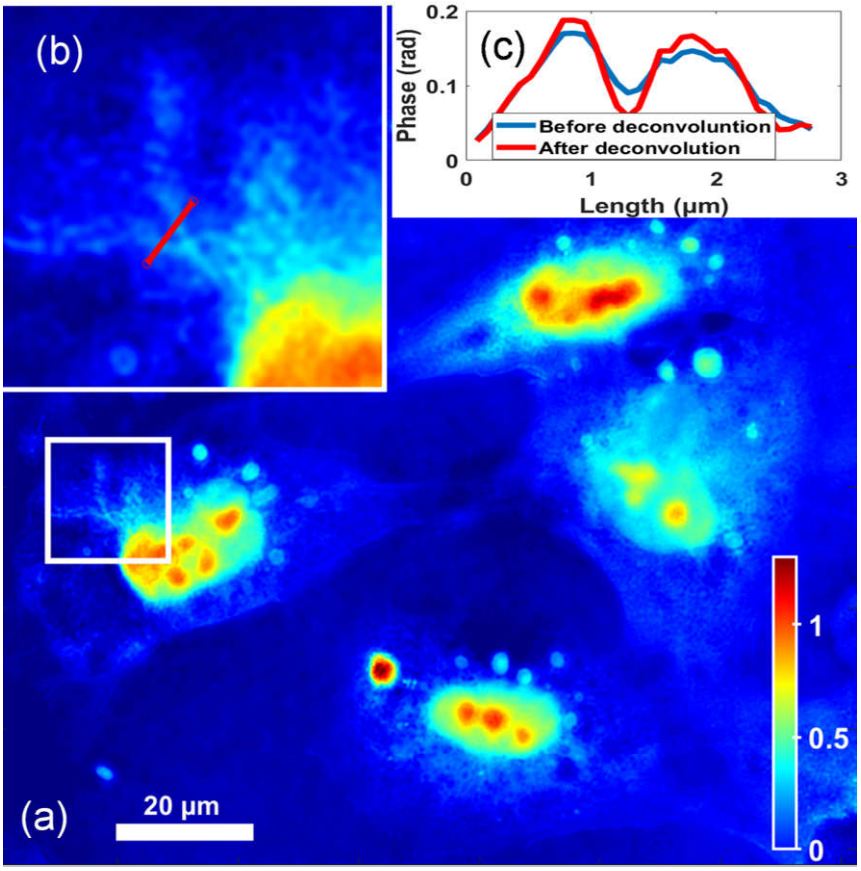

Figure 5.4: (a) Phase image using SA-DHM by adding the raw holograms; (b) A small region in magnified and a profile of the phase values over the red line is shown in (c).

of a coherent source to create the SA-DHM, there is no evidence of coherent noise in the image due to the averaging process. Since, the synthetic aperture profile can easily be determined from Equation 5.7, it is possible to implement real-time non-blind deconvolution by multiplying the filtered twin image by the inverse of H (with a regularisation parameter) in between the two DFT operations; see Chapter 4 Section 4.5 for more details. To highlight the improvement in the image contrast provided by deconvolution, the region in the white box is magnified and shown in Fig. 5.4(a) and a profile of a small sub-cellular feature is shown in Fig. 5.4(c) before and after deconvolution.

5.8 Resolution

The resolution of the final image will depend on the modality that is being used. For the case of ODT, the spatial and axial resolution of the 3D refractive index map are given by: [143, 277]

$$R_{lateral} = \frac{\lambda}{2(NA_{MO} + NA_{ill})} \tag{5.8}$$

$$R_{axial} = \frac{\lambda}{2} \frac{1}{n_i - \sqrt{n_i^2 - NA_{MO}^2}} \tag{5.9}$$

where n_i is the refractive index of the immersion medium. For our setup, (n_i = 1, $NA_{MO} = 0.85, NA_{ill} = 0.68NA_{MO}$), the lateral and axial resolutions of the RI images are given by: $R_{lateral}$ = 222 nm and R_{axial} = 671 nm. Using an oil-immersion (n_i = 1.51) objective of NA_{MO} = 1.3 and the same relative value for NA_{ill} would result in smaller values of $R_{lateral}$ = 145 nm and R_{axial} = 428 nm. For the case of real-time SA-DHM, the spatial and axial resolution of the quantitative phase image is given by:

$$R_{lateral} = \frac{\lambda}{NA_{MO} + NA_{ill}} \tag{5.10}$$

$$R_{axial} = \frac{2\lambda}{NA_{MO}^2} \tag{5.11}$$

with the latter being related to the depth of field. [278] For our setup, the lateral and axial resolutions of the SA phase image are given by: $R_{lateral}$ = 444 nm and R_{axial} = 1.758 μm but would reduce to $R_{lateral}$ = 290 nm and R_{axial} = 752 nm using an immersion objective of NA_{MO} = 1.3.

5.9 Conclusion

In this chapter, we have proposed a new method for recording the 3D ODT tomographic image with several advantages over the state of the art. Firstly the system is modular and employs a self-reference design, such that it can easily be added to any existing life-science microscope and with relatively low cost; the alignment procedure is relatively straightforward and has been automated using a raster-scanning approach that takes approximately 5 minutes. Once aligned, the system records 180 holograms in 10 seconds but this could be reduced using a higher speed DAQ. Secondly, the method is capable of implementing real-time SA-DHM (as described in Chapter 4) if a strobing laser diode is used. Although we do not experimentally demonstrate the real-time implementation, we simulate by simple superposition of the 180 raw holograms and a single DFT to reconstruct the image, which has low levels of coherent noise. We believe this modular bi-modal implementation of ODT/SA-DHM will be of practical use in life-science imaging. This chapter marks the end of any further discussion of SA-DHM and ODT. In the next chapter we return to using coherent DHM (together with Raman spectroscopy) with the application of cell characterisation. SA-DHM was not used due the difficulty in mounting the galvo-scanning illumination module on the Raman system.

Chapter 6

Combining Digital Holographic Microscopy and Raman Spectroscopy for automated Cytology

Part of the work in this chapter has been published in the following: Z. Tang, K. O'Dwyer, A. Dignam, M. Butler, and B.M. Hennelly, "Application of Modular Digital Holographic Microscopy to Clinical Pathology Samples Before Histopathological Staining", in Proceedings Volume 11898, Holography, Diffractive Optics, and Applications XI. SPIE/COS Photonics Asia, 2021. The abstract is not reproduced below as it is not sufficiently general to capture the work in this chapter.

6.1 Introduction

In previous chapters, quantitative phase imaging methods are investigated to reconstruct the phase map or the refractive index map of biological samples of interest. In this chapter, Digital Holography Microscopy (DHM) from QPI field is combined with the complementary modality of Raman spectroscopy in order to investigate biological samples. DHM and Raman spectroscopy are both label-free optical techniques, but they have different abilities to respectively quantify the chemical information and morphological information of desired biological samples. While we are not the first to combine these two modalities for the investigation of cells, we believe we developed and demonstrated the feasibility of an automated manner, such that the system can automatically identify the position of thousands of cells using image processing, and subsequently target each cell using an automated translation stage for concurrent DHM/Raman analysis. As discussed in some detail in Section 2.2 and in Chapter 4, DHM is one type of quantitative phase imaging methods. DHM employs a temporally and spatially (partially) coherent plane wave to illuminate the sample of interest. The resultant sample wavefield is combined with a plane-wave reference wavefield to construct a hologram. Typically, an off-axis angle is created between the reference and object wavefields in order to simplify the numerical processing of holography reconstruction. The reconstructed quantitative phase image is related to the thickness and

refractive index of the sample and can be referred to as a depth map that contains 3D morphological information about the cell. DHM has been extensively applied in the research of cells (both fixed and living) in terms of morphology and behavioural dynamics. One key topic of this DHM research is relevant to the study of cancer cell analysis and diagnosis. [223, 279–283]

As reviewed in Section 2.4, confocal Raman micro-spectroscopy is a complementary technique that generates a spectrum of light that is scattered from a spatially resolved point in a sample. A monochromatic laser source is focused on the sample, which excites vibrations and/or rotations of molecular bonds, and result in the emission of inelastic scattered photons at specific wavelengths. Inelastic scattering is a weak process and only a very small number of photons called 'Stokes-Raman photons' undergo this energy shift to contribute to the Raman spectrum, which is made up of longer wavelengths in comparison with the laser wavelength. The Raman spectrum is recorded by spectrometer with an array detector and is sometimes described as a chemical 'fingerprint', which contains information about the chemical structure of observed biological samples. Peaks at some particular wavenumbers in the Raman spectrum are often indicative of a specific molecule (or more accurately, a specific molecular bond), and the intensity of this peak is linearly proportional to the concentration of this molecule. Raman spectroscopy has been extensively applied in the biological sciences with applications including the investigation of cellular dynamics, cancerous cell diagnosis and the detection of damaged tissues. [284–288]

A key characteristic of both Raman spectroscopy and DHM, is that they are both non-invasive and label free. Both techniques, therefore, can be applied to fixed or living cells in order to provide information on the morphological features and the chemical composition. Such information can be combined in order to generate a classification model that can distinguish between different cell types. The key motivation of the study in this chapter is to research samples prepared using the ThinPrep standard for cyto-histopathology by recording DHM holograms and Raman spectra. The ThinPrep standard is typically used for preparing cervical cancer cytology slides, as well as for urine and oral cytology. [58, 182, 289, 290] Patient cells are obtained (relatively) non-invasively and these are placed in suspension and are deposited in a uniform manner onto a glass slide using the ThinPrep machine. Following this, the H&E standard (or similar) is typically applied whereby the nucleus and cytoplasm are chemically stained to improve image contrast to facilitate imaging for the histopathologist; a mounting medium and coverslip are then added. Recent work has investigated the use of DHM [291] applied to H&E stained cells. However, here we will attempt to record DHM holograms and Raman spectra in advance of H&E staining cells in the ThinPrep process, thereby avoiding any issues that the stain may cause in relation to recording of the phase image and Raman spectrum. Furthermore, the Raman signals can be masked by unwanted signals from biochemicals, we must image cells in the absence of a mounting medium. Unfortunately, this places an unfortunate constraint on DHM, which proves better images when a refractive index matching mounting medium and coverslip are used.

The outline of this chapter is as follows: In Section 6.2, a brief review of previ-

ous contributions in the literature on the analysis of biological samples by combining DHM and Raman spectroscopy is provided. This is followed in Section 6.3 in which we demonstrate the proposed bi-modal setup that can automatically record the Raman spectra and DHM holograms from a sample. This is extended in Section 6.4, where an automation method is described that can be added to the setup for automated analysis of cells. A number of ovarian cancer cell lines are grown and deposited on glass slides using the ThinPrep protocol, which are subject to analysis using the automated Raman/DHM system. Cell culture and preparation are described in Section 6.5. Results are presented for both modalities in Section 6.6 and Section 6.7. And in Section 6.8 the conclusion is presented and ideas for future work are proposed.

6.2 A Brief Review for the dual DHM/Raman biological researches

There have been several reports in the literature on combining Raman and DHM for cellular analysis and these are reviewed in this section. In recent years, the Smith group, developed a dual-modality Raman/DHM microscope to investigate a number of applications [292–294]. The DHM component in their dual-modality setup used a classical Mach-Zehnder off-axis interferometer. A spatially filtered 780 nm laser diode was used as the light source. A beamsplitter is followed to produce two beams: an object beam and a reference beam, which are combined at a small off-axis angle using a second beamsplitter on the sensor plane. The object beam illuminates a sample placed in a customised microscope imaging system using a high-NA microscope objective (MO) 60x/1.27 with a water immersion. For Raman spectroscopy, a 532nm laser beam is input through a cylindrical lens. Then, the beam is focused via the same MO to produce a line profile on the sample plane. Two Gavlo-scanning mirrors are located in conjugate planes between the laser and the MO, which ensures that the excitation line on the sample is always mapped to the spectrograph slit. The epi-scattered Raman photons, and the object wavefield in DHM share a common path behind the MO. In following, the Raman path and the DHM path were separated by a short-pass dichroic mirror. This dichroic mirror has a function to reflect the DHM photons whose wavelength higher than 780nm and allow scattered photons passing straightly. The Raman scattered photons are extracted from all scattered photons via a second long-pass dichroic mirror. At last, the spectrometer collects these Raman photons for constructing a Raman spectrum. This setup can simultaneously record a phase image for DHM and record a hyperspectral image for Raman spectroscopy.

In Ref 292, authors investigated the living HeLa cells, which were immersed in a phosphate buffered solution, and were placed in a quartz bottom dish. In this work, the authors pointed out that both DHM and Raman spectroscopy are the linear response result of light interacting with the sample: DHM is a result of elastic scattering, while the Raman spectroscopy is a result of inelastic scattering. In this study, the authors averaged the magnitudes of wavenumber between 2890 cm^{-1} and 2960 cm^{-1} associated with the C-H band of cells in spectrum. By scanning the entire region of these

cells and calculate the corresponding average magnitudes in this region of cells, a hyperspectral image could be produced. Then, authors cross-correlated the calculated Raman averaged magnitudes with the DHM phase image to examine the relationship between the inelastic and elastic scattering. At last, Independent component analysis (ICA) was performed on the Raman data for a multivariate analysis, and the extracted ICA vectors that contain the principle features of Raman data could quantitatively link the contribution of molecular species, such as lipids and proteins, to the DHM phase shifts induced by cells. This work did not employ any classification metrics directly on the DHM phase images.

In Ref. 293, the authors imaged both water-immersed static polystyrene beads that were mounted on a quartz substrate, and an living embryonic fibroblasts cells (MEF) immersed in a phosphate buffer saline solution and glucose in a quartz dish. In this research, although both DHM and Raman spectroscopy were applied simultaneously, no multivariate analysis or classification methods were performed on both DHM and Raman data. In Ref. 294, authors employed Raman spectroscopy, DHM, and autofluorescence microscopy (AF) to produce three kinds of data, and then input these three kinds of data into a multivariate classification model. In this study, Macrophage cells at different cellular stages were investigated. These macrophage cells were immersed in glucose (5mM) and MgCl2 (2mM) in a quartz container for imaging. For Raman spectroscopy, the variates obtained from PCA loadings, which could represent principle features of the Raman spectral signal, were input into the classification model. For DHM, the phase image was first performed by a cell segmentation algorithm, and followed by a calculation of morphological parameters of cells, such as maximum and mean phase values. The calculated morphological parameters are served as variates used in the classification model. For AF, the morphological parameters, such as the integrated intensity, texture difference, variance, and texture sum average are calculated for classification. The all morphological parameters calculated from AF and DHM can be output by using the CellProfiler open-source software, and the full list of these morphological parameters can be seen in Ref. 294 Table S4(B). Logical regression with Lasso statistics was applied to process all variates from three kinds of data for classifying cells at different stages.

Michael S. Feld's group also combined the modalities of DHM and Raman spectroscopy. [295] In this research, Raman spectroscopy was combined with a standard off-axis DHM setup to study healthy red blood cells (RBCs) and malaria infected RBCs. the correlation between the morphological information obtained from DHM and the chemical information obtained from Raman spectroscopy is investigated. Similar to the work in Ref. 292, no DHM morphological parameters were input to multivariate analysis and classification. PCA was performed on the spectral datasets, and the first two Principal components of PCA are extracted. The first Principal component of PCA contains signal features associated with hemoglobin, which is the material of both healthy and malaria-infected RBCs, while the second Principal Component of PCA contains signal features associated with hemozoin, which a specific cue of malaria infection on partial RBCs. In this work, The DHM and Raman spectroscopy could not be run simultaneously. Additionally, Klossa et. al. [296] also did the work for identifying

the Malaria infected RBCs (smeared on a glass slide and no coverslip used) based on quantitative phase imaging used by the Quadri-Wave Lateral Shearing Interferometer (QWLSI) and Raman spectroscopy. The healthy RBCs and Malaria infected RBCs are classified twice: firstly, the phase image reconstructed from QWLSI was used to qualitatively identify the healthy RBCs and Malaria infected infected RBCs; secondly, the recorded Raman spectra were performed by Hierarchical Clustering Analysis (HCA) to classify RBCs.

Naomi et. al. [297] developed a dual modality of DHM and Raman spectroscopy system for discriminating the different kinds of immune cells: CD4+ T cells, B cells and monocyctes. This system could simultaneously record Raman spectra and DHM holograms. The immune cells were immersed in Phosphate-buffered saline (PBS) containing 0.5% fetal calf serum, and were deposited on a quartz slide. The calculated DHM morphological parameters for each cell include cell size, the maximum phase value, the average phase value over the cell area, contrast, energy and homogeneity. The Raman spectrum and the morphological parameter values from each immune cell were combined and input to multivariate statistical analysis using PCA. The sensitivity and specificity for identifying and clustering the immune cells by Raman spectroscopy + DHM are 93.3% and 96.1%, which is proven to be higher than the prediction result from the individual usage of either DHM or Raman spectroscopy.

The dual modality of DHM and Raman spectroscopy system has also been applied to investigate bull and human sperm cells. [298, 299] All sperm cells used for experiment were suspended in phosphate-buffered saline (PBS), smeared on a quartz slide, and sealed by a quartz coverslip and air-dried. This dual modality of DHM and Raman spectroscopy system allows a simultaneous record of digital hologram and Raman spectrum, but the subsequent numerical analysis on digital holograms and Raman spectral datasets was separated. The authors demonstrated that different subcellular features in sperm cells could be found and discriminated from the Raman spectral datasets and the morphological parameters from DHM phase images. And, additionally, bull X-sperm and bull Y-sperm could be identified by performing PCA on the spectral datasets.

All the biological samples used in the previous Raman/DHM investigations are immersed in growth medium or similar. As we learned in this work, it is very important for DHM to use a surrounding medium that provides a (close) refractive index match with the sample. Unfortunately the Raman spectrum cannot be used with the ThinPrep mounting medium due to the strong corrupting spectrum that is produced from the medium. It is worth emphasizing that mounting media were not used in the research presented in this chapter, with priority given to the quality of the Raman spectra collected.

6.3 Opto-electronic setup

The design of the proposed DHM+Raman spectroscopy setup is displayed in Fig. 6.1. Similar to the work in previous chapters, we employ a modular approach, such that a

DHM module, and a Raman module can be added to an existing life-science microscope in order to augment the microscope functionality and make full use of its high quality imaging platform and translation stage. The decision was taken to use the simpler DHM module in this set-up similar to that proposed in Ref. 266, and not the X-module proposed in Chapter 4. Although SA-DHM, as implemented by the X-module, can record higher quality phase images in terms of both resolution and speckle noise, the illumination module required was too bulky to attach to the Raman microscope. For this reason we resorted to the lower quality coherent DHM module.

The open source Micro-Manager [300] software package (and includes the ImageJ toolbox) is an important component in the setup, which facilitates automated Raman /DHM. The entire setup consists of three components: a microscope, a DHM module and a Raman module. The center of setup is a commercial life-science inverted microscope (IX81, Olympus), in which a halogen lamp (**HL**), a turret of microscope objective (**MO**), and a translation stage (**Z**) that can be manually or electronically adjusted to control the height of **MO**, are linked to a IX2-UCB control box; this IX2-UCB control box is coupled to PC and is controlled via the Olympus IX81 device adapter in Micro-Manager. This enables numerical control of **(i)** the tungsten-halogen lamp intensity; **(ii)** focusing by adjusting the height of MO relative to the sample stage; **(iii)** rotation of the microscope objective turret to change MO as well as several other microscope features that are no important to the automation process. A Micro-Manager device adapter is also used to control **(iv)** the horizontal translation stage (**XY**, 96S108-O3-LE, Ludl) which is coupled and driven by the control system (MAC 5000, Ludl), which links with the Ludl device adapter in Micro-Manager and thereby, the horizontal focal position on the sample could be adjusted numerically.

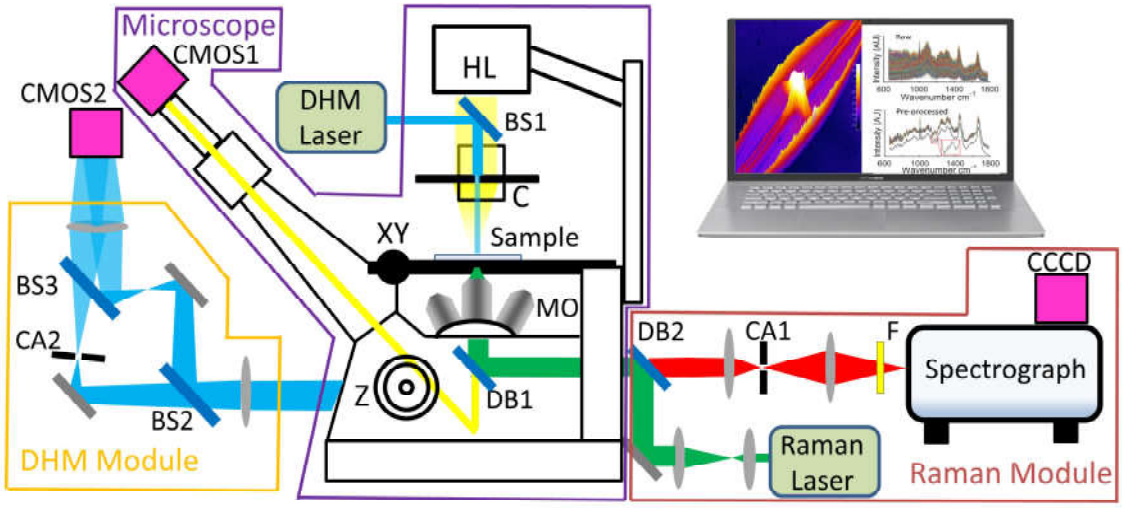

Figure 6.1: The structure of the automated dual-modal Raman spectroscopy and digital holography microscopy system: HL, white light halogen lamp; C, condenser; XY, horizontal translation stage; MO, microscope objective; Z, knob for controlling the height of MO; DB1, short pass dichroic beamsplitter; DB2, long pass dichroic Beamsplitter; CA, circular aperture; BS, beamsplitter; F, long pass filter; CCCD, Cooled CCD camera; CMOS, CMOS camera.

For DHM, a spatially filtering 488nm blue laser (JDSU/Lumentum FCD488, 20mW) is used as a light source input into the microscope. The open/close and **(v)** intensity of laser can also be controlled by the Micro-Manager using 'freeserialport' device adapter. A beamsplitter (**BS1**) is located between the white light lamp and the microscope condenser (**C**), and reflects the laser beam into the condenser. This approach enables either laser or white light illumination to be used and controlled via Micro-Manager. The condenser guides the laser beam to irradiate the sample with a plane wave. An image is produced at the output port of the microscope. The DHM module relays this intermediate image field to the camera described below. This DHM module is self-reference similar to the modules developed in Chapter 4 and 5, and both object and reference wavefields are combined at the camera having travelled approximately equal optical path lengths (the path length difference must be less than the laser's coherence length) and are co-incident at a relative off-axis angle to achieve suitable twin-image separation in the Fourier domain. One benefit of the self-reference design is that the problem of optical path difference between reference beam and object beam caused by the exchange of samples can be avoided. A further advantage of such a small self-reference design is that vibrational interference is mitigated remarkably. Similar to the modules developed in previous chapters, the DHM module here follows a $4f$ design. The image wavefield is located on the front focal plane of the first lens and is imaged to the camera. The first beamsplitter (**BS2**) generates two copies of the object wave one of which is filtered to produce the reference wavefield. This filter is a 100 μm circular pinhole (**CA2**) placed on the back focal plane of first lens, (the Fourier plane of the image), in order to remove the non-zero frequency component, and thereby produce a reference beam. In the object beam path, the image wavefield is preserved and is combined with the reference beam using a beamsplitter (**BS3**); the angles of both wavefields are varied using the different mirrors in the respective object and reference paths, and the resultant off-axis hologram is recorded on the CMOS camera (**CMOS2**, acA3088-57μm, Basler), which is also controlled **(vi)** by Micro-manager via the 'BaslerPylon' adapter.

For Raman spectroscopy, a Raman module is attached on the back side of the microscope via the fluorescence port. A 532 nm green laser (Torus, Laser Quantum) with 150 mW power and ≈100 m coherence length is used for excitation. The laser is driven by a power supply unit (mpc3000, Laser Quantum) that is coupled to PC using the cable RS232. The **(vii)** open/close and the intensity of laser can be controlled in Micro-Manager, also using 'freeserialport' device adapter. The incident 532 nm laser beam is guided to focus on the sample of interest in microscope using a dichroic beamsplitter that is mounted within a fluoresence cube. The back-scattered Raman photons are collected by the MO and reflected back into the Raman module by the dichroic beamsplitter (**DB1**,69-202, Edmund Optic). This **DB1** is a short-pass filter: on one hand, it allows the transmission of white light beam (< 500 nm) and blue laser to the digital camera (**CMOS1**, MU300, Amscope) and the DHM module; on the other hand, it reflects the scattered light back to the Raman module. In the Raman module, the first element is a long-pass dichroic beamsplitter (**DB2**, LPD-01-532RS, Semrock), which prevents the Rayleigh photons of 532 nm wavelength from reaching the spectrograph, while allowing the Raman photons of longer wavelength to pass through. A confo-

cal aperture (**CA1**) is placed after **DB2** on the conjugated sample focused plane. This isolates the desired Raman signal from the focus spot of the laser, and reduces a collection of unwanted background signals from out-of-focus sample regions and from elements in the optical path. A long-pass filter (**F**) further removes the Rayleigh photons, before they entering the spectrograph (Kaiser, Holospec f/1.8). The spectrograph is operated with a 25 μm slit and a holographic grating (HSG-532-LF). A -80 °C cooled CCD camera (**CCCD**, DU920P-BEX2-DD, Andor) records the Raman spectra in a full-vertical-bin mode. The camera can be controlled (**viii**) by the Andor device adapter in Micro-Manager. With respect to spectral recording, the standard deviation of the read noise can be reduced to 4 electrons/spectrum samples, and the average dark current is reduced to 0.0512 electrons/sec/spectrum samples.

6.4 Automation

As mentioned in previous Section, all electronic elements in the proposed setup, including the halogen lamp, translation stage, focus adjustment, laser sources, and cameras can be numerically operated by Micro-Manager software. Micro-Manager is an open source software that not only permits the automated control of such these electronic elements by using a Beanshell script, but also allows for image processing via the ImageJ library. [301, 302] In this study, the automation procedure for automated Raman/DHM cytology is based on the automated Raman cytology protocol proposed in Ref. 2, and similarly the script that controls the automated procedure is written in the Beanshell interface in Micro-Manager. Here we present the steps of the automated procedure, which are also illustrated in Fig. 6.2.

The first step in the automation procedure is to determine the coordinates of the cells on the glass cytology slide. In order to realize this, the halogen lamp is switched on and both laser sources are switched off. The brightfield image of the cells are recorded by an inexpensive CMOS camera (**CMOS1**) attached on the eyepiece port of microscope. The translation stage moves the slide over a fixed set of overlapping positions in both spatial dimensions. The filter iris in the condenser is closed to a minimum in order to generate spatially coherent illumination, which was found to work optimally for identifying cell positions; this enhances the contrast between background and cell-diffracted light. Cell targeting is performed based on the nucleus 'microlens-effect', [2] which can be interpreted as the focusing of the halogen lamp by the cell nucleus to form bright-spots at a specific plane that are closer to the in-focus image plane. These bright-spots provide the coordinates of cells. It should be emphasized that the varying morphology of different kinds of cells can result in the bright-spots plane occurring at different distances from the image plane. Thereby, a vertical scan around the sample plane is a necessary measure to determine the optimal bright-spots plane. In our experiment, a Beanshell script is written to scan a range of 300μm in the vertical direction, and a stack of total 60 brightfield images in the same field-of-view (FOV) are recorded and saved in order to identify the best bright-spots plane that corresponds to the image with the highest variance. In Micro-Manager, the variance of a given image

can be calculated by using an ImageJ function in Beanshell scripting. The profile of the variance as a function of vertical scanning distance is shown on the left side of Fig. 6.2. The bright-spots plane can be determined by the maximum variance, and the in-focus image plane can be identified by the minimum variance.

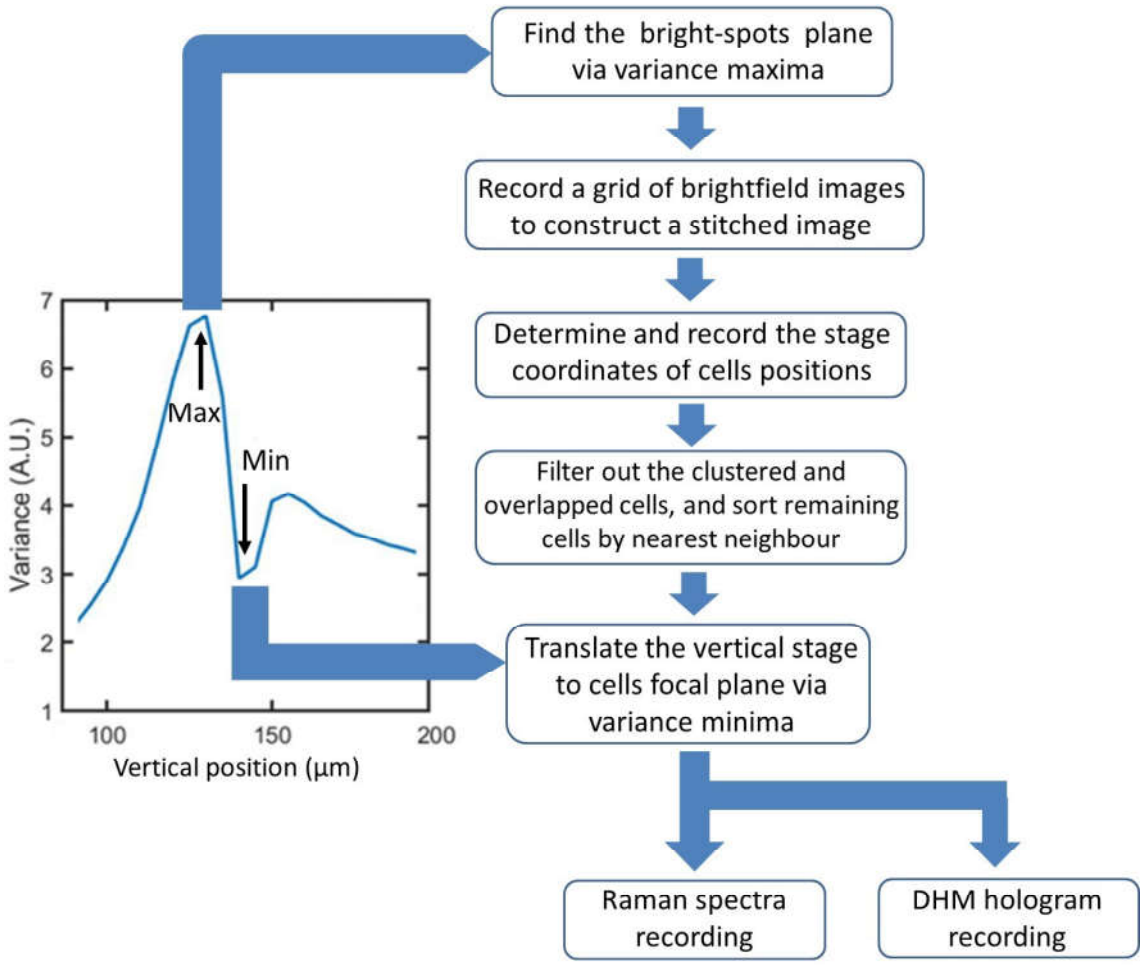

Figure 6.2: The left side: the recorded image variance profile as a function of vertical scanning distance, where Max and Min relate to the maximum and minimum variance, which correspond to the positions of the bright-spot plane and in-focus image plane, respectively: The right side: a flow chart of automation procedure realized by a Beanshell script written in Micro-Manager. (Partially adapted from Ref. [2])

After determining the vertical position of bright-spots plane, an image stitching for obtaining a larger size of FOV is constructed, in order to to record more cells. We numerically translate the horizontal translation stage (**XY**), and record a grid of overlapping brightfield images on the bright-spots plane. The stitching processing could be realized via ImageJ, and the resultant stitched image is saved in disk for the subsequent image processing. Then, by performing an ImageJ function 'Find Maxima' on the stitched brightfield image, all bright-spots that correspond to cell positions could be found. These cell positions in the stitched image can be converted to stage coordinates, recorded as a list and saved on disk. Next, these saved stage coordinates can be transferred as the offsets of horizontal translation stage to make sure each cell targeted by focus spot of Raman laser.

It is notable that not all cells in the final stitched image are suitable for Raman/DHM analysis. ThinPrep processing can result in a considerable number of cells that are clustered and overlapped. As a result, Raman/DHM analysis cannot reliably return single-cell metrics for these cases. Therefore, only cells that are well separated are selected for automated Raman/DHM analysis - based on the distance of the bright spot from its nearest neighbour using a simple algorithm in Beanshell. If the calculated distance between the two nearest cells is smaller than a predfined threshold, such cells are considered to be clustered and overlapped, and their coordinates will be removed from the list. Additionally. the sequence of translation stage coordinates in the refined list will also be sorted based on the closest distance among these cells. The advantage of this approach is to minimise the movement of the translations stage throughout the automation routine, thereby minimising any drift between the relative stage positions and the cell coordinates over time.

Once the list of coordinates for DHM/Raman inspection is finalised, the vertical stage is moved to align the in-focus image plane with the camera. Now, the cells are ready for Raman/DHM recording. Based on the precise coordinates obtained from the bright-spot identification process, the Raman spectroscopy setup is aligned to target each cell nucleus specifically and capture the corresponding Raman spectra. Care should be taken in aligning the DHM camera such that the Raman laser spot is in-focus at the centre of the camera. Should defocus (between the Raman spot and the DHM image) occur, the out-of-focus problem can be solved by the numerical auto-focusing method in DHM reconstruction. [37]

6.5 Sample Preparation

Ovarian cancer cells from A2780, PE01, and PE04 cell lines were respectively cultured by our collaborators in the biology department, in RPMI medium (Gibco) supplemented with 10% fetal bovine serum. The culture flasks were maintained in a humidified environment at $37°C$ and 5% CO_2. When the cells reached 90% confluency the media was removed, and cells were washed with sterile PBS. 2mL of 0.5% trypsin-EDTA solution was added to the cells and the cells were incubated at $37°C$ for 5 minutes until they detached. 8mL of RPMI media was added to the flask neutralise the trypsin and the entire contents of the flask were transferred to a separate sterile falcon tube. The cells were centrifuged for 5 minutes at 1500 rpm. The supernatant was discarded, and the cell pellet was resuspended in fresh RPMI media. The cell number was calculated using a haemocytometer.

After counting, the number of cells, for each cell line, 500,000 cells were transferred to a new falcon tube. The cells were then centrifuged for 5 minutes at 1500 rpm. The supernatant was discarded and the cell pellet was resuspended in 20mL of PreservCyt (Hologic). The cells were incubated at room temperature for 20 minutes. The cell suspension was then loaded into the ThinPrep 2000 (Hologic) machine. Finally, the cells from the three cell lines were transferred onto three glass slides for analysis with the proposed Raman/DHM system. In total we investigated 800 ovarian cancer cells

from each of the three cell lines (total 2400 cells); in each case the DHM hologram was recorded and the corresponding Raman spectrum was also recorded for the numerical analysis later.

6.6 DHM Analysis

6.6.1 Numerical Processing

This section focuses on the numerical processing of the digital holograms of the ovarian cancer cells from the A2780 cell line in particular; similar results were obtained for the other two cell lines. An example of a recorded A2780 ovarian cancer cell hologram is displayed in Fig. 6.3(a). A discrete Fourier transform (DFT) is applied to the recorded hologram and the resultant spectrum is shown in Fig. 6.3(b), in which the frequency bands corresponding to the zero order and twin images are separated. One of twin images frequency bands, marked within the white circle in Fig. 6.3(b), can be extracted by spatial filtering, and following an inverse DFT (IDFT) applied to the extracted frequency band, the phase image of the cell is reconstructed. Numerical propagation algorithms were not required because the edges of the ovarian cancer cells are judged to be approximately in-focus via the alignment of the image planes in the microscope; such algorithms [90, 226] are in general able to achieve focusing of cells with greater accuracy; However, given the large depth of these cells (without using a mounting medium), there is little advantage in applying such algorithms.

Simple aberration compensation is achieved by recording a reference hologram with no sample in the field of view. The aberration-removal phase images for each cell can be obtained by subtracting the phase image reconstructed from the reference hologram from the reconstructed phase images of cells.

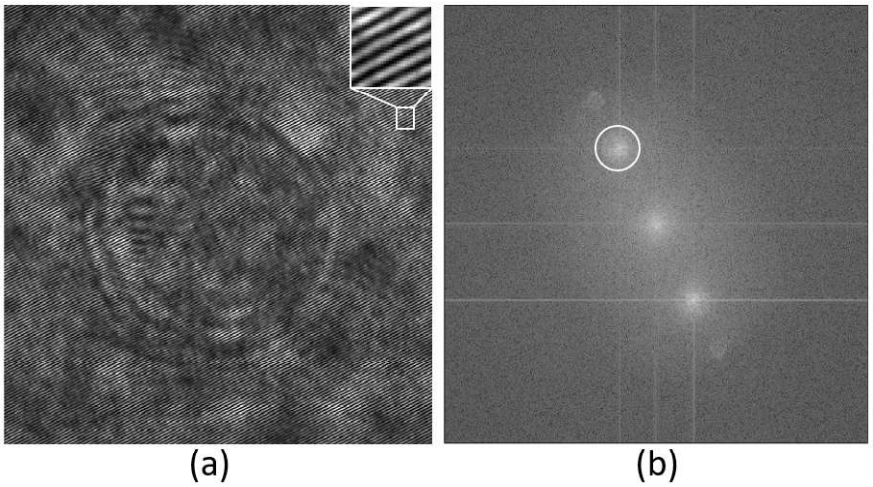

Figure 6.3: (a). An example of a recorded hologram of an ovarian cancer cell. Inset: The magnified interference fringes. (b). The spectrum of the hologram shown in (a); the frequency band enclosed by the white circle is one of twin image bands that could be extracted for reconstructing the desired phase field of such that ovarian cancer cell.

In this study, the ovarian cancer cells of interest are prepared according to a ThinPrep standard, but without using a coverslip and mounting medium in order to facilitate the Raman modality. The cells prepared are relatively thick, which produces an inevitable problem for phase imaging. As well as large areas of the cell being out-of-focus, the phase wrapping problem also presents. These problems could be mitigated through the use of mounting medium with a similar refractive to the sample; however, the mounting medium would cause a significant problem for Raman analysis. Here, we attempt to perform phase unwrapping based on the wavelet transform. [105]

It was found that in many cases, the unwrapped phase image has an uneven phase background or tilt, despite the use of a reference hologram aberration compensation described above. This tilt was removed by applying a polynomial fitting to the background region around the cell. Furthermore, It was also found that the phase within the region of the cell edge is less than the background phase, which appears to relate to sharp changes in phase close to the edge of the nucleus due to the refractive index mismatch between the air and the cell in the absence of a mounting medium. A simple segmentation method (required for applying cytometry to the cell phase image) was applied by thresholding to extract the cell region. However, unfortunately, this method failed for most cell for which the phase values were less than the background, as discussed above.

6.6.2 DHM Results

The hologram of two adjacent ovarian cancer cells is first recorded. The amplitude field and the phase image of the hologram is shown in Fig. 6.4(a) and Fig. 6.4(b), respectively. It can be seen that the coherent speckle noise is present in the background, and the wrapped phase appears in the phase image. The background phase image calculated from a reference (no sample) hologram is shown in Fig. 6.4(c), and the wrapped phase image calculated by subtracting this reference phase from Fig. 6.4(b) is shown in Fig. 6.4(d). The unwrapped phase field after the phase unwrapping methodology and its corresponding 3D rendering are displayed in Fig. 6.4(e) and Fig. 6.4(f), respectively. The phase value in the background area surrounding the cells is approximately 1. Subsequently, phase tilt removal and cell segmentation are performed on Fig.6.4(e) to produce an eventual outcome, which is shown in Fig. 6.4(h). Fig. 6.4(i) is the 3D rendering of Fig. 6.4(h). The brightfield image of such these 2 ovarian cancer cells is displayed in Fig. 6.4(g) for comparison. It can be observed that the region where phase errors occur after phase unwrapping comes from the region where there is a sharp depth gradient from the out-of-focus nucleus to the lower cytoplasm that is shown in Fig. 6.4(g).

The hologram of another ovarian cancer cell is shown in Fig. 6.5. The amplitude field and the phase image of the hologram is shown in Fig. 6.5(a) and Fig. 6.5(b), respectively. Once again, it can be seen that the coherent speckle noise is present in the background, and phase wrapping appears in the phase image. The reference phase image and wrapped phase image after removing aberration are shown in Fig. 6.5(c) and Fig. 6.5(d), respectively. The unwrapped phase image and its corresponding 3D depth map image are displayed in Fig. 6.5(e) and Fig. 6.5(f), respectively. In this case, the

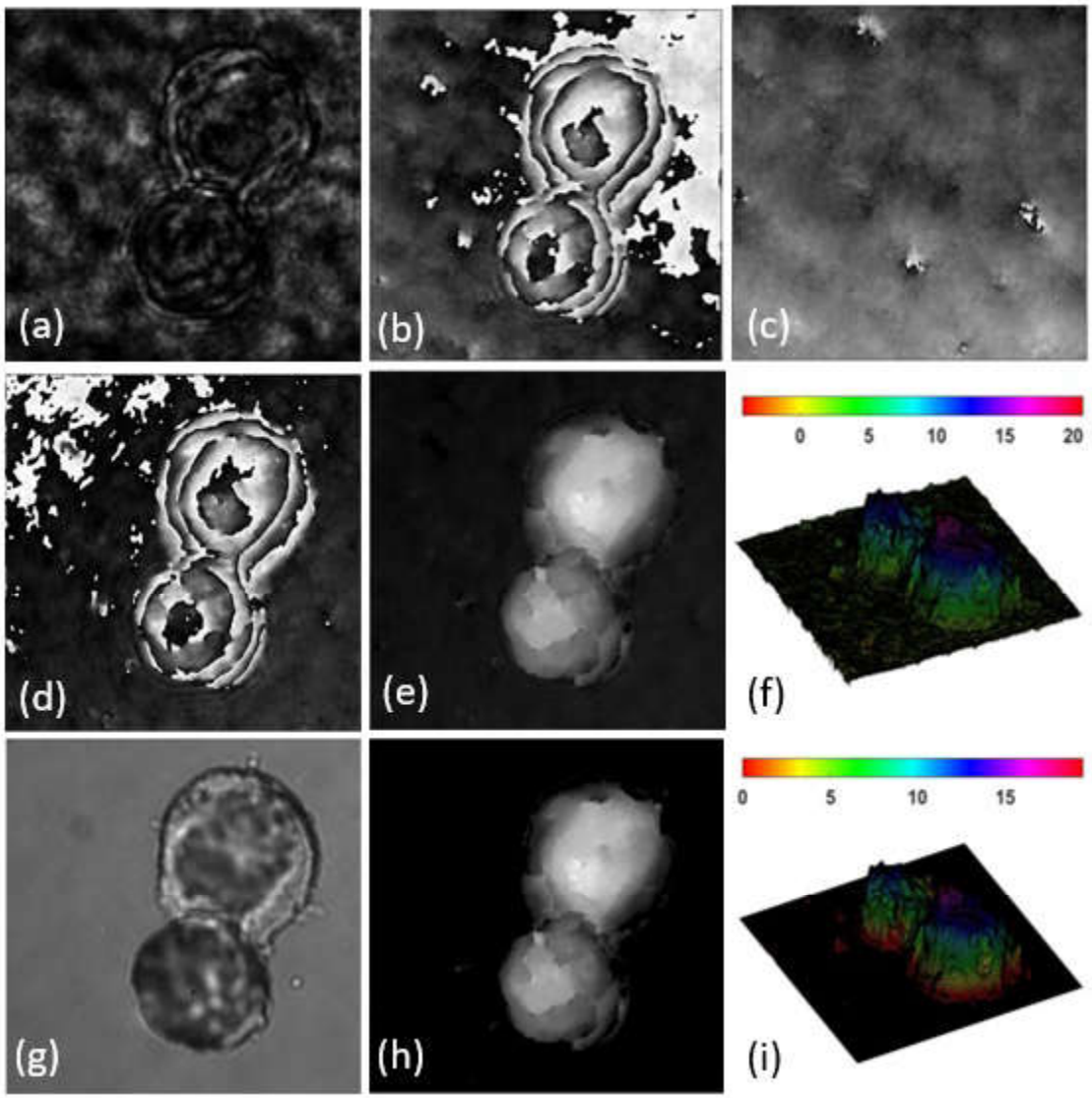

Figure 6.4: A set of images of two adjacent ovarian cancer cells prepared by ThinPrep processing without using no coverslip and mounting medium; (a) Amplitude of the complex image; (b) Phase image; (c) Phase image of reference (no sample) hologram; (d) Phase image after using aberration compensation, i.e. background phase subtraction. (e) Unwrapped phase image that is processed from (d); (f) 3D rendering of (e); (g) Brightfield image of the ovarian caner cells using white light; (h) The unwrapped phase image after removing background phase tilt and cell segmentation; (i) 3D rendering of (h).

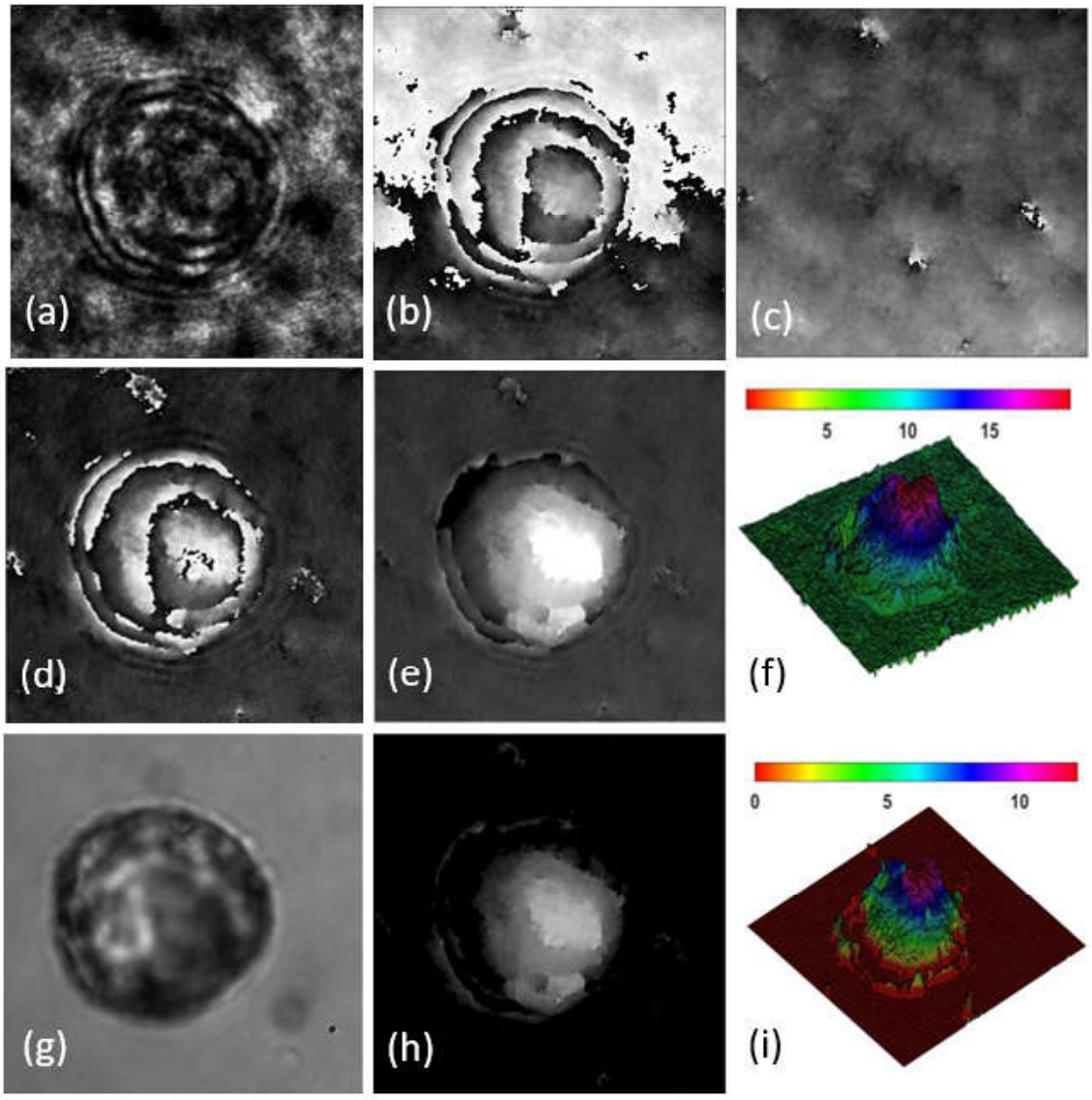

Figure 6.5: Another set of images of a single ovarian cancer cell prepared by ThinPrep processing without using coverslip and mounting medium; (a) Amplitude of the complex image; (b) Phase image; (c) Phase image of reference (no sample) hologram; (d) Phase image after using aberration compensation, i.e. background phase subtraction. (e) Unwrapped phase image that is processed from (d); (f) 3D rendering of (e); (g) Brightfield image of the ovarian cancer cell using white light; (h) The unwrapped phase image after removing background phase tilt and cell segmentation; (i) 3D rendering of (h).

phase values in the background are erroneous; these values are higher than those in most areas within the cell; this results from a difficulty in accurate phase unwrapping at the cell boundary. This background phase error possibly results from the cell edge being slightly out-of-focus and the resultant generation of diffraction artifacts. The removal of phase tilt and cell segmentation are then performed to produce the eventual phase image, which is shown in Fig. 6.5(h). Fig. 6.5(i) is a 3d rendering of Fig. 6.5(h). A brightfield image for this ovarian cancer cell is provided in Fig. 6.5(g). Due to the aforementioned issue caused by out-of-focus cell edge and diffraction artifact, the resultant unwrapped phase image is not ideal.

Given the challenges encountered with the phase unwrapping of ovarian cancer cells prepared by ThinPrep processing without using coverslip and mounting medium, future improvements are being considered. The current method proves inadequate for most cells, which results from defocusing in thick cell regions, coherent speckle noise, and phase unwrapping errors due to the absence of refractive index matching mounting medium. These issues hinder the effective use of DHM metrics and the combination of DHM with Raman information for enhanced classification.

To address these challenges, future efforts will focus on enhancing the quality of the phase image. One approach is to search and test the mounting medium to reduce the refractive index difference between the cells and the background, thereby alleviating the pressure on phase unwrapping. Although the use of a mounting medium will introduce unwanted background signals in Raman recording, it is expected that these can be removed by numerical processing. Additionally, there is an interest in employing the SA-DHM technique, as mentioned in Chapter 4, instead of the traditional DHM used in this chapter. The SA-DHM technique is expected to significantly reduce speckle noise and recover more accurate cellular details in the reconstructed phase image.

6.7 Raman Analysis

6.7.1 Raman spectrum recording

The spectrometer records the spectra in the wavenumber range of -34-2517 cm^{-1} with an average resolution of 5.48 cm^{-1}. The Raman system was wavenumber calibrated using a polymer standard as described in Ref. 303. No intensity calibration was performed for this experiment, since all spectra were recorded from the same system. Firstly, a number of cells were deposited on a Raman grade CaF_2 slide, and the spectra of nucleus from a small number of these cells were recorded. The CaF_2 slide have negligible background spectra in the region > 400 cm^{-1} and the cell spectra recorded from this substrate can provide a reference cell spectrum for use with the glass spectrum subtraction using the Extended Multiplicative Signal Correction (EMSC) that will be described in Section 6.7.2. [289, 304, 305] An acquisition time of 10s was used to record a single spectrum from each nucleus. Ovarian cells from A2780, PE01, and PE04 cell lines were deposited on the ThinPrep glass slides, and spectra were recorded using an acquisition time of 30s. Each recorded raw spectrum contained 1024 samples in

the range -10-2464 cm^{-1}, from which 500 samples that have a wavenumber range of 739–1945 cm^{-1}, which were extracted for further numerical processing.

6.7.2 Pre-processing of Raman Spectra

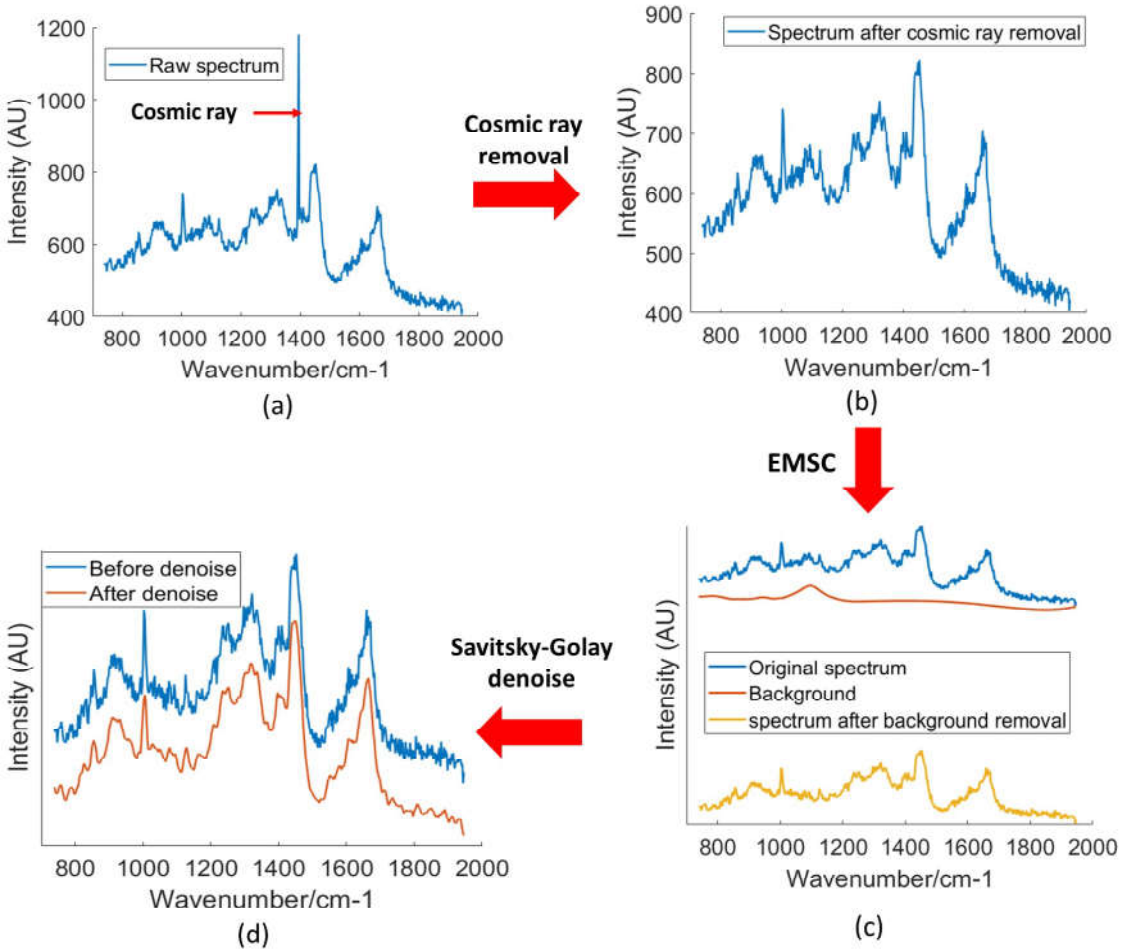

Figure 6.6: The procedure of pre-processing for a raw Raman spectrum: (a) a raw spectrum containing a cosmic ray; (b) a spectrum after cosmic ray removal; (c) a spectrum after using EMSC algorithm to remove background signal; (d) a spectrum after using Savitsky-Golay algorithm for denoise.

The raw Raman spectra were inevitably polluted by several unwanted factors, such as cosmic rays, background signals from the glass substrate, a variable baseline due to fluorescence and the presence of noise. Therefore, the recorded raw Raman spectra must undergo a series of preprocessing steps before applying multivariate statistical analysis. Removing the glass spectrum and the variable baseline is achieved using the EMSC algorithm. The overall pre-processing procedure used in this study for each raw spectrum is demonstrated in Fig. 6.6.

The recorded raw spectrum (shown in Fig. 6.6(a)) was firstly processed by employing a cosmic ray removal algorithm. [306] This algorithm searches for a similar spec-

trum within the dataset, and then replaces the amplitude of a cosmic ray with the corresponding amplitude at the same wavenumber positions in the matching spectrum. Thus, the traditional and most commonly used cosmic ray removal method, [307] which requires double acquisition is no longer to be used, which largely reduces the time of spectral acquisition. The spectrum after cosmic ray removal is provided in Fig. 6.6(b).

After removing cosmic ray, an Extended Multiplicative Signal Correction (EMSC) algorithm is performed on each spectrum to estimate and remove the background signals from different sources. These background signals include the baseline signal from auto-fluorescence, the signal from glass substrate that cells are deposited on, and other signals from optical elements during the optical path. Briefly speaking, EMSC employs a least square fit to (i) an N-order polynomial to represent the baseline signal; (ii) a reference spectrum of glass substrate, which contains background signals from glass substrate and optical elements during the optical path; (iii) a reference cell spectrum, which has been obtained by depositing cells on Raman-grade CaF^2 substrate. The EMSC algorithm returns the weights for terms (i),(ii),(iii). Then, the corrected Raman spectrum after background removal could be obtained by appropriate subtraction as follows:

$$S_c = \frac{S_0 - [B \times w_b] - \sum_{m=0}^{N} w_m x^m}{w_r} \tag{6.1}$$

where S_c is the corrected spectrum after background removal, S_0 is the original spectrum before background removal, B is the reference spectrum of glass substrate, w_b is the weight of reference spectrum of glass substrate determined by the least square algorithm, x^m is the m^{th} power of the wavenumber axis, and w_m is the corresponding weights of the polynomial (also determined by the least squares algorithm), w_r is the weight of reference cell spectrum (also determined by the least squares algorithm), which is used as a denominator in Equation 6.1 to normalize each obtained background removal spectrum, S_c. In Ref. [305], it was shown that the usage of high-order polynomial in a similar EMSC algorithm does not result in an overfitting problem. In this study, a polynomial order of $N = 5$ was applied in EMSC algorithm to remove the background signals. Fig. 6.6(c) shows the estimated background signal calculated by EMSC algorithm and the spectrum after background removal.

Following the background removal after EMSC correction, a Savitsky-Golay algorithm using a polynomial of order 3 and a window size of 15 was used to denoise spectrum. [308] The smooth spectrum after denoising is shown in Fig. 6.6. Next, the resultant denoised spectra of cells were input in a filter to remove the spectra of low quality. This filter evaluates the correlation between each corrected spectrum and the reference cell spectrum by calculating a Pearson correlation coefficient. When the Pearson correlation coefficient is calculated less than 0.9, the corresponding spectrum is removed from the corrected spectra. Finally, 208 spectra of cells from the A2780 cell line, 178 spectra of cells from the PE01 cell line, and 142 spectra of cells from the PE04 cell line were kept for multivariate analysis. These spectra from the three cell lines after pre-processing are shown in Fig. 6.7.

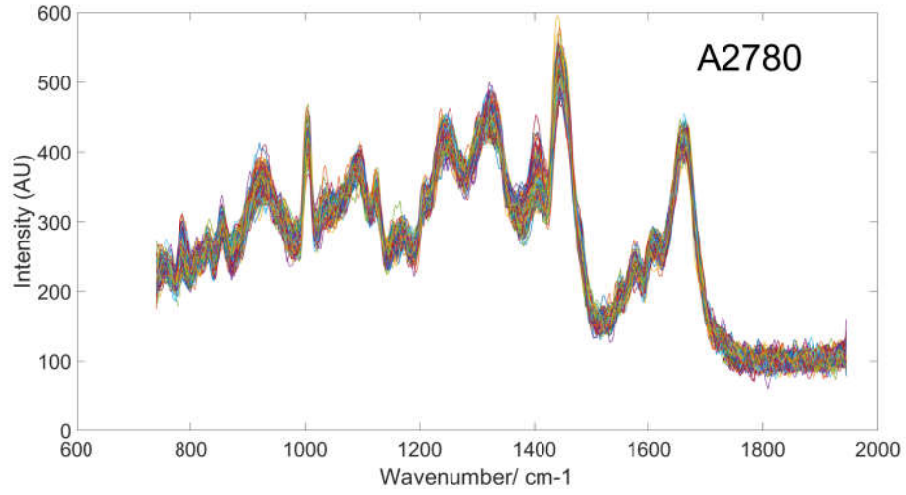

(a)

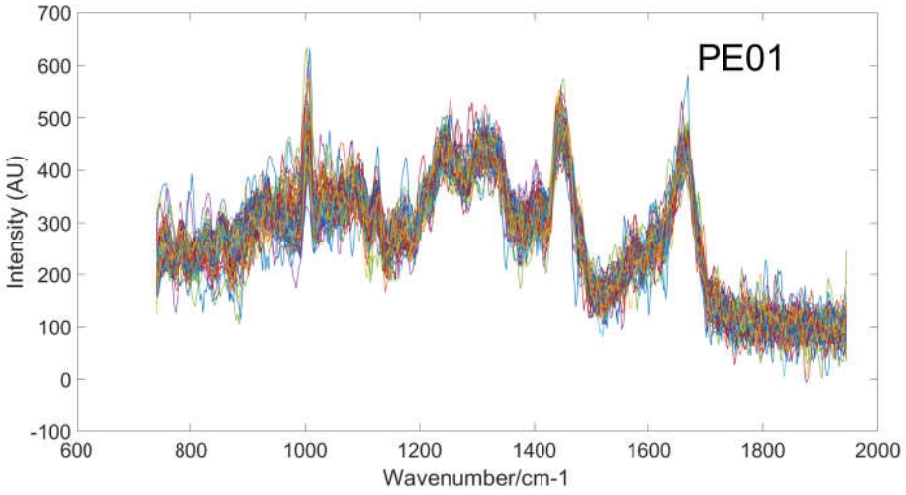

(b)

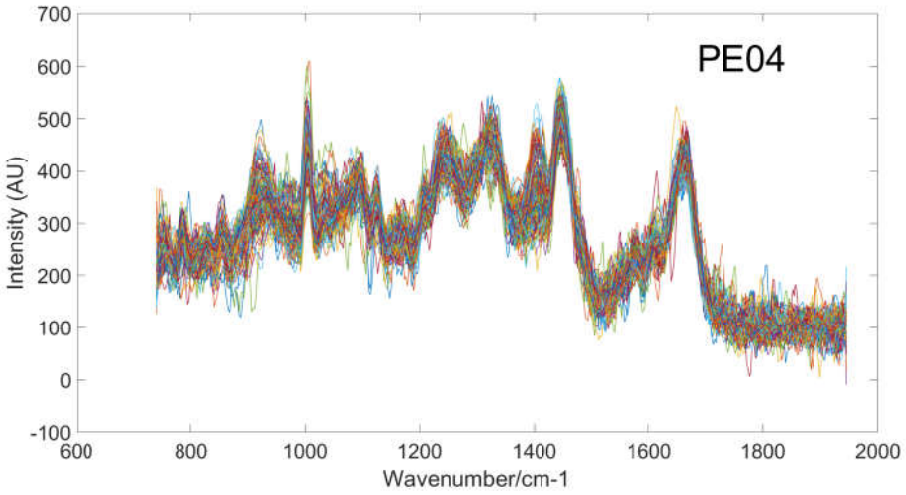

(c)

Figure 6.7: The Raman spectra of the ovarian cancer cells from three cell lines after pre-processing: (a) A2780 cell line; (b) PE01 cell line; (c) PE04 cell line.

6.7.3 Multivariate Statistical Classification

The Raman spectra obtained after pre-processing are input to a multivariate analysis to classify the ovarian cancer cells from three cell lines (classes). The accuracy of classification is a vital factor to evaluate the performance of Raman cytometry. Various methods exist including multivariate classification methods, such as Ridge Regression, [309] Support Vector Machine, [310] Linear Discriminant Analysis (LDA), [311] Decision Trees, [312] k-nearest neighbours (kNN), [313] random forest (RF), [314] which have been applied to Raman spectra for cell classification. [315] In this study, PCA-LDA is used as a classifier to discriminate ovarian cancer cells from different cell lines. Principal Component Analysis (PCA) [316] is first performed on Raman spectra for data reduction.

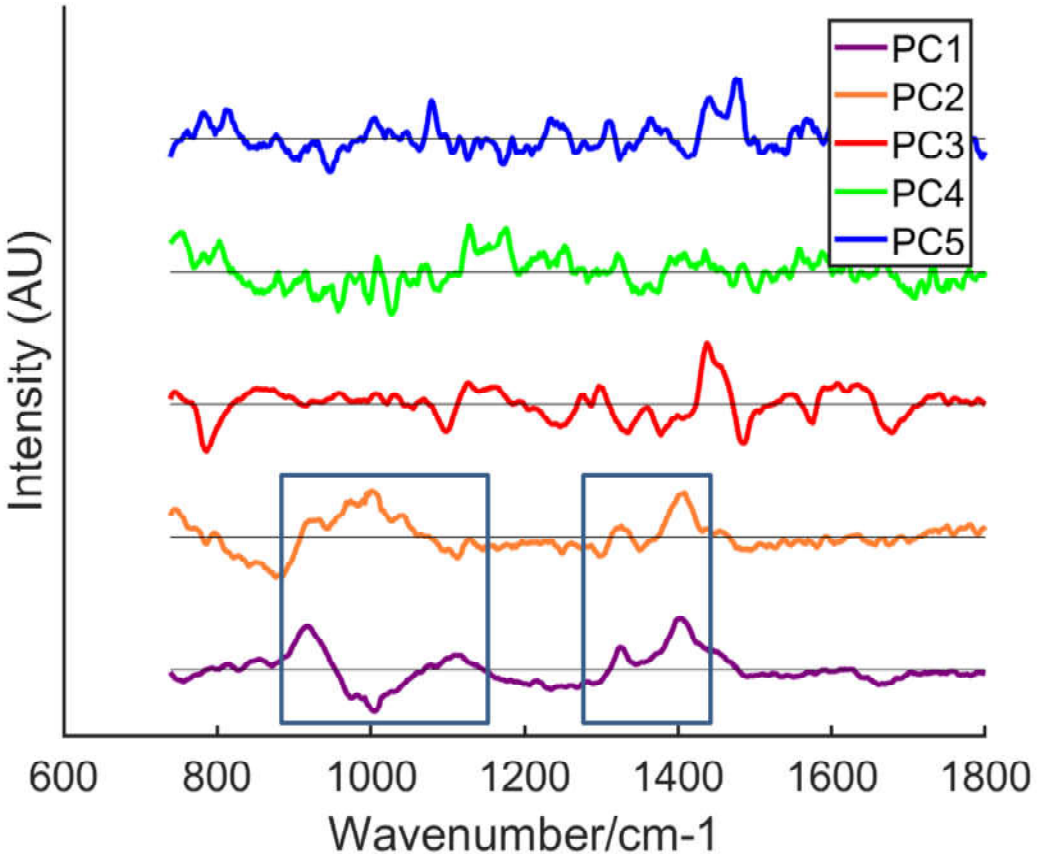

Figure 6.8: The PCA loadings from first five principal components to represent the features extracted from the original Raman dataset.

PCA is a multivariate technique that is able to not only reduce the dimensionality of high-dimensional data, but also preserve as much information as possible from high-dimensional data. For the Raman analysis in this study, the spectra of ovarian cells obtained after pre-processing are combined to construct a large Raman dataset, where each wavenumber unit used in Raman spectra is a dimension of this Raman dataset. PCA projects this high dimensional spectral dataset onto a new space by decomposing

the Raman dataset into a matrix of loadings and a matrix of scores. In the new projected space, mutually orthogonal dimensions are called principal components (PCs), and each PC contains a pair of (i) a loadings vector and (ii) a scores vector; the scores can be understood as the weights for each loading, and these loading vectors could represent the different feature information extracted from original spectral data in terms of variance.

The loadings are sorted in descending order in terms of the variance of these loadings within the dataset. Usually, the first few PCs are sufficient to contain the most important information within the Raman dataset, while the later PCs contain the unimportant information such as noise. Thereby, the data reduction can be realized by preserving the first few PCs and omitting another PCs. In Fig. 6.8, five loadings vectors from first five PCs are displayed to respectively represent the feature information extracted from original Raman dataset. Two spectral bands are highlighted by two blue rectangles in the loadings vectors of first two PCs. The first band covers the spectral region of wavenumber range from 880 cm^{-1} to 1160 cm^{-1}, and the second band covers the spectral region of wavenumber range from 1275 cm^{-1} to 1420 cm^{-1}. Based on the previous Raman research for ovarian cancer cells in Ref. 317, the cell chemical characteristics of hydroxyapatite/carotenoid/cholesterol, symmetric ring breathing mode of phenylalanine, and C–C (& C–N) stretching of proteins (also carotenoids) can be assigned in first band; and the cell chemical characteristics of CH2 deformation (lipid)/adenine and cytosine, polynucleotide chain (DNA-purine bases), Amide III (α-helix) of proteins, and deformation vibration of lipid CH2 and CH3 could be assigned in second band.

The 3D scatter plot of the first three PC scores and as well as 2D projections of these scores for the spectra of the three cell lines are shown in Fig. 6.9. It can be seen from Fig. 6.9(b)(c) that the scores cluster from A2780 cell line (red dots) and the scores cluster from PE01 cell line (green dots) are somewhat separated. However, scores clusters from PE04 cell line (blue dots) are mixed in the middle of another two scores clusters, and for this reason LDA is applied in order to separate these groups using a linear classifier applied to this 10-dimensional dataset.

LDA is a classical classification method that can be used to find the difference between different groups. While PCA is an unsupervised method that aims to find the PCs for data reduction by decomposing the signal according to variance within a dataset, LDA is a supervised method to construct a classifier via finding the proper LDA components (LDs) by maximizing the separation between different sample classes. In Fig. 6.10, the projections of first three LDA components on the new space resulting from LDA is provided. Similar to the distribution of PCA scores shown in Fig. 6.9, from the LDA projection, it can be suggested that the cells from A2780 cell line and the cells from PE01 cell lines can be separated well in two regions in the new space; while cells from PE04 cell line are still difficult to separate. To quantify the performance, 10-fold cross-validation is applied to the model. The LDA estimation for classifying the ovarian cells from three classes of cell lines is concluded in a confusion matrix in Fig. 6.11. This confusion matrix is a basis for calculating the coefficients of sensitivity and specificity in order to evaluate the classification ability of classifier. Based on the confusion

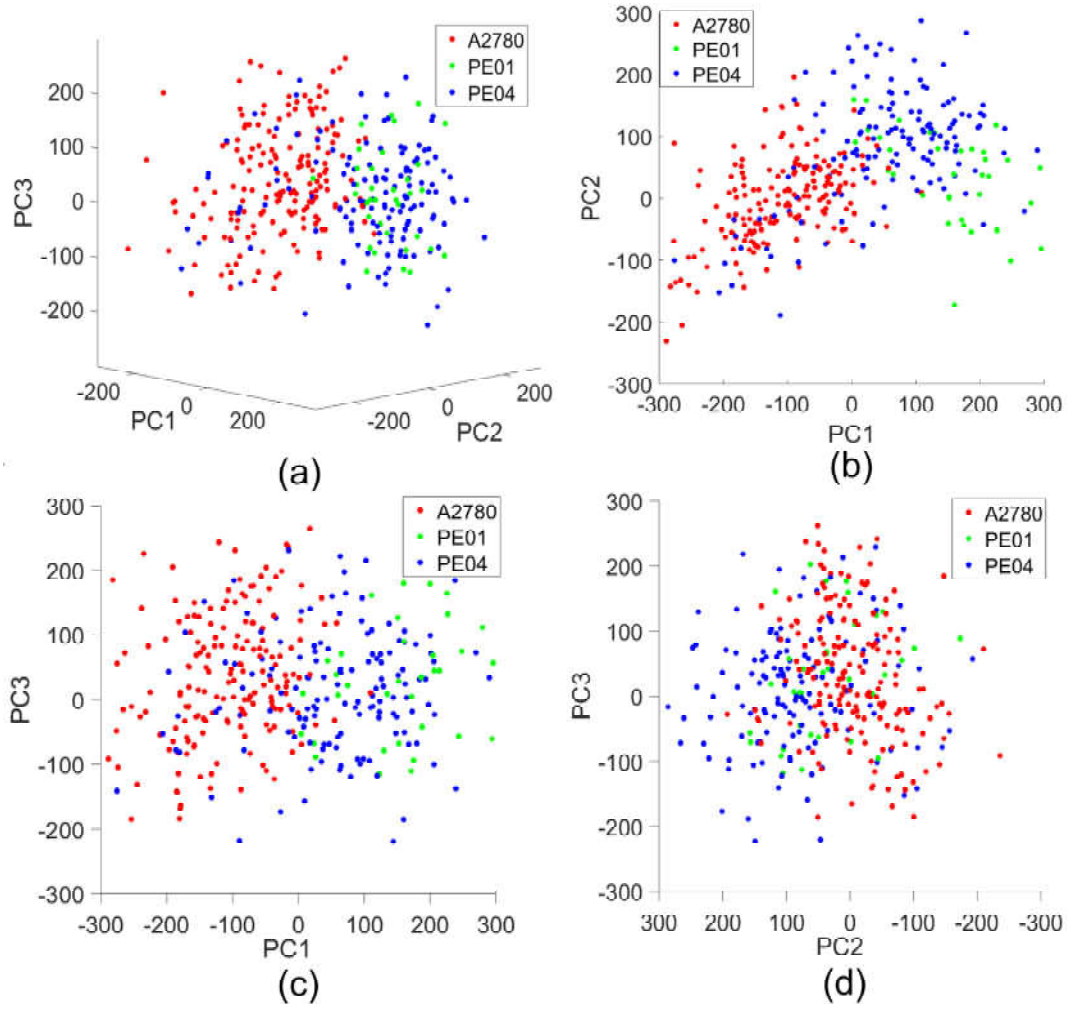

Figure 6.9: The projection of the scores for the first three PCs for all three cell lines: (a) a 3D scores scatter from first three PCs; (b) a 2D scores plane from first PC versus second PC; (c) a 2D scores plane from first PC versus third PC; (d) a 2D scores plane from second PC versus third PC.

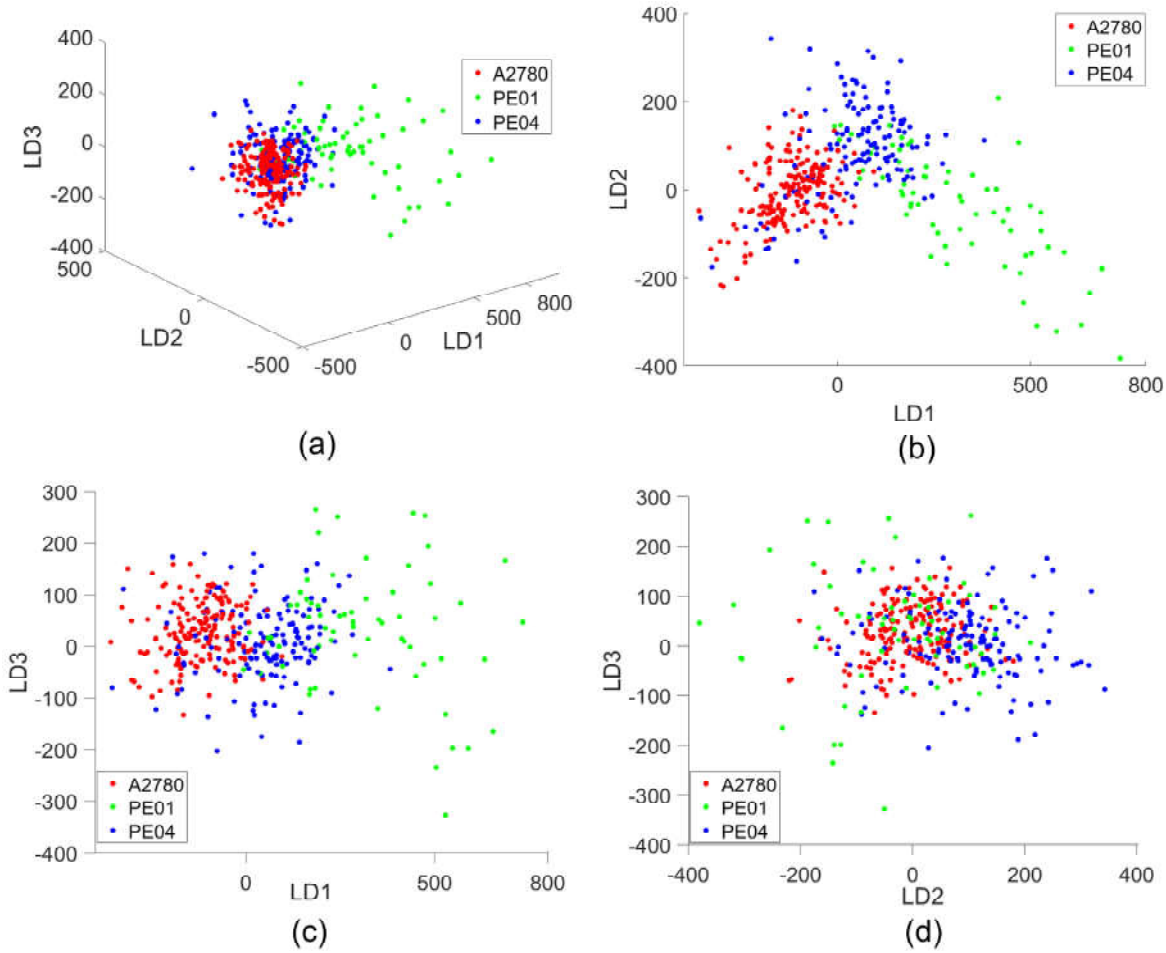

Figure 6.10: The projection of first three LDA components on the new space resulting from LDA applied to the first 10 PC scores: (a) a 3D scatter plot of the first three LDA components; (b) a 2D projection of LDA components 1 and 2; (c) a 2D projection of LDA components 1 and 3; (d) a 2D projection of LDA components 2 and 3.

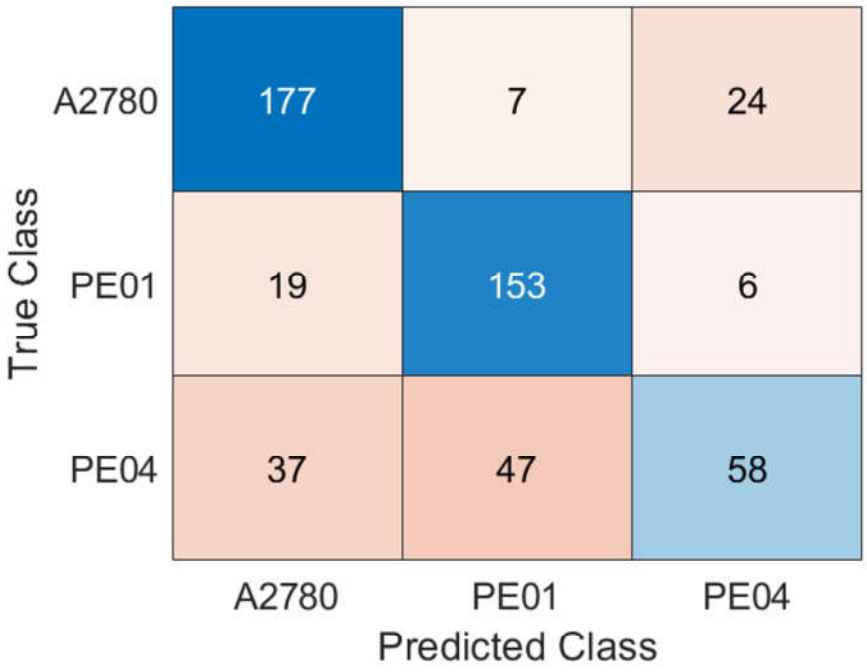

Figure 6.11: The confusion matrix calculated from LDA classifier for the ovarian cancer cells from the three cell lines

matrix, for each cell line, there are four kinds of parameters: True positive (TP), False positive (FP), True negative (TN), False negative (FN). Using the A2780 cell line as an example, these four parameters are calculated as follows:

- TP of A2780 cell line = the number of the ovarian cells from A2780 cell line predicted correctly as cells from A2780 cell line = 177
- FP of A2780 cell line = the number of the ovarian cells from A2780 cell line predicted incorrectly as cells from another PE01 and PE04 cell lines = 19+37 = 56
- TN of A2780 cell line = the number of the ovarian cells from PE01 and PE04 cell lines predicted correctly as cells from non-A2780 cell lines = 153+6+47+58 = 264
- FN of A2780 cell line = the number of the ovarian cells from PE01 and PE04 cell lines predicted incorrectly as cells from A2780 cell line = 7+24 = 31

The sensitivity of the A2780 cell line represents the fraction of cells from the A2780 cell line that are correctly predicted as A2780 cells. The specificity of the A2780 cell line represents the fraction of cells from non-A2780 cell lines are incorrectly predicted as cells from non-A2780 cell lines. These metrics are defined as follows:

$$\begin{aligned} Sensitivity_{A2780} &= \frac{TP}{(TP+FN)} = \frac{177}{177+31} = 85.1\% \\ Specificity_{A2780} &= \frac{TN}{(TN+FP)} = \frac{264}{(264+56)} = 82.5\% \end{aligned} \tag{6.2}$$

Analogous to the calculation of sensitivity and specificity of A2780 cell line, the sensitivity and specificity of PE01, PE04 cell lines and classification model can also be calculated and are concluded in Table 6.1. Note that the parameters used for calculating the sensitivity and specificity of the total classification model are equal to the sum of the corresponding parameters for each cell line (e.g. $TP_{total} = TP_{A2780} + TP_{PE01} + TP_{PE04}$).

Table 6.1: The calculated sensitivity and specificity of each cell line and classification model

	A2780	PE01	PE04	Classification model
Sensitivity	85.1%	86%	66%	81.8%
Specificity	82.5%	84.6%	67.2%	82.5%

Obviously, It can be observed from Table. 6.1 that the sensitivity and specificity of PE04 cell line are only 66% and 67.2% respectively, which is significantly lower than the sensitivity and specificity of the A2780 cell line and PE01 cell line; the sensitivity and specificity of A2780 and PE01 cell line are above 80%. This disparity in results is likely due to the poor quality of spectra obtained from the PE04 cell line, primarily because the confocal pinhole was not ideally positioned in this study. Accurate alignment of the confocal pinhole is critical for data collection. Misalignment can significantly impact the classification performance of PCA and LDA. When the pinhole is not optimally positioned, it leads to a decrease in spatial resolution and an increase in the collection of out-of-focus light. This results in a degradation of the spectral quality, with reduced signal-to-noise ratio and potential spectral distortion. Consequently, when PCA and LDA are applied to such compromised data, their ability to differentiate between cell lines or other samples is impaired. This leads to lower sensitivity and specificity in classification results. Therefore, ensuring precise pinhole alignment in future work is essential for maintaining the quality of collected spectral data and the effectiveness of subsequent classification analysis.

6.8 Conclusion and future work

It is clear from the results in this chapter that the automated Raman system was not optimised in terms of laser alignment and spectral recording; the laser was not optimally focused on the sample and co-aligned with the confocal aperture and spectrograph slit. This resulted in poor quality (low SNR) spectra. Nevertheless, it was possible to achieve sensitivity and specificity of 81.8% and 82.5% for the used LDA classifier. It is expected that these numbers could be improved following improved confocal pinhole alignement, and that the wavenumber assignment in the PCA loadings that contribute to clustering of the data could be better performed.

The DHM system also provided poor results. Without the use of a mounting medium necessitated by the Raman modality, the relatively thick cells that were deposited by the ThinPrep Machine, produce wrapped phase images that were difficult to accurately unwrap and segment. This was further complicated by the presence of coherent noise in the system as well as the large depth of the sample when compared with the depth of

field of the microscope. In the absence of accurate segmentation and unwrapping it is difficult to calculate quantitative spatial signatures of the cells, such as those reported by Shaked et al. [41] In order to render the DHM system useful for cell classification, it is necessary that mounting medium be applied to the ThinPrep slides. However, this would in turn complicate the recording of Raman spectra since any mounting medium will excite an appreciable Raman spectrum which will superimpose and corrupt the spectrum of cell in the same way that the glass spectrum does. Unlike the glass spectrum, which is relatively smooth and can be removed using a least squares algorithm, mounting media produce spectra with sharp peaks. Future work is required in order to understand if a least squares algorithm could subtract such a spectrum from the cell spectrum and render it useful for cellular classification. Another possibility to obtain higher quality phase images would be to use the X-Module presented in Chapter 4 in lieu of the coherent DHM module used in this chapter. This would produce phase images of much higher quality both in terms of resolution and coherent noise. This would require mounting the illumination module into the Raman microscope. Galvo-scanners with small form factors are available that could be added to the microscope. However, this would not solve the aforementioned mounting medium problem which would need to be addressed as well.

The goal of this chapter was to combine the data from the DHM and Raman system and input this data into a single classifier with superior accuracy that could be achieved with either modality in isolation. Although, this was not achieved in the first trial run of the system reported in this chapter, we believe that if the problems described above can be overcome, the system will enable this to be achieved. One obvious approach to do this, may be to work with live adherent cells in a mini-incubator for application in basic research and drug development. Such cells would be in growth medium, which would provide a natural refractive index (phase) matching. Furthermore, adherent cells are thinner than cells deposited by ThinPrep and may therefore mitigate the phase wrapping problem, if it exists at all. Despite the shortcomings of the experimental result, we believe this demonstrates the viability of our automated Raman and DHM system for cellular analysis. A critical aspect of this system is that DHM utilizes a relatively low laser wavelength (488 nm) rather than a higher laser wavelength. This wavelength is strategically chosen as it can be distinctly separated from Raman scattering using a dichroic mirror, thus facilitating the concurrent acquisition of holograms and Raman spectra. In the future, it's also expected to integrate two galvo-mirrors in the Raman module to achieve scanning imaging. This advance will shift the focus from the current single-point imaging on the nucleus to larger regions of the cell, such as the cytoplasm. Such a broadened scanning scope promises to yield a more comprehensive and accurate understanding of cellular composition, thereby significantly improving the precision of cellular metrics.

Here, the journey of phase imaging in this thesis ends. In the next chapter, we focus entirely on Raman spectroscopy. In particular we examine the capacity of Raman spectroscopy to return useful information on the chemical composition of a mixture. In the context of cellular analysis this could be interpreted as a capability to inspect the growth medium for live cell cultures or suspensions.

Chapter 7

Multicomponent analysis using a confocal Raman microscope

The work in this chapter has been published in the following reference: Z. Tang, S.J. Barton, T.E. Ward, J.P. Lowry, M.M. Doran, H.J. Byrne, and B.M. Hennelly, "Multicomponent analysis using a confocal Raman microscope." Applied optics 57, no. 22 (2018): E118-E130 with the following abstract:

Measuring the concentration of multiple chemical components in a low volume aqueous mixture by Raman spectroscopy has received significant interest in the literature. All of the contributions to date focus on the design of optical systems that facilitate the recording of spectra with high signal-to-noise ratio, by collecting as many Raman scattered photons as possible. In this study, the confocal Raman microscope set-up is investigated for multicomponent analysis. Partial Least Squares Regression is used to quantify physiologically relevant aqueous mixtures of glucose, lactic acid, and urea. The predicted error is 17.81 mg/dL for glucose, 10.81 mg/dL for lactic acid and 7.6 mg/dL for urea, although this can be improved with increased acquisition times. A theoretical analysis of the method is proposed, which relates the numerical aperture and the magnification of the microscope objective, as well as the confocal pinhole size, to the performance of the technique.

7.1 Introduction

In Chapter 2 Section 2.4 the subject of Raman spectroscopy was introduced and in Section 2.4.4 the basic structure of the confocal Raman microscope was discussed. This confocal Raman microscope design was used in Chapter 6 together with a digital holographic module for cellular characterisation. In this chapter, this work is extended to investigate the capacity for this confocal Raman microscope to quantify the concentration of chemical components in a mixture. In the context of the previous work, one could imagine that confocal Raman spectroscopy could be used to assess the quality of the growth medium in which a live cell culture is under investigation and to detect if changes to that medium need to be addressed.

Raman spectroscopy is a non-invasive optical technique that can be used to identify the presence of, and quantify the concentration of, chemicals substances by detecting the vibrations of molecules within the sample. Raman spectroscopy is based on the inelastic scattering of light, and occurs when photons from a monochromatic laser source are incident on, and interact with, these molecular vibrations. This results in a change in the energy of the incident photons, or more specifically a shift in wavelength. The Raman scattered photons' wavelength and magnitude contain information relating to the identity and concentration of a specific chemical, respectively.

Well-established methods for measuring analytes in blood and urine typically require large volumes of fluid or lengthy processing time. In order to overcome these drawbacks, Raman spectroscopy has been proposed to quantify multiple components simultaneously and in real time with the advantage of small volume sampling and less sample contact. [4, 163, 318–327] A key advantage of Raman spectroscopy is that it is non-destructive; the sample can be reused for further analysis following inspection with Raman spectroscopy. Multivariate statistical analysis of the recorded spectra is central to the approach; most commonly, Partial Least Square (PLS) regression [328] is used to provide a predictive model that can estimate the relationship between a set of independent variables (peak areas in the Raman Spectra) and dependent variables (chemical concentrations).

Measuring the concentration of chemical metabolites in body fluids is important in clinical and biological analysis. Three examples, which are highlighted in this chapter are urea, glucose, and lactic acid. Urea, a common metabolite existing in urine, reflects information on the condition of the body in terms of nutrition, and provides information about renal disorder. [318] The measurement of glucose is of obvious importance in the context of diabetes; diabetic patients must measure blood glucose concentration in order to avoid the possible complication of kidney failure, blindness, and heart disease. [319] The concentration of lactic acid in blood provides information regarding the degree of fatigue, especially for athletes. [320] The investigation presented in this chapter is focused only on these three chemicals in aqueous mixture; however, it should be noted that many other blood analytes have also been measured by Raman spectroscopy including bicarbonate, triactin, ethanol, acetaminophen, creatinine, triglyceride, albumin, protein, globulin , cholesterol, and haemoglobin. [163, 321–324]

Over the past two decades, a number of independent research groups have investigated the potential of Raman spectroscopy to measure the concentration of multiple chemical components in aqueous mixture. In 1995, Goetz et al. [3] used an Argon-ion laser to measure the concentration of urea, glucose, and lactic acid simultaneously in aqueous mixture solution. Following on from this initial experiment, Berger et al. [4, 329, 330], Qu et al. [322], Enejder et al. [5] Rohleder et al. [331] and Qi et al. [332] all attempted to further exploit Raman spectroscopy in order to predict the concentration of multiple components in greater number and with greater accuracy in terms of the smallest measurable concentration. In Section 7.2, the background research is briefly reviewed, as are the principles and experimental methods that underpin Raman spectroscopy. Particular attention is given to the various optical architectures that have been proposed for multicomponent analysis to date. The motivation in all of these de-

signs is to maximise the number of Raman scattered photons that can be collected by the detector from the sample container, thereby maximizing the signal-to-noise ratio (SNR) of the recorded spectra.

In Section 7.3, the conventional confocal Raman microscope is discussed in the context of analysing an aqueous solution. Variants of this type of microscope are produced by Horiba, Renishaw, and Princeton Instruments, and are commonly found in research laboratories. The optical architecture of a confocal Raman microscope is ubiquitous in the sense that it is not optimized for a specific application and is as likely to be found in a material science laboratory as it is to be found in a clinical setting. The optical system is designed to reduce the unwanted background signal from the microscope objective, in addition to any other optical elements that are common to both the delivery and collection paths, based on the traditional epi-illumination approach. In the context of analysing samples on a glass slide, the confocal aperture also serves to reduce the spectrum from the substrate. [333] This background reduction is achieved by introducing a confocal aperture into an intermediate image plane in the collection path, thereby providing a depth resolution when obtaining spectra from a bulk three dimensional sample. However, this limited depth resolution will reduce the number of collected Raman scattered photons, and will therefore reduce the SNR of the spectrum recorded from a bulk aqueous solution; in this regard, a theoretical analysis of the performance of a confocal Raman microscope is presented. In Section 7.4, we extend this model to facilitate a comparison of the confocal Raman system with the bespoke designs that are reviewed in Section 7.2.1, in terms of collection efficiency.

In Section 7.5, an experiment is outlined that repeats the initial investigation of Goetz et al. [3] using a conventional confocal Raman microscope to measure the concentrations of glucose, lactic acid, and urea in aqueous mixtures. The results of this experiment are provided in Section 7.6, and a brief conclusion is offered in Section 7.7.

7.2 Background

7.2.1 Optical System for Multicomponent Analysis with Raman Spectroscopy

Over the past two decades, a number of research groups have proposed different optical systems and methods for multicomponent analysis using Raman spectroscopy. In 1995, Goetz et al. [3] proposed the application of Raman spectroscopy to identify and quantify the concentration of three different chemicals (glucose, urea, and lactic acid) in aqueous mixture. The experimental setup that was used is shown in Fig. 7.1(a) and used an Argon-ion laser source with wavelength of 514.5 nm, 10 mW power. The scattered Raman irradiance was collected at 90° with respect to the source delivery path and focused onto the spectrograph slit using a lens (not shown). A total acquisition time of 40 seconds was used.

In 1996 and 1997, Berger et al. applied a similar Raman system with a near-infrared (NIR) source in order to measure the concentrations of glucose, lactic acid, and cre-

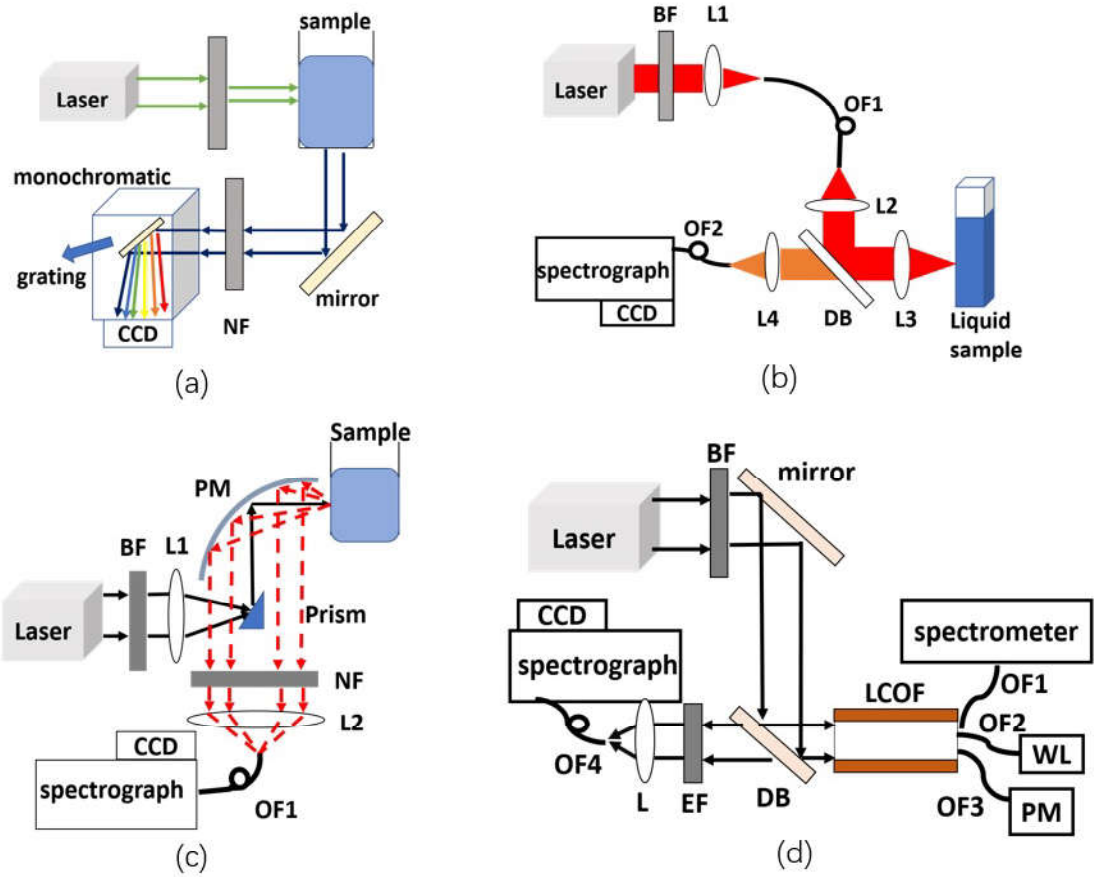

Figure 7.1: Raman spectroscopy systems that have previously been proposed for multicomponent analysis. (a) Optical system similar with basic system used by Goetz et al. in 1995 [3]: LF, line pass filter; NF, notch filter. (b) Raman setup using optical fiber bundle used by Berger et al. [4] in 1996: BF, bandpass filter; L, lens; OF1, optical fiber; OF2, a bundle of seven optical fibers; DB, dichoric beam splitter filter. (c) Optical system with parabolic mirror used by Enejder et al. [5] in 2002: BF, bandpass filter; L, lens; NF, notch filter; PM, parabolic mirror. (d) LCOF Raman setup used by Qi and Berger [6]: BF, bandpass filter; DB, dichoic beam splitter; LCOF; liquid-core optical fiber; OF, optical fiber; EF, edge filter.

atinine in saline solutions, and in a second experiment, to measure the concentration of glucose in blood; [4, 329] Fig. 7.1(b) illustrates the Raman system used in these experiments. NIR wavelengths have been demonstrated to be optimal for tissue and biosamples due to the significantly reduced unwanted background signal. [4, 327] The source excitation in these experiments was produced by an Argon-ion pump laser and an 830 nm dye laser with 200 mW power, and for the second experiment a NIR diode laser with 150 mW power. In order to collect photons from as large an area as possible and couple these photons into a narrow spectrograph slit (to ensure high spectral resolution), in the first experiment the scattered photons were coupled into a fiber array bundle that was subsequently separated into individual fibers, which were input to the spectrograph along the linear slit (only one fiber was used to input to the spectrograph in the second experiment). The integration time for each spectrum was 100 seconds for the first experiment and 5 min for the second experiment.

Qu and Shao [323] and Rohleder et al. [331] subsequently proposed an ultrafiltration technique in order to remove macromolecules from their samples, thereby enhancing the predictive accuracy for small molecules in the multicomponent mixture. Qu et al. [323] also proposed a waveguide capillary cell that guided the source laser irradiance over an extended volume of the sample. Enejder et al. [5] designed and optimized a Raman system [Fig. 7.1(c)] using a Monte Carlo model that estimated the brightness and the spatial support of the scattered light. The resulting design is based on the trade-off between solid angle and area and uses a parabolic mirror with high f-number and numerical aperture in order to collect a large number of Raman scattered photons.

Increasing collection solid angles, collection area, integration time, and laser power can effectively increase the number of Raman scattered photons that can be collected and will, therefore, increase the SNR of the recorded spectrum. Liquid-core optical fibers (LCOF) currently offer the gold standard for Raman multicomponent analysis by providing the highest SNRs from aqueous solutions to date. This approach relies on a significantly increased collection volume by guiding the laser over the entire length of an LCOF often many meters in length that is filled with the solution. LCOFs greatly enhance the number of scattered photons that can be collected over a given integration time, with the additional advantage of requiring a small sample volume in the order of 1 μL. [334] Building on the work of Altkorn et al. [335, 336], the experiments of Qi and Berger [6, 332, 334, 337] demonstrated the application of LCOFs for multicomponent analysis. An illustration of the LCOF Raman system used by Qi and Berger in 2007 [6] for quantifying different analytes in blood serum and urine samples is given in Fig. 7.1(d). The experiment is complicated by the effect of wavelength-dependent absorption as the scattered photons are guided back to the fiber input from where these photons are coupled to the spectrograph using a fiber bundle. This absorption is both wavelength- and distance-dependent, and is modelled using the Beer–Lambert law. In order to compensate for this effect, a calibrated white light source must be included in the setup, as well as additional spectrometer.

7.2.2 Limitation of Measurement

Experimental noise places an unavoidable limitation on the capacity of multicomponent Raman analysis both in terms of the number of analytes that can be simultaneously measured for a given mixture, as well as the smallest concentration that can be measured for each analyte. Noise sources result from (i) shot noise, the random arrival of photons collected by detector, (ii) dark current noise, generated by thermally excited electrons within the detector pixels, and (iii) read noise, resulting from the imperfect conversion of electrons into a digital voltage in the camera. The shot noise and dark current noise are both modelled by a Poisson distribution and are both linear functions of the acquisition time. The SNR of the Raman spectrum can be defined in term of the spectral irradiance and the standard deviation of the various noise terms as follows:

$$SNR = \frac{it}{\sqrt{it + ct + \sigma^2}} \tag{7.1}$$

where i denotes the mean irradiance in electrons/second, which also takes into account the quantum efficiency of the detector; c is mean dark current (electrons/second); σ is the standard deviation of the read noise; and t is the integration time. In summary, the numerator in Equation 7.1 represents the signal power at a given detector pixel, and the denominator represents the standard deviation of the total noise term. The SNR increases nonlinearly with respect to exposure time. The SNR increases rapidly in the beginning of the exposure, and this rate of increase gradually reduces over time. For practical reasons, the integration time, t, has been rarely increased beyond five minutes in any of the multicomponent experiments to date.

It has been noted that the noise present in the spectrum places a hard limit on the accuracy of measurement. [172] In particular, the Raman spectrum from water, a weak but abundant Raman scatterer, will generate shot noise that remains after the Raman spectrum of the water is numerically subtracted. Since a biofluid sample, such as urine or blood serum, will inevitably contain water in high concentration, the shot noise will be appreciably large when compared with the Raman spectrum from a chemical with a low concentration, even one with a relative large Raman cross section. The raw spectrum may also contain other undesired background signals for which the same argument can be made, including Raman spectra from the optical elements and the sample's container, as well as the unwanted baseline signal, [333] which is less pronounced for NIR excitation. These unwanted background signals can all be subtracted or reduced, but the shot noise associated with these signals can never be removed. Many of the optical systems discussed in Section 7.2.1 include design features that reduce unwanted signal; for example, the 90° collection geometry in Fig. 7.1(a) will reduce signals emanating from the optical elements in the illumination path and from the sample container. As will be discussed in the following section, the confocal Raman setup permits only signal originating from within a small three-dimensional volume in the sample to contribute to the Raman spectrum, and will, therefore, optically filter much of the unwanted background contaminants from the recorded spectrum. However, the cost of this is a reduction in the SNR, when compared to many of the systems

reviewed in Section 7.2.1. In Section 7.4, the collection efficiency of each of the systems illustrated in Fig. 7.1 is compared with that of a confocal Raman microscope.

7.3 Application of Confocal Raman Microscopy to Aqueous Solutions

7.3.1 Confocal Raman Microscopy

All of the optical systems mentioned in Section 7.2.1 are designed with the goal of enhancing the amount of Raman backscattered photons that can be collected from an aqueous mixture, thereby reducing the impact of shot noise. The resulting complexity of these systems limits their range of application. The most obvious example is the LCOF technique, for which the spectrum is collected from an aqueous sample that has been pumped into an optical fiber. While this setup has demonstrated the best results for multicomponent analysis to date, the system is not readily available for the analysis of cell or tissue samples.

The confocal Raman microscope has been widely applied in biology [172, 338–340] as well as in material science [341–343]. The objective of this chapter is to investigate the application of this ubiquitous and common instrument for multicomponent Raman analysis. The optical setup for a confocal Raman microscope is shown in Fig. 7.2; more details on the design considerations for such a system can be found in Ref. 58. When compared with the optical systems discussed in Section 7.2.1, the design is relatively simple and involves the inclusion of a pinhole in an intermediate image plane in the collection path. In confocal Raman microscopy, only photons that pass through this pinhole can contribute to the recorded spectrum; the spectrum is, therefore, composed of a contribution from a three dimensional, spatially resolved volume. In this way, the scattering from the microscope objective, which can generate a strong unwanted background, particularly for NIR excitation, can be reduced significantly. However, it must be noted that in the context of analyzing bulk samples such an aqueous multicomponent mixture, this advantage comes at the expense of a reduced sampling volume. In particular, the reduced depth of field will result in a weaker Raman spectrum and, therefore, a lower SNR. The laser will propagate over an extended depth within the sample, generating Raman scattering at each point along that path. The confocal aperture will limit the range of depth from which this scattering can be collected. In the following sections, this limitation is explored, and a theoretical analysis of the performance is proposed.

7.3.2 Throughput of Confocal Raman Microscopy

7.3.2.1 Confocal Pinhole Size

Although the confocal aperture greatly reduces unwanted background signals, the depth selectivity limits the number of Raman scattered photons that can be collected from

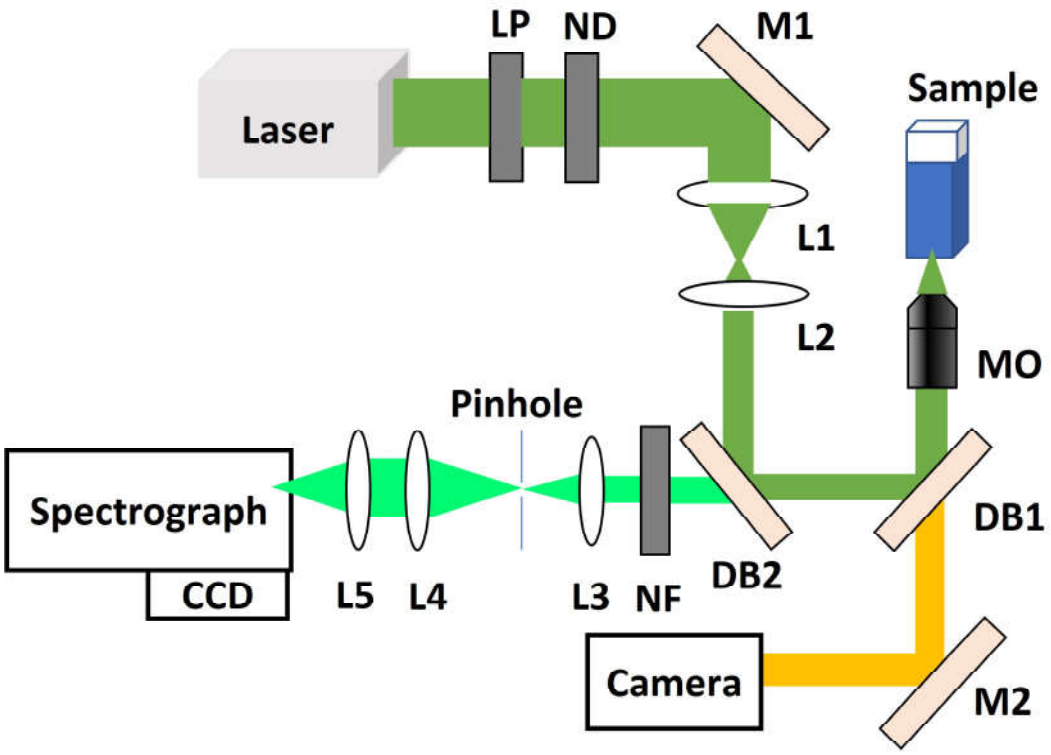

Figure 7.2: Typical confocal Raman microscopy system, similar to that used in Section 5: LP, line pass filter; ND, neutral density filter; L, lens; DB, dichroic beam splitter; M, mirror; MO, microscope objective.

the sample. The result is a relatively low SNR when compared with the systems reviewed in Section 7.2.1, which will limit the capability of the confocal setup for Raman multicomponent analysis. Increasing the pinhole size to mitigate this effect is not an attractive option; it must be noted that the pinhole diameter can also affect the wavenumber (spectral) resolution in the recorded spectrum; increasing the size of the pinhole diameter beyond the width of the pixel size will blur the spectrum, and some spectral features may be obscured (here, it is assumed that the spectrograph slit is at least as wide as the pinhole diameter). In Fig. 7.3, the loss in resolution associated with increasing the pinhole diameter is demonstrated; three Raman spectra recorded from a polymer sample (μ-Slide I Luer, Ibidi GmbH, Munich, Germany) are shown using the Raman system described in Section 7.5.1 with an acquisition time of 15 s and using pinhole sizes of 100, 200, and 400 μm. Two areas of the spectrum are magnified and shown in the left upper corner of Fig. 7.3, which clearly demonstrates that increasing pinhole size results in a loss of spectral resolution, even though the intensity is of the spectrum is increased. In the experiment outlined in Section 7.5, a 200 μm confocal aperture was selected as the best compromise between spectral intensity and resolution, providing an overall resolution of approximately 10 cm^{-1}. In the absence of a confocal aperture, the width of the spectrograph slit will control the spectral resolution and, therefore, will limit the volume of scattering from within the sample that contributes to the spectrum. In order to couple as many photons as possible into the spectrograph, various solutions have been proposed; one method is to disentangle a

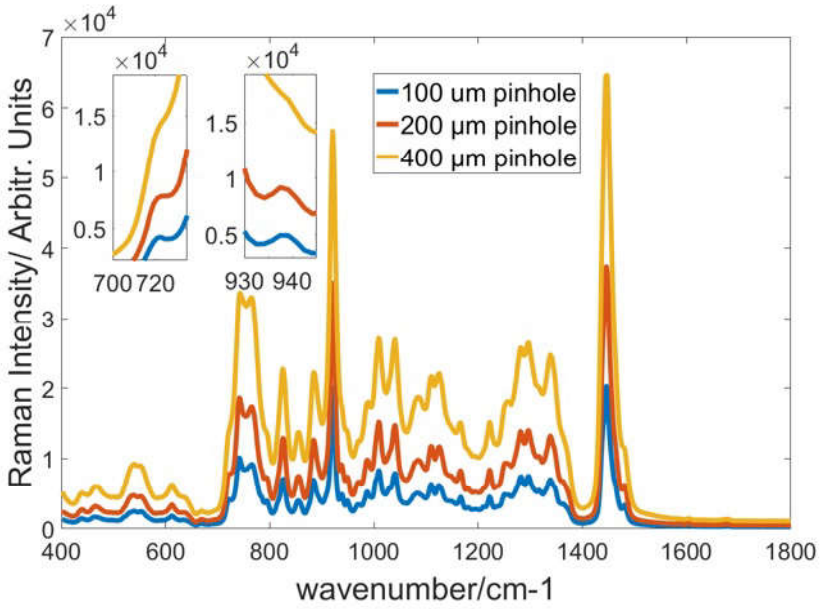

Figure 7.3: Comparison of Raman spectra recorded from a transparent polymer sample using 100, 200, and 400 μm pinholes.

fiber bundle and place each fiber along the slit entrance; [4] another technique involves using coded two-dimensional masks at the entrance to spectrograph, which facilitates the use of a deconvolution algorithm to recover the spectrum. [344] In this way, a high spectral resolution can be obtained from a wide slit.

7.3.2.2 Microscope Objective

The confocal aperture cannot be considered in isolation. The spectral intensity will also depend on the properties of the microscope objective (MO). This dependence is considered here, specifically in terms of numerical aperture (NA) and magnification. NA is defined in terms of the refractive index of the immersion medium, and the maximum angle of light that can be collected from the center of the sample. The NA is related to the minimum spatial resolution of an image as well as the image brightness and the depth of field. The optical sectioning properties of a confocal microscope are related to the NA and the pinhole aperture size. [345] This relationship can be defined in terms of the full width half-maximum (FWHM), which is defined as the width between the axial points where the intensity of an image defocuses to 50% of its peak value in the image plane. The FWHM of a confocal microscope has been defined by Wilson as follows: [345]

$$FWHM = 0.67\frac{\lambda}{(n-\sqrt{n^2-NA^2})} \times \sqrt{1+AU^2} \tag{7.2}$$

where λ is the wavelength of the laser excitation, n denotes the refractive index of the immersion medium, NA is the numerical aperture, and AU is the pinhole size in Airy

units, which are defined as follows:

$$AU = (D \times NA)/(1.22\lambda \times M) \tag{7.3}$$

where D is the pinhole aperture size and M is the magnification of the MO. Raman scattering can be collected from each axial point along the full range of the FWHM if the laser power remains constant over this range, and it can, therefore, be assumed that the irradiance of the Raman scattering at the detector, I_r, will be directly proportional to the FWHM, i.e. $I_r \propto FWHM$. Raman scattering that occurs at axial points outside of the FWHM will not contribute to the value of I_r, even though the laser may remain focused over an extended range of depth. The laser power will spread out at increasing distance from the focal plane of the MO, and the assumption that the laser power remains constant throughout the range of the FWHM requires that the full laser power remains focused over this range. Gaussian optics can be used to determine the width of the beam at various depths, which confirms that the laser beam will remain focused within the area of the pinhole aperture over the full range of the FWHM; for the sake of brevity, this analysis is not presented here.

The number of Raman scattered photons from a single point in a solution is assumed to be isotropic, and, consequently, the number of photons that contribute to the spectrum is determined by the solid angle of light that can be collected by the MO. Therefore, the irradiance of the Raman scattering at the detector is proportional to the square of the NA, i.e., $I_r \propto NA^2$. The intensity of the Raman spectrum will also be dependent on the transmittance of the MO, which represents the fraction of light that is transmitted by the MO. Since the same MO both delivers the source laser and collects the spectrum, the irradiance is also dependent on this quantity as follows: $I_r \propto T_{MO}^2$. The transmittance of the MO is wavelength dependent; here, for the sake of simplicity, only a constant value, T_{MO}, is used to represent the transmittance of the MO for the laser wavelength as well as for all of the wavelengths that make up the Raman spectrum, T_{MO}. Taking into account these various dependencies altogether, the following relationship can be written:

$$I_r \quad \propto \quad FWHM(T_{MO}NA)^2 \tag{7.4}$$

Equation 7.4 must be amended in order to account for the attenuation of the laser as it propagates through the FWHM, due to absorption and scattering by the molecules within the solution. In simple terms, a solution containing a high concentration of molecules will absorb and diffuse the laser light as it propagates over a relatively short distance. This attenuation can be modelled as follows:

$$T = \exp(-\alpha L) \tag{7.5}$$

where T denotes the transmittance of a sample of thickness L, with attenuation coefficient α, which is given by the sum of the absorption coefficient μ_a, and the reduced scattering coefficient μ_s [346] of the sample, $\alpha = \mu_a + \mu_s'$. Both of these quantities are typically measured in terms of cm^{-1}, i.e., the attenuation resulting from a thickness

of 1cm, which should not be confused with the unit of wavenumber used elsewhere in this chapter. The reduced scattering coefficient is a lumped property that takes into account both the traditional scattering coefficient μ_s as well as the anisotropy of the sample g. The purpose of the reduced scattering coefficient, which is defined as $\mu_s' = \mu_s(1-g)$, is to describe the diffusion of photons in a random walk of step size $1/\mu_s'$ cm, where each step involves isotropic scattering. [346] Both the reduced scattering coefficient and the absorption coefficient are wavelength dependent. For the sake of simplicity, a constant value is assumed here for both quantities for all of the wavelengths that make up the Raman spectrum as well as for the source laser wavelength. Taking attenuation into account, Equation 7.4 is rewritten as follows:

$$I_r \propto E = (T_{MO}NA)^2 \int_0^{FWHM} \exp(-2\alpha L)dL \tag{7.6}$$

where the factor 2 appears in the exponential function in order to account for the attenuation of the backscattered Raman photons along the same length of the sample, as well as for the source laser. The term on the right-hand side of Equation 7.6 is named the 'collection efficiency' in the discussion that follows and denoted by E. The value of α for a particular solution is proportional to the concentration of the analyte in solution. Specific values of α for a given mixture can be determined by experiment [346–349]; however, an examination of the literature revealed no information on the value of the scattering and absorptivity coefficients for glucose, lactic acid, or urea solutions. For the purpose of this discussion, a qualitative analysis of Equation 7.6 is given below, for a wide range of α, without focusing on specific values of α for mixtures containing physiologically relevant concentrations of various analytes. For the purpose of providing context, the values of the absorption and reduced scattering coefficients of a number of clinically relevant sample types are as follows [346,347]: skin at 500 nm, $\mu_a \approx 1.3\ cm^{-1}$, $\mu_s' \approx 30.6-68.7\ cm^{-1}$, $\alpha \approx 31.9-70\ cm^{-1}$; whole blood at 500 nm, $\mu_a \approx 100\ cm^{-1}$, $\mu_s' \approx 32\ cm^{-1}$, $\alpha \approx 132\ cm^{-1}$; water at 500 nm, $\mu_a \approx 0.0001\ cm^{-1}$, $\mu_s' < 0.003\ cm^{-1}$, $\alpha \approx 0.003\ cm^{-1}$.

In order to elucidate the variation in the collection efficiency [defined in Equation 7.6 above] as a function of magnification, NA, and α, a number of simulations are presented in Fig. 7.4 and Fig. 7.5. In Fig. 7.4(a)−(c), the collection efficiency E is plotted as a function of NA for $\alpha = 0.00001\ cm^{-1}$, $\alpha = 10\ cm^{-1}$, and $\alpha = 100\ cm^{-1}$, respectively. For all cases, the results are shown for a range of different magnifications that are commonly found in research microscopes: 2×, 4×, 10×, 20×, 40×, 50×, and 100×. The confocal pinhole diameter used in all of these calculations is $200\mu m$. Although the value of E is plotted as a function of the full range of NA for the various magnifications, the NA of low magnification objectives, such as 2× and 4×, is practically limited to approximately 0.05–0.1, while high magnification objectives such as 50× and 100× may have a range of NA from 0.8 to 1.4. MOs with a NA that is >1 require the use of an immersion medium such as water or oil; the results in Fig. 7.4 are based on a refractive index of $n = 1$ (air) for the 2×, 4×, 10×, 20×, and 50× magnifications, and a value of $n = 1.51$ (oil) for the 40× and 100× cases.

A set of high-quality commercial MOs that match the magnifications used in these

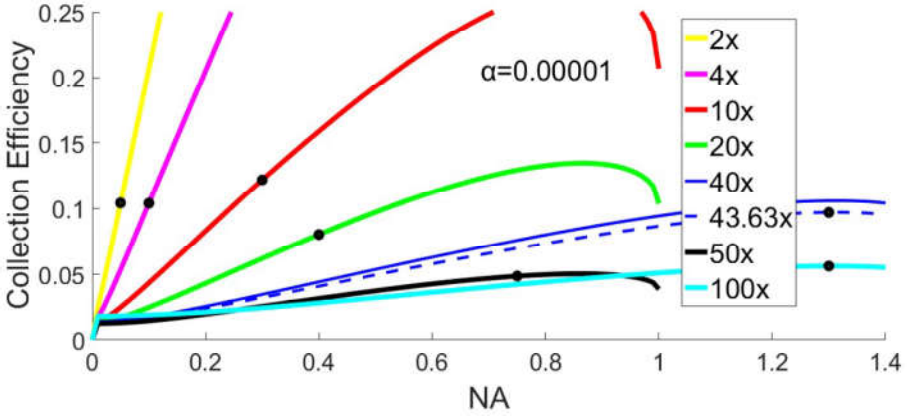

(a)

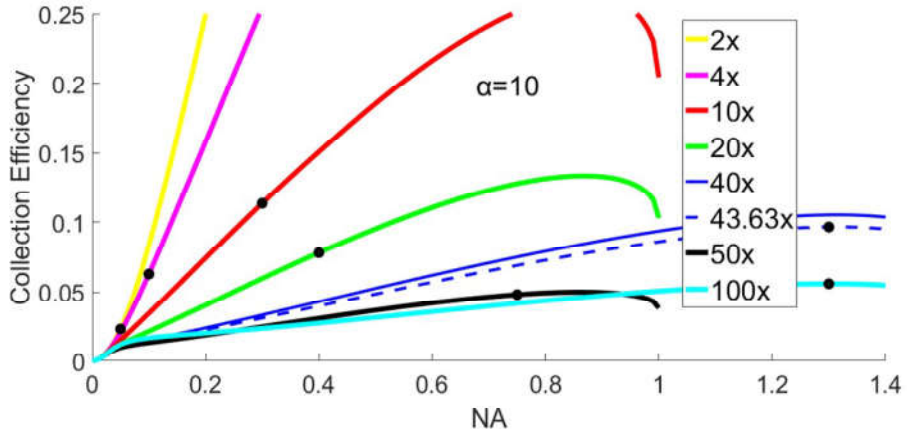

(b)

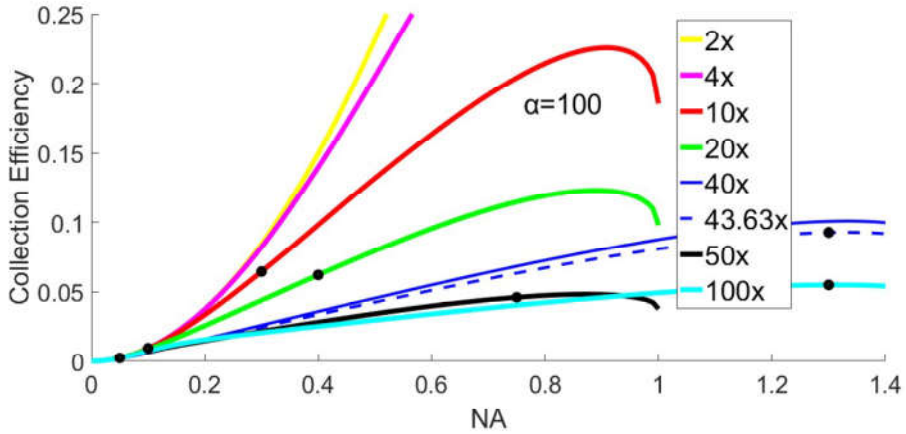

(c)

Figure 7.4: The collection efficiency for various microscope objectives with the different magnification for (a) $\alpha = 0.00001\ cm^{-1}$; (b) $\alpha = 10\ cm^{-1}$; (c) $\alpha = 100\ cm^{-1}$.

calculations are listed in Table 7.1. The properties of each MO are shown in the figure based on the manufacturer specifications; the values of the FWHM for each case are calculated based on Equation 7.2 for $\lambda = 532$ nm and $D = 200\ \mu m$. For each of the MOs, the value of E is also listed corresponding to the three values of α used in Fig. 7.4,

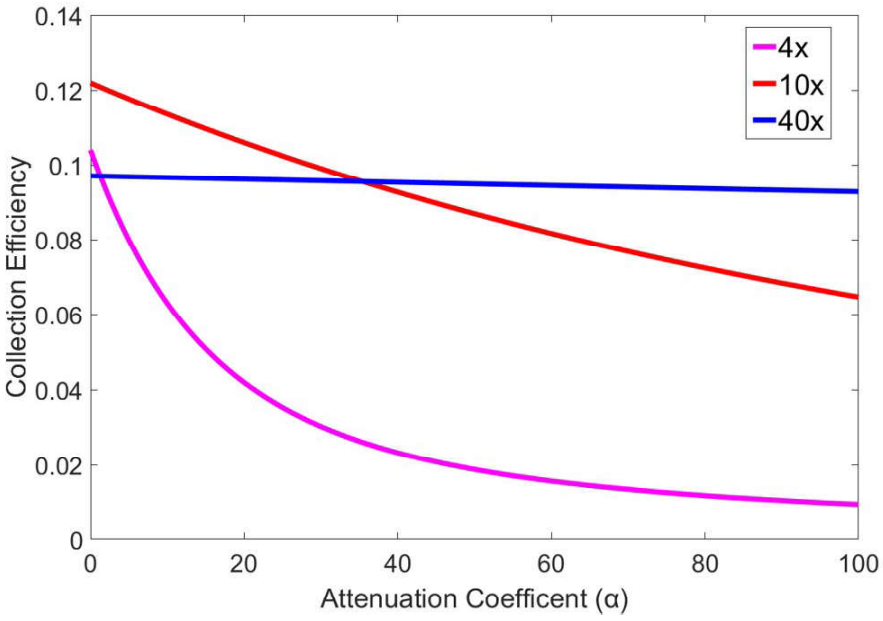

(a)

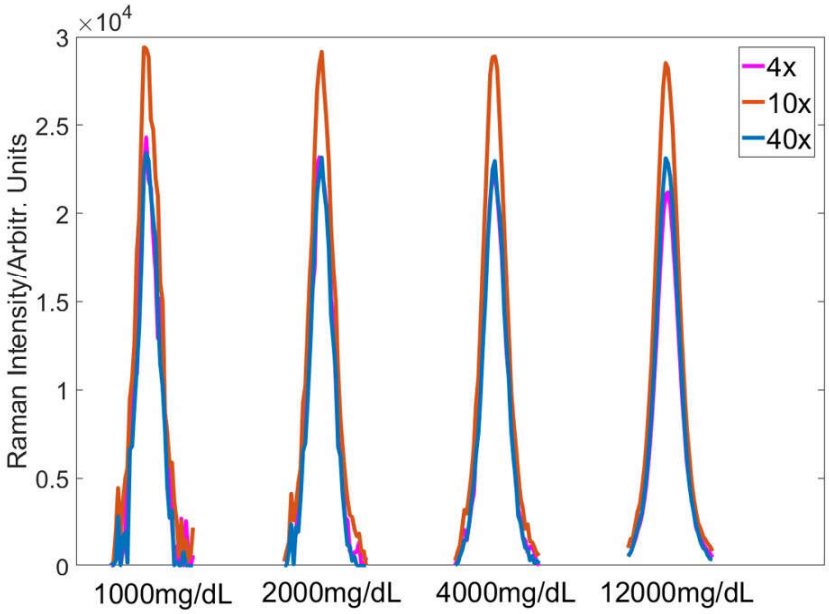

(b)

Figure 7.5: (a) Collection efficiency for the 4 × /0.1, 10 × /0.3, and 40 × /1.3 MOs listed in Table 7.1 as a function of the attenuation coefficient,α; (b) the intensity of the most prominent peak (in the range 801–861cm^{-1}) recorded using the 4×, 10×, and 40× MOs, from a solution with increasing concentrations of lactic acid. For each concentration, the peaks for 4× and 10× are normalized to the peak recorded using the 40× MO. The same exposure time was used in all cases.

and these values are indicated with thick black dots in these three figures.

For the case of the Zeiss 40× /0.13 MO, the effective magnification of this objective when used in an Olympus microscope, such as that in the Horiba system described

Table 7.1: Specifications (Where Available) for Several MOs That Are Indicated in Fig.7.4 Using Black Dots

Microscope Objective	**Olympus PLan 2×/0.05**	**Olympus PLanN 4×/0.05**	**Olympus UpLanFLN 10×/0.3**	**Olympus PLanN 20×/0.4**	**Zeiss Plan-Neofluar 40×/1.3 oil**	**Olympus MPLanN 50×/0.75**	**Olympus UPLFLN 100×/1.3 Oil**
Magnification	2×	4×	10×	20×	43.63×	50×	100×
Numerical aperture	0.05	0.1	0.3	0.4	1.3	0.75	1.3
Immersion medium	air	air	air	air	oil	air	oil
T_{MO}	0.97	0.97	0.97	0.97	0.8-0.9	0.93	0.91
FWHM(cm)	0.22	5.52×10^{-2}	7.2×10^{-3}	2.7×10^{-3}	4.83×10^{-4}	4.97×10^{-4}	1.98×10^{-4}
$E_{(\alpha=0.00001)}$	0.104	0.104	0.121	0.08	0.097	0.049	0.056
$E_{(\alpha=10)}$	0.023	0.063	0.114	0.078	0.096	0.048	0.056
$E_{(\alpha=100)}$	0.002	0.009	0.065	0.062	0.093	0.046	0.055

in Section 7.5, it will be greater than 40×. Since Olympus and Zeiss microscopes use tube lenses with focal lengths of 180 mm and 165 mm, respectively, the effective magnification the Zeiss objective is $40\times(180/165) = 43.636$. A dashed blue line is included in each part of Fig. 7.4, representing this magnification. The transmittance of the 40× varies between 0.8 and 0.9 in the visible range of wavelengths; a value of 0.8 is selected to calculate the collection efficiency in the results presented here.

Fig. 7.4(a) indicates that the collection efficiency is maximized for high NA and low magnification; however, these two properties are, in general, mutually exclusive for conventional MOs. It is clear that for low levels of scattering and absorption (α = 0.00001 cm^{-1}) similar to the case of pure water, the lower magnification MOs, 2×, 4×, and 10× provide superior performance when compared with the higher magnification MOs, 20×, 50×, and 100× (with the 10× providing the optimal performance), which is due to the significantly higher values of FWHM for these objectives. This was confirmed experimentally by testing the performance of the various MOs listed in Table 7.1. The 40×/1.3 MO also provides high performance due to the relatively high NA for this level of magnification, which increases the number of photons that are collected from the relatively narrow FWHM.

The equivalent results are shown in Fig. 7.4(b) for a significantly higher attenuation (α = 10 cm^{-1}). The performance of the lower-magnification objectives, 2× and 4×, deteriorates for this case; this is due to the increased attenuation over the relatively large FWHM for these objectives. In contrast, the MOs with a narrow FWHM remain almost unchanged. The 10×/0.3 MO provide optimal performance for all cases for the range of $0 < \alpha < 10$ cm^{-1} due to its competitive values for both FWHM and NA when compared with the other objectives.

The case of α = 100 cm^{-1} is shown in Fig. 7.4(c), where the attenuation is similar to that for whole blood. The low magnification MOs suffer a significant drop in performance, and the collection efficiency of the 10× MO reduces by ~45% compared with the previous cases. The performance of the higher-NA lenses remains relatively stable. One can extend this argument to the case where the concentration becomes so high that the sample becomes solid powder. In this case, the high-NA MOs will continue to provide high performance while MOs with low NA will provide poor results due to the limited depth that the source can penetrate into the sample.

Three of the objectives (4×/0.1, 10×/0.3, and 40×/1.3) were selected for further in-

vestigation. In Fig. 7.5(a), the collection efficiency of these three objectives is plotted as a function of the attenuation coefficient in the range $0 < \alpha < 100\ cm^{-1}$. The 10× MO is predicted to provide the best performance over the range $0 < \alpha < 35.43\ cm{-}1$, and beyond this range the 40× MO will provide optimal performance. The performance of the 10× MO is predicted to reduce by 45% over the full range, while the performance of the 4× is predicted to decrease more rapidly to ~ 10% of its initial value. An experiment was carried out to investigate this behavior qualitatively by recording spectra from a solution of lactic acid with increasing concentration using these three MOs, and the results are shown in Fig. 7.5(b). The most prominent peak, located in the region of 801–861 cm^{-1}, is shown for concentrations of 1000, 2000, 4000, and 12,000 mg/dL. An attempt to quantitatively relate the value of α to a specific concentration of lactic acid is beyond the scope of this chapter; however, it is possible to make a number of qualitative observations that support the theory presented here. For all four cases, the peak intensities are normalized to the intensity of the peak recorded using the 40× MO, since this objective is predicted to provide the most stable performance over all values of α. For the four different concentrations, the 10× MO provides the best performance,which is predicted by the theory for the range of $0 < \alpha < 35.43\ cm^{-1}$. It is clear that as the concentration of lactic acid is increased, the performance of both the 4× and 10× MOs reduce relative to the 40× case, with the 4× MO deteriorating more rapidly, which is also predicted by the theory. Although these observations support the theory proposed here, a more comprehensive investigation is required for a full validation.

This section is concluded by defining the wavelength dependent version of Equation 7.6. In this case, $I_r(\lambda)$ refers to the irradiance of a specific wavelength component λ of the Raman spectrum on the detector,

$$I_r(\lambda) \propto T_{MO}^{\lambda} T_{MO}^{\lambda_s} NA^2 \int_0^Q \exp\left[-L(\alpha_\lambda + \alpha_{\lambda_s})\right] dL \qquad Q = min(FWHM_{\lambda_s}, FWHM_\lambda) \tag{7.7}$$

where λ_s denotes the source laser wavelength. The transmittance of the MO is now considered separately for λ_s and λ. The attenuation is also considered separately for both wavelengths; the value of the FWHM is wavelength dependent as are the absorption and scattering coefficients.

7.4 Comparison of Collection Efficiencies of different Raman Systems

In this section, a comparison of the collection efficiencies of the four systems illustrated in Fig. 7.1, as well as the confocal architecture, is provided. This comparison is approximate and is not intended to provide a rigorous analysis of each of these systems. In order to compare the various architectures, a more general definition of the

collection efficiency is presented here:

$$E = T_{fb} N A^2 \int_0^Q e^{-2\alpha L} dL \tag{7.8}$$

This equation is similar in form to that derived earlier for confocal microscopy [see Equation 7.6]; however, in this case the term T_{MO}^2 is dropped for the sake of simplicity, as the transmission loss associated with the delivery and collection paths will be similar for all cases and will be approximately equal to 1. An additional term, T_{fb}, is included to take into account loss in coupling the Raman scattered photons into the spectrograph for the case of using a fiber bundle, which has a limited collection area due to the physical separation of fibers. In addition, the term FWHM is replaced with Q to more generally represent the depth into the sample that the laser can be delivered to and the scattered photons can be collected from. For the sake of convenience, it is assumed that the same microscope objective (10×/0.3) is used to collect the scattered photons from the sample. For cases in which a fiber bundle is used, the value of T_{fb} is taken to be 0.68, based on the design of commercially available bundles (Thorlabs; BFL200HS02); in all other cases, T_{fb} is taken to be 1. The collection efficiency is examined for the three cases of $\alpha = 0.5$, 10, and 100 cm^{-1}. For the sake of simplicity, it is assumed that all values of transmission, absorption, and scattering are constant for all wavelengths.

The setup in Fig. 7.1(a) employs a 90° collection geometry, which can significantly reduce the unwanted background signal by separating the delivery and collection paths. For the ideal case, it can be assumed that the source laser remains focused over an extended length within the sample, which can be imaged to the full length of spectrograph slit. Therefore, the value of Q in Equation 7.8 is given by the spectrograph slit length divided by the magnification, which for the spectrograph/charge-coupled device (CCD) used in our experiment, this gives a value of $Q = 0.64$ mm.

Equation 7.8 takes into account the propagation of the Raman scattered photons back along the same path from which the laser was delivered. In this case, however, if the scattering takes place close to the edge of the container, it can be assumed that the path length of the Raman scattered photons within the sample is approximately zero. Rather than adapt Equation 7.8 for this special case, the value of Q is halved to give $Q = 0.32$ mm.

The setup in Fig. 7.1(b) employs a fiber bundle. The fibers are arranged linearly in the terminal end and coupled with the slit of spectrograph. The finite diameter of the collection end of the fiber bundle has the same effect as a confocal aperture. This diameter is taken to be 640 μm (Thorlabs; BFL200HS02). This system can be considered to be the same as the confocal Raman microscope considered in this chapter; however, it has a significantly larger confocal aperture, which will result in greater collection efficiency. In this case, the large confocal aperture will not reduce the spectral resolution, due to the linear arrangement of the fibers at the output. However, the large confocal aperture will capture a more intense background signal, which will limit the performance of the system, as discussed in Section 7.3.1. For this system, the calculation of Q is based on the FWHM in Equation 7.2 and is calculated to be $Q = 0.23$ mm. The

setup in Fig. 7.1(c) employs a non-imaging paraboloidal mirror to maximize the signal that can be collected from a 1 mm^2 spot area with a large collection solid angle, and is designed to achieve optimal collection efficiency for a whole blood sample. The optical properties of this system, in terms of collecting photons from an extended depth in a sample, cannot be discerned, and it is, therefore, not possible to describe this system using Equation 7.8, so it is not included in Table 7.2.

The LCOF system illustrated in Fig. 7.1(d) enhances the Raman spectrum by guiding the laser over the length of a waveguide and collecting the Raman photons that are guided back to the end of the fiber. A comprehensive analysis of the collection efficiency of this system is provided by Qi. [332] Here we provide a simplified model, once again using Equation 7.8, where Q is taken to be the length of the LCOF, which is assumed to be 2 m.

Table 7.2: Comparison of Setups Illustrated in Fig.7.1

	Fig.7.1(a) [3]	**Fig.7.1(b) [4]**	**Fig.7.1(d) [6]**	**Confocal**
Q	320 μm	230 μm	2 m	72 μm
Back-ground	low	high	low	low
$E_{(\alpha=0.5)}$	0.567	0.275	12.30	0.129
$E_{(\alpha=10)}$	0.425	0.226	0.615	0.121
$E_{(\alpha=100)}$	0.089	0.061	0.061	0.068

In Table 7.2, the four systems illustrated in Fig. 7.1 are compared using the definition of collection efficiency given in Equation 7.8. The value of Q relates to the depth in the sample from which scattering can be collected, and it can be seen that the confocal architecture has the worst performance in this regard. For samples with low attenuation ($\alpha = 0.5\ cm^{-1}$), the LCOF system is the best performer with a collection efficiency that is between 25 and 100 times better than the other systems, while the confocal system has approximately half the collection efficiency of the traditional architecture for Raman multicomponent analysis proposed in Ref. 4. For highly attenuating samples, such as whole blood, the confocal architectures are predicted to perform as well as the other systems.

7.5 Materials and methods

In this section, we outline an experiment to examine the performance of the confocal Raman microscope for multicomponent analysis. In terms of chemicals, concentrations, mixtures, and processing, the experiment is similar to that used in Ref. 3.

7.5.1 Confocal Raman Microscope

All spectra were recorded using a commercial confocal Raman microscope (Horiba Jobin Yvon LabRam 800 HR). All of the experiments used a 600 lines/mm diffraction

grating in a spectrograph with focal length of 800 mm. This system uses a 100mW single-mode diode-pumped solid-state (DPSS) laser with a wavelength of 532 nm (Torus; Laser Quantum, UK). A back-illuminated, cooled, CCD detector (Synapse; Horiba, Japan) operating at $-80°C$, was used to record all spectra. This camera has a typical read noise of 5 electrons and a dark current of 0.002 electrons/pixel/s. A 10× microscope objective (UMPlanFl 10 ×/0.3; Olympus, Japan) and a confocal aperture of 200 μm were used for all experiments unless otherwise indicated. The MO focuses the laser onto the sample, which is contained within a cuvette, with a base made from a Raman grade calcium fluoride coverslip with a thickness of ~ 200 μm (Crystran, UK), which provides a spectral resolution of approximately 10 cm^{-1} using the spectrograph and grating mentioned above. In order to reduce the effect of wavenumber shifting due to temperature variation, all experiments were conducted in a temperature-controlled laboratory. The wavenumber range of all Raman spectra recorded was $402-2048$ cm^{-1}.

Raman spectra are recorded from all solutions using the UplanFLN 10×/0.3 MO; for all cases, three spectra with 20s integration time were recorded and averaged together to produce a single spectrum with an effective acquisition time of 60 s.

7.5.2 Sample Preparation

Powders of glucose (≥ 99.5%, G7528; Sigma-Aldrich, Ireland), urea (≥ 98%, U5378; Sigma-Aldrich, Ireland), and lactic acid (≥ 98%, L1750; Sigma-Aldrich, Ireland) were mixed based on the specific weight and diluted in deionized water into 19 mixtures with varying concentrations. The concentration of each chemical used in all 19 mixtures is shown in Table 7.3. Since lactic acid in solution can dissociate depending on different pH environments, the measurable concentration of lactic acid will change in solution. [3] In this experiment, the pH of each solution was measured using a pH meter (Eu Tech Instrument). Based on the measured concentration of lactic acid and the measured pH, the actual weight of lactic acid that was added to each solution can be calculated using the formula below:

$$C_{la} = (1 - 1.38 \times 10^{(-4+pH)}) \times C_{ex} \tag{7.9}$$

where C_{ex} is the actual concentration (in the sense of the mass of lactic acid that was added to the volume of water), and 1.38×10^{-4} is the dissociation constant of lactic acid. Table 7.3 shows the list of concentrations and pH values for each solution.

In addition to the 19 mixtures listed in Table 7.3, three Raman spectra were recorded from "pure" solutions of glucose, lactic acid, and urea in isolation; these spectra are used in the final pre-processing step discussed below. A concentration of 5 g/dL was used for each case.

7.5.3 Numerical Pre-processing

The raw spectra that were recorded cannot be immediately input to a multivariate statistical analysis for the purpose of estimating component concentration due to the presence of noise and the unwanted baseline signal that varies across the set of recorded

Table 7.3: List of the Concentrations (mg/dL) of Glucose, Urea, and Lactic Acid in the 19 Mixtures Used in This Experiment

	Glucose (mg/dL)	**Lactic acid (mg/dL)**	**Urea (mg/dL)**	**pH**
1	415.32	191.89	88.4	2.69
2	606.52	133.13	108.6	2.78
3	675.24	54.87	172.2	2.98
4	271.24	155.11	189.16	2.78
5	255.78	84.56	253.94	2.89
6	208.06	141.31	70	2.76
7	183.6	183.52	126.25	2.63
8	255.36	191.09	51.9	2.68
9	546.46	55.25	132.16	2.96
10	569.82	200.21	201.74	2.66
11	497.82	133.05	244.6	2.77
12	233.74	89.22	252.36	2.83
13	363.98	212.20	56.54	2.64
14	160.18	172.70	228.76	2.76
15	682.92	225.40	227.5	2.69
16	785.1	91.13	101.9	2.93
17	203.38	144.27	131.89	2.72
18	180.08	184.12	131.89	2.72
19	302.7	215.46	54.79	2.68

spectra. Therefore, it is necessary to remove or reduce the impact of these interferences before performing multicomponent analysis.

Cosmic ray artefacts appear in the spectrum in the form of spurious, narrow-band peaks with high intensity. The three raw 20 s spectra are used to remove cosmic rays; corresponding pixels are compared across the three spectra, and an intensity difference that is greater than the expected noise amplitude identifies the presence of a cosmic ray. Regions of the spectra that contain cosmic rays are omitted from the averaging process.

Following cosmic ray removal, smoothing is performed in order to reduce the impact of shot noise, using an algorithm that combines maximum likelihood estimation and Savitzky-Golay (SG) smoothing. [308] This algorithm has been demonstrated to perform better than other smoothing algorithms such as traditional SG smoothing filter and can improve the SNR of the input spectrum by > 100% while also preserving the underlying spectral peaks. [308]

The final pre-processing step is to subtract the unwanted baseline that varies for each recording. In order to estimate this baseline, a classical least-squares algorithm is applied to the raw spectrum that calculates the best fit of a set of component background spectra that make up the raw spectrum, as well as an N-order polynomial. This algorithm is similar to the well-known extended multiplicative signal correction (EMSC) algorithm that is commonly used to remove the unwanted baseline, including background signals such as the spectrum from glass components. [350] The least-

squares algorithm used here assumes that the raw spectrum is composed of a linear weighted sum of reference spectra recorded from samples of (i) glucose, (ii) lactic acid, and (iii) urea, shown in Fig. 7.6(a) (for each of these three reference spectra, an automated background subtraction algorithm was applied; [350]) (iv) a spectrum recorded from a pure water sample; this spectrum contains contributions from the water, the calcium fluoride window, the MO, and other optical elements (no baseline subtraction is applied to this spectrum), and finally (v) an N-order polynomial to account for the varying baseline. [172] The least-squares algorithm determines the weight of each of these five components (this is implemented separately for each term in the N-order polynomial) to optimally fit their sum to the raw spectrum. The final spectrum is obtained by subtracting each of the weighted background components from the raw spectrum. A polynomial of order $N = 7$ is used in this algorithm.

7.5.4 Partial Least-Squares Regression

PLSR is a multivariate statistical method that is commonly used in Raman multicomponent analysis. All the experiments reviewed in Section 7.2.1 employed PLSR. The principle of this technique is to decompose a set of independent variables (in this case, the concentrations of the various analytes) and a set of corresponding dependent variables (a matrix of Raman spectra related to these components) into sets of scores and sets of corresponding loadings, and to find the maximum covariance between the scores of the independent variables and the scores of the dependent variables. In the process of establishing the PLS predictive model, choosing an optimal number of components is important in order to reduce the presence of noise.

The root mean square error (RMSE; the error between the reference concentrations and the predicted concentration) and the coefficient of determination (R2; the correlation between the predicted and reference values), are two important metrics that are commonly employed to determine the appropriate number of components to use and to estimate the error of the model in terms of predicting the concentrations of an unknown mixture. [3–5, 163, 318–327, 329, 331, 332, 351] In the experiment presented here, RMSE and R^2 are used to evaluate the performance of the model based on leave-one-out cross-validation.

7.6 Results

Raw spectra were recorded from individual solutions of glucose, lactic acid, and urea, in deionised water, as well as from a pure water sample; these spectra were processed for cosmic ray removal, smoothing, and background subtraction, as described in Section 7.5, to create the set of reference spectra for input to the EMSC algorithm. The reference spectra for glucose, lactic acid, and urea are shown in Fig. 7.6(a). As described in Section 7.5.3 and Fig. 7.6(b), this algorithm estimates (and subtracts) the unwanted baseline from each of the spectra recorded from the 19 mixtures. These 19 pure spectra are independent variables for use in the PLS model for the three chemicals. The RMSE

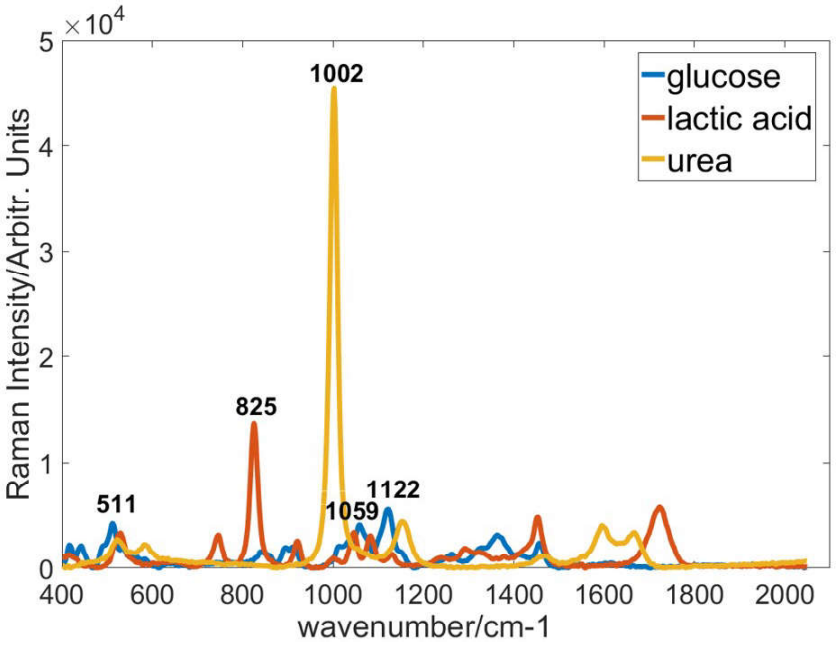

(a)

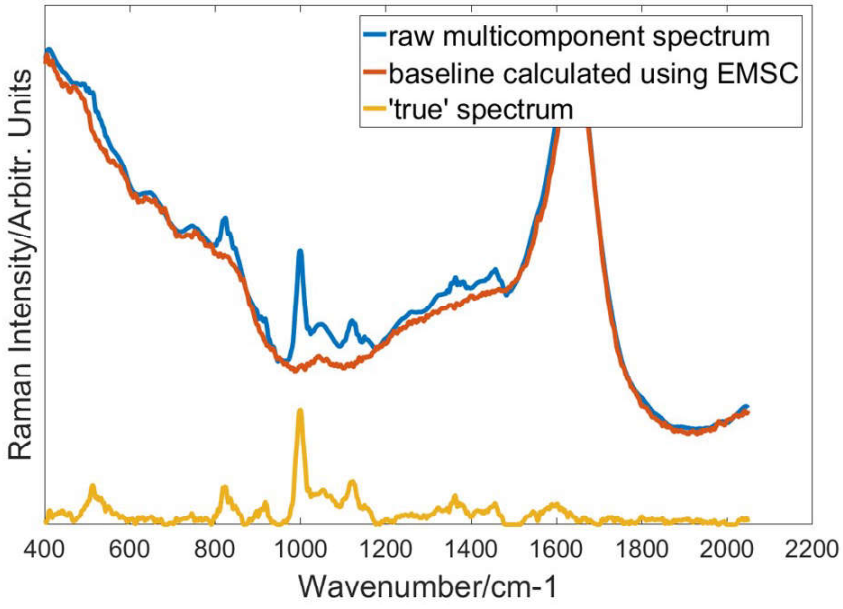

(b)

Figure 7.6: (a) Reference spectra of glucose, lactic acid, and urea after processing. These spectra are used in the EMSC algorithm for removing the background from each component spectrum. (b) A raw spectrum from one of the 19 mixtures following cosmic ray removal and smoothing (blue), the baseline that is calculated using the EMSC algorithm (red), and the corrected spectrum (yellow).

of the predictions vary as a function of the number of PLS components that are used in the model for each of the three chemicals, and this variation is shown in Fig. 7.7(a).

The optimal number of components to be used by the PLS algorithm is the number that results in the smallest RMSE. A crucial property of these components is that they

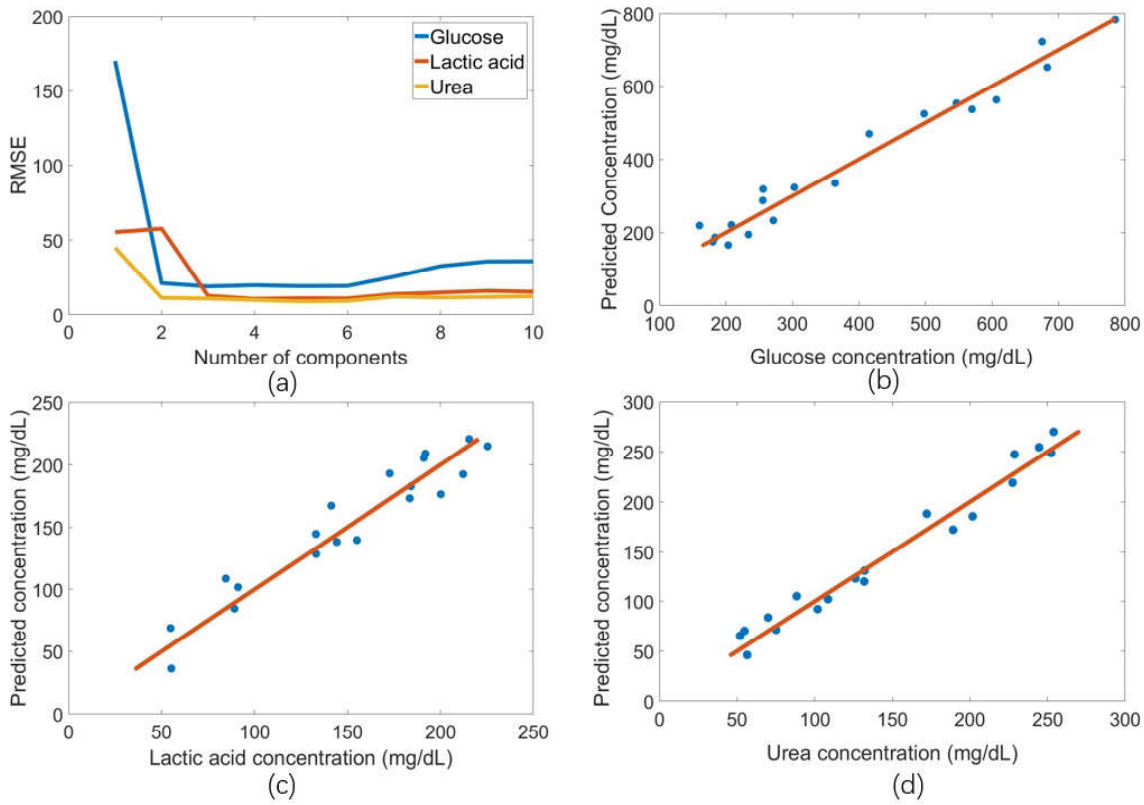

Figure 7.7: (a) Number of components used in the PLS model versus RMSE for glucose, lactic acid, and urea; (b) result of PLS for glucose using five components; (c) prediction result of PLS for lactic acid using four components; (d) result of PLS for urea using five components.

should accurately represent the characteristics of the signal. The number of components that are selected should include many of the key spectral features of the analyte spectra, while omitting components with low SNRs. The coefficient of determinant (R2) can be used to represent the robustness of the PLS model; in this experiment, both RMSE and R2 are used to determine that the optimal number of components for glucose and urea is five, and for lactic acid the optimal number of components is four.

The predictions of PLS cross-validation are plotted for the three chemicals in Fig. 7.7 (b)-(d). The RMSE of the model for glucose is calculated to be 17.81 mg/dL with R^2 = 0.93; the RMSE for lactic acid is 10.6 mg/dL with R^2 = 0.91; and the RMSE for urea is 7.6 mg/dL with R^2 = 0.96. The accuracy of these predictions and the accuracy of similar predictions found in previous studies are compared in Table 7.4. The results presented here are comparable with those found in Goetz et al. [3] and Berger et al. [4], which were also based on three analyte mixtures. Also included in the table are the results of Enejder et al. [5] and Qi and Berger [332], both of which are based on body fluid (whole blood, blood serum, and urine), and, therefore, include several more analytes. Disregarding the increased complexity in these models due to the inclusion of more analytes, the results of the predictions presented here for the three chemical mixtures are similar to the prediction results in these studies. The acquisition time used in the experiment presented here is 60s, which is also consistent with the acquisition times used in the previous experiments, which vary significantly from 40 s to 5 min.

7.7 Conclusion

In this chapter, the conventional confocal Raman microscope has been investigated to simultaneously measure the concentration of multiple chemicals in aqueous solution, which is commonly referred to as multicomponent analysis. Previous investigations have focused on developing optical systems that maximize the number of Raman scattered photons that can be collected from blood and urine samples, thereby maximizing the SNR of the recorded spectrum and reducing the necessary acquisition times, and these systems have been reviewed in Section 7.2.1. The best performing system that has been proposed to date, in terms of acquisition time, the number of analytes that can be simultaneously measured, and the minimum concentration that can be detected for each analyte, is based on the use of liquid-core optical fibers. These fibers can deliver the source laser over an increased volume of the solution and guide the scattered photons to the detector. While the confocal Raman microscope cannot match the same level of performance for multicomponent analysis, it has the advantage of being readily applicable to a multitude of different sample types and can be found in many research laboratories. Here, we have investigated the performance that can be expected from a confocal Raman microscope for multicomponent analysis both theoretically and experimentally.

In Section 7.3, the confocal Raman microscope is discussed. In particular, the efficiency of this system is analyzed in terms of the collection of Raman scattered photons from an aqueous solution. The role of the confocal pinhole is to (i) to provide a

Table 7.4: Comparison of Results with Other Raman Setups

Results Using Confocal Raman Microscopy (60s Acquisition Time)		
Analytes	**RMSE (mg/dL)**	R^2
Glucose	17.81	0.93
Lactic acid	10.6	0.91
Urea	7.6	0.96
Goetz et al. (1995) [3] (40s Acquisition Time)		
Analytes	**RMSE (mg/dL)**	R^2
Glucose	20.17	0.99
Lactic acid	12.92	0.94
Urea	19.07	0.92
Berger et al. (1996) [4] (100s Acquisition Time)		
Analytes	**RMSE (mg/dL)**	R^2
Glucose	21.62	N/A
Creatinine	13.57	N/A
lactic acid	11.71	N/A
Enejder et al. Using Parabolic Mirror [5] (5min Acquisition Time)		
Analytes	**RMSE (mg/dL)**	R^2
Glucose	21	0.97
Urea	4.9	0.94
Qi and Berger (2007) [332] Using LCOFs (64s Acquisition Time for Creatinine, 150s for Glucose)		
Analytes	**RMSE (mg/dL)**	R^2
Glucose	8.8	N/A
Creatinine	4.3	N/A

depth resolution and (ii) to reduce unwanted scattering that originates in optical elements that are common to the (laser) delivery and collection paths, such as the microscope objective. While the reduction of the unwanted background signal is especially important in Raman multicomponent analysis, the limited depth resolution is counterproductive, as this significantly reduces the scattering that can be obtained from a homogenous scatterer such as an aqueous solution. Increasing the pinhole size is an obvious solution to this problem; however, as demonstrated in Section 7.3.2.1, an increase in pinhole size has the unwanted effect of increasing the spectral resolution. A pinhole size of 200 μm was found to be a good compromise between these two effects, providing a resolution of $\sim 10\ cm^{-1}$.

The interaction between the confocal aperture and the microscope objective was also investigated in terms of collection efficiency. Objectives with low NA can collect scattering over a significantly larger depth of field when compared to high-NA lenses for a given confocal pinhole size; however, high-NA lenses have the advantage of a larger solid angle over which scattered photons are collected. A theoretical investigation of these properties reveals that, in general, a high ratio of NA to magnification is desirable. The theory proposed here also takes into account scattering and absorption within the sample and the resulting attenuation of the source laser as it propagates (and diffuses) through the sample. For highly absorbing/scattering samples, the depth of field over which Raman scattering can be collected is reduced, and thus the advantage of low-magnification, low-NA objectives is negated. The experimental results presented in the chapter are consistent with the theory, and it was found that a 10×/0.3 microscope objective provided the best results for all mixtures that were investigated in this chapter.

In Section 7.4 we extended the model for collection efficiency to estimate the performance of the various customized systems reviewed in Section 7.2.1. This analysis predicts that the LCOF system provides significantly superior performance for samples with low absorption and scattering coefficients for equivalent exposure times; however, as sample absorption/scattering increases, the confocal Raman system offers similar performance to the other systems.

Multicomponent analysis was performed using 19 mixtures of glucose, urea, and lactic acid in an experiment that closely emulates the initial work of Goetz et al. [3]. The experiment is described in detail in Section 7.5 and used a commercial high resolution confocal microscope with a 60 s acquisition time. A rigorous pre-processing protocol is also proposed in Section 7.5 to reduce the noise in the recorded spectra and to remove the unwanted baseline that varies across the recordings. The latter technique is based on the extended multiplicative scattering correction algorithm and is similar to that used in previous investigations. The results of PSLR applied to the 19 pre-processed spectra are presented in Section 7.6 and evaluated using the commonly used metrics of RMSE and the coefficient of determination. The results are shown to be similar to those obtained in previous studies, with only the liquid-core optical fiber approach showing markedly better measurements. It must be noted that the confocal Raman microscope can match the performance of any of the systems described in Section 7.2.1, including the liquid-core optical fiber system, if a sufficiently long

acquisition time is used. Modern detectors have dark current values that are almost negligible (< 0.001 electrons/pixel/second), and, therefore, shot noise is the only noise source that needs to be considered. Increasing the acquisition time will, therefore increase the SNR; however, the rate of increase over time will slow down. Recording time in the order of several minutes may be required to fully match the performance of the liquid-core systems.

It has been previously suggested that the shot noise associated with the water in the sample poses a fundamental limit for Raman multicomponent analysis in terms of the minimum concentration that can be measured. Although water is a relatively weak Raman scatterer, the abundance of water molecules relative to the molecules of interest results in an appreciably large spectrum from the water. The mean water spectrum can be subtracted, but the shot noise from this spectrum remains, the amplitude of which places a limit on the smallest peak that can be detected. The same argument can be applied to any of the background spectra that are subtracted in the preprocessing step described in Section 7.5. Since the confocal aperture optically filters much of this unwanted background from reaching the detector, the confocal Raman microscope is well suited to reducing this noise source (shot noise from background signals). Noise from the water spectrum cannot be removed in the same way; however, recently it has been proposed that removing water from the sample can help improve the spectroscopic measurement of human serum. [352] This approach could significantly reduce the minimum measurable concentrations using confocal Raman multicomponent analysis and may offer an exciting avenue for future research.

In the context of the overall contribution in this thesis, this chapter offers a method to probe the quality of the growth medium of live cells in culture using confocal Raman, while the contributions in previous chapters address the characterisation of the cells themselves using confocal Raman and or digital holographic microscopy and possibly optical diffraction tomography. All of these methods have the common link of being label free and non-invasive in the sense that the cells will not be damaged during the recording process.

Chapter 8

Conclusion

The main goal of this thesis was to develop an array of *non-invasive* and *label-free* cellular analysis methods for the purpose of diagnostics and/or basic research. In particular, quantitative phase imaging methods were developed for the quantitative measurement of morphological features of cells. The related technique of optical diffraction tomography was also of interest, which can provide information on features internal to the cells. Also of particular interest was Raman spectroscopy, which can provide chemical information on the cell structure. A secondary goal of the thesis was to combine the morphological and chemical information provided by these complementary techniques in order to better characterise the cells.

Chapters 3-7 are all contributory chapters in the sense that these all progress the field of phase imaging, diffraction tomography and Raman spectroscopy for cellular analysis, and each of these has an associated publication or planned publication. The first four of these chapters are related to quantitative phase imaging and diffraction tomography, while the latter two relate to Raman spectroscopy. Chapter 6 serves a bridge between these two topics since it develops both modalities combined.

In the first contributory chapter, Chapter 3, the technique of spatial light interference microscopy (SLIM) was investigated for cellular analysis. SLIM is one of several phase imaging modalities and has several advantages over interferometric techniques; Firstly, it uses white light resulting in low noise images and high resolution. It is also relatively simple to build and to use once calibration of the spatial light modulator (SLM), the key component in the setup, has been implemented. The main contribution in Chapter 3 was the development of an improved calibration protocol for the SLM, which can provide more accurate phase images. However, despite this improvement, we discovered that the presence of the halo artifact makes SLIM an unreliable technique for cellular classification based on morphology. Halo removal remains an unsolved problem in SLIM research and the presence of the halo presented a difficulty that could not be tolerated for our own research goal, which is ultimately to be able to characterise cells in a label free manner. For this reason, we turned our attention to digital holographic microscopy (DHM) in Chapter 4, which although is more challenging experimentally, provides an accurate estimate of the phase image that contains no halo artifacts.

Two significant limitations of DHM when compared with SLIM are (i) high levels of

coherent noise that corrupt the phase image and (ii) a lower resolution. In Chapter 4, a novel synthetic aperture method for DHM (SA-DHM) is proposed that overcomes these two problems. At the heart of this contribution is the so-called X-module, based on self reference interferometry, which is the most significant contribution in this thesis. This module is placed at the image port of an existing microscope and is aligned with an illumination module, which uses a galvo-scanner to illuminate an annular scanning laser onto the filter plane of the microscope condenser. The narrow annular filter inside the X-module matches the annular scan of the focused laser in the filter plane of the condenser. A mathematical model of the system predicts the improvement in coherent noise and the shape of the real-time synthetic aperture transfer function, which is subsequently used to design a simple single step non-blind deconvolution that can be included in the real-time numerical reconstruction of the image. Several images of biological cell samples clearly demonstrate the improved noise and frequency response of the system when compared with traditional coherent DHM. We believe the high phase accuracy, low noise, and low cost of the real-time SA-DHM method as well as its simple modular nature that facilitates the addition to any existing microscope will make it practically useful in life-science laboratories.

In the next chapter, we demonstrate how the X-module can be adapted to implement optical diffraction tomography (ODT), which is a label-free microscopic imaging method that enables visualisation of the three-dimensional (3D) refractive index (RI) variation within a sample and provides powerful images of the internal sub-cellular structure of living cells. The adaptation of the X-module involves only a change in the filter used within the module and a different illumination and alignment protocol and the mathematical formulation developed in Chapter 4 serves as the foundation for Chapter 5; such are the close similarities between the ODT module in Chapter 5 and the X-module presented in Chapter 4, we demonstrate that the ODT module can also record the SA-DHM single capture hologram as well if a strobing laser is used in the illumination module. In addition to the bi-modality, the ODT module presented in Chapter 5 also has other advantages over the state of the art in ODT; it is modular and employs a self-reference design that can readily be attached to any existing life-science microscope with a short and simple alignment protocol making it much more affordable than commercial ODT microscopes. We believe that the module presented in Chapter 5 could be a powerful tool in the life-science community.

In Chapter 6 we return to using coherent DHM (together with Raman spectroscopy) for the purpose of cellular characterisation with the potential for diagnostics in those disease groups that can be investigated using cytology such as cervical cytology, urine cytology and oral cytology. The goal of this chapter was to implement a proof-of-concept automated Raman and DHM system that could automatically and without any user intervention scan a pathology slide and record Raman spectra from the nucleus of the cells while also recording the 3D phase image of the cells at the same time. This goal also includes the combination of the chemical data and the morphological data into a single enhanced statistical model for the classification of the disease groups. This work builds on a recent contribution within the research group on automated Raman cytology whereby cell nuclei could be targeted based on identifying the nuclei

via their 'microlens effect' whereby the denser and thicker nucleus focuses the white light illumination to a bright spot. The decision was made not to use the SA-DHM and ODT modules developed in earlier chapters due the difficulty in mounting the galvo-scanning illumination module on the Raman system that was available and so we used a simpler modular implementation of DHM. This chapter was a success in the sense that it successfully implements automated Raman and DHM in parallel for clinical cytology. However, the chapter was a failure in the sense that the results from both modalities were poor (DHM - due to the presence of coherent noise and the issues with not using a phase matching mounting medium that was problematic for Raman; and Raman - due to issues with alignment of the system) and also in the sense that we did not combine the results from both modalities into a single statistical classification model as we had hoped. Indeed, the morphological features of the cells could not be used for classification at all due to the poor quality of the phase images. A classification model was developed for the Raman data, which despite the relatively low SNR values for the spectra was capable of classifying three ovarian cancer cell lines with high sensitivity and specificity. Although the work in this chapter does not meet the initial goals, the basic platform was developed and we believe that there is significant opportunity to further develop this bi-modal platform in the future with the potential for clinical trial. To this end, we believe the SA-DHM module should be used to provide better phase images, and the issue of the mounting medium should be investigated, perhaps by enhancing background subtraction currently used to remove the glass slide spectrum to also account for the spectrum from the medium. Chapter 6 marks the end of the work on phase imaging.

The final contributory chapter, Chapter 7, focuses solely on Raman spectroscopy. In this case we move away from cellular analysis and instead focus on the capability of Raman to quantify the concentration of multiple chemicals in a mixture making use of the statistical method of partial least squares. Multi-component analysis with Raman is not a new area of research and there is much precedent with many different optical systems proposed to seek out every last scattered photon in order to push the limits of the approach to smaller and smaller concentrations, with liquid core optical fibers offering the gold standard. In Chapter 7 we do not attempt to improve on these systems; rather we seek to investigate the potential for the ubiquitous Raman microscope to be used for multi-component analysis. In the context of the overall thesis, we seek to characterise the growth media of cells as they grow within their growth medium; perhaps identifying if issues with the medium are present that could hinder growth or perhaps identifying the culture medium conditions that are optimal for growth.

Appendix A

Sets of reconstructed phase images from diatom cell, buccal epithelial cell and hela cells

The reconstructed phase images of the diatom cell from the coherent hologram, the SA hologram before using deconvolution algorithm, and the SA hologram after using deconvolution algorithm in Fig. 4.5(a), (b) and (c) are displayed at the same size in Fig. A.1-A.3 below.

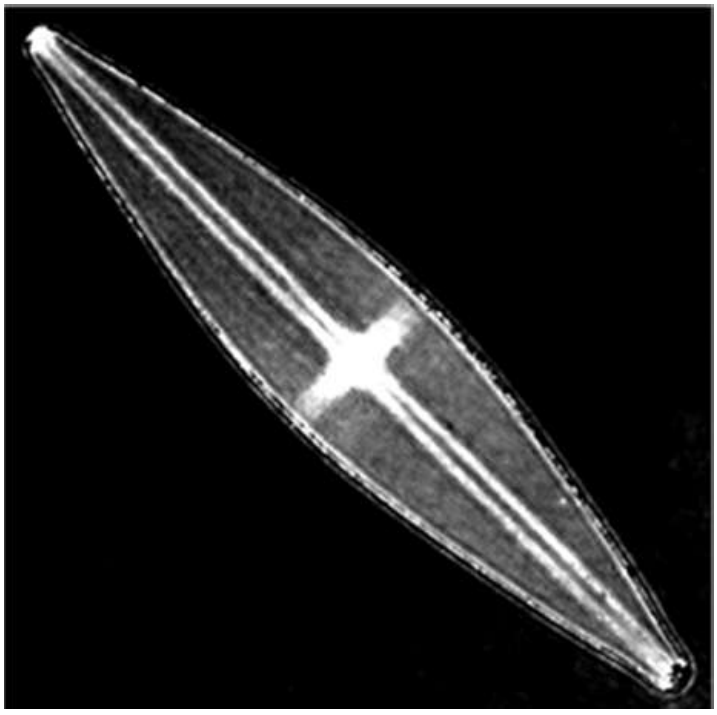

Figure A.1: The phase image of the diatom cell reconstructed from the coherent hologram

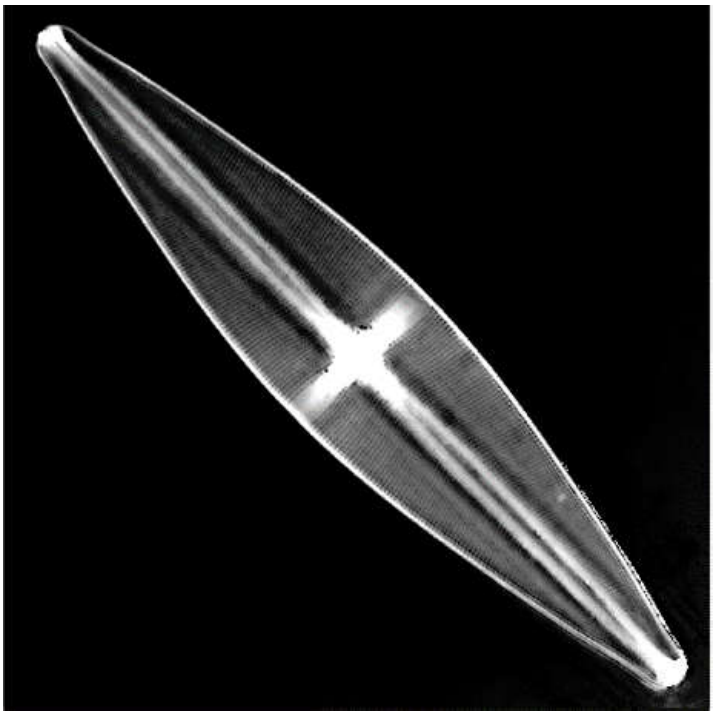

Figure A.2: The phase image of the diatom cell reconstructed from the SA hologram before using deconvolution algorithm

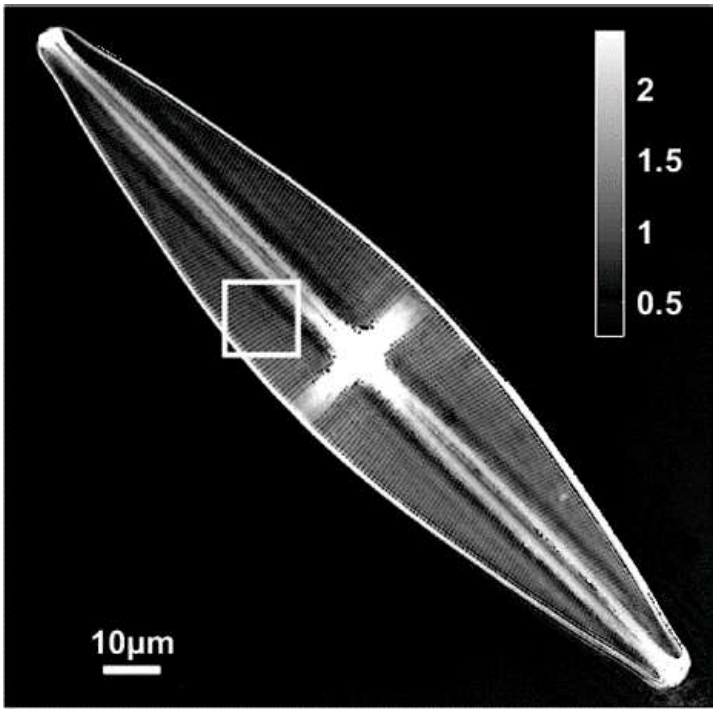

Figure A.3: The phase image of the diatom cell reconstructed from the SA hologram after using deconvolution algorithm

The reconstructed phase images of the buccal epithelial cell from the coherent hologram, the SA hologram before using deconvolution algorithm, and the SA hologram after using deconvolution algorithm in Fig. 4.6(a), (b) and (c) are displayed at the same size in Fig. A.4-A.6 below .

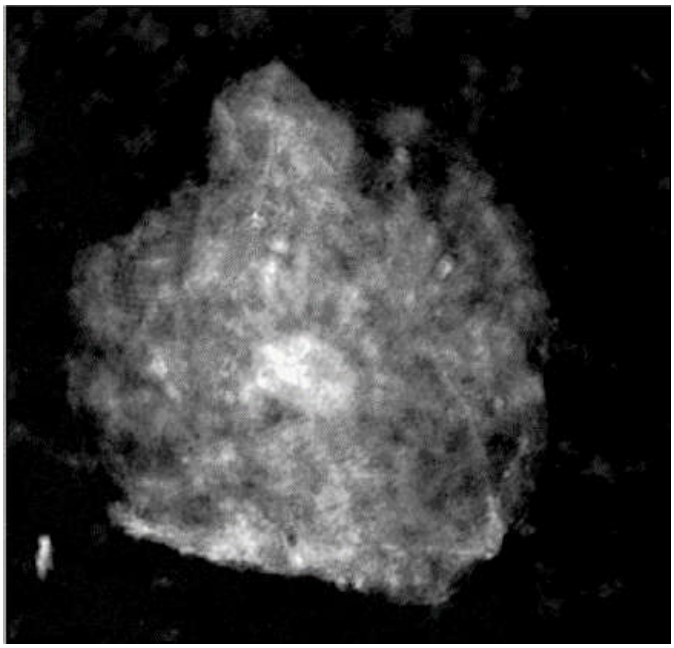

Figure A.4: The phase image of the buccal epithelial cell reconstructed from the coherent hologram

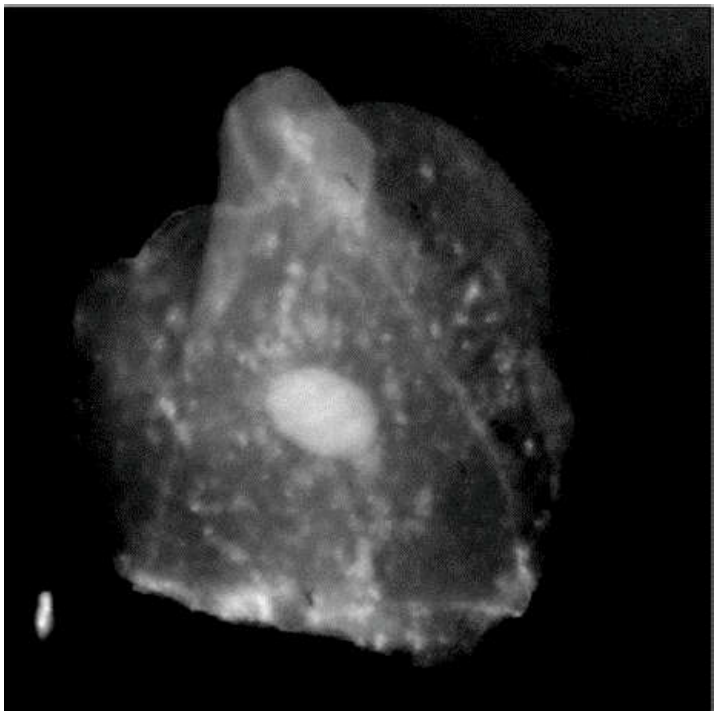

Figure A.5: The phase image of the buccal epithelial cell reconstructed from the SA hologram before using deconvolution algorithm

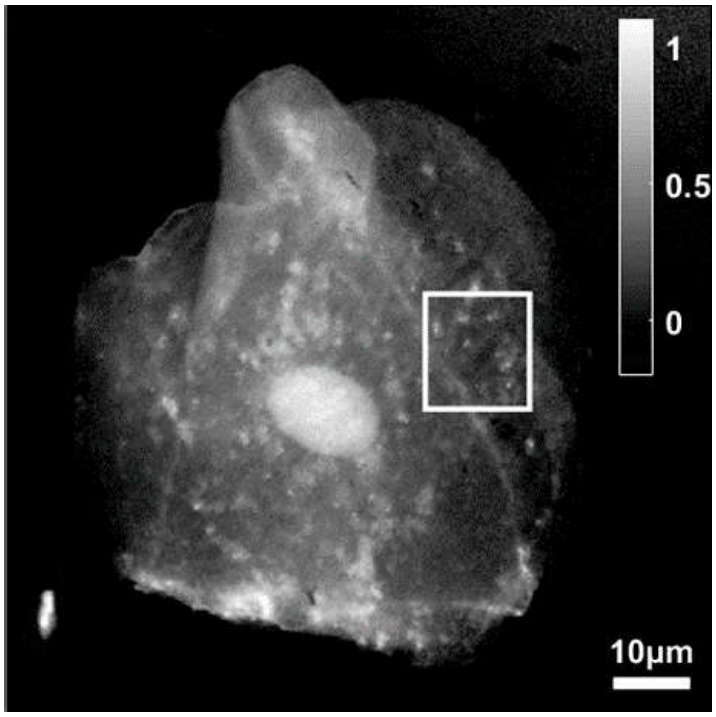

Figure A.6: The phase image of the diatom cell reconstructed from the SA hologram after using deconvolution algorithm

The reconstructed phase images of the HeLa cells from the coherent hologram, the SA hologram before using deconvolution algorithm, and the SA hologram after using deconvolution algorithm in Fig. 4.7(a), (b) and (c) are displayed at the same size in Fig A.7-A.9 below.

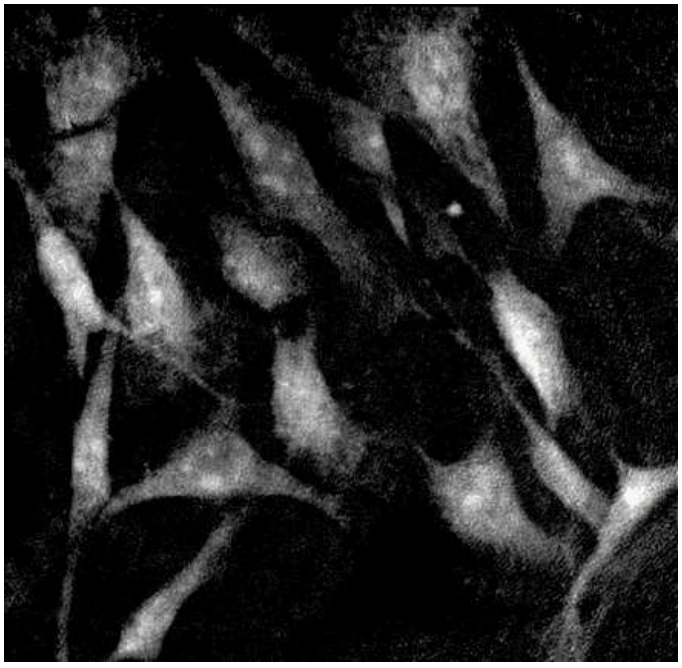

Figure A.7: The phase image of the HeLa cells reconstructed from the coherent hologram

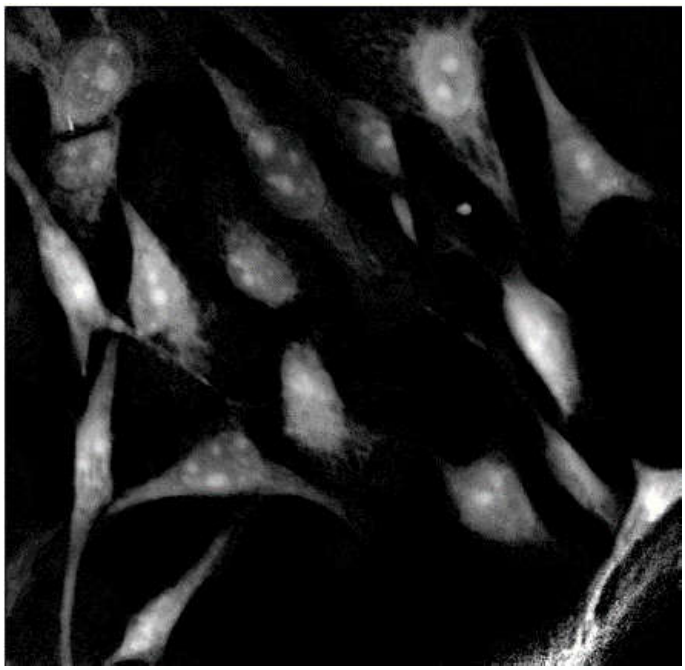

Figure A.8: The phase image of the HeLa cells reconstructed from the SA hologram before using deconvolution algorithm

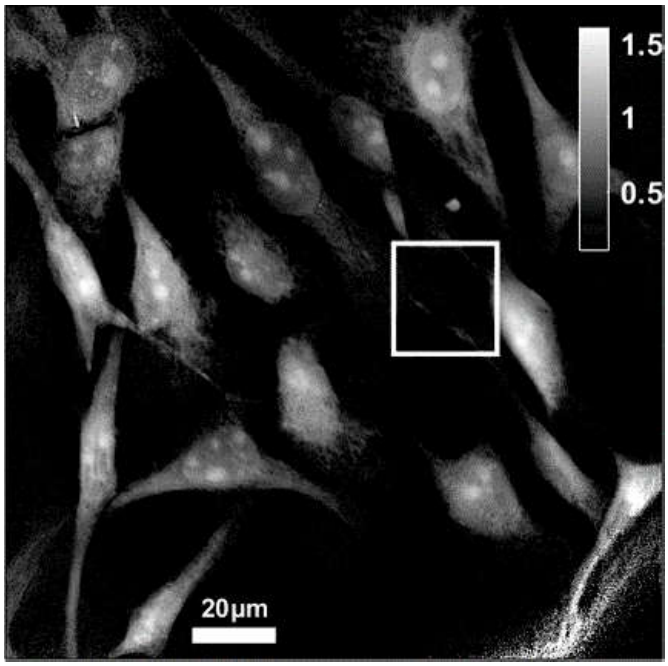

Figure A.9: The phase image of the HeLa cells reconstructed from the SA hologram after using deconvolution algorithm

References

[1] F. Charrière, J. Kühn, T. Colomb, F. Montfort, E. Cuche, Y. Emery, K. Weible, P. Marquet, and C. Depeursinge, "Characterization of microlenses by digital holographic microscopy," *Applied Optics*, vol. 45, no. 5, pp. 829–835, 2006.

[2] K. O'Dwyer, K. Domijan, A. Dignam, M. Butler, and B. M. Hennelly, "Automated raman micro-spectroscopy of epithelial cell nuclei for high-throughput classification," *Cancers*, vol. 13, no. 19, p. 4767, 2021.

[3] M. J. Goetz, G. L. Cote, R. Erckens, W. March, and M. Motamedi, "Application of a multivariate technique to raman spectra for quantification of body chemicals," *IEEE transactions on biomedical engineering*, vol. 42, no. 7, pp. 728–731, 1995.

[4] A. J. Berger, Y. Wang, and M. S. Feld, "Rapid, noninvasive concentration measurements of aqueous biological analytes by near-infrared raman spectroscopy," *Applied optics*, vol. 35, no. 1, pp. 209–212, 1996.

[5] A. M. Enejder, T.-W. Koo, J. Oh, M. Hunter, S. Sasic, M. S. Feld, and G. L. Horowitz, "Blood analysis by raman spectroscopy," *Optics letters*, vol. 27, no. 22, pp. 2004–2006, 2002.

[6] D. Qi and A. J. Berger, "Chemical concentration measurement in blood serum and urine samples using liquid-core optical fiber raman spectroscopy," *Applied optics*, vol. 46, no. 10, pp. 1726–1734, 2007.

[7] P. A. Santi, "Light sheet fluorescence microscopy: a review," *Journal of Histochemistry & Cytochemistry*, vol. 59, no. 2, pp. 129–138, 2011.

[8] F. Zernike, "Phase contrast, a new method for the microscopic observation of transparent objects," *Physica*, vol. 9, no. 7, pp. 686–698, 1942.

[9] W. Lang, *Nomarski differential interference-contrast microscopy*. Carl Zeiss Oberkochen, 1982.

[10] M. Mir, B. Bhaduri, R. Wang, R. Zhu, and G. Popescu, "Quantitative phase imaging," *Progress in optics*, vol. 57, pp. 133–217, 2012.

[11] K. Lee, K. Kim, J. Jung, J. Heo, S. Cho, S. Lee, G. Chang, Y. Jo, H. Park, and Y. Park, "Quantitative phase imaging techniques for the study of cell pathophysiology: from principles to applications," *Sensors*, vol. 13, no. 4, pp. 4170–4191, 2013.

[12] B. Kemper and G. Von Bally, "Digital holographic microscopy for live cell applications and technical inspection," *Applied optics*, vol. 47, no. 4, pp. A52–A61, 2008.

[13] P. Marquet, B. Rappaz, P. J. Magistretti, E. Cuche, Y. Emery, T. Colomb, and C. Depeursinge, "Digital holographic microscopy: a noninvasive contrast imaging technique allowing quantitative visualization of living cells with subwavelength axial accuracy," *Optics letters*, vol. 30, no. 5, pp. 468–470, 2005.

[14] R. Zhou, C. Edwards, A. Arbabi, G. Popescu, and L. L. Goddard, "Detecting 20 nm wide defects in large area nanopatterns using optical interferometric microscopy," *Nano letters*, vol. 13, no. 8, pp. 3716–3721, 2013.

[15] S. Khadir, P. Bon, D. Vignaud, E. Galopin, N. McEvoy, D. McCloskey, S. Monneret, and G. Baffou, "Optical imaging and characterization of graphene and other 2d materials using quantitative phase microscopy," *ACS photonics*, vol. 4, no. 12, pp. 3130–3139, 2017.

[16] E. Cuche, P. Marquet, and C. Depeursinge, "Simultaneous amplitude-contrast and quantitative phase-contrast microscopy by numerical reconstruction of fresnel off-axis holograms," *Applied optics*, vol. 38, no. 34, pp. 6994–7001, 1999.

[17] C. J. Mann, L. Yu, C.-M. Lo, and M. K. Kim, "High-resolution quantitative phase-contrast microscopy by digital holography," *Optics Express*, vol. 13, no. 22, pp. 8693–8698, 2005.

[18] D. O. Hogenboom and C. A. DiMarzio, "Quadrature detection of a doppler signal," *Applied optics*, vol. 37, no. 13, pp. 2569–2572, 1998.

[19] D. Hogenboom, C. A. DiMarzio, T. J. Gaudette, A. J. Devaney, and S. C. Lindberg, "Three-dimensional images generated by quadrature interferometry," *Optics Letters*, vol. 23, no. 10, pp. 783–785, 1998.

[20] W. C. Warger and C. A. DiMarzio, "Computational signal-to-noise ratio analysis for optical quadrature microscopy," *Optics Express*, vol. 17, no. 4, pp. 2400–2422, 2009.

[21] Z. Wang, L. Millet, M. Mir, H. Ding, S. Unarunotai, J. Rogers, M. U. Gillette, and G. Popescu, "Spatial light interference microscopy (slim)," *Optics express*, vol. 19, no. 2, pp. 1016–1026, 2011.

[22] B. Bhaduri, H. Pham, M. Mir, and G. Popescu, "Diffraction phase microscopy with white light," *Optics letters*, vol. 37, no. 6, pp. 1094–1096, 2012.

[23] L. Tian and L. Waller, "Quantitative differential phase contrast imaging in an led array microscope," *Optics express*, vol. 23, no. 9, pp. 11394–11403, 2015.

[24] D. B. Phillips, M.-J. Sun, J. M. Taylor, M. P. Edgar, S. M. Barnett, G. M. Gibson, and M. J. Padgett, "Adaptive foveated single-pixel imaging with dynamic supersampling," *Science advances*, vol. 3, no. 4, p. e1601782, 2017.

[25] C. Zuo, J. Sun, J. Li, J. Zhang, A. Asundi, and Q. Chen, "High-resolution transport-of-intensity quantitative phase microscopy with annular illumination," *Scientific reports*, vol. 7, no. 1, pp. 1–22, 2017.

[26] C. Zuo, Q. Chen, G. Gu, S. Feng, F. Feng, R. Li, and G. Shen, "High-speed three-dimensional shape measurement for dynamic scenes using bi-frequency tripolar pulse-width-modulation fringe projection," *Optics and Lasers in Engineering*, vol. 51, no. 8, pp. 953–960, 2013.

[27] A. Ozcan and E. McLeod, "Lensless imaging and sensing," *Annual review of biomedical engineering*, vol. 18, pp. 77–102, 2016.

[28] Y. Rivenson, Y. Zhang, H. Günaydın, D. Teng, and A. Ozcan, "Phase recovery and holographic image reconstruction using deep learning in neural networks," *Light: Science & Applications*, vol. 7, no. 2, pp. 17141–17141, 2018.

[29] D. Gabor, "A new microscopic principle," *nature*, vol. 161, pp. 777–778, 1948.

[30] E. N. Leith and J. Upatnieks, "Reconstructed wavefronts and communication theory," *JOSA*, vol. 52, no. 10, pp. 1123–1130, 1962.

[31] J. W. Goodman and R. Lawrence, "Digital image formation from electronically detected holograms," *Applied physics letters*, vol. 11, no. 3, pp. 77–79, 1967.

[32] U. Schnars and W. Jüptner, "Direct recording of holograms by a ccd target and numerical reconstruction," *Applied optics*, vol. 33, no. 2, pp. 179–181, 1994.

[33] T. Colomb, E. Cuche, F. Charrière, J. Kühn, N. Aspert, F. Montfort, P. Marquet, and C. Depeursinge, "Automatic procedure for aberration compensation in digital holographic microscopy and applications to specimen shape compensation," *Applied optics*, vol. 45, no. 5, pp. 851–863, 2006.

[34] T. Colomb, J. Kühn, F. Charrière, C. Depeursinge, P. Marquet, and N. Aspert, "Total aberrations compensation in digital holographic microscopy with a reference conjugated hologram," *Optics Express*, vol. 14, no. 10, pp. 4300–4306, 2006.

[35] K. M. Molony, B. M. Hennelly, D. P. Kelly, and T. J. Naughton, "Reconstruction algorithms applied to in-line gabor digital holographic microscopy," *Optics Communications*, vol. 283, no. 6, pp. 903–909, 2010.

[36] D. Kelly, B. M. Hennelly, C. McElhinney, and T. J. Naughton, "A practical guide to digital holography and generalized sampling," in *Optics and Photonics for Information Processing II*, vol. 7072, p. 707215, International Society for Optics and Photonics, 2008.

[37] P. Langehanenberg, B. Kemper, D. Dirksen, and G. Von Bally, "Autofocusing in digital holographic phase contrast microscopy on pure phase objects for live cell imaging," *Applied optics*, vol. 47, no. 19, pp. D176–D182, 2008.

[38] X. Fan, J. J. Healy, and B. M. Hennelly, "Investigation of sparsity metrics for autofocusing in digital holographic microscopy," *Optical Engineering*, vol. 56, no. 5, p. 053112, 2017.

[39] H. Gabai and N. T. Shaked, "Dual-channel low-coherence interferometry and its application to quantitative phase imaging of fingerprints," *Optics express*, vol. 20, no. 24, pp. 26906–26912, 2012.

[40] S. K. Mirsky, I. Barnea, M. Levi, H. Greenspan, and N. T. Shaked, "Automated analysis of individual sperm cells using stain-free interferometric phase microscopy and machine learning," *Cytometry Part A*, no. 9, pp. 893–900, 2017.

[41] D. Roitshtain, L. Wolbromsky, E. Bal, H. Greenspan, L. L. Satterwhite, and N. T. Shaked, "Quantitative phase microscopy spatial signatures of cancer cells," *Cytometry Part A*, vol. 91, no. 5, pp. 482–493, 2017.

[42] B. Rappaz, P. Marquet, E. Cuche, Y. Emery, C. Depeursinge, and P. J. Magistretti, "Measurement of the integral refractive index and dynamic cell morphometry of living cells with digital holographic microscopy," *Optics express*, vol. 13, no. 23, pp. 9361–9373, 2005.

[43] D. Carl, B. Kemper, G. Wernicke, and G. von Bally, "Parameter-optimized digital holographic microscope for high-resolution living-cell analysis," *Applied optics*, vol. 43, no. 36, pp. 6536–6544, 2004.

[44] P. Langehanenberg, L. Ivanova, I. Bernhardt, S. Ketelhut, A. Vollmer, D. Dirksen, G. K. Georgiev, G. von Bally, and B. Kemper, "Automated three-dimensional tracking of living cells by digital holographic microscopy," *Journal of biomedical optics*, vol. 14, no. 1, p. 014018, 2009.

[45] B. Kemper, S. Kosmeier, P. Langehanenberg, G. von Bally, I. Bredebusch, W. Domschke, and J. Schnekenburger, "Integral refractive index determination of living suspension cells by multifocus digital holographic phase contrast microscopy," *Journal of biomedical optics*, vol. 12, no. 5, p. 054009, 2007.

[46] M. K. Kim, "Principles and techniques of digital holographic microscopy," *SPIE reviews*, vol. 1, no. 1, p. 018005, 2010.

[47] I. Peruhov and E. Mihaylova, *Applications of holographic microscopy in life sciences.* intechopen, 2013.

[48] C. Pasquini, "Near infrared spectroscopy: fundamentals, practical aspects and analytical applications," *Journal of the Brazilian chemical society*, vol. 14, pp. 198–219, 2003.

[49] B. C. Smith, *Fundamentals of Fourier transform infrared spectroscopy.* CRC press, 2011.

[50] J. R. Lakowicz, *Principles of fluorescence spectroscopy*. Springer science & business media, 2013.

[51] S. A. Johansson, J. L. Campbell, and K. G. Malmqvist, *Particle-induced X-ray emission spectrometry (PIXE)*, vol. 133. Wiley New York, 1995.

[52] D. Shindo and T. Oikawa, "Energy dispersive x-ray spectroscopy," in *Analytical electron microscopy for materials science*, pp. 81–102, Springer, 2002.

[53] C. V. Raman and K. S. Krishnan, "The optical analogue of the compton effect," *Nature*, vol. 121, no. 3053, pp. 711–711, 1928.

[54] R. S. Das and Y. Agrawal, "Raman spectroscopy: recent advancements, techniques and applications," *Vibrational spectroscopy*, vol. 57, no. 2, pp. 163–176, 2011.

[55] S. Inoué, "Foundations of confocal scanned imaging in light microscopy," in *Handbook of biological confocal microscopy*, pp. 1–19, Springer, 2006.

[56] R. E. Kast, S. C. Tucker, K. Killian, M. Trexler, K. V. Honn, and G. W. Auner, "Emerging technology: applications of raman spectroscopy for prostate cancer," *Cancer and Metastasis Reviews*, vol. 33, no. 2, pp. 673–693, 2014.

[57] A. Taleb, J. Diamond, J. J. McGarvey, J. R. Beattie, C. Toland, and P. W. Hamilton, "Raman microscopy for the chemometric analysis of tumor cells," *The Journal of Physical Chemistry B*, vol. 110, no. 39, pp. 19625–19631, 2006.

[58] L. T. Kerr, T. M. Lynn, I. M. Cullen, P. J. Daly, N. Shah, S. O'Dea, A. Malkin, and B. M. Hennelly, "Methodologies for bladder cancer detection with raman based urine cytology," *Analytical Methods*, vol. 8, no. 25, pp. 4991–5000, 2016.

[59] I. Barman, N. C. Dingari, G. P. Singh, R. Kumar, S. Lang, and G. Nabi, "Selective sampling using confocal raman spectroscopy provides enhanced specificity for urinary bladder cancer diagnosis," *Analytical and bioanalytical chemistry*, vol. 404, no. 10, pp. 3091–3099, 2012.

[60] R. O. Draga, M. C. Grimbergen, P. L. Vijverberg, C. F. v. Swol, T. G. Jonges, J. A. Kummer, and J. Ruud Bosch, "In vivo bladder cancer diagnosis by high-volume raman spectroscopy," *Analytical chemistry*, vol. 82, no. 14, pp. 5993–5999, 2010.

[61] S. Duraipandian, W. Zheng, J. Ng, J. J. Low, A. Ilancheran, and Z. Huang, "Simultaneous fingerprint and high-wavenumber confocal raman spectroscopy enhances early detection of cervical precancer in vivo," *Analytical chemistry*, vol. 84, no. 14, pp. 5913–5919, 2012.

[62] P. R. Jess, D. D. Smith, M. Mazilu, K. Dholakia, A. C. Riches, and C. S. Herrington, "Early detection of cervical neoplasia by raman spectroscopy," *International journal of cancer*, vol. 121, no. 12, pp. 2723–2728, 2007.

[63] M. D. Keller, E. M. Kanter, and A. Mahadevan-Jansen, "Raman spectroscopy for cancer diagnosis," *SPECTROSCOPY-SPRINGFIELD THEN EUGENE THEN DULUTH-*, vol. 21, no. 11, p. 33, 2006.

[64] A. Vysakh, S. J. Midhun, K. Jayesh, M. Jyothis, and M. Latha, "Studies on biofilm formation and virulence factors associated with uropathogenic escherichia coli isolated from patient with acute pyelonephritis," *Pathophysiology*, vol. 25, no. 4, pp. 381–387, 2018.

[65] K. M. Tripathi, A. K. Sonker, S. K. Sonkar, and S. Sarkar, "Pollutant soot of diesel engine exhaust transformed to carbon dots for multicoloured imaging of e. coli and sensing cholesterol," *Rsc Advances*, vol. 4, no. 57, pp. 30100–30107, 2014.

[66] S. León-Ríos, R. Espinoza González, S. Fuentes, E. Chávez Ángel, A. Echeverría, A. E. Serrano, C. S. Demergasso, and R. A. Zárate, "One-dimensional tio2-b crystals synthesised by hydrothermal process and their antibacterial behaviour on escherichia coli," *Journal of Nanomaterials*, vol. 2016, 2016.

[67] S. G. da Costa, A. Richter, U. Schmidt, S. Breuninger, and O. Hollricher, "Confocal raman microscopy in life sciences," *Morphologie*, vol. 103, no. 341, pp. 11–16, 2019.

[68] P. J. Caspers, G. W. Lucassen, and G. J. Puppels, "Combined in vivo confocal raman spectroscopy and confocal microscopy of human skin," *Biophysical journal*, vol. 85, no. 1, pp. 572–580, 2003.

[69] Y. Zhou, C.-H. Liu, Y. Sun, Y. Pu, S. Boydston-White, Y. Liu, and R. R. Alfano, "Human brain cancer studied by resonance raman spectroscopy," *Journal of biomedical optics*, vol. 17, no. 11, p. 116021, 2012.

[70] W. M. Tolles, J. W. Nibler, J. McDonald, and A. B. Harvey, "A review of the theory and application of coherent anti-stokes raman spectroscopy (cars)," *Applied Spectroscopy*, vol. 31, no. 4, pp. 253–271, 1977.

[71] T. Harkonen, L. Roininen, M. T. Moores, and E. M. Vartiainen, "Bayesian quantification for coherent anti-stokes raman scattering spectroscopy," *The Journal of Physical Chemistry B*, vol. 124, no. 32, pp. 7005–7012, 2020.

[72] M. Fleischmann, P. J. Hendra, and A. J. McQuillan, "Raman spectra of pyridine adsorbed at a silver electrode," *Chemical physics letters*, vol. 26, no. 2, pp. 163–166, 1974.

[73] E. C. Le Ru, E. Blackie, M. Meyer, and P. G. Etchegoin, "Surface enhanced raman scattering enhancement factors: a comprehensive study," *The Journal of Physical Chemistry C*, vol. 111, no. 37, pp. 13794–13803, 2007.

[74] E. J. Blackie, E. C. Le Ru, and P. G. Etchegoin, "Single-molecule surface-enhanced raman spectroscopy of nonresonant molecules," *Journal of the American Chemical Society*, vol. 131, no. 40, pp. 14466–14472, 2009.

[75] R. Goodacre, D. Graham, and K. Faulds, "Recent developments in quantitative sers: Moving towards absolute quantification," *TrAC Trends in Analytical Chemistry*, vol. 102, pp. 359–368, 2018.

[76] J. C. Maxwell, "Xxv. on physical lines of force: Part i.–the theory of molecular vortices applied to magnetic phenomena," *The London, Edinburgh, and Dublin Philosophical Magazine and Journal of Science*, vol. 21, no. 139, pp. 161–175, 1861.

[77] J. C. Maxwell, *A treatise on electricity and magnetism*, vol. 1. Clarendon press, 1873.

[78] A. Sommerfeld, "Optics lectures on theortical physics, vol. iv," *Optics Lectures on Theortical Physics*, 1954.

[79] M. Pluta, *Advanced light microscopy*. Distribution for the USA and Canada, Elsevier Science Publishing Co., 1988.

[80] F. Zernike, "How i discovered phase contrast," *Science*, vol. 121, no. 3141, pp. 345–349, 1955.

[81] R. Allen and G. David, "The zeiss-nomarski differential interference equipment for transmitted-light microscopy," *Zeitschrift fur wissenschaftliche Mikroskopie und mikroskopische Technik*, vol. 69, no. 4, pp. 193–221, 1969.

[82] J. Rheinberg, "On an addition to the methods of microscopical research, by a new way optically producing colour-contrast between an object and its background, or between definite parts of the object itself," *JR Microsc. Soc*, vol. 16, pp. 373–388, 1896.

[83] E. C. Samson and C. M. Blanca, "Dynamic contrast enhancement in widefield microscopy using projector-generated illumination patterns," *New Journal of Physics*, vol. 9, no. 10, p. 363, 2007.

[84] C. Zuo, J. Sun, S. Feng, Y. Hu, and Q. Chen, "Programmable colored illumination microscopy (pcim): A practical and flexible optical staining approach for microscopic contrast enhancement," *Optics and Lasers in Engineering*, vol. 78, pp. 35–47, 2016.

[85] R. W. Gerchberg, "A practical algorithm for the determination of phase from image and diffraction plane pictures," *Optik*, vol. 35, pp. 237–246, 1972.

[86] H. Wang, W. Yue, Q. Song, J. Liu, and G. Situ, "A hybrid gerchberg–saxton-like algorithm for doe and cgh calculation," *Optics and Lasers in Engineering*, vol. 89, pp. 109–115, 2017.

[87] H. M. L. Faulkner and J. Rodenburg, "Movable aperture lensless transmission microscopy: a novel phase retrieval algorithm," *Physical review letters*, vol. 93, no. 2, p. 023903, 2004.

[88] H. M. L. Faulkner and J. M. Rodenburg, "Error tolerance of an iterative phase retrieval algorithm for moveable illumination microscopy," *Ultramicroscopy*, vol. 103, no. 2, pp. 153–164, 2005.

[89] J. H. Bruning, D. R. Herriott, J. Gallagher, D. Rosenfeld, A. White, and D. Brangaccio, "Digital wavefront measuring interferometer for testing optical surfaces and lenses," *Applied optics*, vol. 13, no. 11, pp. 2693–2703, 1974.

[90] B. M. Hennelly and J. T. Sheridan, "Generalizing, optimizing, and inventing numerical algorithms for the fractional fourier, fresnel, and linear canonical transforms," *JOSA A*, vol. 22, no. 5, pp. 917–927, 2005.

[91] B. M. Hennelly, D. P. Kelly, D. S. Monaghan, and N. Pandey, "Zoom algorithms for digital holography," in *Information Optics and Photonics*, pp. 187–204, Springer, 2010.

[92] H. Takajo and T. Takahashi, "Noniterative method for obtaining the exact solution for the normal equation in least-squares phase estimation from the phase difference," *JOSA A*, vol. 5, no. 11, pp. 1818–1827, 1988.

[93] E. Barnhill, P. Kennedy, C. L. Johnson, M. Mada, and N. Roberts, "Real-time 4d phase unwrapping applied to magnetic resonance elastography," *Magnetic resonance in medicine*, vol. 73, no. 6, pp. 2321–2331, 2015.

[94] H. Zhang, M. J. Lalor, and D. R. Burton, "Spatiotemporal phase unwrapping for the measurement of discontinuous objects in dynamic fringe-projection phase-shifting profilometry," *Applied Optics*, vol. 38, no. 16, pp. 3534–3541, 1999.

[95] A. Hooper and H. A. Zebker, "Phase unwrapping in three dimensions with application to insar time series," *JOSA A*, vol. 24, no. 9, pp. 2737–2747, 2007.

[96] R. M. Goldstein, H. A. Zebker, and C. L. Werner, "Satellite radar interferometry: Two-dimensional phase unwrapping," *Radio science*, vol. 23, no. 4, pp. 713–720, 1988.

[97] M. A. Herráez, D. R. Burton, M. J. Lalor, and M. A. Gdeisat, "Fast two-dimensional phase-unwrapping algorithm based on sorting by reliability following a noncontinuous path," *Applied optics*, vol. 41, no. 35, pp. 7437–7444, 2002.

[98] I. V. Lyuboshenko, H. Maıtre, and A. Maruani, "Least-mean-squares phase unwrapping by use of an incomplete set of residue branch cuts," *Applied optics*, vol. 41, no. 11, pp. 2129–2148, 2002.

[99] M. Zhao, L. Huang, Q. Zhang, X. Su, A. Asundi, and Q. Kemao, "Quality-guided phase unwrapping technique: comparison of quality maps and guiding strategies," *Applied optics*, vol. 50, no. 33, pp. 6214–6224, 2011.

[100] T. J. Flynn, "Two-dimensional phase unwrapping with minimum weighted discontinuity," *JOSA A*, vol. 14, no. 10, pp. 2692–2701, 1997.

[101] B. Friedlander and J. M. Francos, "Model based phase unwrapping of 2-d signals," *IEEE Transactions on Signal Processing*, vol. 44, no. 12, pp. 2999–3007, 1996.

[102] J. M. Bioucas-Dias and G. Valadao, "Phase unwrapping via graph cuts," *IEEE Transactions on Image processing*, vol. 16, no. 3, pp. 698–709, 2007.

[103] H. Y. Huang, L. Tian, Z. Zhang, Y. Liu, Z. Chen, and G. Barbastathis, "Path-independent phase unwrapping using phase gradient and total-variation (tv) denoising," *Optics express*, vol. 20, no. 13, pp. 14075–14089, 2012.

[104] K. Itoh, "Analysis of the phase unwrapping algorithm," *Applied optics*, vol. 21, no. 14, pp. 2470–2470, 1982.

[105] D. Blinder, H. Ottevaere, A. Munteanu, and P. Schelkens, "Efficient multiscale phase unwrapping methodology with modulo wavelet transform," *Optics express*, vol. 24, no. 20, pp. 23094–23108, 2016.

[106] A. Barty, K. Nugent, D. Paganin, and A. Roberts, "Quantitative optical phase microscopy," *Optics Letters*, vol. 23, no. 11, pp. 817–819, 1998.

[107] C. Zuo, Q. Chen, W. Qu, and A. Asundi, "Noninterferometric single-shot quantitative phase microscopy," *Optics letters*, vol. 38, no. 18, pp. 3538–3541, 2013.

[108] E. Wolf, "Three-dimensional structure determination of semi-transparent objects from holographic data," *Optics communications*, vol. 1, no. 4, pp. 153–156, 1969.

[109] A. Fercher, H. Bartelt, H. Becker, and E. Wiltschko, "Image formation by inversion of scattered field data: experiments and computational simulation," *Applied optics*, vol. 18, no. 14, pp. 2427–2439, 1979.

[110] N. Streibl, "Three-dimensional imaging by a microscope," *JOSA A*, vol. 2, no. 2, pp. 121–127, 1985.

[111] S. Kawata, O. Nakamura, and S. Minami, "Optical microscope tomography. i. support constraint," *JOSA A*, vol. 4, no. 1, pp. 292–297, 1987.

[112] T. Noda, S. Kawata, and S. Minami, "Three-dimensional phase contrast imaging by an annular illumination microscope," *Applied optics*, vol. 29, no. 26, pp. 3810–3815, 1990.

[113] G. Vishnyakov and G. Levin, "Optical microtomography of phase objects," *Optics and Spectroscopy*, vol. 85, no. 1, pp. 73–77, 1998.

[114] A. J. Devaney and A. Schatzberg, "Coherent optical tomographic microscope," in *Inverse Problems in Scattering and Imaging*, vol. 1767, pp. 62–71, SPIE, 1992.

[115] Y. Sung, W. Choi, C. Fang-Yen, K. Badizadegan, R. R. Dasari, and M. S. Feld, "Optical diffraction tomography for high resolution live cell imaging," *Optics express*, vol. 17, no. 1, pp. 266–277, 2009.

[116] S. Shin, K. Kim, J. Yoon, and Y. Park, "Active illumination using a digital micromirror device for quantitative phase imaging," *Optics letters*, vol. 40, no. 22, pp. 5407–5410, 2015.

[117] S. Shin, K. Kim, T. Kim, J. Yoon, K. Hong, J. Park, and Y. Park, "Optical diffraction tomography using a digital micromirror device for stable measurements of 4d refractive index tomography of cells," in *Quantitative Phase Imaging II*, vol. 9718, p. 971814, International Society for Optics and Photonics, 2016.

[118] M. Kim, Y. Choi, C. Fang-Yen, Y. Sung, R. R. Dasari, M. S. Feld, and W. Choi, "High-speed synthetic aperture microscopy for live cell imaging," *Optics letters*, vol. 36, no. 2, pp. 148–150, 2011.

[119] Y. Kim, H. Shim, K. Kim, H. Park, S. Jang, and Y. Park, "Profiling individual human red blood cells using common-path diffraction optical tomography," *Scientific reports*, vol. 4, p. 6659, 2014.

[120] Y. Kim, H. Shim, K. Kim, H. Park, J. H. Heo, J. Yoon, C. Choi, S. Jang, and Y. Park, "Common-path diffraction optical tomography for investigation of three-dimensional structures and dynamics of biological cells," *Optics express*, vol. 22, no. 9, pp. 10398–10407, 2014.

[121] H. Park, T. Ahn, K. Kim, S. Lee, S.-y. Kook, D. Lee, I. B. Suh, S. Na, and Y. Park, "Three-dimensional refractive index tomograms and deformability of individual human red blood cells from cord blood of newborn infants and maternal blood," *Journal of biomedical optics*, vol. 20, no. 11, p. 111208, 2015.

[122] H. Park, M. Ji, S. Lee, K. Kim, Y.-H. Sohn, S. Jang, and Y. Park, "Alterations in cell surface area and deformability of individual human red blood cells in stored blood," *arXiv preprint arXiv:1506.05259*, 2015.

[123] S. Y. Lee, H. J. Park, C. Best-Popescu, S. Jang, and Y. K. Park, "The effects of ethanol on the morphological and biochemical properties of individual human red blood cells," *PloS one*, vol. 10, no. 12, p. e0145327, 2015.

[124] H. Park, S.-H. Hong, K. Kim, S.-H. Cho, W.-J. Lee, Y. Kim, S.-E. Lee, and Y. Park, "Characterizations of individual mouse red blood cells parasitized by babesia microti using 3-d holographic microscopy," *Scientific reports*, vol. 5, no. 1, pp. 1–11, 2015.

[125] A. Kuś, M. Dudek, B. Kemper, M. Kujawińska, and A. Vollmer, "Tomographic phase microscopy of living three-dimensional cell cultures," *Journal of biomedical optics*, vol. 19, no. 4, p. 046009, 2014.

[126] J. Yoon, K. Kim, H. Park, C. Choi, S. Jang, and Y. Park, "Label-free characterization of white blood cells by measuring 3d refractive index maps," *Biomedical optics express*, vol. 6, no. 10, pp. 3865–3875, 2015.

[127] K. Kim, J. Yoon, and Y. Park, "Simultaneous 3d visualization and position tracking of optically trapped particles using optical diffraction tomography," *Optica*, vol. 2, no. 4, pp. 343–346, 2015.

[128] Y. Sung, N. Lue, B. Hamza, J. Martel, D. Irimia, R. R. Dasari, W. Choi, Z. Yaqoob, and P. So, "Three-dimensional holographic refractive-index measurement of continuously flowing cells in a microfluidic channel," *Physical review applied*, vol. 1, no. 1, p. 014002, 2014.

[129] Y. Sung, W. Choi, N. Lue, R. R. Dasari, and Z. Yaqoob, "Stain-free quantification of chromosomes in live cells using regularized tomographic phase microscopy," *PloS one*, vol. 7, no. 11, p. e49502, 2012.

[130] S. E. Lee, K. Kim, J. Yoon, J. H. Heo, H. Park, C. Choi, and Y. Park, "Label-free quantitative imaging of lipid droplets using quantitative phase imaging techniques," in *Asia Communications and Photonics Conference*, pp. ATh1I–3, Optical Society of America, 2014.

[131] J. Jung, K. Kim, J. Yoon, and Y. Park, "Hyperspectral optical diffraction tomography," *Optics express*, vol. 24, no. 3, pp. 2006–2012, 2016.

[132] W. Krauze, P. Makowski, M. Kujawińska, and A. Kuś, "Generalized total variation iterative constraint strategy in limited angle optical diffraction tomography," *Optics Express*, vol. 24, no. 5, pp. 4924–4936, 2016.

[133] Y. Park, M. Diez-Silva, G. Popescu, G. Lykotrafitis, W. Choi, M. S. Feld, and S. Suresh, "Refractive index maps and membrane dynamics of human red blood cells parasitized by plasmodium falciparum," *Proceedings of the National Academy of Sciences*, vol. 105, no. 37, pp. 13730–13735, 2008.

[134] A. Barty, K. Nugent, A. Roberts, and D. Paganin, "Quantitative phase tomography," *Optics Communications*, vol. 175, no. 4-6, pp. 329–336, 2000.

[135] F. Charrière, A. Marian, F. Montfort, J. Kuehn, T. Colomb, E. Cuche, P. Marquet, and C. Depeursinge, "Cell refractive index tomography by digital holographic microscopy," *Optics letters*, vol. 31, no. 2, pp. 178–180, 2006.

[136] Y. Cotte, F. Toy, P. Jourdain, N. Pavillon, D. Boss, P. Magistretti, P. Marquet, and C. Depeursinge, "Marker-free phase nanoscopy," *Nature Photonics*, vol. 7, no. 2, p. 113, 2013.

[137] K. Kim, Z. Yaqoob, K. Lee, J. W. Kang, Y. Choi, P. Hosseini, P. T. So, and Y. Park, "Diffraction optical tomography using a quantitative phase imaging unit," *Optics letters*, vol. 39, no. 24, pp. 6935–6938, 2014.

[138] W. Choi, C. Fang-Yen, K. Badizadegan, S. Oh, N. Lue, R. R. Dasari, and M. S. Feld, "Tomographic phase microscopy," *Nature methods*, vol. 4, no. 9, pp. 717–719, 2007.

[139] R. Fiolka, K. Wicker, R. Heintzmann, and A. Stemmer, "Simplified approach to diffraction tomography in optical microscopy," *Optics express*, vol. 17, no. 15, pp. 12407–12417, 2009.

[140] A. Kuś, W. Krauze, and M. Kujawińska, "Active limited-angle tomographic phase microscope," *Journal of biomedical optics*, vol. 20, no. 11, p. 111216, 2015.

[141] M. Habaza, B. Gilboa, Y. Roichman, and N. T. Shaked, "Tomographic phase microscopy with 180 rotation of live cells in suspension by holographic optical tweezers," *Optics letters*, vol. 40, no. 8, pp. 1881–1884, 2015.

[142] S. Chowdhury, W. J. Eldridge, A. Wax, and J. Izatt, "Refractive index tomography with structured illumination," *Optica*, vol. 4, no. 5, pp. 537–545, 2017.

[143] K. Kim, J. Yoon, S. Shin, S. Lee, S.-A. Yang, and Y. Park, "Optical diffraction tomography techniques for the study of cell pathophysiology," *Journal of Biomedical Photonics & Engineering*, vol. 2, no. 2, 2016.

[144] S. L. Wellington and H. J. Vinegar, "X-ray computerized tomography," *Journal of petroleum technology*, vol. 39, no. 08, pp. 885–898, 1987.

[145] A. C. Kak and M. Slaney, *Principles of computerized tomographic imaging*. SIAM, 2001.

[146] C. Cohen-Tannoudji, B. Diu, F. Laloe, and B. Dui, "Quantum mechanics (2 vol. set)," 2006.

[147] P. Müller, "Optical diffraction tomography for single cells," 2016.

[148] A. Baños, *Dipole radiation in the presence of a conducting halfspace*, vol. 9. Pergamon, 1966.

[149] A. Kuś, W. Krauze, P. L. Makowski, and M. Kujawińska, "Holographic tomography: hardware and software solutions for 3d quantitative biomedical imaging," *ETRI Journal*, vol. 41, no. 1, pp. 61–72, 2019.

[150] A. Kuś, W. Krauze, and M. Kujawińska, "Limited-angle holographic tomography with optically controlled projection generation," in *Three-Dimensional and Multidimensional Microscopy: Image Acquisition and Processing XXII*, vol. 9330, pp. 15–22, SPIE, 2015.

[151] E. Y. Sidky, C.-M. Kao, and X. Pan, "Accurate image reconstruction from few-views and limited-angle data in divergent-beam ct," *Journal of X-ray Science and Technology*, vol. 14, no. 2, pp. 119–139, 2006.

[152] X. Jin, L. Li, Z. Chen, L. Zhang, and Y. Xing, "Anisotropic total variation for limited-angle ct reconstruction," in *IEEE Nuclear Science Symposuim & Medical Imaging Conference*, pp. 2232–2238, IEEE, 2010.

[153] E. Y. Sidky, J. H. Jørgensen, and X. Pan, "Convex optimization problem prototyping for image reconstruction in computed tomography with the chambolle–pock algorithm," *Physics in Medicine & Biology*, vol. 57, no. 10, p. 3065, 2012.

[154] A. Chambolle and T. Pock, "A first-order primal-dual algorithm for convex problems with applications to imaging," *Journal of mathematical imaging and vision*, vol. 40, no. 1, pp. 120–145, 2011.

[155] S. J. LaRoque, E. Y. Sidky, and X. Pan, "Accurate image reconstruction from few-view and limited-angle data in diffraction tomography," *JOSA A*, vol. 25, no. 7, pp. 1772–1782, 2008.

[156] K. Kim, H. Yoon, M. Diez-Silva, M. Dao, R. R. Dasari, and Y. Park, "High-resolution three-dimensional imaging of red blood cells parasitized by plasmodium falciparum and in situ hemozoin crystals using optical diffraction tomography," *Journal of biomedical optics*, vol. 19, no. 1, p. 011005, 2013.

[157] D. C. Harris and M. D. Bertolucci, *Symmetry and spectroscopy: an introduction to vibrational and electronic spectroscopy*. Courier Corporation, 1989.

[158] B. E. Saleh and M. C. Teich, *Fundamentals of photonics*. john Wiley & sons, 2019.

[159] J. M. Hollas, *Modern spectroscopy*. John Wiley & Sons, 2004.

[160] F. M. Lyng, E. Ó. Faoláin, J. Conroy, A. Meade, P. Knief, B. Duffy, M. Hunter, J. Byrne, P. Kelehan, and H. Byrne, "Vibrational spectroscopy for cervical cancer pathology, from biochemical analysis to diagnostic tool," *Experimental and molecular pathology*, vol. 82, no. 2, pp. 121–129, 2007.

[161] G. Clemens, J. R. Hands, K. M. Dorling, and M. J. Baker, "Vibrational spectroscopic methods for cytology and cellular research," *Analyst*, vol. 139, no. 18, pp. 4411–4444, 2014.

[162] M. Diem, A. Mazur, K. Lenau, J. Schubert, B. Bird, M. Miljković, C. Krafft, and J. Popp, "Molecular pathology via ir and raman spectral imaging," *Journal of biophotonics*, vol. 6, no. 11-12, pp. 855–886, 2013.

[163] A. M. Enejder, T. G. Scecina, J. Oh, M. Hunter, W. Shih, S. Sasic, G. L. Horowitz, and M. S. Feld, "Raman spectroscopy for noninvasive glucose measurements," *Journal of biomedical optics*, vol. 10, no. 3, p. 031114, 2005.

[164] P. Atkins and T. Overton, *Shriver and Atkins' inorganic chemistry*. Oxford University Press, USA, 2010.

[165] C. Kittel, "Introduction to solid state physics, john wiley & sons," *Inc., Sixth edition,(New York, 1986)*, 2005.

[166] E. Smith and G. Dent, *Modern Raman spectroscopy: a practical approach*. John Wiley & Sons, 2019.

[167] L. Ornstein, J. Rekveld, *et al.*, "Intensity measurements in the raman effect and the distribution law of maxwell-boltzmann," *Physical Review*, vol. 34, no. 5, p. 720, 1929.

[168] S. T. Thornton and A. Rex, *Modern physics for scientists and engineers*. Cengage Learning, 2012.

[169] D. N. Sathyanarayana, *Vibrational spectroscopy: theory and applications*. New Age International, 2015.

[170] J. R. Ferraro, *Introductory raman spectroscopy*. Elsevier, 2003.

[171] F. Bonnier, A. Mehmood, P. Knief, A. Meade, W. Hornebeck, H. Lambkin, K. Flynn, V. McDonagh, C. Healy, T. Lee, *et al.*, "In vitro analysis of immersed human tissues by raman microspectroscopy," *Journal of Raman spectroscopy*, vol. 42, no. 5, pp. 888–896, 2011.

[172] F. Bonnier, S. M. Ali, P. Knief, H. Lambkin, K. Flynn, V. McDonagh, C. Healy, T. Lee, F. M. Lyng, and H. J. Byrne, "Analysis of human skin tissue by raman microspectroscopy: dealing with the background," *Vibrational Spectroscopy*, vol. 61, pp. 124–132, 2012.

[173] K. Svoboda and S. M. Block, "Biological applications of optical forces," *Annual review of biophysics and biomolecular structure*, vol. 23, no. 1, pp. 247–285, 1994.

[174] J. R. Lepock, H. E. Frey, and K. P. Ritchie, "Protein denaturation in intact hepatocytes and isolated cellular organelles during heat shock," *The Journal of cell biology*, vol. 122, no. 6, pp. 1267–1276, 1993.

[175] K. Ritchie, B. Keller, K. Syed, and J. Lepock, "Hyperthermia (heat shock)-induced protein denaturation in liver, muscle and lens tissue as determined by differential scanning calorimetry," *International Journal of Hyperthermia*, vol. 10, no. 5, pp. 605–618, 1994.

[176] L. Cui, H. J. Butler, P. L. Martin-Hirsch, and F. L. Martin, "Aluminium foil as a potential substrate for atr-ftir, transflection ftir or raman spectrochemical analysis of biological specimens," *Analytical Methods*, vol. 8, no. 3, pp. 481–487, 2016.

[177] A. Shapiro, O. N. Gofrit, G. Pizov, J. K. Cohen, and J. Maier, "Raman molecular imaging: a novel spectroscopic technique for diagnosis of bladder cancer in urine specimens," *European urology*, vol. 59, no. 1, pp. 106–112, 2011.

[178] M. Grimbergen, C. Van Swol, R. Draga, P. Van Diest, R. Verdaasdonk, N. Stone, and J. Bosch, "Bladder cancer diagnosis during cystoscopy using raman spectroscopy," in *Photonic Therapeutics and Diagnostics V*, vol. 7161, p. 716114, International Society for Optics and Photonics, 2009.

[179] E. Canetta, M. Mazilu, A. C. De Luca, A. E. Carruthers, K. Dholakia, S. Neilson, H. Sargeant, T. Briscoe, C. S. Herrington, and A. C. Riches, "Modulated raman spectroscopy for enhanced identification of bladder tumor cells in urine samples," *Journal of biomedical optics*, vol. 16, no. 3, p. 037002, 2011.

[180] M. C. H. Prieto, P. Matousek, M. Towrie, A. W. Parker, M. P. Wright, A. Ritchie, and N. Stone, "Use of picosecond kerr-gated raman spectroscopy to suppress signals from both surface and deep layers in bladder and prostate tissue," *Journal of biomedical optics*, vol. 10, no. 4, p. 044006, 2005.

[181] M. M. Mariani, P. Lampen, J. Popp, B. R. Wood, and V. Deckert, "Impact of fixation on in vitro cell culture lines monitored with raman spectroscopy," *Analyst*, vol. 134, no. 6, pp. 1154–1161, 2009.

[182] F. Bonnier, D. Traynor, P. Kearney, C. Clarke, P. Knief, C. Martin, J. J. O'Leary, H. J. Byrne, and F. Lyng, "Processing thinprep cervical cytological samples for raman spectroscopic analysis," *Analytical Methods*, vol. 6, no. 19, pp. 7831–7841, 2014.

[183] L. Mikoliunaite, R. D. Rodriguez, E. Sheremet, V. Kolchuzhin, J. Mehner, A. Ramanavicius, and D. R. Zahn, "The substrate matters in the raman spectroscopy analysis of cells," *Scientific reports*, vol. 5, no. 1, pp. 1–10, 2015.

[184] B. W. De Jong, T. C. Bakker Schut, K. Maquelin, T. van der Kwast, C. H. Bangma, D.-J. Kok, and G. J. Puppels, "Discrimination between nontumor bladder tissue and tumor by raman spectroscopy," *Analytical chemistry*, vol. 78, no. 22, pp. 7761–7769, 2006.

[185] N. Stone, M. C. H. Prieto, P. Crow, J. Uff, and A. W. Ritchie, "The use of raman spectroscopy to provide an estimation of the gross biochemistry associated with urological pathologies," *Analytical and bioanalytical chemistry*, vol. 387, no. 5, pp. 1657–1668, 2007.

[186] M. Grimbergen, C. van Swol, R. van Moorselaar, J. Uff, A. Mahadevan-Jansen, and N. Stone, "Raman spectroscopy of bladder tissue in the presence of 5-aminolevulinic acid," *Journal of Photochemistry and Photobiology B: Biology*, vol. 95, no. 3, pp. 170–176, 2009.

[187] L. M. Fullwood, D. Griffiths, K. Ashton, T. Dawson, R. W. Lea, C. Davis, F. Bonnier, H. J. Byrne, and M. J. Baker, "Effect of substrate choice and tissue type on tissue preparation for spectral histopathology by raman microspectroscopy," *Analyst*, vol. 139, no. 2, pp. 446–454, 2014.

[188] F. Bonnier, P. Knief, A. Meade, J. Dorney, K. Bhattacharya, F. Lyng, and H. Byrne, "Collagen matrices as an improved model for in vitro study of live cells using raman microspectroscopy," in *European Conference on Biomedical Optics*, p. 80870F, Optical Society of America, 2011.

[189] J. M. Lerner, "Imaging spectrometer fundamentals for researchers in the biosciences—a tutorial," *Cytometry Part A: the journal of the International Society for Analytical Cytology*, vol. 69, no. 8, pp. 712–734, 2006.

[190] R. Kasprowicz, R. Suman, and P. O'Toole, "Characterising live cell behaviour: Traditional label-free and quantitative phase imaging approaches," *The international journal of biochemistry & cell biology*, vol. 84, pp. 89–95, 2017.

[191] S. Huh, R. Bise, M. Chen, T. Kanade, *et al.*, "Automated mitosis detection of stem cell populations in phase-contrast microscopy images," *IEEE transactions on medical imaging*, vol. 30, no. 3, pp. 586–596, 2010.

[192] M. Mir, Z. Wang, Z. Shen, M. Bednarz, R. Bashir, I. Golding, S. G. Prasanth, and G. Popescu, "Optical measurement of cycle-dependent cell growth," *Proceedings of the National Academy of Sciences*, vol. 108, no. 32, pp. 13124–13129, 2011.

[193] G. Popescu, L. P. Deflores, J. C. Vaughan, K. Badizadegan, H. Iwai, R. R. Dasari, and M. S. Feld, "Fourier phase microscopy for investigation of biological structures and dynamics," *Optics letters*, vol. 29, no. 21, pp. 2503–2505, 2004.

[194] A. F. Huxley and R. Niedergerke, "Structural changes in muscle during contraction: interference microscopy of living muscle fibres," *Nature*, vol. 173, no. 4412, pp. 971–973, 1954.

[195] P. Gao, B. Yao, I. Harder, N. Lindlein, and F. J. Torcal-Milla, "Phase-shifting zernike phase contrast microscopy for quantitative phase measurement," *Optics letters*, vol. 36, no. 21, pp. 4305–4307, 2011.

[196] C. Maurer, A. Jesacher, S. Bernet, and M. Ritsch-Marte, "Phase contrast microscopy with full numerical aperture illumination," *Optics express*, vol. 16, no. 24, pp. 19821–19829, 2008.

[197] I. Vartiainen, R. Mokso, M. Stampanoni, and C. David, "Halo suppression in full-field x-ray zernike phase contrast microscopy," *Optics letters*, vol. 39, no. 6, pp. 1601–1604, 2014.

[198] T. Otaki, "Artifact halo reduction in phase contrast microscopy using apodization," *Optical review*, vol. 7, no. 2, pp. 119–122, 2000.

[199] M. Rinehart, Y. Zhu, and A. Wax, "Quantitative phase spectroscopy," *Biomedical optics express*, vol. 3, no. 5, pp. 958–965, 2012.

[200] G. Popescu, T. Ikeda, R. R. Dasari, and M. S. Feld, "Diffraction phase microscopy for quantifying cell structure and dynamics," *Optics letters*, vol. 31, no. 6, pp. 775–777, 2006.

[201] Z. Yin, T. Kanade, and M. Chen, "Understanding the phase contrast optics to restore artifact-free microscopy images for segmentation," *Medical image analysis*, vol. 16, no. 5, pp. 1047–1062, 2012.

[202] I. Ersoy, F. Bunyak, M. A. Mackey, and K. Palaniappan, "Cell segmentation using hessian-based detection and contour evolution with directional derivatives," in *2008 15th IEEE International Conference on Image Processing*, pp. 1804–1807, IEEE, 2008.

[203] H. Su, Z. Yin, S. Huh, T. Kanade, and J. Zhu, "Interactive cell segmentation based on active and semi-supervised learning," *IEEE transactions on medical imaging*, vol. 35, no. 3, pp. 762–777, 2015.

[204] J. Pan, T. Kanade, and M. Chen, "Learning to detect different types of cells under phase contrast microscopy," *Microscopic Image Analysis with Applications in Biology (MIAAB)*, vol. 2009, 2009.

[205] M. E. Ambühl, C. Brepsant, J.-J. Meister, A. B. Verkhovsky, and I. F. Sbalzarini, "High-resolution cell outline segmentation and tracking from phase-contrast microscopy images," *Journal of microscopy*, vol. 245, no. 2, pp. 161–170, 2012.

[206] M. E. Kandel, M. Fanous, C. Best-Popescu, and G. Popescu, "Real-time halo correction in phase contrast imaging," *Biomedical optics express*, vol. 9, no. 2, pp. 623–635, 2018.

[207] D. Malacara, *Optical shop testing*, vol. 59. John Wiley & Sons, 2007.

[208] J. Otón, P. Ambs, M. S. Millán, and E. Pérez-Cabré, "Multipoint phase calibration for improved compensation of inherent wavefront distortion in parallel aligned liquid crystal on silicon displays," *Applied optics*, vol. 46, no. 23, pp. 5667–5679, 2007.

[209] L. Yang, J. Xia, C. Chang, X. Zhang, Z. Yang, and J. Chen, "Nonlinear dynamic phase response calibration by digital holographic microscopy," *Applied optics*, vol. 54, no. 25, pp. 7799–7806, 2015.

[210] S. Reichelt, "Spatially resolved phase-response calibration of liquid-crystal-based spatial light modulators," *Applied optics*, vol. 52, no. 12, pp. 2610–2618, 2013.

[211] J. Stigwall, "Optimization of a spatial light modulator for beam steering and tracking applications," *Department of physics and measurement technology lincÖping university. lincÖping Sweden*, 2002.

[212] D. Engström, M. Persson, J. Bengtsson, and M. Goksör, "Calibration of spatial light modulators suffering from spatially varying phase response," *Optics express*, vol. 21, no. 13, pp. 16086–16103, 2013.

[213] E. Ronzitti, M. Guillon, V. de Sars, and V. Emiliani, "Lcos nematic slm characterization and modeling for diffraction efficiency optimization, zero and ghost orders suppression," *Optics express*, vol. 20, no. 16, pp. 17843–17855, 2012.

[214] C.-J. Yu, J.-H. Park, J. Kim, M.-S. Jung, and S.-D. Lee, "Design of binary diffraction gratings of liquid crystals in a linearly graded phase model," *Applied optics*, vol. 43, no. 9, pp. 1783–1788, 2004.

[215] A. Browar, M. Shusteff, R. Panas, J. Ellis, and C. Spadaccini, "Overview and comparison of spatial light modulator calibration methods," tech. rep., Lawrence Livermore National Lab.(LLNL), Livermore, CA (United States), 2016.

[216] S. A. Benton and V. M. Bove Jr, *Holographic imaging*. John Wiley & Sons, 2008.

[217] R. Li and L. Cao, "Progress in phase calibration for liquid crystal spatial light modulators," *Applied Sciences*, vol. 9, no. 10, p. 2012, 2019.

[218] Y. Dai, J. Antonello, and M. J. Booth, "Calibration of a phase-only spatial light modulator for both phase and retardance modulation," *Optics express*, vol. 27, no. 13, pp. 17912–17926, 2019.

[219] Z. Zhao, Z. Xiao, Y. Zhuang, H. Zhang, and H. Zhao, "An interferometric method for local phase modulation calibration of lc-slm using self-generated phase grating," *Review of Scientific Instruments*, vol. 89, no. 8, p. 083116, 2018.

[220] M.-K. Kim, "Applications of digital holography in biomedical microscopy," *Journal of the Optical Society of Korea*, vol. 14, no. 2, pp. 77–89, 2010.

[221] M. K. Kim, "Digital holographic microscopy," in *Digital Holographic Microscopy*, pp. 149–190, Springer, 2011.

[222] G. Popescu, *Quantitative phase imaging of cells and tissues*. McGraw Hill Professional, 2011.

[223] G. Popescu, Y. Park, W. Choi, R. R. Dasari, M. S. Feld, and K. Badizadegan, "Imaging red blood cell dynamics by quantitative phase microscopy," *Blood Cells, Molecules, and Diseases*, vol. 41, no. 1, pp. 10–16, 2008.

[224] L. Tian, J. Wang, and L. Waller, "3d differential phase-contrast microscopy with computational illumination using an LED array," *Optics Letters*, vol. 39, no. 5, pp. 1326–1329, 2014.

[225] Z. F. Phillips, M. Chen, and L. Waller, "Single-shot quantitative phase microscopy with color-multiplexed differential phase contrast (cDPC)," *PloS One*, vol. 12, no. 2, p. e0171228, 2017.

[226] L. Ahrenberg, A. J. Page, B. M. Hennelly, J. B. McDonald, and T. J. Naughton, "Using commodity graphics hardware for real-time digital hologram view-reconstruction," *Journal of display technology*, vol. 5, no. 4, pp. 111–119, 2009.

[227] V. Micó, J. Zheng, J. Garcia, Z. Zalevsky, and P. Gao, "Resolution enhancement in quantitative phase microscopy," *Advances in Optics and Photonics*, vol. 11, no. 1, pp. 135–214, 2019.

[228] M. Ueda and T. Sato, "Superresolution by holography," *JOSA*, vol. 61, no. 3, pp. 418–419, 1971.

[229] M. Ueda, T. Sato, and M. Kondo, "Superresolution by multiple superposition of image holograms having different carrier frequencies," *Optica Acta: International Journal of Optics*, vol. 20, no. 5, pp. 403–410, 1973.

[230] V. Mico, Z. Zalevsky, P. Garcia-Martinez, and J. Garcia, "Single-step superresolution by interferometric imaging," *Optics express*, vol. 12, no. 12, pp. 2589–2596, 2004.

[231] V. Mico, Z. Zalevsky, P. García-Martínez, and J. García, "Superresolved imaging in digital holography by superposition of tilted wavefronts," *Applied optics*, vol. 45, no. 5, pp. 822–828, 2006.

[232] V. Mico, Z. Zalevsky, P. García-Martínez, and J. García, "Synthetic aperture superresolution with multiple off-axis holograms," *JOSA A*, vol. 23, no. 12, pp. 3162–3170, 2006.

[233] V. Mico, Z. Zalevsky, and J. Garcia, "Superresolution optical system by common-path interferometry," *Optics Express*, vol. 14, no. 12, pp. 5168–5177, 2006.

[234] T. Gutzler, T. R. Hillman, S. A. Alexandrov, and D. D. Sampson, "Coherent aperture-synthesis, wide-field, high-resolution holographic microscopy of biological tissue," *Optics letters*, vol. 35, no. 8, pp. 1136–1138, 2010.

[235] T. R. Hillman, T. Gutzler, S. A. Alexandrov, and D. D. Sampson, "High-resolution, wide-field object reconstruction with synthetic aperture fourier holographic optical microscopy," *Optics express*, vol. 17, no. 10, pp. 7873–7892, 2009.

[236] V. Mico, Z. Zalevsky, and J. García, "Synthetic aperture microscopy using off-axis illumination and polarization coding," *Optics communications*, vol. 276, no. 2, pp. 209–217, 2007.

[237] V. Micó, J. García, and Z. Zalevsky, "Axial superresolution by synthetic aperture generation," *Journal of Optics A: Pure and Applied Optics*, vol. 10, no. 12, p. 125001, 2008.

[238] D. J. Lee and A. M. Weiner, "Optical phase imaging using a synthetic aperture phase retrieval technique," *Optics express*, vol. 22, no. 8, pp. 9380–9394, 2014.

[239] G. Indebetouw, A. El Maghnouji, and R. Foster, "Scanning holographic microscopy with transverse resolution exceeding the rayleigh limit and extended depth of focus," *JOSA A*, vol. 22, no. 5, pp. 892–898, 2005.

[240] G. Indebetouw, Y. Tada, J. Rosen, and G. Brooker, "Scanning holographic microscopy with resolution exceeding the rayleigh limit of the objective by superposition of off-axis holograms," *Applied Optics*, vol. 46, no. 6, pp. 993–1000, 2007.

[241] X.-J. Lai, H.-Y. Tu, C.-H. Wu, Y.-C. Lin, and C.-J. Cheng, "Resolution enhancement of spectrum normalization in synthetic aperture digital holographic microscopy," *Applied optics*, vol. 54, no. 1, pp. A51–A58, 2015.

[242] Y. Choi, M. Kim, C. Yoon, T. D. Yang, K. J. Lee, and W. Choi, "Synthetic aperture microscopy for high resolution imaging through a turbid medium," *Optics letters*, vol. 36, no. 21, pp. 4263–4265, 2011.

[243] M. Kim, Y. Choi, W. Choi, C. M. Fang-Yen, Y. Sung, R. R. Dasari, M. S. Feld, and K. Kim, "Three-dimensional differential interference contrast microscopy using synthetic aperture imaging," *Journal of biomedical optics*, vol. 17, no. 2, p. 026003, 2012.

[244] J. Bühl, H. Babovsky, A. Kiessling, and R. Kowarschik, "Digital synthesis of multiple off-axis holograms with overlapping fourier spectra," *Optics communications*, vol. 283, no. 19, pp. 3631–3638, 2010.

[245] V. Micó, Z. Zalevsky, and J. Garcia, "Superresolved common-path phase-shifting digital inline holographic microscopy using a spatial light modulator," *Optics letters*, vol. 37, no. 23, pp. 4988–4990, 2012.

[246] A. Hussain, J. Martínez, A. Lizana, and J. Campos, "Super resolution imaging achieved by using on-axis interferometry based on a spatial light modulator," *Optics Express*, vol. 21, no. 8, pp. 9615–9623, 2013.

[247] Y.-C. Lin, H.-Y. Tu, X.-R. Wu, X.-J. Lai, and C.-J. Cheng, "One-shot synthetic aperture digital holographic microscopy with non-coplanar angular-multiplexing and coherence gating," *Optics express*, vol. 26, no. 10, pp. 12620–12631, 2018.

[248] S. Shin, D. Kim, K. Kim, and Y. Park, "Super-resolution three-dimensional fluorescence and optical diffraction tomography of live cells using structured illumination generated by a digital micromirror device," *Scientific reports*, vol. 8, no. 1, pp. 1–8, 2018.

[249] C. J. Schwarz, Y. Kuznetsova, and S. Brueck, "Imaging interferometric microscopy," *Optics letters*, vol. 28, no. 16, pp. 1424–1426, 2003.

[250] Y. Kuznetsova, A. Neumann, and S. Brueck, "–approaching the linear systems limits of optical resolution," *Optics express*, vol. 15, no. 11, pp. 6651–6663, 2007.

[251] A. Neumann, Y. Kuznetsova, and S. Brueck, "Structured illumination for the extension of imaging interferometric microscopy," *Optics express*, vol. 16, no. 10, pp. 6785–6793, 2008.

[252] Y. Kuznetsova, A. Neumann, and S. R. Brueck, "Imaging interferometric microscopy," *JOSA A*, vol. 25, no. 3, pp. 811–822, 2008.

[253] Y. Kuznetsova, A. Neumann, and S. Brueck, "Solid-immersion imaging interferometric nanoscopy to the limits of available frequency space," *JOSA A*, vol. 29, no. 5, pp. 772–781, 2012.

[254] A. Calabuig, J. Garcia, C. Ferreira, Z. Zalevsky, and V. Micó, "Resolution improvement by single-exposure superresolved interferometric microscopy with a monochrome sensor," *JOSA A*, vol. 28, no. 11, pp. 2346–2358, 2011.

[255] C. Yuan, H. Zhai, and H. Liu, "Angular multiplexing in pulsed digital holography for aperture synthesis," *Optics letters*, vol. 33, no. 20, pp. 2356–2358, 2008.

[256] L. Granero, C. Ferreira, Z. Zalevsky, J. García, and V. Micó, "Single-exposure super-resolved interferometric microscopy by rgb multiplexing in lensless configuration," *Optics and Lasers in Engineering*, vol. 82, pp. 104–112, 2016.

[257] D. Ruh, J. Mutschler, M. Michelbach, and A. Rohrbach, "Superior contrast and resolution by image formation in rotating coherent scattering (rocs) microscopy," *Optica*, vol. 5, no. 11, pp. 1371–1381, 2018.

[258] G. Maire, H. Giovannini, A. Talneau, P. C. Chaumet, K. Belkebir, and A. Sentenac, "Phase imaging and synthetic aperture super-resolution via total internal reflection microscopy," *Optics letters*, vol. 43, no. 9, pp. 2173–2176, 2018.

[259] S. Shin, Y. Kim, K. Lee, K. Kim, Y.-J. Kim, H. Park, and Y. Park, "Common-path diffraction optical tomography with a low-coherence illumination for reducing speckle noise," in *Quantitative Phase Imaging*, vol. 9336, p. 933629, International Society for Optics and Photonics, 2015.

[260] W.-C. Hsu, J.-W. Su, T.-Y. Tseng, and K.-B. Sung, "Tomographic diffractive microscopy of living cells based on a common-path configuration," *Optics letters*, vol. 39, no. 7, pp. 2210–2213, 2014.

[261] A. Calabuig, V. Micó, J. Garcia, Z. Zalevsky, and C. Ferreira, "Single-exposure super-resolved interferometric microscopy by red–green–blue multiplexing," *Optics letters*, vol. 36, no. 6, pp. 885–887, 2011.

[262] C. Yuan, G. Situ, G. Pedrini, J. Ma, and W. Osten, "Resolution improvement in digital holography by angular and polarization multiplexing," *Applied optics*, vol. 50, no. 7, pp. B6–B11, 2011.

[263] X.-J. Lai, C.-J. Cheng, Y.-C. Lin, and H.-Y. Tu, "Angular-polarization multiplexing with spatial light modulators for resolution enhancement in digital holographic microscopy," *Journal of Optics*, vol. 19, no. 5, p. 055607, 2017.

[264] Y. Fan, J. Sun, Q. Chen, X. Pan, L. Tian, and C. Zuo, "Optimal illumination scheme for isotropic quantitative differential phase contrast microscopy," *Photonics Research*, vol. 7, no. 8, pp. 890–904, 2019.

[265] A. D. Edelstein, M. A. Tsuchida, N. Amodaj, H. Pinkard, R. D. Vale, and N. Stuurman, "Advanced methods of microscope control using μmanager software," *Journal of biological methods*, vol. 1, no. 2, 2014.

[266] X. Fan, Z. Tang, K. O'Dwyer, and B. M. Hennelly, "An inexpensive portable self-reference module for digital holographic microscopy," in *Photonics*, vol. 8, p. 277, Multidisciplinary Digital Publishing Institute, 2021.

[267] N. T. Shaked, "Quantitative phase microscopy of biological samples using a portable interferometer," *Optics letters*, vol. 37, no. 11, pp. 2016–2018, 2012.

[268] R. N. Bracewell and R. N. Bracewell, *The Fourier transform and its applications*, vol. 31999. McGraw-hill New York, 1986.

[269] S. T. Thurman and J. R. Fienup, "Phase-error correction in digital holography," *JOSA A*, vol. 25, no. 4, pp. 983–994, 2008.

[270] H. Ding and G. Popescu, "Instantaneous spatial light interference microscopy," *Optics express*, vol. 18, no. 2, pp. 1569–1575, 2010.

[271] P. Kolman and R. Chmelík, "Coherence-controlled holographic microscope," *Optics Express*, vol. 18, no. 21, pp. 21990–22004, 2010.

[272] A. C. Kak, M. Slaney, and G. Wang, "Principles of computerized tomographic imaging," 2002.

[273] P. Müller, M. Schürmann, and J. Guck, "The theory of diffraction tomography," *arXiv preprint arXiv:1507.00466*, 2015.

[274] O. Haeberlé, K. Belkebir, H. Giovaninni, and A. Sentenac, "Tomographic diffractive microscopy: basics, techniques and perspectives," *Journal of Modern Optics*, vol. 57, no. 9, pp. 686–699, 2010.

[275] V. Lauer, "New approach to optical diffraction tomography yielding a vector equation of diffraction tomography and a novel tomographic microscope," *Journal of microscopy*, vol. 205, no. 2, pp. 165–176, 2002.

[276] L. Pollaro, S. Equis, B. Dalla Piazza, and Y. Cotte, "Stain-free 3d nanoscopy of living cells: A new holographic tomographic microscope for quantitative and non-invasive 3d live cell nanoscopy," *Optik & Photonik*, vol. 11, no. 1, pp. 38–42, 2016.

[277] S. Vertu, J. Flügge, J.-J. Delaunay, and O. Haeberlé, "Improved and isotropic resolution in tomographic diffractive microscopy combining sample and illumination rotation," *Central European Journal of Physics*, vol. 9, no. 4, pp. 969–974, 2011.

[278] T. Latychevskaia, "Lateral and axial resolution criteria in incoherent and coherent optics and holography, near-and far-field regimes," *Applied Optics*, vol. 58, no. 13, pp. 3597–3603, 2019.

[279] F. Dubois, C. Yourassowsky, O. Monnom, J.-C. Legros, O. Debeir IV, P. Van Ham, R. Kiss, and C. Decaestecker, "Digital holographic microscopy for the three-dimensional dynamic analysis of in vitro cancer cell migration," *Journal of biomedical optics*, vol. 11, no. 5, p. 054032, 2006.

[280] Z. El-Schich, A. Leida Mölder, and A. Gjörloff Wingren, "Quantitative phase imaging for label-free analysis of cancer cells—focus on digital holographic microscopy," *Applied Sciences*, vol. 8, no. 7, p. 1027, 2018.

[281] A. Mölder, M. Sebesta, M. Gustafsson, L. Gisselson, A. G. Wingren, and K. Alm, "Non-invasive, label-free cell counting and quantitative analysis of adherent cells using digital holography," *Journal of microscopy*, vol. 232, no. 2, pp. 240–247, 2008.

[282] B. Kemper, D. D. Carl, J. Schnekenburger, I. Bredebusch, M. Schäfer, W. Domschke, and G. von Bally, "Investigation of living pancreas tumor cells by digital holographic microscopy," *Journal of biomedical optics*, vol. 11, no. 3, p. 034005, 2006.

[283] Z. El-Schich, A. Mölder, H. Tassidis, P. Härkönen, M. F. Miniotis, and A. G. Wingren, "Induction of morphological changes in death-induced cancer cells monitored by holographic microscopy," *Journal of structural biology*, vol. 189, no. 3, pp. 207–212, 2015.

[284] Z. Movasaghi, S. Rehman, and I. U. Rehman, "Raman spectroscopy of biological tissues," *Applied Spectroscopy Reviews*, vol. 42, no. 5, pp. 493–541, 2007.

[285] A. Mahadevan-Jansen and R. R. Richards-Kortum, "Raman spectroscopy for the detection of cancers and precancers," *Journal of biomedical optics*, vol. 1, no. 1, pp. 31–70, 1996.

[286] G. W. Auner, S. K. Koya, C. Huang, B. Broadbent, M. Trexler, Z. Auner, A. Elias, K. C. Mehne, and M. A. Brusatori, "Applications of raman spectroscopy in cancer diagnosis," *Cancer and Metastasis Reviews*, vol. 37, no. 4, pp. 691–717, 2018.

[287] A. C. S. Talari, Z. Movasaghi, S. Rehman, and I. U. Rehman, "Raman spectroscopy of biological tissues," *Applied spectroscopy reviews*, vol. 50, no. 1, pp. 46–111, 2015.

[288] R. Smith, K. L. Wright, and L. Ashton, "Raman spectroscopy: an evolving technique for live cell studies," *Analyst*, vol. 141, no. 12, pp. 3590–3600, 2016.

[289] L. Kerr and B. Hennelly, "A multivariate statistical investigation of background subtraction algorithms for raman spectra of cytology samples recorded on glass slides," *Chemometrics and Intelligent Laboratory Systems*, vol. 158, pp. 61–68, 2016.

[290] D. Traynor, S. Duraipandian, C. M. Martin, J. J. O'Leary, and F. M. Lyng, "Improved removal of blood contamination from thinprep cervical cytology samples for raman spectroscopic analysis," *Journal of biomedical optics*, vol. 23, no. 5, p. 055001, 2018.

[291] S. H. B. Norazman, T. Nakamura, F. Kimura, and M. Yamaguchi, "Analysis of quantitative phase obtained by digital holography on h&e-stained pathological samples," *Artificial Life and Robotics*, vol. 24, no. 1, pp. 38–43, 2019.

[292] N. Pavillon, A. J. Hobro, and N. I. Smith, "Cell optical density and molecular composition revealed by simultaneous multimodal label-free imaging," *Biophysical journal*, vol. 105, no. 5, pp. 1123–1132, 2013.

[293] N. Pavillon and N. I. Smith, "Implementation of simultaneous quantitative phase with raman imaging," *EPJ Techniques and Instrumentation*, vol. 2, pp. 1–11, 2015.

[294] N. Pavillon, A. J. Hobro, S. Akira, and N. I. Smith, "Noninvasive detection of macrophage activation with single-cell resolution through machine learning," *Proceedings of the National Academy of Sciences*, vol. 115, no. 12, pp. E2676–E2685, 2018.

[295] J. W. Kang, N. Lue, C.-R. Kong, I. Barman, N. C. Dingari, S. J. Goldfless, J. C. Niles, R. R. Dasari, and M. S. Feld, "Combined confocal raman and quantitative phase microscopy system for biomedical diagnosis," *Biomedical optics express*, vol. 2, no. 9, pp. 2484–2492, 2011.

[296] J. Klossa, B. Wattelier, T. Happillon, D. Toubas, L. de Laulanie, V. Untereiner, P. Bon, and M. Manfait, "Quantitative phase imaging and raman microspectroscopy applied to malaria," in *Diagnostic pathology*, vol. 8, pp. 1–4, BioMed Central, 2013.

[297] N. McReynolds, F. G. Cooke, M. Chen, S. J. Powis, and K. Dholakia, "Multimodal discrimination of immune cells using a combination of raman spectroscopy and digital holographic microscopy," *Scientific reports*, vol. 7, no. 1, pp. 1–11, 2017.

[298] M. A. Ferrara, A. De Angelis, A. C. De Luca, G. Coppola, B. Dale, and G. Coppola, "Simultaneous holographic microscopy and raman spectroscopy monitoring of human spermatozoa photodegradation," *IEEE Journal of Selected Topics in Quantum Electronics*, vol. 22, no. 3, pp. 27–34, 2015.

[299] A. De Angelis, S. Managò, M. Ferrara, M. Napolitano, G. Coppola, and A. De Luca, "Combined raman spectroscopy and digital holographic microscopy for sperm cell quality analysis," *Journal of Spectroscopy*, vol. 2017, 2017.

[300] N. Stuurman, N. Amdodaj, and R. Vale, "μmanager: open source software for light microscope imaging," *Microscopy Today*, vol. 15, no. 3, pp. 42–43, 2007.

[301] J. Schindelin, C. T. Rueden, M. C. Hiner, and K. W. Eliceiri, "The imagej ecosystem: An open platform for biomedical image analysis," *Molecular reproduction and development*, vol. 82, no. 7-8, pp. 518–529, 2015.

[302] J. Schindelin, I. Arganda-Carreras, E. Frise, V. Kaynig, M. Longair, T. Pietzsch, S. Preibisch, C. Rueden, S. Saalfeld, B. Schmid, *et al.*, "Fiji: an open-source platform for biological-image analysis," *Nature methods*, vol. 9, no. 7, pp. 676–682, 2012.

[303] D. Liu, H. J. Byrne, L. O'Neill, and B. Hennelly, "Investigation of wavenumber calibration for raman spectroscopy using a polymer reference," in *Optical Sensing and Detection V*, vol. 10680, p. 1068027, International Society for Optics and Photonics, 2018.

[304] H. Martens and E. Stark, "Extended multiplicative signal correction and spectral interference subtraction: new preprocessing methods for near infrared spectroscopy," *Journal of pharmaceutical and biomedical analysis*, vol. 9, no. 8, pp. 625–635, 1991.

[305] K. H. Liland, T. Almöy, and B.-H. Mevik, "Optimal choice of baseline correction for multivariate calibration of spectra," *Applied spectroscopy*, vol. 64, no. 9, pp. 1007–1016, 2010.

[306] S. J. Barton and B. M. Hennelly, "An algorithm for the removal of cosmic ray artifacts in spectral data sets," *Applied spectroscopy*, p. 0003702819839098, 2019.

[307] H. Takeuchi, S. Hashimoto, and I. Harada, "Simple and efficient method to eliminate spike noise from spectra recorded on charge-coupled device detectors," *Applied spectroscopy*, vol. 47, no. 1, pp. 129–131, 1993.

[308] S. J. Barton, T. E. Ward, and B. M. Hennelly, "Algorithm for optimal denoising of raman spectra," *Analytical methods*, vol. 10, no. 30, pp. 3759–3769, 2018.

[309] A. E. Hoerl and R. W. Kennard, "Ridge regression: Biased estimation for nonorthogonal problems," *Technometrics*, vol. 12, no. 1, pp. 55–67, 1970.

[310] M. A. Hearst, S. T. Dumais, E. Osuna, J. Platt, and B. Scholkopf, "Support vector machines," *IEEE Intelligent Systems and their applications*, vol. 13, no. 4, pp. 18–28, 1998.

[311] S. Balakrishnama and A. Ganapathiraju, "Linear discriminant analysis-a brief tutorial," *Institute for Signal and information Processing*, vol. 18, no. 1998, pp. 1–8, 1998.

[312] J. R. Quinlan, *C4. 5: programs for machine learning*. Elsevier, 2014.

[313] L. E. Peterson, "K-nearest neighbor," *Scholarpedia*, vol. 4, no. 2, p. 1883, 2009.

[314] L. Breiman, "Random forests," *Machine learning*, vol. 45, no. 1, pp. 5–32, 2001.

[315] J. F. Díez-Pastor, S. E. Jorge-Villar, Á. Arnaiz-González, C. I. García-Osorio, Y. Díaz-Acha, M. Campeny, J. Bosch, and J. C. Melgarejo, "Machine learning algorithms applied to r aman spectra for the identification of variscite originating from the mining complex of g avà," *Journal of Raman Spectroscopy*, vol. 51, no. 9, pp. 1563–1574, 2020.

[316] H. Abdi and L. J. Williams, "Principal component analysis," *Wiley interdisciplinary reviews: computational statistics*, vol. 2, no. 4, pp. 433–459, 2010.

[317] L. Fan, H. Wang, X. Wu, S. Wang, Y. Han, and J. Wang, "Raman spectroscopic study of benign and malignant ovarian tissues," *Laser Physics*, vol. 32, no. 3, p. 035601, 2022.

[318] J. A. M. Bispo, E. E. de Sousa Vieira, L. Silveira Jr, and A. B. Fernandes, "Correlating the amount of urea, creatinine, and glucose in urine from patients with diabetes mellitus and hypertension with the risk of developing renal lesions by means of raman spectroscopy and principal component analysis," *Journal of biomedical optics*, vol. 18, no. 8, p. 087004, 2013.

[319] R. Pandey, S. K. Paidi, T. A. Valdez, C. Zhang, N. Spegazzini, R. R. Dasari, and I. Barman, "Noninvasive monitoring of blood glucose with raman spectroscopy," *Accounts of chemical research*, vol. 50, no. 2, pp. 264–272, 2017.

[320] S. Pilotto, M. Pacheco, L. Silveira Jr, A. Balbin Villaverde, and R. Zangaro, "Analysis of near-infrared raman spectroscopy as a new technique for a transcutaneous non-invasive diagnosis of blood components," *Lasers in medical science*, vol. 16, no. 1, pp. 2–9, 2001.

[321] K. Virkler and I. K. Lednev, "Raman spectroscopic signature of blood and its potential application to forensic body fluid identification," *Analytical and bioanalytical chemistry*, vol. 396, no. 1, pp. 525–534, 2010.

[322] J. Y. Qu, B. C. Wilson, and D. Suria, "Concentration measurements of multiple analytes in human sera by near-infrared laser raman spectroscopy," *Applied optics*, vol. 38, no. 25, pp. 5491–5498, 1999.

[323] J. Y. Qu and L. Shao, "Near-infrared raman instrument for rapid and quantitative measurements of clinically important analytes," *Review of Scientific Instruments*, vol. 72, no. 6, pp. 2717–2723, 2001.

[324] C. J. Saatkamp, M. L. de Almeida, J. A. M. Bispo, A. L. B. Pinheiro, A. B. Fernandes, and L. Silveira Jr, "Quantifying creatinine and urea in human urine through raman spectroscopy aiming at diagnosis of kidney disease," *Journal of biomedical optics*, vol. 21, no. 3, p. 037001, 2016.

[325] S. J. Barton, B. M. Hennelly, T. Ward, K. Domijan, and J. Lowry, "A review of raman for multicomponent analysis," *Biophotonics: Photonic Solutions for Better Health Care IV*, vol. 9129, pp. 16–28, 2014.

[326] J. W. McMurdy III and A. J. Berger, "Raman spectroscopy-based creatinine measurement in urine samples from a multipatient population," *Applied spectroscopy*, vol. 57, no. 5, pp. 522–525, 2003.

[327] H. J. Butler, L. Ashton, B. Bird, G. Cinque, K. Curtis, J. Dorney, K. Esmonde-White, N. J. Fullwood, B. Gardner, P. L. Martin-Hirsch, *et al.*, "Using raman spectroscopy to characterize biological materials," *Nature protocols*, vol. 11, no. 4, pp. 664–687, 2016.

[328] D. M. Haaland and E. V. Thomas, "Partial least-squares methods for spectral analyses. 1. relation to other quantitative calibration methods and the extraction of qualitative information," *Analytical chemistry*, vol. 60, no. 11, pp. 1193–1202, 1988.

[329] A. J. Berger, I. Itzkan, and M. S. Feld, "Feasibility of measuring blood glucose concentration by near-infrared raman spectroscopy," *Spectrochimica Acta Part A: Molecular and Biomolecular Spectroscopy*, vol. 53, no. 2, pp. 287–292, 1997.

[330] A. J. Berger, T.-W. Koo, I. Itzkan, G. Horowitz, and M. S. Feld, "Multicomponent blood analysis by near-infrared raman spectroscopy," *Applied optics*, vol. 38, no. 13, pp. 2916–2926, 1999.

[331] D. Rohleder, W. Kiefer, and W. Petrich, "Quantitative analysis of serum and serum ultrafiltrate by means of raman spectroscopy," *Analyst*, vol. 129, no. 10, pp. 906–911, 2004.

[332] D. Qi and A. J. Berger, "Quantitative analysis of raman signal enhancement from aqueous samples in liquid core optical fibers," *Applied spectroscopy*, vol. 58, no. 10, pp. 1165–1171, 2004.

[333] L. T. Kerr, H. J. Byrne, and B. M. Hennelly, "Optimal choice of sample substrate and laser wavelength for raman spectroscopic analysis of biological specimen," *Analytical Methods*, vol. 7, no. 12, pp. 5041–5052, 2015.

[334] D. Qi and A. J. Berger, "Quantitative concentration measurements of creatinine dissolved in water and urine using raman spectroscopy and a liquid core optical fiber," *Journal of biomedical optics*, vol. 10, no. 3, p. 031115, 2005.

[335] R. Altkorn, I. Koev, and M. J. Pelletier, "Raman performance characteristics of teflon®-af 2400 liquid-core optical-fiber sample cells," *Applied spectroscopy*, vol. 53, no. 10, pp. 1169–1176, 1999.

[336] R. Altkorn, M. D. Malinsky, R. P. Van Duyne, and I. Koev, "Intensity considerations in liquid core optical fiber raman spectroscopy," *Applied Spectroscopy*, vol. 55, no. 4, pp. 373–381, 2001.

[337] D. Qi and A. J. Berger, "Correction method for absorption-dependent signal enhancement by a liquid-core optical fiber," *Applied optics*, vol. 45, no. 3, pp. 489–494, 2006.

[338] C. Hammond, M. Cayre, A. Panatier, and E. Avignone, "Neuron–glial cell cooperation," *Cellular and molecular neurophysiology*, vol. 25, 2014.

[339] S. P. Reddy, P. Ramani, and P. Nainani, "Confocal microscopy and exfoliative cytology," *Journal of oral and maxillofacial pathology: JOMFP*, vol. 17, no. 2, p. 217, 2013.

[340] B. Matsumoto, *Cell biological applications of confocal microscopy*. Elsevier, 2003.

[341] W. Hoheisel, W. Jacobsen, B. Lüttge, and W. Weiner, "Confocal microscopy: applications in materials science," *Macromolecular Materials and Engineering*, vol. 286, no. 11, pp. 663–668, 2001.

[342] D. Hovis and A. Heuer, "The use of laser scanning confocal microscopy (lscm) in materials science," *Journal of microscopy*, vol. 240, no. 3, pp. 173–180, 2010.

[343] C. Franck, S. Hong, S. Maskarinec, D. Tirrell, and G. Ravichandran, "Three-dimensional full-field measurements of large deformations in soft materials using confocal microscopy and digital volume correlation," *Experimental mechanics*, vol. 47, no. 3, pp. 427–438, 2007.

[344] S. McCain, M. Gehm, Y. Wang, N. Pitsianis, and D. Brady, "Coded aperture raman spectroscopy for quantitative measurements of ethanol in a tissue phantom," *Applied spectroscopy*, vol. 60, no. 6, pp. 663–671, 2006.

[345] T. Wilson, "Resolution and optical sectioning in the confocal microscope," *Journal of microscopy*, vol. 244, no. 2, pp. 113–121, 2011.

[346] S. L. Jacques, "Optical properties of biological tissues: a review," *Physics in Medicine & Biology*, vol. 58, no. 11, p. R37, 2013.

[347] I. S. Saidi, *Transcutaneous optical measurement of hyperbilirubinemia in neonates*. PhD thesis, Rice University, 1992.

[348] L. Wang and S. L. Jacques, "Use of a laser beam with an oblique angle of incidence to measure the reduced scattering coefficient of a turbid medium," *Applied optics*, vol. 34, no. 13, pp. 2362–2366, 1995.

[349] M. Johns, C. A. Giller, D. C. German, and H. Liu, "Determination of reduced scattering coefficient of biological tissue from a needle-like probe," *Optics express*, vol. 13, no. 13, pp. 4828–4842, 2005.

[350] B. D. Beier and A. J. Berger, "Method for automated background subtraction from raman spectra containing known contaminants," *Analyst*, vol. 134, no. 6, pp. 1198–1202, 2009.

[351] I. R. Lewis and H. Edwards, *Handbook of Raman spectroscopy: from the research laboratory to the process line*. CRC press, 2001.

[352] F. Bonnier, F. Petitjean, M. J. Baker, and H. J. Byrne, “Improved protocols for vibrational spectroscopic analysis of body fluids,” 2014.